

**Unclassified**

AD A 285 265

MASSACHUSETTS INSTITUTE OF TECHNOLOGY  
LINCOLN LABORATORY

**PROCEEDINGS OF THE 1994  
SPACE SURVEILLANCE WORKSHOP**

PROJECT REPORT STK-221  
VOLUME I

5-7 APRIL 1994

The twelfth Annual Space Surveillance Workshop held on 5-7 April 1994 was hosted by MIT Lincoln Laboratory and provided a forum for space surveillance issues. This *Proceedings* documents most of the presentations, with minor changes where necessary.

Approved for public release; distribution is unlimited.

DTIC QUALITY INSPECTED 3

LEXINGTON

MASSACHUSETTS


Unclassified

## PREFACE

The Twelfth Annual Space Surveillance Workshop sponsored by ESC/ MIT Lincoln Laboratory will be held on 5, 6 and 7 April 1994. The purpose of this series of workshops is to provide a forum for the presentation and discussion of space surveillance issues.

This *Proceedings* documents most of the presentations from this workshop. The papers contained were reproduced directly from copies supplied by their authors (with minor mechanical changes where necessary). It is hoped that this publication will enhance the utility of the workshop.

Mr. Kurt P. Schwan  
Editor

Accession For	
NTIS CRA&I DTIC TAB Unannounced Justification .....	
By .....	
Distribution /	
Availability Codes	
Dist	Avail and/or Special
A-1	

## TABLE OF CONTENTS

<b>The Russian Space Surveillance System: Characteristics and Comparisons with the US SSN</b>	1
<i>David N. Rodvold and Nicholas L. Johnson - Kaman Sciences Corp.</i>	
<b>Education With Global Reach</b>	7
<i>Lt. Col. Michael J. Muolo - Air Command and Staff College (ACSC) - Space Applications Facility</i>	
<b>Uncorrelated Track Processing and Identification in SPADOC 4C</b>	15
<i>David Cappellucci - Loral Command and Control Systems</i>	
<b>Improved Space Surveillance Capability at the Naval Space Operations Center</b>	25
<i>Stephen H. Knowles - Naval Space Command</i>	
<b>A Feasibility Analysis System for Surveillance Experiments with the MSX</b>	35
<i>Ramaswamy Sridharan, Gary F. Duff, Tony L. Hayes and Andrew J. Wiseman - MIT Lincoln Laboratory</i>	
<b>MSX Reference Sphere Detection and Tracking</b>	53
<i>James M. Rumreich and Ramaswamy Sridharan - MIT Lincoln Laboratory</i>	
<b>Space-Based Space Surveillance Cost and Performance Study Results</b>	71
<i>Maj. Rudolfo Firpo and Capt. Gordon Peredo - USAF SMC Arthur O. Morse - Aerospace Corp.</i>	
<b>Analysing and Modelling Debris in the Geostationary Transfer Orbit</b>	77
<i>Rudiger Jehn - European Space Agency</i>	
<b>The Use of Radar Cross Section Measurements to Characterize the Space Debris Environment</b>	91
<i>Mark J. Matney - Lockheed Engineering &amp; Sciences Co. Donald J. Kessler - NASA Johnson Space Center</i>	
<b>Analysis of Orbital Debris Data Collected Using the Haystack Radar</b>	101
<i>Thomas E. Tracy - Lockheed Engineering &amp; Sciences Co. Eugene G. Stansbery and John F. Stanley - NASA Johnson Space Center</i>	

<b>Modelling of Satellite Breakup and Fragment Detection</b>	113
<i>J.S.B. Dick - Greenwich Observatory</i>	
<i>R. Crowther - Defence Research Agency</i>	
<b>A CCD Search For Geosynchronous Debris From the Breakup of SSC 3432</b>	121
<i>Peter D. Tennyson and G. Edward Powell - MIT Lincoln Laboratory</i>	
<b>Space Debris Measurements: Phase One Final Report</b>	125
<i>Eric C. Pearce, Matthew S. Blythe, David M. Gibson and Peter J. Trujillo - MIT Lincoln Laboratory</i>	
<b>An Active Imaging Technique That Attains Ultra-High Resolution With Ultra-Low Transmitter Power</b>	135
<i>Richard B. Holmes, A. MacGovern, A. Bhowmik, P. White, P. Idenn - Rocketdyne Division, Rockwell International Corporation</i>	
<b>Proposal of a Coherent Bistatic Radar Correlated by VLBI Technique</b>	141
<i>Tadashi Takano and Masanobu Yajima - Institute of Space &amp; Astronautical Sciences</i>	
<b>Prospects For Observing Space Debris With Solar Coronagraphs</b>	147
<i>Donald F. Neidig - Phillips Laboratory</i>	
<i>Edward E. Deluca - Harvard-Smithsonian Astro. Obs.</i>	
<i>Iraida S. Kim - Sternberg Sate Astro. Inst., Moscow</i>	
<i>Serge Koutchmy - Institut d'Astrophysique de Paris</i>	
<i>Raymond N. Smartt - National Solar Observatory</i>	
<b>The AEOS 3.67 m Telescope and Facility</b>	153
<i>S. Tapia, I.A. DeLaRue, R.A. Frosch, K.E. Kern, K. Kuo and K. Zeringue - Phillips Laboratory</i>	
<i>D. Forrester - S Systems Co.</i>	
<i>T. Jakab, D. Mooney and S. Smith - Contraves Inc.</i>	
<i>R. Richmond - Rockwell Power Systems</i>	
<b>Hyperspectral Imaging of Near-Earth Space Objects at the Phillips Laboratory</b>	163
<i>Amy E. Prochko - W.J. Schafer Assoc.</i>	
<i>Susan Durham and Tamara Payne - Phillips Laboratory</i>	
<i>E. Holbert and J. Bruce Rafert - Florida Institute of Technology</i>	
<i>Richard Horton - SAIC</i>	
<i>S.A. Gregory - U of New Mexico</i>	
<b>Coherent Laser Radiometric Measurements of LEO Satellites</b>	173
<i>David G. Voelz, William Richard, Douglas B. Rider, David H. Stoke - Phillips Laboratory</i>	
<i>Kathy J. Schulze - Rockwell Power Systems</i>	
<i>David Dean - Hughes Aircraft</i>	

<b>GEODSS Upgrade Prototype System (GUPS)</b>	<b>181</b>
<i>C. Max Williams and Sam D. Redford - TRW</i>	
<b>Angles-Only Data Association in the Naval Space Surveillance System</b>	<b>191</b>
<i>Paul W. Schumacher, Jr. and D.A. Cooper - Naval Space Command</i>	
<b>A UNIX-Processor Based High-Altitude Satellite Monitoring Capability That Uses Narrowband Signatures</b>	<b>207</b>
<i>Richard C. Raup - MIT Lincoln Laboratory</i>	
<b>A Sensitivity Upgrade for the Millimeter Wave Radar at Kwajalein</b>	<b>217</b>
<i>Jeffrey C. McHarg and William D. Fitzgerald - MIT Lincoln Laboratory</i>	
<b>Recent Improvements at the ALTAIR Radar</b>	<b>229</b>
<i>Stephen J. Chapman, Andrew D. Gerber, Gregory G. Hogan and Stephen M. Hunt -MIT Lincoln Laboratory</i>	
<i>Robert M. Anderson, John B. Conrad, Dale L. Sponseller and Mark J. Schlueter -Raytheon Range Systems Engineering</i>	
<b>Recent and Planned Improvements to the Kwajalein Imaging Radar</b>	<b>241</b>
<i>Randy K. Avent, Christopher H. Moulton and Stephan B. Rejto - MIT Lincoln Laboratory</i>	
<b>Enhancements to the UK SOI Facility at Hertsmonceux</b>	<b>247</b>
<i>J.S.B. Dick - Royal Greenwich Observatory</i>	
<i>A. Greenaway and Peter Liddell - Defence Research Agency</i>	

## The Russian Space Surveillance System: Characteristics and Comparisons with the US SSN

D.M. Rodvold and N. L. Johnson (Kaman Sciences Corporation)

In early 1992 Kaman Sciences Corporation began direct communications and a series of cooperative efforts with principal space surveillance organizations within the Russian Federation for the purpose of better understanding the nature and evolutionary trends of the orbital debris environment. Non-functional satellites now make up approximately 94% of the tracked Earth satellite population, significantly impacting the operations and the design of all space surveillance systems. Moreover, the much larger number of smaller debris produced by satellite fragmentations pose real hazards to the survivability of active spacecraft, including manned vehicles.

For more than two years Kaman Sciences has worked closely with its colleagues at the Kosmos Scientific Research Center, the Vympel Corporation (formerly, the Vympel Central Scientific Production Association), and the Institute of Astronomy of the Russian Academy of Sciences (RAN). The objective of these technical interchanges has been to develop a baseline understanding of respective orbital debris surveillance capabilities, data transformation techniques (Russian format to US format and vice versa), and the feasibility of routine sharing of orbital debris surveillance data.

To date Kaman Sciences has received a significant volume of Russian data including:

- (1) the identification, location, and coverage parameters of radar, optical, and electro-optical space surveillance facilities capable of detecting orbital debris in low Earth orbits (LEO) and in high Earth orbits (HEO);
- (2) orbital parameters and size estimates on approximately 2,300 orbital debris in LEO;
- (3) orbital parameters and satellite characterization data and techniques on geosynchronous Earth orbit (GEO) satellites; and
- (4) the official standard Russian atmospheric model, including FORTRAN code.

In addition, more than 120 Russian papers on space surveillance operational practices and on special studies have been acquired and specific dialogs have been undertaken to gain insight into specialized software and algorithms employed by SSS personnel. Kaman Sciences is currently exploring the possibility of the routine exchange of space surveillance data and the temporary exchange of space surveillance specialists to improve orbital debris monitoring techniques.

The three organizations identified above play significant roles in the operation of the Russian Space Surveillance System (SSS), formerly known as the System for Monitoring Outer Space (SKKP) of the USSR. The space surveillance mission using national defense assets evolved into a separate organization during 1969-1970. Space surveillance of LEO is primarily conducted by a network comprised of ten radar facilities: 8 Ballistic Missile Early Warning System (BMEWS) and 2 closely linked Anti-Ballistic Missile (ABM) sites. These facilities are located across the former Soviet Union, i.e., Russia (Irkutsk, Moscow (2), Murmansk, Pechora), Ukraine (Sevastopol, Uzhgorod), Kazakhstan (Balkhash), Azerbaijan (Mingechar), and Latvia (Riga). The majority of these facilities operate at VHF frequencies, but some operate at UHF. Typical minimum and maximum space surveillance elevations are 1-5 deg and 50-55 deg, respectively. The breadth of azimuth coverage varies considerably from site to site.

A space object catalog of more than 5,000 satellites is maintained by this radar network, although entries for only 90% of the objects possess "current" orbital data. Approximately 50,000 observations are collected by the network each day with a 99% correlation rate focused at the Information Processing Center rather than at the individual sites. Normally, fewer than 100 objects are maintained in a temporary file awaiting track confirmation and official cataloging.

In March, 1992, Kaman Sciences examined statistical Russian satellite catalog data on 2,319 objects assigned to 37 international designators, almost all debris from satellite fragmentations. One of the conclusions of this study was that the Russian small satellite catalog was approximately 75% of its US counterpart, after taking into consideration low inclination coverage limitations of the Russian SSS. To understand better the causes of this discrepancy, Kaman Sciences and the Vympel Corporation with support from the Kosmos Scientific Research Center agreed to cooperate on a discrete satellite correlation effort. Vympel and Kosmos Scientific Research Center provided a database of orbital parameters for 2,312 satellites assigned to 49 international designators as of 22 August 1992.

Unfortunately, the set of orbital parameters (inclination, perigee, apogee, right ascension of the ascending node, argument of perigee, ballistic coefficient, the decline in orbital period per revolution, and integer date) was insufficient to create a complete state vector for each satellite for comparison with a saved US satellite catalog database of the same date. Therefore, the correlation process was largely performed on a cloud-by-cloud basis using a correlation difference variable which was a function,  $F$ , of inclination, period, perigee, right ascension, and size estimates derived from radar cross-section data. For each cloud,  $F$  was calculated for all possible pairings, and  $\Sigma F$  was minimized while disallowing excessive values of  $F$ . The technique was validated by comparison with previous manual correlations of clouds with small or moderate numbers of constituents.

The correlation process was hindered by a number of problems, including the incompleteness of the Vympel data, the round-off of epoch values, the age of some orbital data, different geodetic models, uncataloged satellites (particularly in the US), and miscataloged satellites (in both US and Russian catalogs). However, 90.5% of the Russian database was eventually correlated with confidence to the US satellite catalog. Figure 1 indicates the distribution of both correlated and uncorrelated satellites in the Russian database with mean altitudes below 4,000 km. Figure 2 is a similar plot of the US database which contained 2986 satellites. The distribution of the uncorrelated satellites in both figures is relatively uniform.

An analysis of apparent size (Figures 3 and 4) suggests that the Russian SSS is less sensitive to small orbital debris than is the US Space Surveillance Network (SSN). This hypothesis has been supported by further studies. In addition, a slight bias in satellite size estimates may exist between the two systems with the Russian estimates being lower below approximately 1,250 km and higher above that altitude. Size and altitude were also clear factors in the ability of the Russian SSS to maintain current orbital elements (Figures 5 and 6). Finally, radar space surveillance in the SSS is also hampered by apparent range limitations.

To perform surveillance of satellites in GEO and other high altitude orbits, the former Soviet Union deployed at least 21 optical or electro-optical facilities at 14 geographic locations: Russia (Irkutsk, Kourovka, Krasnodar, Uzhno-Sakhalinsk, Zvenigorod), Ukraine (Kiev, Odessa, Simeiz, Uzhgorod), Kazakhstan (Alma Ata), Armenia (Burokan), Georgia (Abastumani), Tadjikistan (Dushanbe), and Turkmenia (Ashgabad). Seven of these sites are supported jointly by the SSS and the RAN, while five sites belong principally to the SSS and two to the RAN. The RAN has operated additional equipment at sites in Bolivia, Chile, Ecuador, and Egypt. Typical optical diameters of all facilities are 45-100 cm.

Positional surveys in GEO are conducted by the RAN for the SSS as well as for internal studies. The principal instruments used for these surveys are the Russian-designed VAU at Hissar (Dushanbe) and Zvenigorod and the German-designed SBG at Kourovka and Simeiz. The VAU has an optical diameter of 50 cm, a focal length of 70 cm, a field-of-view of 5 deg x 30 deg, and a limiting magnitude of 15. Similarly, the SBG has an optical diameter of 42.5 cm, focal length of 77 cm, field-of-view of 6 deg by 8 deg, and a limiting magnitude of 14. Positional accuracies for GEO satellites are reported to be 1-2 arc seconds. Due to their relatively close geographical locations, these four sites are essentially restricted to viewing the geosynchronous ring between 25 W and 120 E.

In a recent (late 1993) 4-night GEO survey conducted at Zvenigorod, a total of 153 objects (stabilized and drifting) were observed at least twice. Of these 117 objects were positively identified with US SSN data provided to RAN via Goddard and the European Space Operations Center (ESOC).

At Kaman Sciences' request, the Institute of Astronomy observed the 1968-81E Transtage for purpose of discerning its general configuration following the reported breakup on 21 February 1992. With facilities at Zvenigorod (60 cm telescope), Hissar (70 cm telescope), and Simeiz (100 cm telescope), the institute had demonstrated the ability to perform inverse photometric analyses using long-duration observations in U, B, V, and R. These impressive analyses produced structural and material reconstructions of the observed satellites.

However, since the 1968-81E Transtage was in an orbit with an inclination in excess of 3 deg, the primary instrument available for the observations was the Zeiss-1000/PG-3M system at Simeiz. The Zeiss-1000 has an optical diameter 101.6 cm, a focal length of 1330 cm, a field-of-view of 2.5', and a limiting magnitude of 17.46. The PG-3M is a 2-stage cascade image tube with a 256 x 256 CCD. The integrated light observations were calibrated with star clusters NGC 6981, IC 4665, and the Pleiades. The conclusion of institute personnel after analyzing considerable data from numerous observations is that a hole exists in the side of the 1968-81E Transtage.

In summary, the Russian SSS LEO accuracies and size estimates appear to be comparable to the US SSN. General deficiencies noted in the SSS data involve the tracking of low inclination orbits and highly elliptical orbits, radar range limitations, and invisibility of most of the Western Hemisphere portion of the GEO arc. Russian radar surveillance of LEO appears to be slightly less sensitive than that of the US SSN, while Russian GEO SOI techniques offer potential means for investigating spacecraft anomalies at high altitudes.



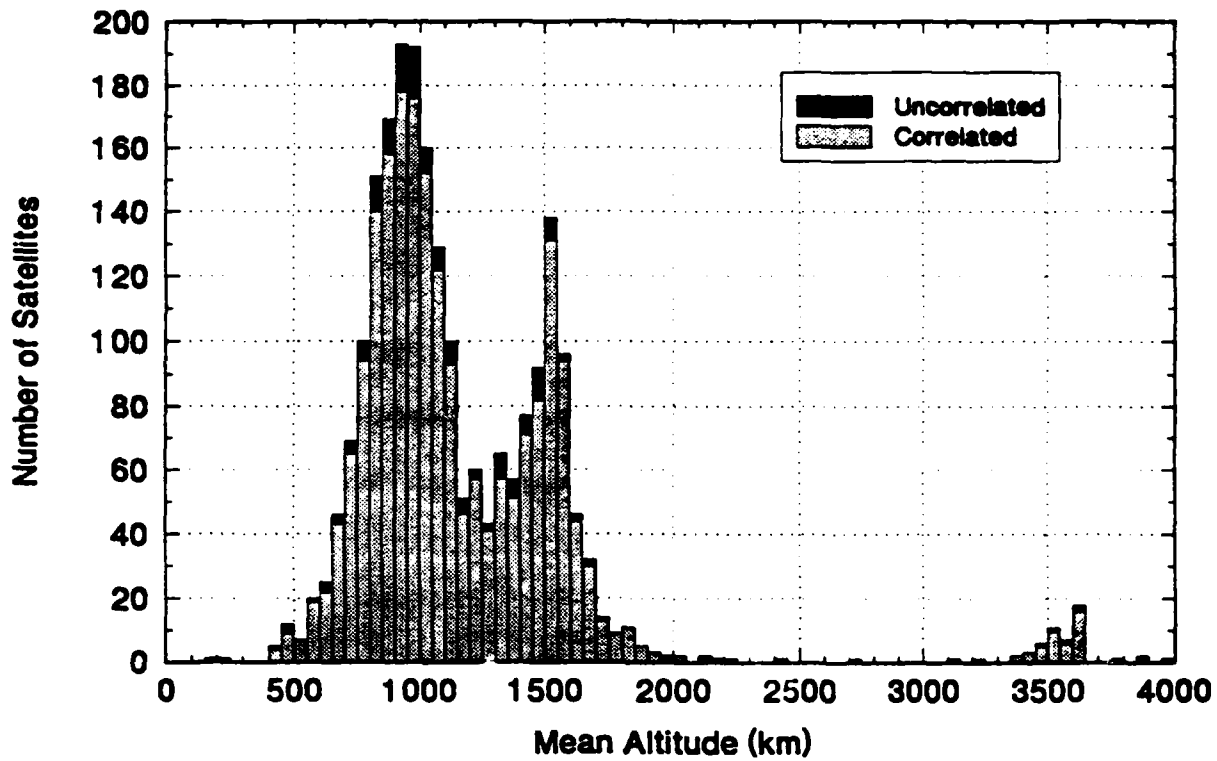


Figure 1. Altitude Distribution of Correlated and Uncorrelated Satellites from Russian Database.

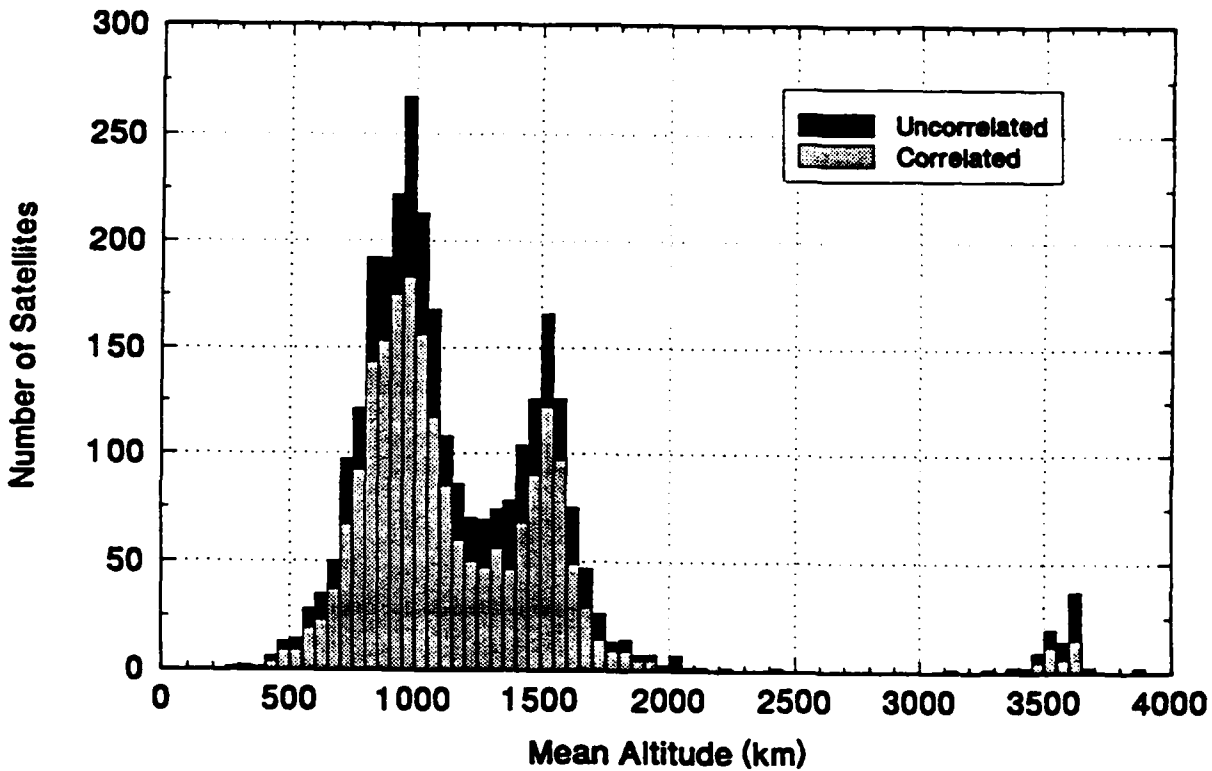


Figure 2. Altitude Distribution of Correlated and Uncorrelated Satellites from US Database.

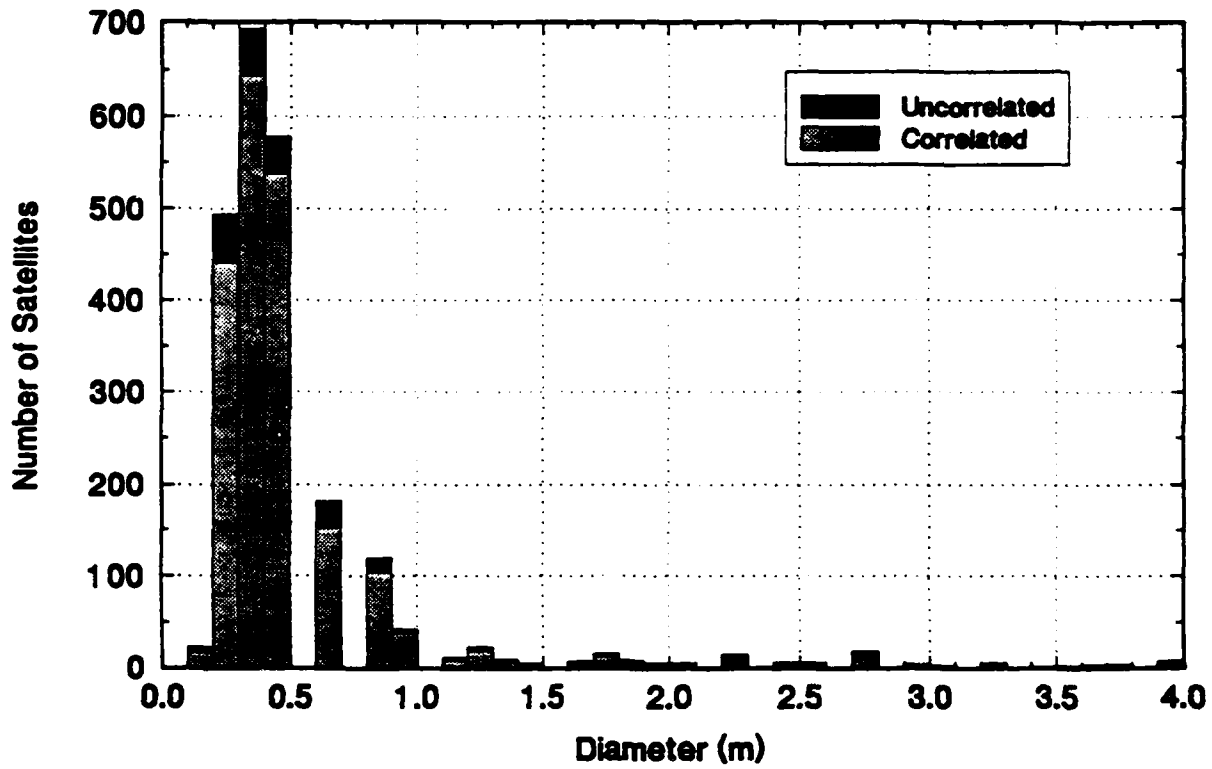


Figure 3. Size Distribution of Correlated and Uncorrelated Satellites from Russian Database.

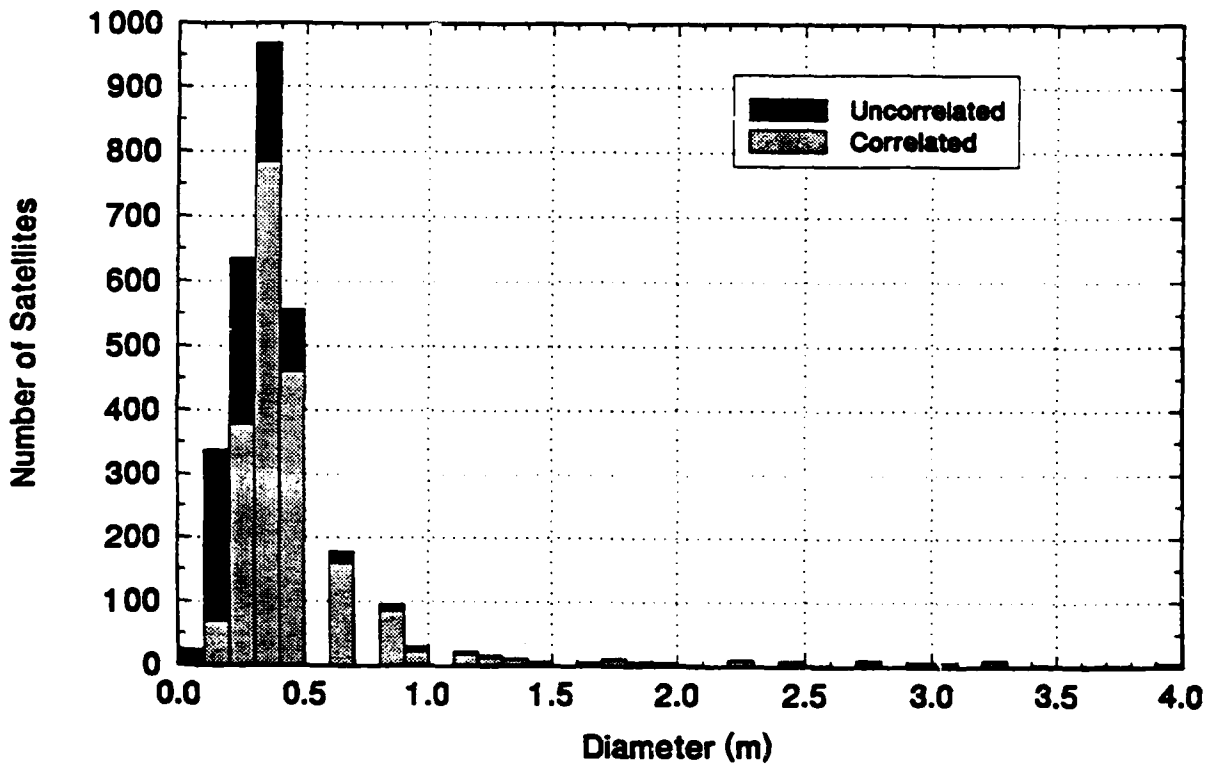


Figure 4. Size Distribution of Correlated and Uncorrelated Satellites from US Database.

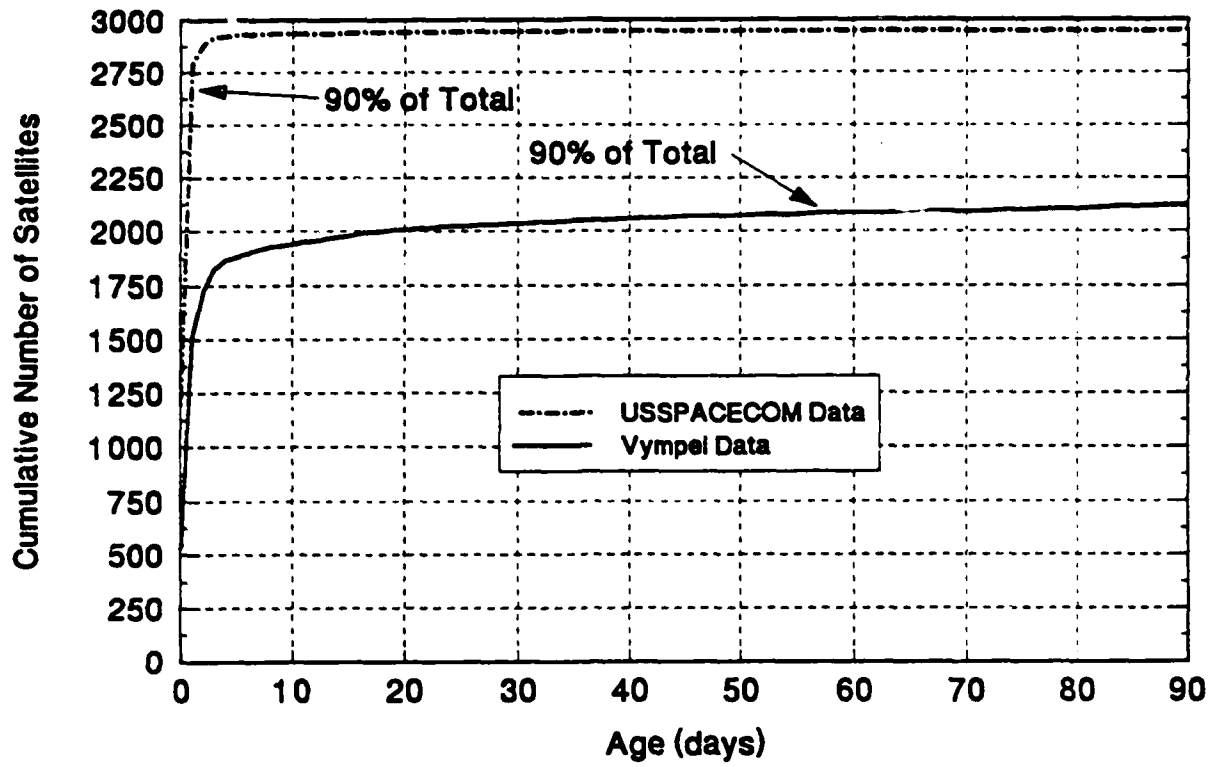


Figure 5. Comparative Currency of US and Russian Satellite Catalog Data.

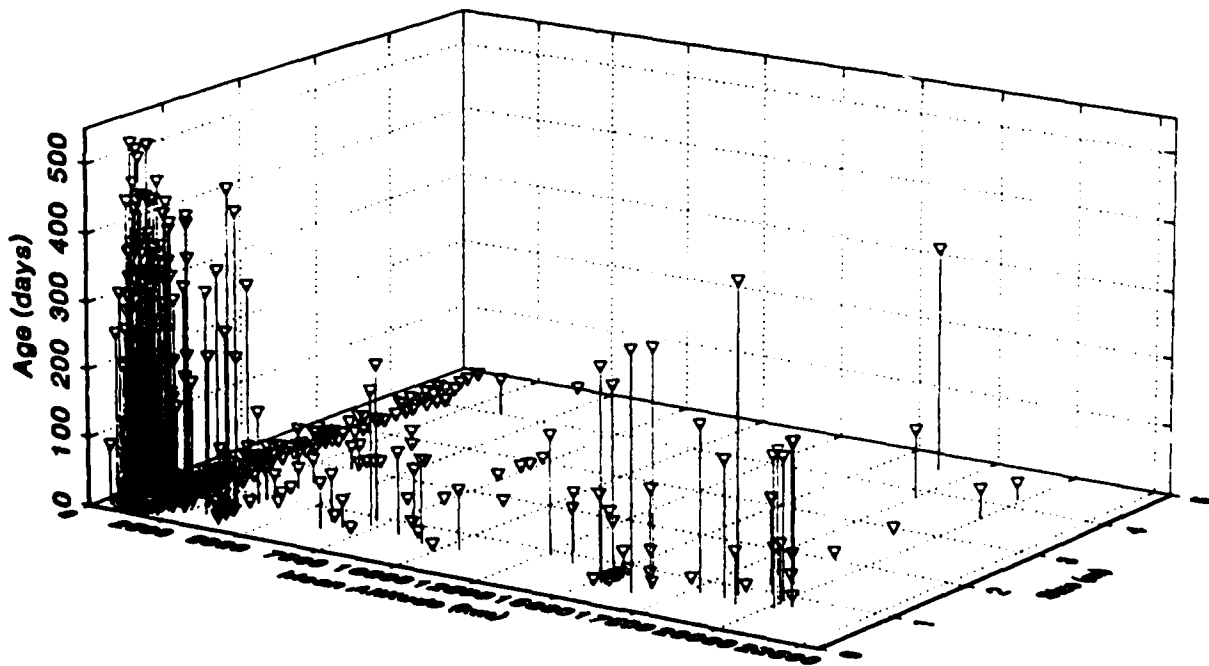


Figure 6. Size and Altitude Distribution of Russian Satellite Catalog as a Function of Element Age.

## **AIR COMMAND AND STAFF COLLEGE (ACSC) - SPACE APPLICATIONS FACILITY**

### **"EDUCATION WITH GLOBAL REACH"**

**By Lt Col Michael J. Muolo, Campaign Concepts Director (Air Command and Staff College)**

#### **EMPLOYMENT OF AEROSPACE POWER**

1. Land power and aerospace power are co-equal and interdependent forces; neither is an auxiliary of the other.
2. The gaining of air and space superiority is the first requirement for the success of any major land operation.
3. The inherent flexibility of aerospace power is its greatest asset.
  - This flexibility makes it possible to employ the whole weight of the available aerospace power against selected areas in turn.
  - Such concentrated use of the aerospace striking force is a battle winning factor of the first importance.
4. The information of hostile air and space activities gained by the aircraft warning service will be furnished by the air commander to missions prior to take-off; and when urgent, to the reconnaissance unit in the air.

**SOURCE: War Department Field Manual 100-20, Command and Employment of Air Power 21 July 1943.**

#### **ACSC SPACE APPLICATIONS FACILITY...EDUCATION WITH GLOBAL REACH**

#### **INTRODUCTION**

The Air Command and Staff College (ACSC) has assembled a space infrastructure consisting of equipment technology essential for curriculum development, demonstrations training, exercises, war games, and independent research at the "Operational Level of War." Students and faculty now integrate aerospace doctrine and the SAF infrastructure equipment into their campaign planning exercises and operational level war games to greatly enhance their understanding of operational forces planning and execution support. This SAF is critical to the successful execution of the Academic Year (AY) 1994 and future AY curriculums. Students and faculty have access to real-time tactical command and control and near-real time battlefield information by taking advantage of available space technology. This high quality real world situation display training, war game support, and technology applications research is available throughout the entire academic year. The equipment in this Space Application Facility is fully integrated into the ACSC curriculum, including, the ACSC PC based series of exercises and war games designed by the ACSC faculty from "Toolbook" software. The Space Applications Facility allows for training and education to be relevant to the theater and the threat we intend to face. The SAF will also eventually provide for real-time internet with worldwide exercises and war games, to include the National Training Center. Central to this concept is the ACSC PC based war game system and aerospace power technology application initiative.

The current SAF was designed and developed by Major Michael J. Muolo, Course Director for Campaign Concepts under the leadership of Colonel John A. Warden III Commandant. The idea to develop an SAF followed Space User Days in March 93 and became fully operational in September 93.

## **PURPOSE AND SCOPE**

The purpose of the ACSC SAF is to provide the ACSC students with the ability to inject live and packaged data into the way that we conduct training, exercises, and war games. This SAF Facility ensures we train and educate using state of the art equipment in the Tactical Exploitation of National Capabilities (TENCAP) and Space Applications arena. The facility provides for education with Global Reach, and demonstrates the methods for bringing the capabilities of the aerospace medium to the premier air campaign planning school in the Department of Defense.

This paper describes the philosophy and function of the SAF. It also provides a facility description, equipment in place, system description, future considerations, mission statement, and description of project. Also included is the technology application and research initiative which is a fundamental component of the SAF.

## **ACSC CURRICULUM AND GOALS**

The RAISON DETRE for ACSC is to be the premier intermediate professional military education institution which develops and teaches the concepts needed to defend the United States through the control and exploitation of air and space. As such, the ACSC mission is to develop leaders who understand the profession of arms, the nature of war, and the **application of aerospace power at the operational level**; and to advance air and space concepts.

Among the goals are:

**Prepare leaders to develop, articulate, apply, and exploit aerospace power during peace and war.**

**Prepare leaders to plan and execute joint and combined campaigns with emphasis on airpower.**

**Prepare leaders to think critically**

**Expand and advance the aerospace body of knowledge**

Given these goals, the ACSC curriculum for AY94 has several major thrusts:

**Provides a conceptual framework (The Theater Air Campaign) which underpins and integrates the entire curriculum**

**Focuses on airpower application**

**Provides a research capability for the Air Force - Critical Analysis and problem solving**

**Enable the advancement of airpower knowledge**

ACSC provides for the application and analysis of aerospace power. Wargaming is integrated throughout the curriculum via:

- Introductory exposure to air power exercise**
- Crisis development exercise**
- Campaign planning aid Strategic attack analysis**
- Deployment and employment exercises**
- Multiple scenarios throughout curriculum**

### TENCAP/SPACE APPLICATIONS

In 1977, Congress directed the military services to implement a program to use the capabilities of centralized national assets in support of their force employment, rather than seek to develop separate tactical systems. The Air Force began their TENCAP initiative in 1979 and, in 1988, Air Force Space Command was designated the Executive Agent and implementing command for the Air Force TENCAP. The purpose of the Air Force TENCAP program is to improve the combat effectiveness of the Air Force through more effective use of national systems.

Air Force Space Command was charged to identify, advocate and help develop space assets, applications and information into the tactical force employment environment. DOXW quickly realized that paper studies were not sufficient to develop and test space capabilities for tactical operations and pursued initiatives to investigate the utility of space derived information tailored to the warfighter. Part of this effort was to provide support to Air Command and Staff College and Air University in educating warfighters on national systems and various TENCAP and Space Application activities and initiatives to leverage national capabilities in support of military operations.

ACSC Campaign Concepts Course Director currently prepares instructional materials required to educate ACSC students on TENCAP/Space Applications through student research initiatives. This effort also involves the dissemination and integration of these products into the education and training environment, especially in seminar demonstrations and war games and campaign planning.

In February 1993, the ACSC Commandant requested and secured AFSPACECOM/DOXW support for "ACSC Space User Days." The objective was to bring space infrastructure equipment to the warfighter to demonstrate the Global Reach of space power and the role that space forces play in planning and executing the air campaign. The demonstration included the Air Defense System Integrator, CONSTANT SOURCE, Multi-Spectral Imagery, and numerous other demonstrations related to near-real time intelligence, communications, weather, navigation, and imagery. The Space User Days was a resounding success. From this effort the concept of the ACSC Space Applications Facility was born. Likewise, this demonstration solidified the understanding of technology applications in support of an ACSC PC based war game network.

The ACSC curriculum for AY94 and beyond will focus on campaign planning at the operational level of war. The United States is currently in the most revolutionary period in history (Geopolitical Revolution, 2nd Industrial Revolution, and Military Technological Revolution) and the ACSC must keep abreast with these changes to administer effective state-of-the-art education and training. With the use of selected TENCAP/Space Application equipment, ACSC now can receive a series of space related products of direct impact on the application of aerospace power. This facility provides for receipt of real time and near-real time intelligence data, as well as non-time sensitive environmental data.

The SAF provides for demonstrating the global reach of aerospace power, injecting space infrastructure products into ACSC war games, and serve as a test bed for the applications of aerospace power. This facility provides for adaptive training for the theater and threat that we face. The ACSC SAF is education with Global Reach.

#### PROJECT OBJECTIVES

- a. Acquire selected TENCAP/Space Applications equipment and products. This suite will replicate, as much as feasible, the combat Air Forces standard equipage and capabilities.
- b. Integrate live data into ACSC curriculum and war games.
- c. Inject multi-spectral data into the ACSC curriculum and war games.
- d. Exploit technology for Aerospace Power research via architecting and implementing multi-media aerospace power application and research stations.
- e. Provide a "Educate like we fight" capability.
- f. Demonstrate the Global Reach of Aerospace Power.
- g. Construct a Space Applications Facility from a single office room.
- h. Educate selected ACSC faculty on TENCAP/Space Applications equipment use, who in turn will train other faculty and students. Initial training is available from Department of Defense schools or vendors.
- i. Ensure selected TENCAP equipment is maintainable and supportable.

#### FACILITY DESCRIPTION

ACSC currently has five selected TENCAP/Space Applications equipment for student and faculty use, curriculum development, and wargame/training/exercise support. These capabilities include; The Tactical Receive Equipment Simulation (TRESIM), the Standard Tactical Receive Display (S-TRED), The Graphic Intelligence Support Display (GIST), the Stand Alone TENCAP Simulator (SATS), and the Tactical Information Broadcast System TIBS). In addition ACSC has purchased three Magellan GPS Receivers and will have live weather information by 1 Feb 94. There is a dedicated classified work area to store and operate TENCAP/Space Applications equipment at the SECRET collateral level.

#### SYSTEM DESCRIPTION

The SAF is composed of multiple workstations which are linked together and include a server/workstation design. In the interim, stand along workstations will be pursued with interactive operations being one of the drivers for the equipment selection process. Future equipment will include, but not be limited to, CONSTANT SOURCE, Air Defense System Integrator, Weather TRAC II, Multi Spectral Intelligence/Imagery Workstation(s), Target Intelligence/Imagery Workstation, Imagery Production Node, and Secondary Imagery Receipt/Handling Communications and Navigation equipment, and the infrastructure required to become embedded with the ACSC PC based war games. This equipment suite will grow to link with the Defense Simulation Internet and worldwide exercises and war games, to include the National Training Center. Current equipment and configuration are listed at Attachment.

## FUNCTIONALITY

The SAF can work in several broad functional areas. The most critical of these is acquisition of real-time or near-real time data and the display and dissemination of space applications information. This data is integrated into ACSC war games. Brief descriptions and a compilation of the activities associated with these areas follows.

- a. Intelligence processing. Real time and near-real time data will be injected into the SAF to provide a view of the battlefield. This data will also be used in the ACSC PC based wargame activities.
- b. Multimedia space technology application research. Develop multimedia space and technology application research stations and prototype a seminar applications and research capability, with expansion to team research capability and ultimately from a single seminar system to a full class of ACSC technology exploitation and application suites.
- c. Data Display and Dissemination. The objective is to integrate the data products at the SAF into the ACSC PC based wargames for application throughout ACSC. Additionally, capability will exist to project the displayed data to large screen projectors in both the SAF and in an auditorium setting. Visual representations of complex scenarios, using SAF data, allow quick assimilation and high-level understanding of large amounts of data.

## EXTERNAL CONNECTIVITY

The following external connectivities will exist in support of the SAF.

- a. CONSTANT SOURCE Receiver Suite (CSRS) with capability to capture Trap/Tadix-B
- b. Secondary imagery dissemination feed to imagery workstation.
- c. MSI production node connectivity with EROS data center Global Land Information system data base (archives all federally owned commercial satellite imagery).

## FUTURE CONSIDERATIONS

While nothing is locked in, the future holds several new possibilities for the SAF. The external connectivity can be expanded to include the Theater Air Command and Control Simulation Facility, providing access to AWACS, PATRIOT, etc. Additionally, the potential exists for input of data into the SAF from various external sources, to include numerous external exercises and maneuvers, as well as links to the National Training Center. It is the goal of the SAF to "bring the battlefield to the schoolhouse". The underlying assumption is that if only the participants benefit from a live exercise or actual conflict, then we are not using the word education properly. The SAF provides for education with Global Reach. The intent is to provide continuous support for the upgrade, expansion, and/or replacement of SAF equipment and capabilities. Additionally, the SAF can serve as a test bed for prototype equipment to advance the applications of space forces to the aerospace campaign and the battlefield environments.

- a. Enhancements to the physical facility will be evaluated on an ongoing basis. The search for new equipments, capabilities, and applications will be continuous.
- b. The capability to upgrade the SAF from SECRET Collateral to SCI is possible.



c. The current and proposed configurations together form the technical basis for the way the SAF does business. The next section will further bound the project by defining the concept of operations.

### **SPACE APPLICATIONS FACILITY MISSION STATEMENT**

The mission of the SAF is to bring space applications information to the warfighter. Associated with this mission is providing live and archived data to integrate space into the ACSC curriculum, during time of peace or war. Additionally, multi-media technology application and research stations are a fundamental component of the SAF. The space applications products provided will be integrated into the ACSC wargames, worldwide wargames, and the Defense Simulation Internet. The SAF will perform these functions by establishing a facility, resource base, and consolidated expertise to draw on, as needed, to satisfy requirements. Multi-spectral Imagery production will compile data from a variety of sources to build MSI packages for use during ACSC wargames and demonstrations. This facility will integrate data from SPOT, LANDSAT, DMA, and other sources to provide for use on the SAF Intelligence/Imagery Workstation suite, to include mission planning and rehearsals.

### **PROJECT DESCRIPTION**

SAF is a unique concept providing a specialized niche in the TENCAP and Space Applications environment. The SAF provides the opportunity to educate 500+ students per year on TENCAP and allows for the normalization of space in the premier Air Campaign school in the Department of Defense. It allows for a case-by-case test bed facility for incorporation of very selective prototype equipment into the education and training environment. The SAF also provides for the development of a multimedia computer based technology application and research center. This center would capitalize on the "Education with Global Reach" aspects of the SAF, providing aerospace power students the data collection and processing facility to understand today's battlefield and architect tomorrow's.

### **SPACE APPLICATIONS FACILITY UTILIZATION**

The SAF is used on a full time basis. The degree of utilization at any given time will be dependent on a number of factors.

a. Day-to-day Operations: The facility is integrated into the core ACSC curriculum and opportunities pursued that will match the curriculum coverage to the SAF capability. As an example, the GIST equipment can be integrated to the electronic battlefield curriculum and the TIBS Equipment can be integrated into the aerospace superiority segment of the curriculum. Obviously, the SAF will be fully integrated into those segments of the curriculum which focus on space support to warfighting.

b. Wargame/Exercise Support: The SAF is fully integrated into the ACSC PC based wargame scenarios. There are many opportunities to integrate the data received into the planning and execution of wargames.

c. War/conflict access. A vital element of the SAF is to provide the warfighter the view of the battlefield. As conflict develops/occurs, the SAF will provide an opportunity to "bring the battlefield to the schoolhouse". The SAF will also mature to bring worldwide exercises and the National Training Center activities to ACSC.

d. Visit tailored activities: These are primarily system demonstrations showing what is available, system capabilities, and activities to integrate the SAF into the ACSC curriculum. Demonstrations are typically the same for each visitor.

e. **Operational utility:** As required, this facility equipment could be used to support real world operations, e.g., use of the Weather TRAC II system to support weather altering procedures.

f. **Student and faculty research support:** Students and faculty will be capable of extensive research at the Operational Level of War and be able to integrate ideas and equipment into their campaign planning exercises and operational level wargames. This training and student research will be available throughout the entire academic year.

### **EDUCATION AND TRAINING**

One of the functional requirements of TENCAP is to conduct various level of education and training; the SAF provides a forum for this activity. The system ensures students are aware of space applications equipment and initiatives, train for employment of these systems, and are the beneficiaries of education with Global Reach. The SAF provides for "Train like we Fight". This is education and adaptive training at its best - preparing for today's battlefield by providing live and packaged data to conduct wargames, research, and mission rehearsals. As the SAF matures, the vision is to bring the major national wargames to ACSC electronically, insuring that the participants in an exercise, or actual conflict, are not the only ones to learn from the encounter.

### **RESEARCH INTEGRATION**

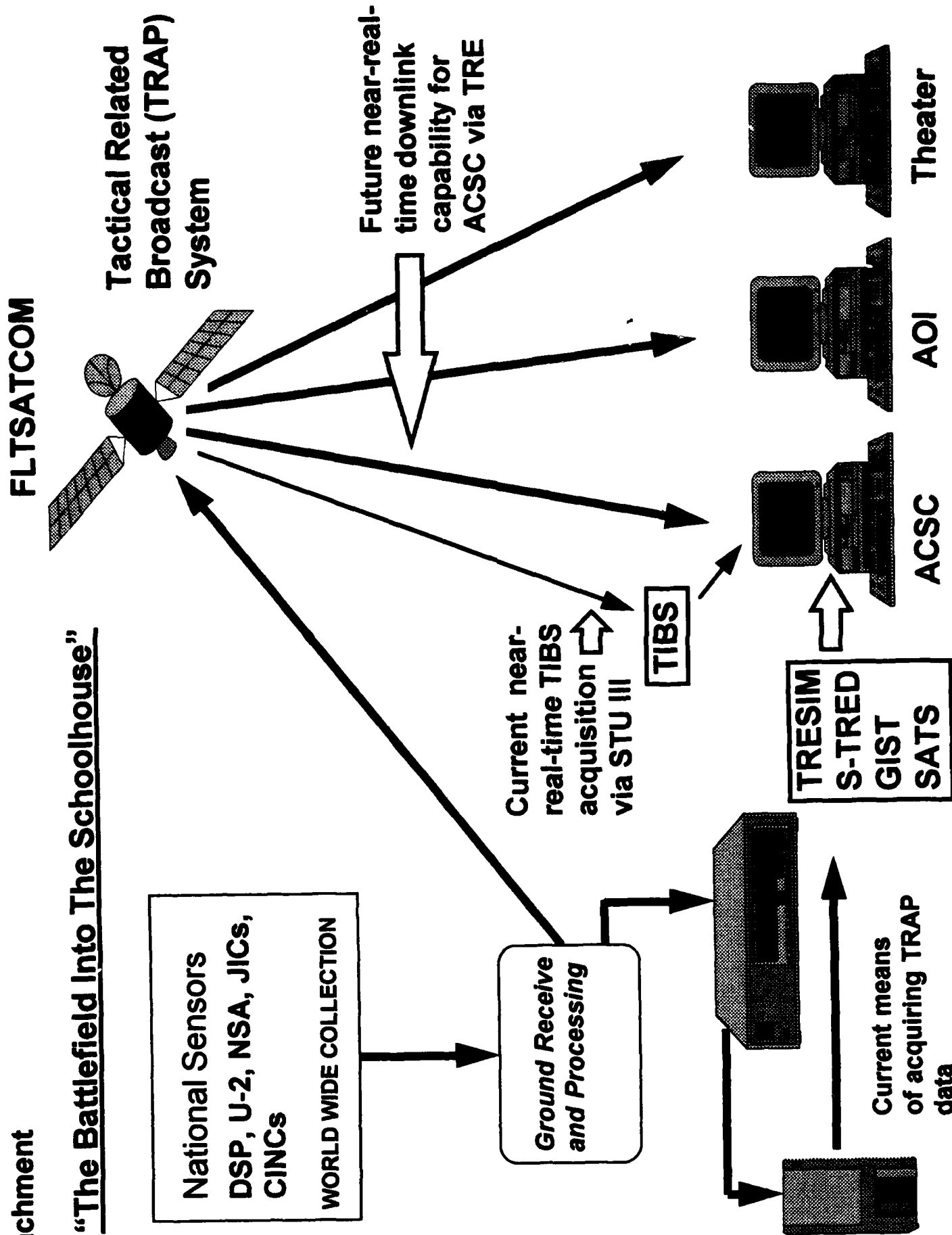
To effectively integrate the SAF into the ACSC curriculum student research assistants, under the supervision of faculty, coordinate individual course requirements with each of the eight course directors. Students researchers are for the most part not associated with the space career field to demonstrate the "user-friendly" nature of the SAF. These researchers develop specific products that are incorporated directly into each PC based exercise. For example; a course exercise may involve a contingency operation against a specific country. Research assistance would use the SAF resources to develop a comparable input allowing each student to gain valuable "hands-on" education as to how TENCAP capabilities are used to support warfighting. Students filter into the SAF and extract the necessary information to support their individual Course of Action. This method has been extremely successful and beneficial to the students.

### **CONCLUSIONS**

Since its conception the SAF has become a high interest item to all services and has received a great deal of notoriety in local and national news releases. The ACSC SAF is the only one of its kind anywhere in the PME Schools. Comparable facilities are at two other locations; HQ USAF/XOOR and Nellis but for demonstration only. The ACSC facility has proven to be a valuable educational tool and critical to the understanding of campaign planning and the application of space power.

**Attachment**

**"The Battlefield Into The Schoolhouse"**



## Uncorrelated Track Processing and Identification in SPADOC 4C

David Cappellucci, (Loral Command and Control Systems)

### Background

The mission of the Space Defense Operations Center (SPADOC) includes identification and tracking of all objects in earth orbit that are visible to the Space Surveillance Network (SSN). SPADOC receives observations on these objects from individual sensors within the network. The observations are used to create and maintain element sets which represent the orbits of the satellites. The element sets are used, in turn, to generate messages to the SSN which task the sensors for observations on the corresponding objects. When the sensors make the requested observations, the observation data is returned to SPADOC which uses the data to further update the element sets. This process goes on continuously to maintain a database, or catalog, of all of the objects in orbit about the earth.

The tasking feed-back loop is generally very successful in maintaining a catalog of orbital elements sufficient to locate the great majority of orbiting objects. For a variety of reasons, the loop sometimes fails and the element sets become obsolete for the purposes of position prediction. This results in the satellite going "lost", which means that the current element set is no longer capable of correctly tasking the network. When this happens, no further observations (obs) are received that correlate with the element set (elset). Since the object is still in orbit and being observed, the observations on the object come into SPADOC as uncorrelated tracks (UCTs) of observations or as isolated uncorrelated obs depending on the sensor type.

UCTs may also enter the system from objects which are new to the network. New satellites can arise in a number of ways, the most obvious being a newly launched satellite or from debris related to a launch. Other processing in SPADOC has specific responsibility for identifying these objects and cataloging them as quickly as possible. But, on occasion, pieces of debris may be missed and this will eventually result in UCTs entering the system. Other sources of UCTs include maneuvers or orbital separations (eg, the release of the Hubble solar panel from the shuttle) which may be missed by the SSN.

The biggest source of new orbiting objects is the breakup of a payload or rocket body. This happens with an unfortunate degree of regularity and is responsible for nearly half of the objects being tracked at any given time. Orbital fragmentations may happen for a variety of reasons, but are most often associated with the explosion of a spent rocket body which has not vented all of the residual fuel and oxidizer. When a satellite breaks up in orbit, the resulting fragments tend to end up in orbits that are similar to the pre-breakup parent object. Depending on the nature of this orbit, the fragments may end up in long-lived orbits. Many of these fragments are large enough to be observed by the network and result in large numbers of UCTs coming into SPADOC after a breakup event.

This paper focuses on the role of new breakup and lost/UO processing software in SPADOC 4C in determining element sets for objects which are producing UCTs and in identifying the source of those objects. This code is responsible for UCTs for both breakup and lost/UO processing. Lost/UO processing combines the software necessary to recover lost satellites as well as that which is necessary to identify element sets from purely unknown observations (UOs). Breakup processing is similar except that it focuses on observations believed to be on breakup fragments. In the pages that follow, this paper describes how the breakup and lost/UO software, working in conjunction with other SPADOC software, generates new element sets from incoming UCTs, identifies the most

likely source for the associated object, and then provides a mechanism for the orderly cataloging of these new objects.

#### Observation Routing in SPADOC 4C

As observations are received from the sensor network, they are processed to ensure that they correctly associate with the expected satellite. Obs that come in tagged by the sensor are checked against the element set corresponding to the tag and if the association is close, the observation is immediately filed for later use in updating the element set. If the observation does not correlate with its tagged object or if the observation comes in untagged, it goes on for retag processing.

The first step in retag processing is to identify tracks of observations. These are defined as sets of obs coming from the same sensor on a single object during a single pass over the sensor. When a track of obs is identified, it is processed to create a track element set by performing an initial orbit determination using the individual obs in the track (assuming sufficient obs are available) followed by a non-linear, least-squares, differential correction (DC) on those obs. Since a track element set is formed from obs over a short arc of the orbit, its representation of the whole orbit is subject to a relatively high level of uncertainty.

Once a track elset has been formed, it provides a mechanism to quickly associate a whole track of obs with an element set. The incoming unassociated tracks (and non-track obs) are subjected to a hierarchical series of checks to determine if they belong to any known satellite. In order, the obs are checked against current or recent launches, known maneuverable satellites and separation candidates, special analyst designated satellites, decaying satellites (TIPs) and finally active breakups. If track elsets or non-track obs associate with one of these, they are retagged and added to the appropriate file.

Special routing is performed when there is an active breakup. An active breakup is one which has recently occurred and which is being worked by an analyst. At the time that the breakup is initialized, inclination and right ascension limits, based on the breakup parent's element set, are specified. These define the bounding orbital planes within which the breakup fragments are expected to be found. As new UCTs enter the system, the track elsets and single hit obs are processed to determine if they may have come from an object with an orbit lying within these limiting planes. If true, the obs and tracks are routed into the Breakup Observations (BOBS) file for breakup processing. Any obs which fail this check end up in the Unassociated Observations (UOBS) file for lost/UO processing. As will be seen below, the element sets should still be correlated back to the correct parent using the new breakup correlation algorithm.

Any obs which do not correlate with any of these possibilities are compared against each of the elsets in the current catalog. The observations are assigned an association status (ASTAT) of one through four with each of the element sets. ASTAT 1 means that the ob fully associates in-plane, in-track and radially with the reference element set within pre-defined limits. ASTAT 2 obs are those that are within the plane limits and are within four times the in-track and radial limits. ASTAT 3 obs are within the plane limits only. ASTAT 4 obs show no association with the reference elset. Obs that associate ASTAT 1 with an elset are retagged with the corresponding satellite number and placed in the Associated Observations (AOBS) file. Obs that do not associate ASTAT 1 with any elset, but do associate at the 2 or 3 level are retagged with the closest associating elset and also placed in the AOBS file. Obs that do not associate with any elset are placed in the UOBS file along with the associated track elset if one exists.

### Automated Candidate Element Set Formation

The real job of the new software is to form element sets which best represent sets of UCTs. These element sets are formed by clustering groups of UCT track elsets and single hit obs which appear to be related and then subjecting the clusters of track elsets and obs to a two-stage DC process to form a "candidate" element set.

The clustering process uses the Cuthbert-Morris period matching algorithm which compares the periods of the track elsets and selects those that are within thresholds for inclusion into a fine cluster for use in forming a composite elset. This algorithm has a history which goes back over 30 years to the very first orbital breakup. This was the breakup of the Transit 4A rocket body (1961-Omicron) in June of 1961. Mr. Larry Cuthbert, of the Air Force's Electronic System Center, developed a computer program called SWEEP to cluster individual obs to form composite element sets. The algorithm was later extended by Mr. Bob Morris, of Air Force Space Command, to include track element sets in the clustering. The algorithm has been used successfully the 427M SSC for high-eccentricity orbits since the mid-eighties.

Candidate formation is performed in three different modes: breakup, lost and UO. The three modes differ primarily in the type of gross clustering that is performed prior to the start of the Cuthbert-Morris algorithm. Additional differences in the form of sort criteria and the values of various limits extend throughout. In breakup mode, gross clusters of track elsets are formed by finding all of the track elsets in BOBS which are tagged with an active breakup parent satellite number. In lost mode, gross clusters are formed by finding all track elsets and single hit obs in the UOBS file which "loosely" associate with a known lost satellite. In UO mode, a single gross cluster is formed which consists of all track elsets and single hit obs in the UOBS file which do not associate with any lost satellite and which are reasonably "fresh". In lost and UO mode, all of the track elsets in each gross cluster are sorted by inclination. In breakup mode, the track elsets are sorted by epoch time.

Processing begins on the sorted gross cluster by arbitrarily selecting the first track elset as a reference elset against which the remaining subset is compared. Each successive track elset is subjected to a preliminary comparison on each of the individual elements (mean motion, eccentricity, inclination, etc.) to ensure that it is at least close to the reference track. All of the track elsets that pass this check now form an initial fine cluster. The elements of the reference track are checked in order to set thresholds for subsequent comparisons. Different values for period limits are used based on the period, inclination and eccentricity of the reference track. The specific values for different orbital regimes have been determined by experience over the 30 years that this algorithm has been in use. Depending on the eccentricity of the reference tracklet, its period is estimated in one of two ways. If the eccentricity is less than 0.25, the period is estimated from the times of successive nodal crossings. If the eccentricity is greater than 0.25, the period is estimated from the times of successive perigee passages.

Once the period of the reference track elset has been determined, the number of revolutions,  $n$ , that a candidate track elset would make between the epoch of the reference track and its own epoch is determined. Then the periods which would result in  $n-1$ ,  $n$ ,  $n+1$  and  $n+2$  revs are computed and placed in a table. Each period is then compared to the period of the reference track. If the periods match within specified limits, the candidate track elset is added to the fine cluster for the first DC. Single hit (radar) obs may also be brought into this process by postulating a track elset centered on the observation using the elements of the reference track to complete the elset. If the reference track elset is in an orbit that is subject to high drag

conditions, additional processing may be performed to fit the period estimates to a sloping line to account for drag.

When the fine cluster is completed, the resulting set of track elset and single hit obs is subjected to a preliminary DC. This DC uses single hit obs and pseudo-obs formed from the individual track elsets. The pseudo-obs are formed by converting the elements from classical to cartesian form to determine the position of the represented object at the epoch of the track elset. The single hit obs are preprocessed to compute a position vector at the time of the ob. The reference track, using an anomalistic mean motion representing the track elset in the fine clusters, is used as the seed for the DC. If the DC is successful, the resulting elset is a composite elset which represents the entire group of track elset and obs.

The composite elset is used to perform "post-SWEEP" association to identify any additional obs which may have been missed in the preliminary clustering process. During post-SWEEP association, the composite elset is used to associate obs from the UOBS, BOBS and/or AOBS files. An association status is computed for the composite element set with each of the obs from those files. Any obs which associate ASTAT 1 with the composite elset are retagged and written back to the database for processing. This process pulls in all of the obs used in the first DC plus additional obs not used before. The entire set of obs is then passed to the DC package using tighter limits than were used for the first DC. If this DC is successful, the resulting elset is compared against any other new elsets and existing candidate and analyst elsets to ensure that it is unique. If it is unique, the elset is initialized in the database as a new candidate. Otherwise, the associated observations are retagged with the duplicate elset satellite number and the candidate elset is deleted.

#### New Candidate Processing

The newly formed candidates are subjected to a final series of checks prior to being presented for review by the analyst. An attempt is made to find a parent for the elset. If the processing mode is breakup, the candidate elset is assigned to the breakup parent satellite. If the processing mode is lost, the resulting candidate is assigned the lost satellite number used to form the gross cluster as its parent. If the processing mode is UO, the algorithms described below are applied to find a potential parent for the elset. If all attempts fail, no parent is assigned. The elset is then assigned a unique candidate satellite number in the 90000-99998 range and placed in the database. All of the obs associated with the elset are retagged with this number and the classification set to that of the elset.

#### Subsequent Candidate Processing and Existing Candidate Maintenance

A new candidate element set is only known locally to the breakup and lost/UO processing software. As such, the element set has not yet been placed in the catalog and tasking and routine maintenance has not begun. The intent of creating local candidates is to allow the analyst time to decide whether or not the element set is satisfactory before placing it in the catalog. The analyst has the option of retaining a new elset as a candidate or immediately converting it in to an analyst elset and placing it in the catalog (which causes tasking and routine maintenance to begin). If the analyst chooses to keep the elset as a candidate, the elset will be maintained using "stealth" maintenance for as long as it exists as a candidate. In this mode, any new obs coming into either the BOBS or UOBS files are associated with each of the pre-existing candidate elsets. If any of these elsets pick up enough ASTAT 1 obs, the elset is updated using those obs in a DC.

If the analyst chooses to convert the candidate into an analyst satellite, further processing is performed prior to permanently cataloging the elset.

When an analyst element set derived from breakup or lost/UO processing is under routine maintenance, the "health" of that element set is monitored on a daily basis. The status of the most recent DC and the current tasking status (number of obs received vs. number tasked) are measured. When the element set has been successfully maintained for specified period of time, the software sets recommendations for the analyst to go ahead and permanently catalog the elset. The intent of this monitoring is to ensure that these element sets are stable and will not immediately go lost once they are placed in the catalog.

#### Historical Breakup Database

A significant new feature in SPADOC 4C is the inclusion of an on-line database of breakups. This database will initially be populated with all known breakups. Once SPADOC is operational, the database will be updated automatically as new breakups occur and are processed.

The database will contain an entry for each object that has broken up. The entry will contain the following groups of information: Event Data describing where and when the breakup event occurred; Parent Data describing the identity and nature of the pre-event parent satellite including the last good element set prior to the breakup; Fragment Data describing all of the fragments which have been identified and cataloged from the event; and Correlation Data which provides the mechanism for correlating future fragment element sets to the breakup. The data in the database may be viewed at any time by the analyst. In addition, printed summaries, including plots showing the distribution of the fragments may also be made. The data may be modified at any time using the same displays and summaries.

#### Breakup Correlation Coefficients

When new element sets are identified from UCTs, the task of the new breakup correlation algorithm is to determine the probability that the elset represents a fragment from a known breakup. This algorithm is based on the computation of a set of "correlation coefficients" for each breakup. The correlation coefficients are then used to compute the degree of correlation between a new element set and a particular breakup. The computed degree of correlation, or correlation status, provides an indication of correlation not proof of lineage. The breakup correlation coefficients simply consist of the means and standard deviations of the period, eccentricity, inclination and adjusted node for each of the fragments identified for a breakup. These elements were chosen since they are relatively invariant with time (except for the right ascension of the ascending node) and their values provide a means to describe the distribution of the debris cloud.

Since the right ascension of the ascending node (or simply, node) is an angle whose measure varies from 0° to 360°, the mean value for the node becomes meaningless when the distribution of fragments is widely spread as is the case in very old breakups. To compensate for this, an adjusted node is used. This is computed by using the node of the parent elset precessed to the epoch of interest as a reference point. The nodes of each of the fragments are also precessed to the same epoch and then subtracted from the parent node. Since the fragments tend to move randomly away from the parent element set, the adjusted nodal values will tend to be both positive and negative and randomly distributed about 0. Therefore, the mean value of the adjusted node will tend to be near zero. The value of the standard deviation ( $\sigma$ ) is initially low as most of the fragments are clustered tightly about the parent. Over time, since the nodal precession rate is slightly different for each fragment, the fragments will spread away from the parent and the value of  $\sigma$  will increase while the mean stays close to zero. Thus the value of the standard deviation for the node gives an indication of the age of the breakup.

When a new breakup is initialized, the correlation coefficients are set to



default values. The element means are set to those of the parent element set while the mean adjusted node is set to zero. The values for each of the standard deviations are set to constant defaults determined from analysis of historical breakups. As new fragments are identified, the default coefficients are replaced with coefficients computed from actual fragment elsets. The transition occurs when the number identified is greater than a threshold which must be at least 3 but can be adjusted higher as dictated by experience.

The values of the coefficients depend on the elements of the breakup fragments. Due to natural perturbations such as atmospheric drag and the asymmetric geopotential, the values of these elements evolve over time. Consequently, the values of the breakup correlation coefficients also evolve and must be periodically updated. This is done by a program which is initiated once per day and processes each of the breakups in the database. It retrieves all of the fragment elsets for all breakups, processes the adjusted nodes to a common epoch and recomputes the correlation coefficients for each. The database is then updated with the new values for each breakup.

#### New Candidate Breakup Correlation

As soon as a new element set is identified, an attempt is made to identify a parent for it. In the case of potential breakup fragments, this is done by computing the correlation status for each fragment as defined below:

$$\text{CorStat} = \sum_{k=1}^4 \left( \frac{x_k - \bar{x}_k}{\sigma_{x_k}} \right)^2; \quad \text{where } x_k = \text{Period, Ecc, Inc, } (\Omega - \Omega_0)$$

As can be seen from the equation, the correlation status can be interpreted geometrically as an ellipsoid in a four-dimensional space where the axes in this space are defined by the mean element values in the correlation coefficients. The computed value of the correlation status represents the distance of the fragment elements from the center of the breakup debris cloud in this element set space. By placing the standard deviations in the denominator, the units of distance are given in sigmas. In general, the smaller the value for correlation status, the closer the correlation is between the candidate element set and the potential breakup parent.

A close correlation status is, at best, an indicator of the closeness of fit. It is not, by itself, conclusive proof that the candidate belongs to the breakup. In many regions of the breakup element set space, there are several breakups whose debris clouds overlap. When a new fragment is identified which lies in one of these overlap regions, it may have a relatively high correlation with more than one breakup. When this occurs, other factors must be taken into consideration. For a new breakup, the correlation between a new candidate and the parent is driven primarily by the results of the automatic candidate formation described above. Thus a new candidate will almost certainly be associated with the new breakup and not the old.

For older breakups, additional information must be analyzed before making a final assignment. This is provided in the Breakup Signature Plot, which is presented on a new SPADOC 4C display. This plot (see Figure 1) is divided into four quadrants. The first quadrant shows the traditional Gabbard plot which gives a representation of the distribution of fragments with delta-velocity components in-track and radial relative to the parent. The second quadrant contains the Out-of-Plane Plot which gives the distribution of fragments out-of-plane relative to the parent. The third quadrant shows the distribution of the orbital eccentricities of the fragments as a function of period. The fourth quadrant shows the distribution of fragment orbit planes.

Taken together, these four plots provide a unique signature for each breakup. By superimposing the candidate elements on top of a potential parent's

signature plot, the analyst can get a good "eye-ball" indication of how well the candidate fits. By comparing its fit with more than one parent, the analyst may be able to find the best home for the element set. In the end, however, it is up to the analyst to make the final decision; the software is designed only to provide indicators.

### Breakup Fragment Cataloging

When a new fragment element set is cataloged, several things must happen. First, the fragment is assigned a new international designator. The root for the designator (year, launch number) is the same as the breakup fragment. The software keeps track of the character extensions for each fragment and automatically assigns the next available character in the sequence. Second, when the fragment element set is added to the satellite catalog, an entry is made for it in the breakup database as well. In this way, a permanent connection is made between the fragment and the parent so that up-to-date fragment elements are always available for any action involving the breakup parent. Finally, as with all candidates, when the fragment is cataloged for the first time, it's element set goes under routine maintenance which means that sensor tasking commences on the object and automatic differential corrections are performed as new obs are received.

### Lost/UO Correlation

All objects in earth orbit (with the possible exception of captured micrometeors) were placed there by human activities. When new objects are found, the source of the object must be identified. Aside from the purely practical reasons of maintaining a complete and accurate database, there are also international treaties which dictate that all orbiting fragments must be assigned a unique international designator. This establishes the ownership for all orbiting objects should liability claims be necessary.

The possible sources for these unknown objects include lost satellites, missed maneuvers or separations, launch debris or breakup fragments. The job of lost/UO correlation is to determine the source of a new element set obtained from UCT processing. The preceding sections described the algorithms used for breakup correlation. This section describes the algorithms for correlating the element set associated with a new object for each of these possible sources.

### Lost Satellite Recovery

Before a satellite can go lost, it must have been tracked for some period of time. Having been tracked in the past, it has left a history which can be exploited for recovery. The SPADOC 4C system has a new file called the

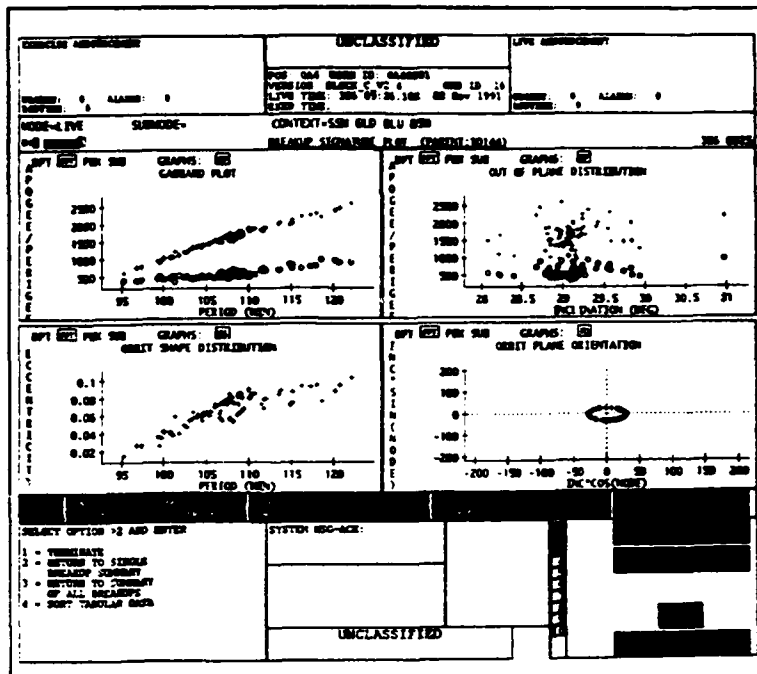


Figure 1 - Breakup Signature Plot

Historical Elements (HELs) file which contains historical element sets for every satellite that is currently being tracked. The file contains at least one element set per LUPI for the last 25 LUPIs. A LUPI (length of update interval) is a time span, defined for satellites in related classes, during which the elset should be updated at least once in order to maintain data good enough for satellite tracking.

This history is exploited by fitting a data model to the element sets. The model can then be projected into the future to compare the candidate element set with the expected values for the elements of the lost satellite had it not gone lost in the first place. The data model to be used should represent those elements which change with time as the elset evolves but are relatively non-dynamic. The chosen elements are the period, inclination and right ascension of the ascending node. The period gradually decreases for all satellites (more for near-earth, less-for deep-space) until the satellite nears decay, at which time the period drops off rapidly. The rate at which the period changes is generally not predictable for any instant in time, but evolves over a longer period of time in a well behaved fashion. The right ascension of the ascending node of a satellite precesses in an easily modeled way for all satellites in orbits inclined at other than 90° (where the precession rate is zero). The inclination is nearly constant for most orbits and is used to scale the node model. Both the inclination and right ascension are brought into the model by using the x and y components of the W vector (normal to the orbit plane). The equations below define the model used:

$$P = P_0 + P_1 * \Delta t + P_2 * \Delta t^2 = \frac{2 * \pi}{\text{MeanMotion}}$$

$$W_x = A * \sin(\omega \Delta t + \Theta) = \sin(\Omega) * \sin(i) \quad \text{where } P_0, P_1, P_2, A, \omega, \Theta \text{ are the model parameters}$$

$$W_y = A * \cos(\omega \Delta t + \Theta) = -\cos(\Omega) \sin(i)$$

The six parameters in the model are obtained for each satellite by using a non-linear least squares fit of the individual elements as a function of time. These six parameters are referred to as the lost satellite correlation coefficients.

Operationally, whenever a satellite is first declared to be lost, the software automatically generates a set of lost satellite correlation coefficients and stores them in the Lost Satellites (TLOS) system file. When ever a new element set is created which is suspected of being a potential lost satellite recovery candidate, it's elements are compared with the fit model projected to the epoch of the element set using the correlation coefficients and the model. If there is a close correlation (as defined by a "short" distance between the candidate and the model), the candidate is marked as a potential recovery candidate for the lost satellite.

This processing is performed automatically at the time that the candidate is initialized and may be performed manually at any time by the analyst through the Manual Satellite Correlation function. When lost correlation processing is initiated manually, a new display, called the Historical Trend Plot, is available for the analyst. This display is shown in Figure 2. Like the Breakup Signature Plot, this display is presented in four quadrants or windows. Three of the four windows are made up of points derived from the element values shown as a function of time (period, Wx and Wy). In each of the three windows, the fit model is shown as a smooth curve drawn as the best fit through the points. The corresponding points for the candidate element set are shown superimposed on these windows, drawn in a different color for ease of visual distinction. The fourth window on the plot allows the analyst to view several other of the individual elements as a function of time. Note the lines through the points are drawn in a "connect the dots" fashion and do not represent any kind of fit.

When an analyst has concluded that a candidate element set is in fact a known lost satellite, the next step in the recovery process is to update the catalog with the element set. Prior to permanently cataloging the new element set, the analyst will first place the elset into the catalog as an analyst satellite (i.e., it is assigned a number in the 80,000 to 89,999 range). Once the candidate is placed in the catalog as an analyst satellite, routine tasking and maintenance begins on the element set. This allows the analyst to monitor the element set for awhile, prior to permanent cataloging, to ensure that the object does not immediately go lost again.

Once the analyst is satisfied with the quality of the element set, the final step in the recovery process is to replace the current element set in the catalog for the lost satellite (which is no longer any good) with the candidate element set.

#### Maneuver and Separation Correlation

When a satellite maneuvers, it enters a new orbit. If the orbital maneuver is large enough, the element set for the pre-maneuver orbit will no longer predict the post-maneuver orbit well enough to task sensors. The same situation applies to separations except that a new object is detached from a parent to move in a new orbit. In either case, the object in the new orbit will, at some point, appear to the SSN as a new satellite and UCT observations will be generated.

Special processing has been added to SPADOC to identify maneuvers and separations automatically. This processing is given high priority and generally works well for most maneuvers and separations. If the maneuver or separation delta-velocity is great enough, the post-maneuver orbit may be so different that the maneuver is not recognized. In this case, obs on the post-maneuver object will enter SPADOC as UCTs and a new element set will be formed as described above.

In order to correctly correlate the new element set to the proper parent, manual processing is provided to allow the analyst to connect the pre- and post-maneuver (or separation) element sets. This is done by performing relative motion analysis (generally referred to as a "COMBO" run) using the new candidate element set and element sets for satellites which are known to be maneuverable or capable of deploying payloads. The COMBO run is made so that it spans a period of time likely to catch a recent maneuver or separation. If the COMBO run detects any close approaches (< 50 km) between the candidate and maneuverable satellite, that satellite is marked as a potential parent for the candidate. When all potential parents have been identified, the results are presented to the analyst for review. The analyst must make the final decision as to whether or not the candidate belongs to a

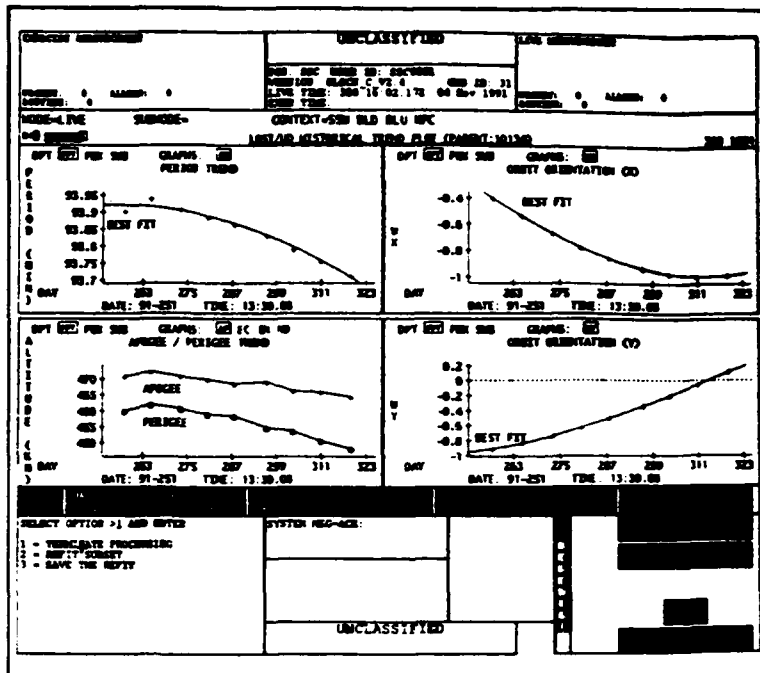


Figure 2 - Historical Trend Plot

particular parent. Once a decision is made, the candidate may be cataloged correctly as described above.

#### Launch Correlation

The final means of identifying a parent for a new candidate is to correlate the element sets with recent launches. This represents a last-ditch effort to find a parent and assign a correct international designator. The correlation approach is relatively simple and is based on matching the orbit plane of the candidate element set with the orbit planes of objects resulting from recent launches.

A new file is available in SPADOC 4C, the Launch Profile (LPRO) file, which contains representative element sets for each of the legs of all recent launches. The candidate element set is compared with each leg of these launches by preprocessing the nodes of both element sets to a common time and computing their respective W vectors at that time. A simple dot product then determines the angle between the orbit planes. If this angle is less than a threshold value, the associated launch is marked as a potential parent for the candidate.

As is the case for maneuvers and separations, this option is only available manually. When one or more potential parents have been identified for a candidate, a summary display is prepared and presented to the analyst. The analyst must make the final assignment of a candidate to a particular launch parent.

#### Summary

SPADOC 4C is adding a robust set of automated and manual processes to the orbital analyst's toolchest that will enable the analyst to quickly identify unknown orbiting objects. These tools represent a significant improvement over the set of tools available to the analyst on the 427M SSC system. The major improvements in automating the creation of candidate element sets should reduce the workload of the analyst and free them for other important tasks. The new correlation algorithms will enhance the analyst's ability to determine the source of an orbiting object and correctly catalog it. This should reduce number of incorrectly cataloged and cross-tagged objects in the catalog.

#### Acknowledgements

Any significant new software capability is almost by definition the result of a team effort. SPADOC's new breakup, lost and UO processing enhancements are not an exception. Therefore, author wishes to acknowledge the efforts of the other members of the development team, Matt Jahelka, Evan Pedersen and Brent Petersen, without whom this work would have been impossible. Additionally, much insight into the nature of the Cuthbert-Morris algorithm and the history and mechanics of UCT processing was gained through numerous conversations with Larry Cuthbert and Bob Morris. Finally, special thanks to Roger Mansfield for his early contributions to the development of the lost correlation algorithm and his help in preparation of this manuscript.

## **Improved Space Surveillance Capability at the Naval Space Operations Center**

**presenter: Stephen H. Knowles  
Naval Space Command  
Dahlgren, Va.**

Naval Space Command is presently undertaking installation of a new computer support system for the Naval Space Operations Center. A number of improvements to the astrodynamics processing are planned as part of this changeover. The present aging computers will be replaced by an IBM RISC based distributed processing system. The new system will operate on an event-driven basis, which means that every event will be responded to as it occurs, rather than in a batch mode. The event-driven functionality provides an opportunity to improve timeliness and accuracy of results by insuring optimal and automatic response to any input. Differential correction will be performed for all orbits automatically based on tolerance, resulting in a continuously optimum catalog that incorporates the latest observations. This is expected to improve orbital accuracy significantly for most objects, and improve response to atmospheric density fluctuations caused by solar storms. Observations from both the Naval Space Command fence and other sensors will be identified or flagged as unknown within 2 minutes. Automatic data base maintenance will result in generation of messages for release whenever lack of observations places a satellite on the attention or lost list. Maneuver alerts will be generated automatically when observations indicate, and follow-on processing will be initiated. The VERIFY program, which attempts to correlate false UCTs, will be run continuously vice once per day. HANSA and TIP processing will be initiated automatically, as will generation of Fleet Support products. Breakup processing will be integrated for better response.

The increased processing power of the new system brings timely performance of the above on-demand tasks easily within system capability. This capability has also led to astrodynamics software augmentations. Processing capability will be increased to at least 50000 elsets and 250000 observations per day. A new version of PPT will provide better GEO orbit accuracy by including lunisolar terms. The prediction data base will contain 36 hours of fence crossing predictions as well as PASCHED predictions. GOBS software will be included for tracing lost GEO satellites. These processing improvements are planned for IOC in summer 1994. A planned numerically intensive processor will enable a more extensive augmentation of the astrodynamics analysis capability of the NAVSPOC.

The inherent capabilities of current workstations will make possible a much improved man-machine interface. This will result in easier operation, and will enable use of new and improved graphics tools for orbital analysis. Industry

standards are being used in all development, which will make use at other facilities easy.

The improved astrodynamics capabilities will be a direct result of the new computer architecture, hardware and software being implemented. As a result, the new architecture will be described in considerable detail.

### **Network Architecture**

The Naval Space Command tactical mission processing system is implemented in a hierarchical arrangement. At the top of the processing tree is the Technical Control Facility (TCF). The TCF provides the interface between the mission processing local area networks and all communications networks providing and accepting data from Naval Space Command. At the next layer (processing layer A, or PLA) are positioned front end processors responsible for communications, data preprocessing and event processing. Each processor is connected to two high-speed networks allowing optimum network selection for processor-to-processor communications.

The next layer down from PLA is processing layer B (PLB). PLB forms the central core of processing power and provides the following functions:

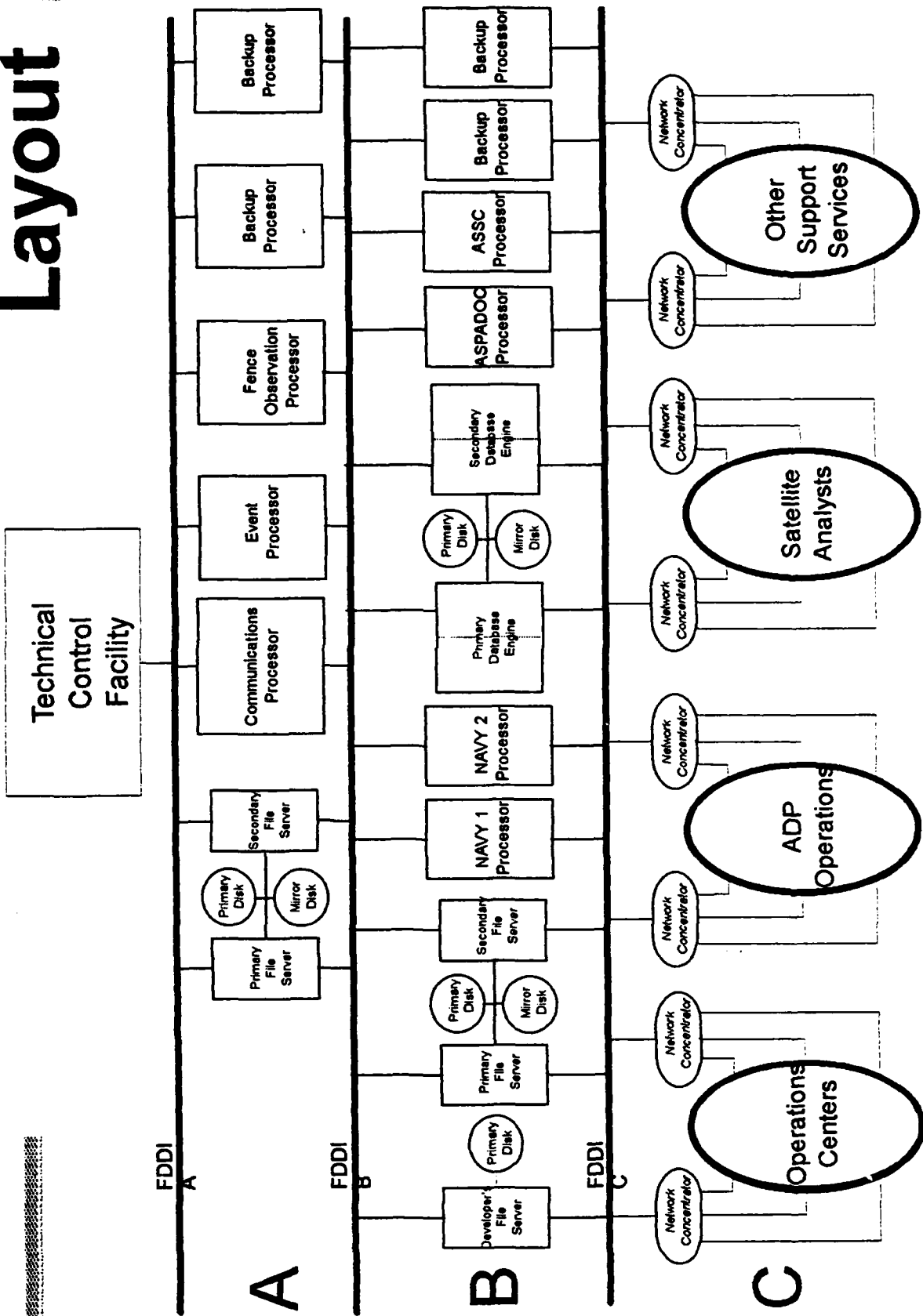
- High availability file services
- Fleet support product generation
- Space Catalog data services
- ASSC/ASPADOC mission processing, and
- Special computationally intense product generation

In addition to the above functions, PLB must consist of a configuration flexible enough to support rigorous validation testing, development and other support actions.

Processing layer C (PLC) consists of work group sub-networks that support all end user requirements. This includes mission operations, satellite analysis, development and testing. Each major function is supported in a work group allowing like functions to be grouped together. The work groups supporting critical mission operations must contain sufficient redundant equipment to prevent loss of capability in the event of single component failures. Failover of equipment will be automatic and transparent to the end user.

High performance networking is achieved through the use of Fiber Distributed Data Interface (FDDI) networks. These networks are highly fault tolerant in that the network backbone can be severed at any single point without loss of operational capability. Highly redundant intelligent hubs with multiple path routing is employed to ensure maximum network up-time. Sub-networks are partitioned to prevent network congestion and isolate related mission functions. All network hardware and software are available as unmodified standard releases of commercial products.

# Network Layout





## **Processor architecture**

Six classes of computer processors were identified to meet all processing requirements for the tactical mission network. Two major areas of processing capability were identified; centralized ADP mission processor and file servers, and end user terminal equipment. Mission processing requires a high compute capability with efficient access to large quantities of stored data. End user functions have been separated into two classes: high end operational and normal support. High end operational functions include those critical to mission operations and in general require significant computational capability in both algorithmic processing and high performance 3-dimensional graphics presentation. Normal support functions require some local processing capability, and a graphical user interface of moderate speed.

## **Mission processors.**

Mission processors perform the bulk of mission-specific processing in support of operations. Most of the software executing on mission processors was developed by NAVSPACECOM personnel. Because of the general purpose nature of today's computer processor technology, an off-the-shelf system was selected and configured to form a standard mission processor configuration. All mission functions that require a mission processor for execution use this standard configuration. This provides a great deal of flexibility in allowing a consistent environment for development, testing and operations. Seven mission processors (3 in PLA and 4 in PLB) are employed to meet operational requirements. Four additional processors (2 each in PLA and PLB) of this standard configuration are included in the network to support system redundancy, testing and software development.

Each mission processor consists of the following:

- IBM RISC 6000 model 980B CPU
- 4 Gbyte internal fixed disk
- 512 Mbyte central memory
- CD-ROM
- 5 Gbyte 8 mm tape cartridge drive, and
- FDDI DAS network interfaces

## **File Servers**

Central to the operational readiness of the network is the availability of critical data to all mission processing components. The NAVSPACECOM tactical network has, located in PLA and PLB, high availability file servers. All file server hardware and software is commercially available and consists of unmodified COTS versions. Each server configuration contains two high-speed computer processors connected to 24 Gbytes of high-performance dual access disk. Two processors are used to provide a primary operational system with a backup

secondary processor. High availability cluster multiprocessing (HACMP) software is used to provide the ability for the second processor to assume the identity and function of the primary processor automatically in the event of its failure. All end user applications will be unaware when such a failover occurs. The 24 Gbyte of disk storage can be segmented into logical volumes and file systems and mirrored in up to three ways. A journaling file system is employed to ensure data integrity in the event of a system crash or power outage. The use of an uninterruptable power system and stable COTS software and hardware should minimize the risk of this occurrence. Specific hardware components of the file servers are:

- BM RISC 6000 model 980B CPU
- 2 Gbyte internal fixed disk
- 512 Mbyte central memory
- CD-ROM
- 5 Gbyte 8 mm tape cartridge drive
- 4 FDDI DAS network interfaces
- 7 High-performance serial copper disk controllers, and
- 24 Gbyte high-performance serial copper disk drive rack

#### Database Engine

The database engine serves the satellite catalog to all mission processing components requiring access to observations and element sets. This configuration consists of the basic file server described in the preceding paragraph, with additional resources added to satisfy the high computational load of observation and element set processing. Thus each primary and secondary database engine component consists of a file server connected to dual-access high-speed disks with a compute engine connected to each file server processor by a 220 M bit per second serial optical channel converter. It is anticipated that the database engine, as implemented, will support a catalog of well over 10,000 objects. Increased capability can be achieved by replacing the processing components with faster technology when it becomes available.

#### Work Group Servers

PLC consists of 13 work group sub-networks to connect the mission processors in the ADP center to the end-user terminal equipment. Each work group that supports end-user workstations contains a server processor to supply boot images, applications and security passwords. These servers are small desktype processors located in the network distribution racks positioned throughout the facility.

### **High Performance Workstations**

High performance workstations are used in support of three functions in the NAVSPACECOM system; (1) Space Control Operations Center (SCOC) functions, (2) satellite database maintenance, and (3) software development. A high performance workstation class has been configured to meet the needs of persons performing these functions. This class workstation provides a high performance RISC central processor, 1 Gbyte fixed disk, and 3-dimensional high performance graphics hardware. The SCOC machines have redundant network connections to diverse network hubs. This provides automatic failover of network distribution equipment in the event of hub or router failure. The development machines contain additional COTS software such as compilers, language sensitive editors and configuration management tools to support software development.

### **Entry Level Workstations**

All users not requiring a local high-performance computational capability have been provided with low end entry level workstations. These systems consist of dataless workstations of approximately one-half the speed of the high-performance workstations described above. Each of these systems is attached to a work group intelligent hub via fiber optic ethernet and is considered non-critical to mission operations. They do, however, support mission functions as a less time-critical lower priority. A graphical user interface is provided. Being of the same processor architecture as other processors in the network they can run most of the same applications programs as other system components. Because the workstations are dataless, operating system and application programs are served from the work group servers providing centralized software management and maintenance for these processing nodes. Four hundred megabytes of local disk storage are available for virtual memory paging, thus minimizing the effect of network loading on the performance of these machines.

### **Software Architecture**

Mission processor software can be divided into three areas; operating system, COTS applications and support, and NAVSPACECOM specific applications.

### **Operating System Software**

Operating system software consists of IBM's version of the UNIX operating system called AIX. AIX is compliant with UNIX System V, Berkeley V4.2, and OSF/1. Software is provided as binary releases and no modifications were required to support the mission processor network. OSF Distributed Computing Environment provides distributed processing capabilities in the areas of remote procedure calls, network security, distributed time services and distributed file services (DFS). Current the industry standard for remote file

access, NFS, is employed to access file servers. Future efforts will implement the DCE DFS, as it matures. All operating system software components are compliant with state-of-the-art industry standards and provide an environment emphasizing machine independence of applications programs.

#### **Commercial Off-The-Shelf Applications**

Commercial application and application support environments have been employed whenever possible to lower development and maintenance costs. The Oracle relational database management system provides access to all structured data in the system. Logicon message dissemination system software, a fast text analysis and retrieval package, forms the heart of the event processor. Commercial data analysis and visualization software will be added as the program continues.

#### **NAVSPACECOM specific applications**

The core of the satellite tracking and product generation software is being developed at Naval Space Command by government and contractor personnel. This software suite includes considerable new code to take advantage of the capabilities of the new hardware. There is, however, a great deal of carryover, particularly of the algorithmic software for orbit computation and sensor data reduction. This carryover will ensure a stable performance of the new system that will keep the well-known software reliability of the old NAVSPASUR system at the same time improved capability is introduced. A top-level list of developmental software items includes:

**Communications host** - This component provides for the reception and transmission of messages to communications systems external to NAVSPACECOM.

**Event processor** - This component accepts and analyzes messages from the communications host and from internal network sources and initiates applications on processors in response to this input. Its primary function is to automate routine data processing functions in response to external events.

**Fence Data Reduction (FDR)** - FDR receives data from the six NAVSPACECOM fence receiver sites and either identifies it as caused by a known satellite or declares it an unknown object.

**Catalog maintenance** - This component performs all of the processing required to accept satellite observations from the Space Surveillance Network or the NAVSPACECOM fence and stores them for future access by mission processors. Additionally this component stores orbital element sets for all identified objects.

**Navy fleet support processing** - This component generates data satellite vulnerability and other products required in support of the fleet.

**ASSC/ASPADO**C - This component performs data processing in support of ASSC/ASPADO space control operations center functions.

The above processing components are being developed in FORTRAN 77 (with FORTRAN 90 on the way), C, and Ada. ANSI Structured Query Language (SQL) provides database access. All software is coded to industry Application Programming Interface specifications, providing a high degree of portability.

#### **Event Driven Capability**

The use of an event-driven architecture marks a fundamental difference in strategy that makes possible the responsiveness improvements mentioned in the introduction by ensuring that each incoming bit of information is processed and responded to in an optimum way, both in terms of timeliness and in terms of processing. This will apply to all incoming data, including Autodin messages, radar data from the NAVSPACECOM sensor, ADCCP/Mode 1 data from Colorado Springs, etc. This is accomplished by message parsing that identifies each type of message and initiates the appropriate response. This includes alerts for messages requiring action. In general, all message parsing is performed in the Communications Processor, which then routes messages to the Event Processor to determine optimum system action. This is made easily possible by the high degree of reserve capacity in the new system. It also makes possible facile adaptation to changes in mission and tasking that may (and will) occur in the future. Although most orbital elements change only slightly from one sensor pass to the next, this capability is important in ensuring rapid detection of anomalous event, including maneuvers.

#### **Numerically Intensive Processor (NIP)**

The IOC processor system, is designed to reproduce the capability of the existing Cyber system. Although it will easily do that, it does not have the additional capability to perform a number of additional capabilities that will clearly improve surveillance capability and are possible with state-of-the-art hardware. Some of these applications include:

- More general COMBO predictions for asset and astronaut protection
- Self correction of the catalog for drag variations from exoatmospheric density fluctuations.
- More thorough hypothesis testing for UCTs.
- The keeping of a larger space catalog for debris tracking or other purposes

Procurement of a NIP will be undertaken in FY95. It will no doubt be some type of parallel processor.

#### **Improved Man-Machine Interface (MMI) and Graphical User Interface (GUI)**

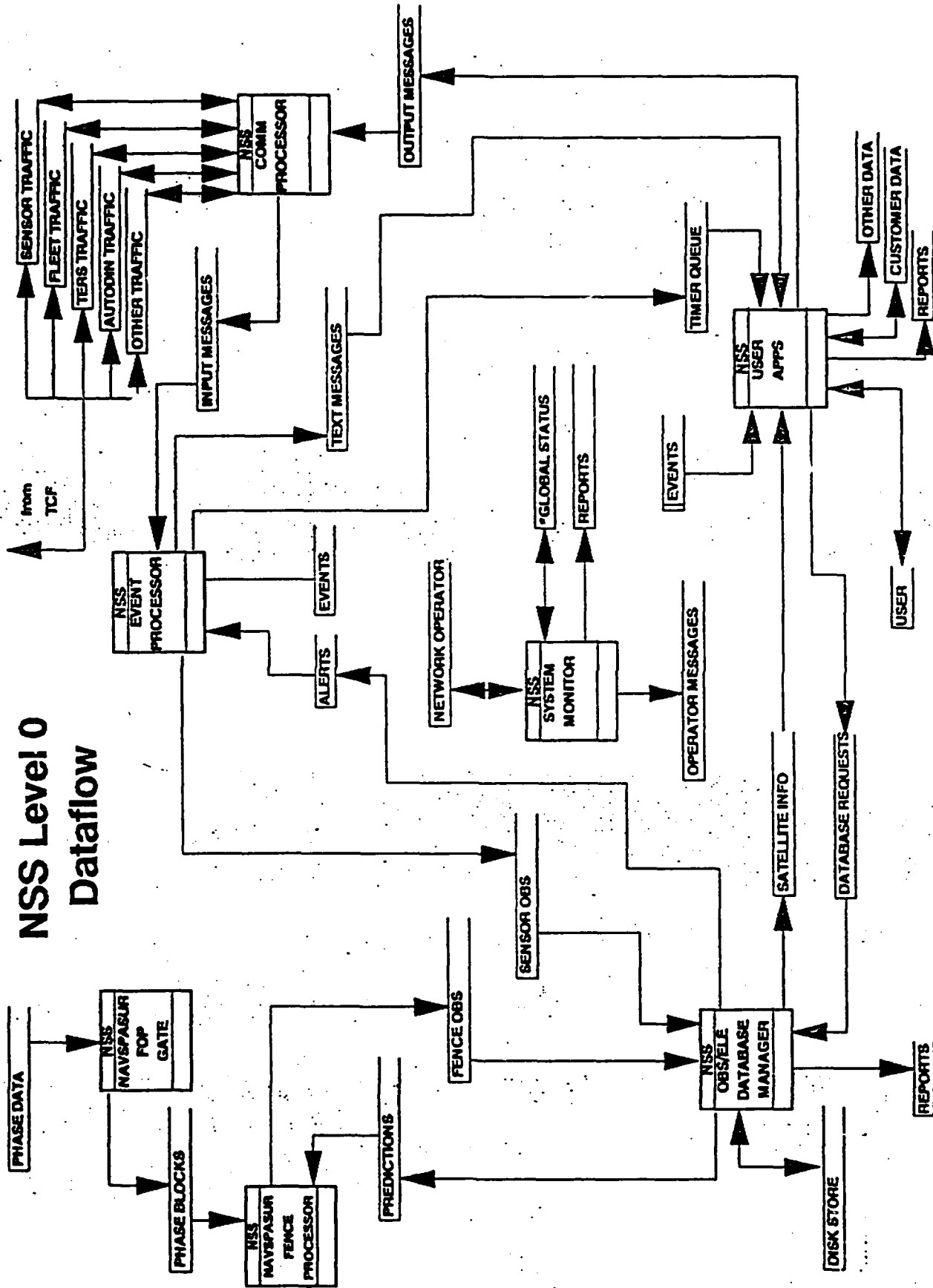
Many new concepts and possibilities can be undertaken with state-of-the-art tools that are simply not possible with any currently operational system. Windowing and graphical display of various orbit views provide exciting

possibilities to the watchstander, both of easier comprehension and of better analysis and action through deeper understanding of the situation. Our programming staff will introduce and utilize many of these innovations. The complete effect of these innovations will not be apparent until some time after IOC, because a close and extended interaction between development and operational personnel is required to ensure maximum effectiveness. The improvement will clearly be substantial, however.

### Summary

In summary, the use of state-of-the-art computer capabilities, together with innovative planning on the part of Naval Space Command personnel, will make possible a space surveillance capability that is significantly improved when the new NAVSPOC system is operational. Astrodynamics capability will clearly be significantly improved at initial operation (IOC), in terms of accuracy, timeliness, lower error rate and improved response to stressing events such as breakups and solar storms. After installation of the numerically intensive processor and tuning of the system, a further dramatic improvement in capability is expected. The system will also retain the ability to respond to any new mission or tasking by incremental change because of its distributed architecture. New hardware can be installed, and obsolete equipment deleted, in the same incremental manner.

# NSS Level 0 Dataflow



# A FEASIBILITY ANALYSIS SYSTEM FOR SURVEILLANCE EXPERIMENTS WITH THE MSX

by  
R.Sridharan, Gary Duff, Tony Hayes,  
and Andy Wiseman  
MIT Lincoln Laboratory

## 1. INTRODUCTION

The Mid-Course Space Experiment consists of a set of payloads on a satellite being designed and built under the sponsorship of Ballistic Missile Defense Office (formerly, Strategic Defense Initiative Office) of the Department of Defense. The major instruments are :

1. A set of long-wave infra red sensors being built by Utah State University.
2. A set of sensors operating in the visible wavelength and ultraviolet wavelengths, being built by Johns Hopkins University's Applied Physics Laboratory.
3. A broad-band visible wavelength sensor designed and built by Massachusetts Institute of Technology's Lincoln Laboratory.

The satellite bus is being built by JHU/APL who is also acting as the integrator for all the sensors and associated systems. The MSX satellite, shown in Fig. 1, is due for launch in late 94 from the Vandenberg launch complex into a near-sun-synchronous orbit.

### 1.1. MSX Mission and Operations

The MSX satellite will conduct a series of measurements on phenomenology of backgrounds, missile targets, plumes and resident space objects (RSOs); and will engage in functional demonstrations in support of detection, acquisition and tracking for ballistic missile defense and space-based space surveillance missions.

The MSX has two mechanisms for storage of experiment data and two methods for dumping these data.

High bandwidth science data are stored in on-board tape recorders. These are read down to the APL's control station directly at 25 Mb/s. A typical full tape takes 2-3 passes over APL to download fully.

Low bandwidth science data are stored in on-board memory associated with the instrument generating the data (eg., the SBV ). These data are read down at 1 Mb/s either at APL or over one of the Air Force's Satellite Control Network (AFSCN) stations.

Eight Principal Investigators are associated with the MSX project. The PIs develop experiment plans that are then prioritized by the BMDO's Mission Planning Team. JHU/APL's Mission Operations Center commands the MSX to carry out the experiments and collect science data. The data are returned to the PIs for analysis and for refining the experiments.

The SBV Processing and Operations Control Center, located at MIT Lincoln Laboratory, is a component of the APL's Mission Operations Center. In this role, SPOCC generates the necessary commanding for the MSX and its sensors for all space-based space surveillance experiments generated by the PI for Surveillance; and converts and calibrates the returned science



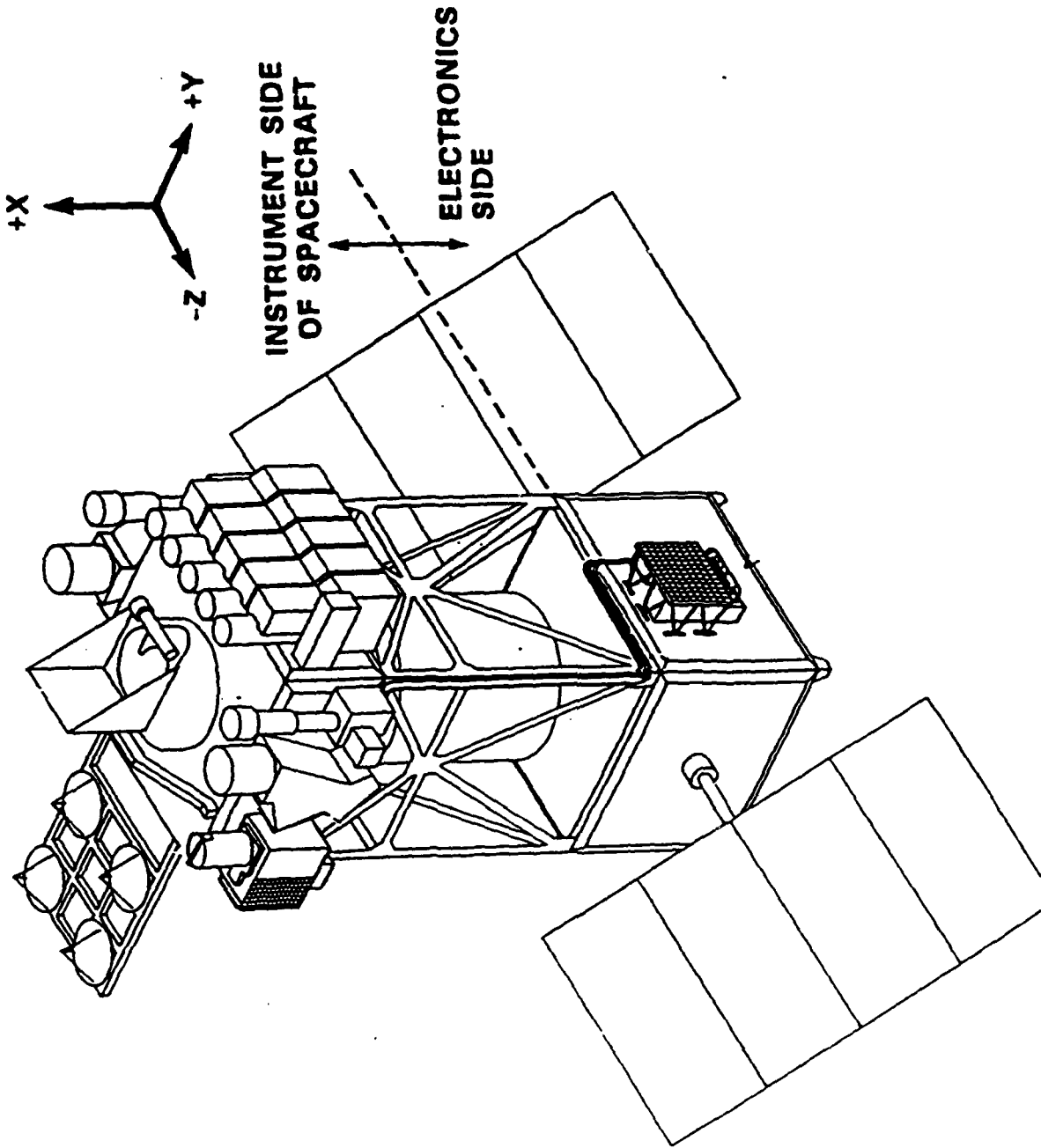


FIGURE 1 MSX SPACECRAFT

data before turning them over the SPI's Surveillance Data Analysis Center. Further, SPOCC maintains the health and status of the Lincoln Laboratory's SBV sensor on board the MSX.

## **1.2. Feasibility Analysis for Experiments**

A complex satellite like the MSX has several constraints imposed on its operation by the sensors, the supporting instrumentation, power resources, data recording capability, communications and the environment in which all these operate. Even reasonable automation of the conduct of experiments requires a system to assess the feasibility of the experiment within the constraints imposed by the safety and health of the spacecraft and the sensors. This paper describes the implementation of a Feasibility Analysis System, developed in SPOCC, specifically to support the experiments of the Principal Investigator for space-based surveillance.

## **2.0. MSX and Its Instruments**

It is necessary to have a working knowledge of the MSX spacecraft and its sensors and their interaction to understand the functioning of the Feasibility Analysis System.

Figure 1 shows the body reference axes defined for the MSX spacecraft. All major sensors on the MSX have their fields of view substantially co-aligned along the +X-axis. The star, earth limb and sun sensors are offset from the X-axis but are not considered in feasibility analyses.

The MSX is powered by solar panels that have freedom of rotation about the Z-axis. The MSX will be in a 99 deg. inclination orbit with an orbital period of 103 minutes. The MSX will have shadow periods as long as a third of the orbit. Hence, it also carries a set of Nickel-Hydrogen batteries for powering the spacecraft operations during eclipse. The batteries are recharged by the solar panels.

The MSX carries two redundant tape recorders for high bandwidth data recording. The tape recorders are operated singly (or in parallel for critical data). Each unit is capable of recording 36 minutes of data at 25 Mb/s or 180 minutes of data at 5 Mb/s.

The SPIRIT 3 infrared sensor carries a dewar containing solid hydrogen to cool its focal planes to 10° K. The lifetime of the sensor is critically affected by the rate of dissipation of the Hydrogen. This sensor writes out its data almost entirely to the tape recorder.

There is a set of ultra-violet and visible wavelength imagers and spectrometers on board, collectively called the UVISI. These instruments also use the tape recorder for storage of experiment data.

The SBV is the third major sensor on board the MSX. This sensor is comprised of a 6-inch aperture off-axis rejection telescope, a camera with 4 CCD chips with a total field-of-view of 6° x 1.4°, a Signal Processor for data compression and an Experiment Controller. The Experiment Controller controls experiment operations and has a large data buffer to store processed science data.

The MSX supplies power, data handling, telemetry, commanding and pointing capability for all the sensors on board.

## **3.0. SPOCC SUPPORT OF MISSION PLANNING**

SPOCC, as mentioned earlier, is the mission planning node for all experiments of the Principal Investigator for Surveillance.

The major tasks of the mission planning system in SPOCC are:

- 1) to permit a study of the feasibility of an experiment;
- and 2) to generate the necessary commands to the sensors and the spacecraft to execute the experiment.

This paper concentrates on the feasibility analysis.

Feasibility implies that the experiment, as defined, can be conducted within the available time and without violating constraints on the spacecraft or the sensors; and, further, the spacecraft resources consumed ( both renewable and non-renewable ) by the experiment are within limits allocated to the experiment.

Figure 2 captures the essential components of the Feasibility Analysis System in SPOCC. This system is invoked by a file of commands in a high level interface language called Surveillance Language for Experiment Design (Ref. 1). The SLED code can be written by a user, which is the predominant mode for most single RSO experiments. It can also be generated automatically by the Space Surveillance Interface Processor (SSIP), which is the mode for multi-RSO experiments and for experiments which have to be conducted with short notice (called quick reaction events).

The components of the Feasibility Analysis System are described below.

### **3.1. Simulator**

The Simulator is the heart of the Feasibility Analysis System.

The Simulator is driven by SLED code. An example experiment written in high level SLED is shown in Figure 3. This experiment conducts a short observation sequence on an orbiting sphere for metric calibration. The Simulator parses the SLED code and models the temporal flow of the experiment as a set of timed events for the sensors and the spacecraft. These events imply state changes for the MSX and its instruments whose time and resource costs are also accumulated by the Simulator.

#### **3.1.1. Resource Usage Constraints**

The Simulator has a detailed model for the power usage on board and the power generated by the solar panels. Knowing the initial state of the battery, the depth of discharge is computed.

The tape recorder and the data memory in the SBV are finite resources. The Simulator monitors their usage and either terminates the experiment, in the case of the tape recorder, or requires a downlink contact, in the case of the SBV memory, when no more data can be written out.

The SPIRIT 3 instrument has a finite quantity of solid hydrogen for cooling its focal planes. A cryogen depletion model has been developed by the instrument manufacturers that predicts the quantity of hydrogen lost as a function of thermal input from the earth and the sun. The Simulator uses this model while simulating an experiment.

The Simulator has a thermal model for key parts of the spacecraft, viz., the SPIRIT 3 baffle, the tape recorder heads and the battery. The temperature rise in these elements during an experiment is computed.

# FEASIBILITY ANALYSIS

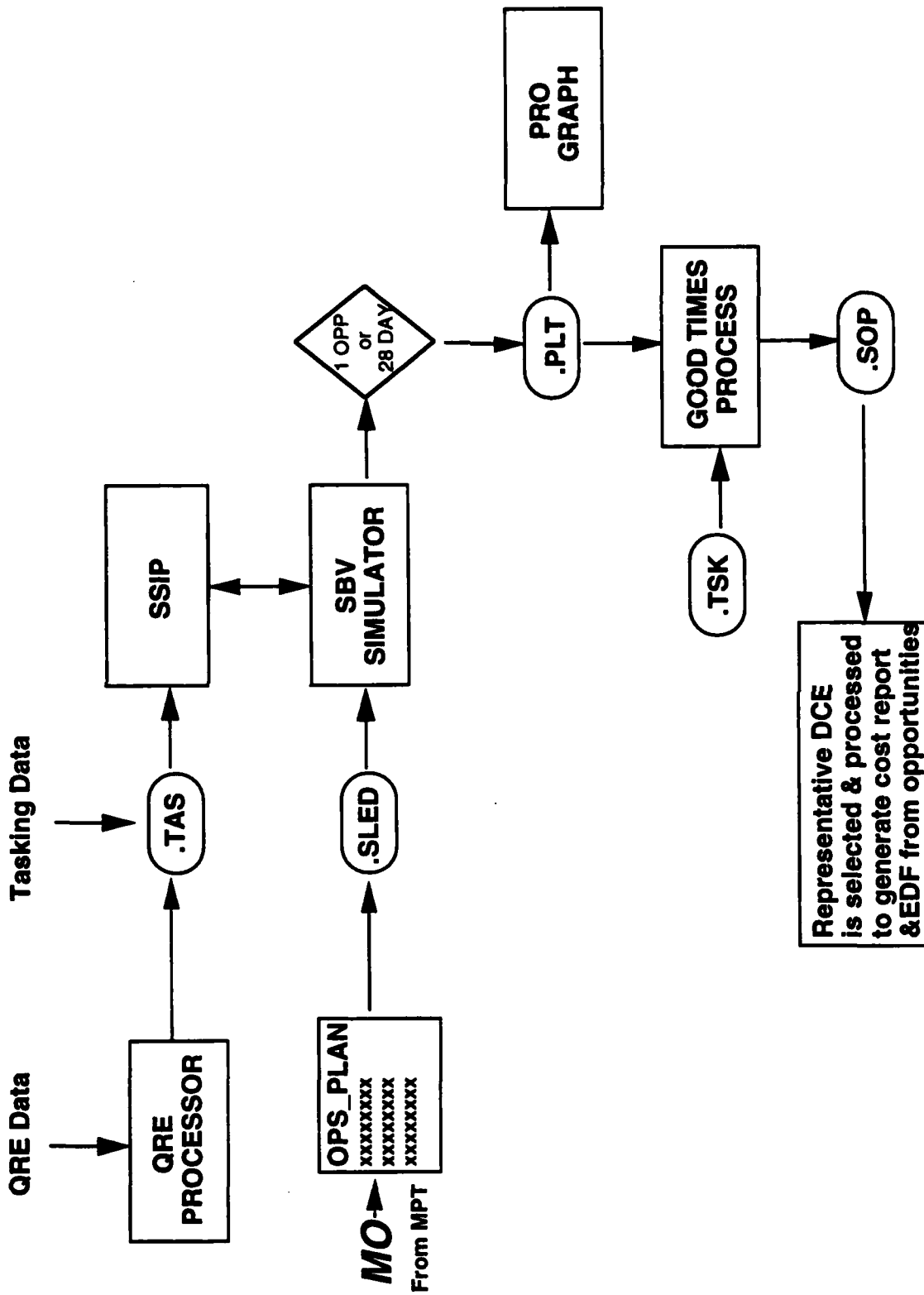


FIGURE 2

```

DEF:MISSION (METRIC CALIBRATION)
  SIMDIR( START-TIME = 94:209:23:14:00.0
    ,STEP-SIZE = .1
    ,PROGRAPH-DATA=YES
    ,ATTITUDE-DATA=YES
    ,MSX-ORBIT(OBJ-ID=69002)           ! 69002 = MSX element set
    ,CONTACT-SCHEDULING=EXAMPLE-EDF
  )
  SEQUENCE(CRUISE-MODE)
ENDDEF()

```

```

DEF:SEQ(CRUISE-MODE)
  DATA-COLLECTION (DC_CRUISE-MODE)
  POINT(ORIGIN(CCD=3,X=210,Y=210)
    ,ROLL(LAW=-Y-TO-SUN,ANGLE=0)
    ,ELEMENTS(INCL-KEP=55.150         ! ELEMENTS = 20533 calibration satellite
      ,RA-KEP=329.442
      ,ECC-KEP=.0043834
      ,AP-KEP=87.772
      ,MA-KEP=200.0
      ,SMA-KEP=26560.84494
      ,EPOCH-KEP=94:224.9
    )
    ,STARE(TIME1)
    ,DURATION(TIME=8:00.0)
    ,EXPOSURES(10)
  )

```

```

DEF:PIC( PIC3 )
  CCD(3)
  EXPOSURE-TIME(1.6)
  FRAME-COUNT(FRAMES=8)
  GAIN(HIGH)
ENDDEF:PIC

```

```

DEF:PROC(PROC1)
  STREAKS(1)
  STARS(0)
  SIGNATURES(NO)
ENDDEF:PROC( PROC1)

```

```

DEF:DATA-COLLECTION(DC_CRUISE-MODE)
  SBV-MODE(CRUISE-MODE)
ENDDEF:DATA-COLLECTION()

```

### 3.1.2. Geometrical Constraints

The instruments on the MSX, and the MSX itself, impose several geometrical constraints on the pointing and orientation of the spacecraft. These constraints are divided into hard (potential for damage) and soft (high resource usage).

Control of cryogen depletion on the SPIRIT 3 instrument is required to prolong its useful life. Hence the thermal input into the telescope axis from the sun and the earth must be kept low. This results in the following pointing constraints (see Figure 1 for body reference axes):

- 1) The X-axis (which is the common telescope axis) should be kept away ( $> 10^\circ$ ) from the sun direction(hard) and  $> 8^\circ$  from the nadir (soft) ;
  - 2) The +Y-axis, which defines the open or exposed side of the dewar containing the cryogen, should be kept  $> 10^\circ$  from the nadir (soft).
- and
- 3) The -Y-axis which defines the convex side of the SPIRIT 3 sunshade, should be kept  $> 10^\circ$  away from the nadir (soft);

The UVISI instruments require that the X-axis be not pointed near the sun(hard) or at the solar specular point on the earth(hard) when they are on.

The SBV cannot be pointed at the sun for more than 15 minutes (hard).

The -X axis of the spacecraft cannot be pointed at the sun directly for fear of heating the battery (soft).

The Simulator models all the angles relevant to these geometrical constraints during a data collection event.

The precise values for the constraints are yet to be refined. The MOCARH (Ref. 2) will be the formal document for operational constraints.

The Simulator also propagates the orbit of the MSX and of any RSOs requested. Geometrical visibility of the RSOs and solar illumination of both the RSOs and the MSX are computed. Further various relevant phase and aspect angles are computed. Finally, visibility from a set of ground-based contact stations is also computed.

### 3.2. PROGRAPH Display System

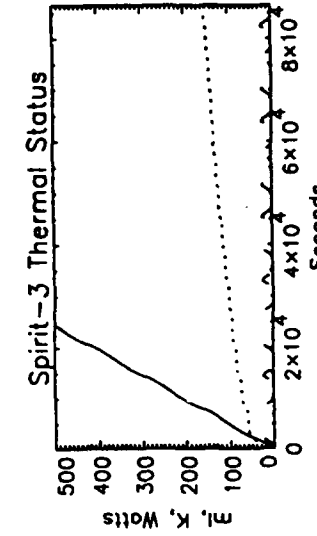
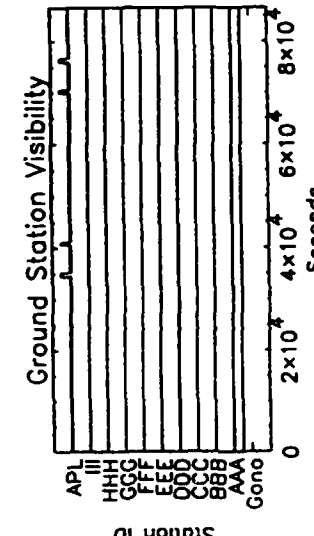
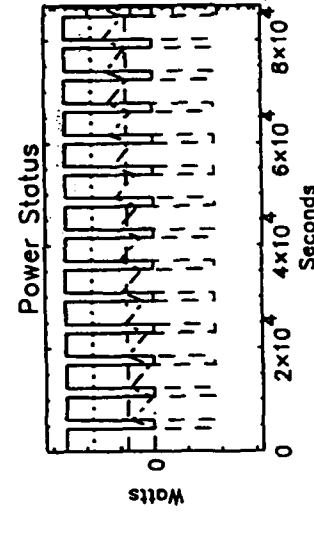
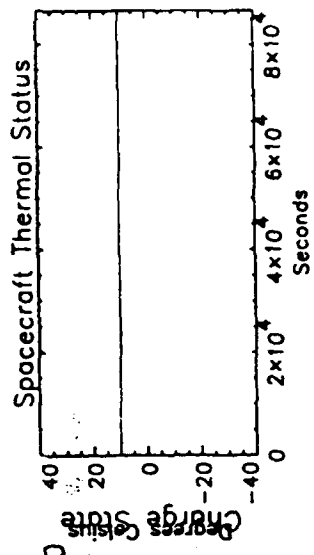
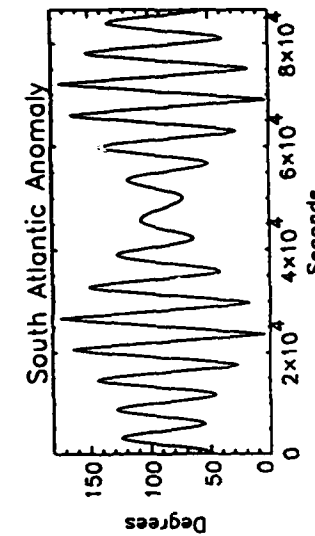
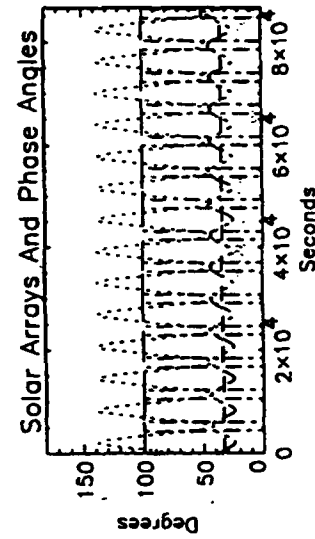
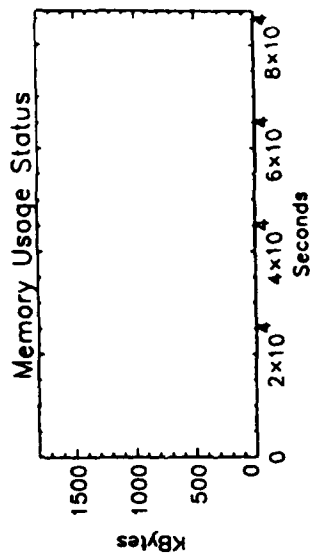
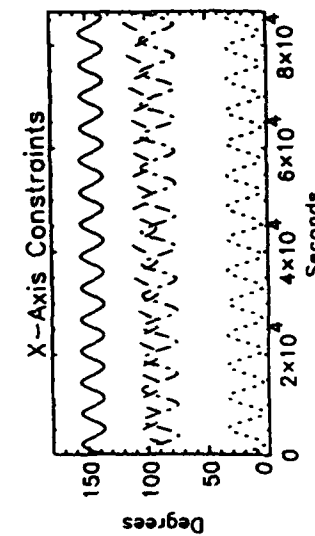
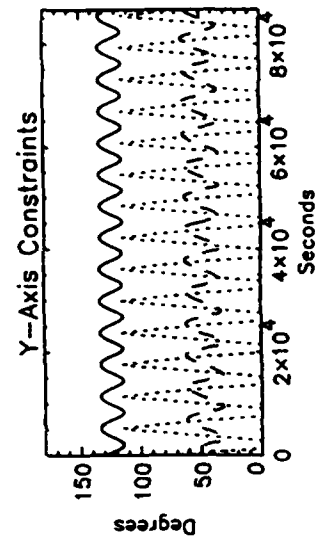
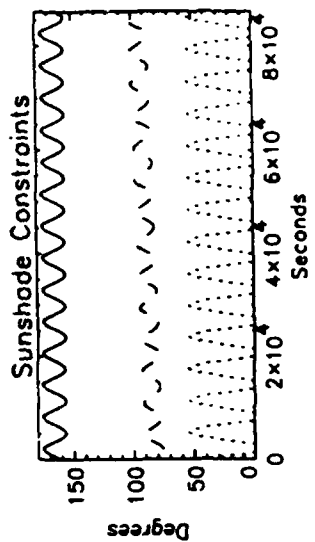
The graphical user interaction for the Feasibility Analysis System is provided by the PROGRAPH graphical display processor.

The Simulator writes out into a file all the resource usage and geometrical computations during the data collection event simulated. PROGRAPH displays all these variables in graphical form on a display. This enables the user to visualize the experiment cost and modify the SLED code appropriately to reduce the cost if necessary.

PROGRAPH is implemented with a commercial software package called PVWAVE (Ref. 3). The default is to display all the variables in a series of graphs on one screen (Figure 4).

Visual analysis is aided by the following capabilities of PROGRAPH:

- 1) Display of a selected graph.



Start Time : 1994/07/28 23:14:00.000  
 End Time : 1994/07/29 23:19:00.000

FIGURE 4

2) Display of selected variables in a graph.

3) Re-scaling of x and y axes on the graph (time elapsed during the data collection event is always the x-axis in the graph).

Generally, the analyst uses the X-axis constraints and the power usage graphs as key indicators of the feasibility of an experiment. Annotated examples are shown in Figures 5 and 6.

### 3.3. GOOD\_TIMES Process

The input data to PROGRAPH can be automatically analyzed by a process called GOOD\_TIMES. This process examines the various parameters and their values with respect to time and picks intervals during the period analyzed when the experiment can be conducted without constraint or resource usage violation.

The Mission Operations Constraint and Requirements Handbook (MOCARH) is the bible for mission operations. The MOCARH (Ref. 2) documents all the hard constraints on the MSX; and also specifies cost functions for soft constraints. All experiments must observe the rules in the MOCARH except when the Mission Planning Team of the MSX gives special dispensation for particular constraints to be violated for some experiments.

Apart from the PROGRAPH data, a task file drives the GOOD\_TIMES processor. The task file (Figure 7) specifies the range of values permitted for each parameter. When invoked, the GOOD\_TIMES process examines the entire PROGRAPH data and finds time intervals that satisfy all the constraints. The output is captured in a Surveillance Opportunities File which is a data product that is sent to the MOC at JHU/APL.

### 4.0. Examples

The Feasibility Analysis System is used by analysts in SPOCC to generate the necessary products for the entire mission planning cycle. This section will illustrate the process with examples.

#### 4.1. Monthly Planning

MSX is an experimental satellite. The Mission Planning Team sets objectives 6 weeks before the first day of the MSX month for which planning is in process. These objectives are provided to the MOC. The MOC provides Surveillance event identification numbers, corresponding to the Surveillance experiments on the list of objectives, to SPOCC.

SPOCC analysts write the necessary SLED code to support each experiment. The first task is to assess the time intervals during the month when the experiments are feasible.

A geosynchronous surveillance experiment will be taken as an example here. The requirement, as set by the Surveillance PI's experiment plan, is to survey any part of the geosynchronous belt for 3 consecutive hours using the SBV and its on-board signal processor. In the present case, the search strategy chosen was to point at a location in right ascension in the geostationary belt and vary the declination in steps between  $+3.5^\circ$  and  $-3.5^\circ$ . The SLED code written for the purpose is shown in Fig. 8. Notice that the experiment consists of a long data collection in the geosynchronous belt. Two optional roll laws are shown here:

- 1) the  $-Y$  axis is pointed as close as possible to the nadir;
- and 2) the  $-Y$  axis is pointed as close as possible to the sun.



- X-Axis to Sun
- ..... X-Axis to Earth Tangent
- - - X-Axis to Moon
- · - · X-Axis to Velocity

Start Time : 1994/07/28 23:14:00.000  
 End Time : 1994/07/29 02:14:20.000

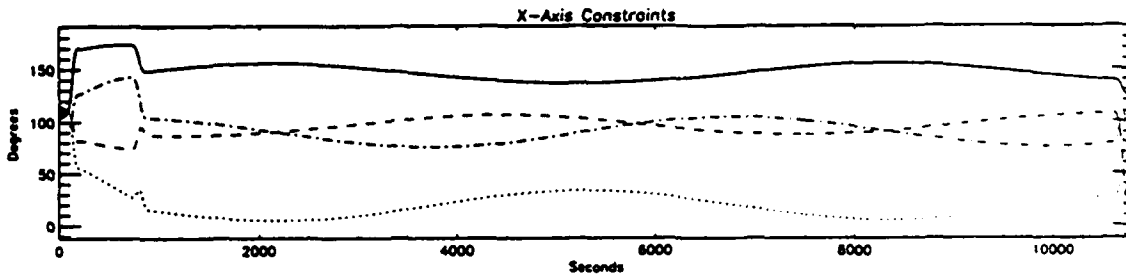
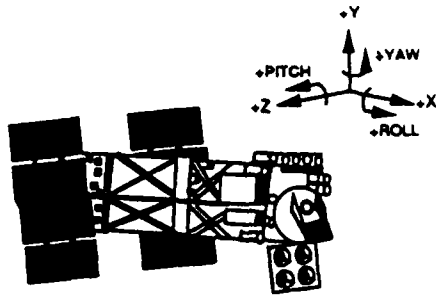
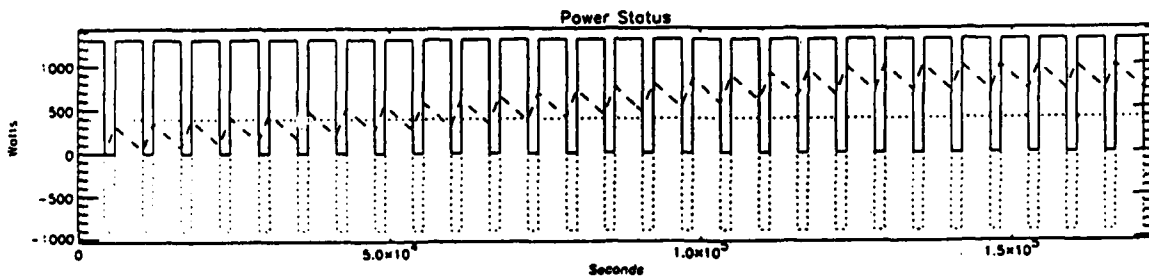
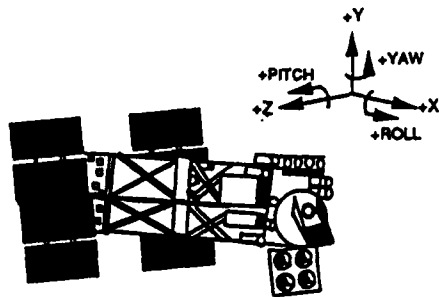


FIGURE 5

- Solar Array Output
- ..... Battery Power
- - - Battery Depth Of Discharge

Start Time : 1994/07/28 23:14:00.000  
 End Time : 1994/07/30 23:19:00.000



GEO BELT SEARCH EXPERIMENT

FIGURE 6

### SAMPLE .TSK FILE

TASK	experiment	<b>SU14010001401_01</b>
START_TIME - END_TIME	minutes	<b>min</b>
X_TO_SUN	0-150 degrees	<b>min / max</b>
X_TO_EARTH	0-180 degrees	<b>min / max</b>
X_TO_MOON	0-180 degrees	<b>min / max</b>
X_TO_VELOCITY	0-180 degrees	<b>min / max</b>
Y_TO_SUN	0-180 degrees	<b>min / max</b>
Y_TO_EARTH	0-180 degrees	<b>min / max</b>
Y_TO_MOON	0-180 degrees	<b>min / max</b>
SHADE_TO_SUN	0-180 degrees	<b>min / max</b>
SHADE_TO_EARTH	0-180 degrees	<b>min / max</b>
SHADE_TO_MOON	0-180 degrees	<b>min / max</b>
SOLAR-ARRAY_TO_SUN	0-90 degrees	<b>min / max</b>
SUN_MSX_EARTH_PHASE	0-180 degrees	<b>min / max</b>
SUN_TARGET_MSX_PHASE	0-150 degrees	<b>min / max</b>

**Bold = User Input**

FIGURE 7

```

DEF:MISSION (GEO BELT SEARCH)
  SIMDIR( START-TIME = 94:209:23:14:00.0
    .STEP-SIZE = .1
    .PROGRAPH-DATA=YES
    .CONSTRAINT-FLAGS(MEMORY=OFF)
    .MSX-ORBIT(OBJ-ID=69001)
    .CONTACT-SCHEDULING=OPP-ANALYSIS
  )
  SEQUENCE(CRUISE-MODE)
ENDDF()

DEF:SEQ(CRUISE-MODE)
  DATA-COLLECTION (DC_CRUISE-MODE)

  POINT(ORIGIN(CCD=3,X=210,Y=210)
    .ROLL(LAW=Y-TO-EARTH,ANGLE=0)
    ! .ROLL(LAW=Y-TO-SUN,ANGLE=0)           commented out
    .POSITION(RA=280,DEC=0.0,RANGE=42000)
    .STARE(GEOBELT)
    .DURATION(TIME=28:0:0:0)

ENDDF:SEQ()

DEF:STARE(GEOBELT)
  all(1,PICTURE=PIC4,PROCESSOR=PROC1)
  ! N(1,PICTURE=PIC4,PROCESSOR=PROC1)
  ! N(2,PICTURE=PIC3,PROCESSOR=PROC1)
  ! N(3,PICTURE=PIC2,PROCESSOR=PROC1)
  ! N(4,PICTURE=PIC1,PROCESSOR=PROC1)
ENDDF:STARE()

DEF:PIC( PIC1 )
  CCD(1)
  EXPOSURE-TIME(1.6)
  FRAME-COUNT(FRAMES=8)
  GAIN(HIGH)
ENDDF:PIC

DEF:PIC( PIC2 )
  CCD(2)
  EXPOSURE-TIME(1.6)
  FRAME-COUNT(FRAMES=8)
  GAIN(HIGH)
ENDDF:PIC

DEF:PIC( PIC3 )
  CCD(3)
  EXPOSURE-TIME(1.6)
  FRAME-COUNT(FRAMES=8)
  GAIN(HIGH)
ENDDF:PIC

DEF:PIC( PIC4 )
  CCD(4)

  EXPOSURE-TIME(1.6)
  FRAME-COUNT(FRAMES=8)
  GAIN(HIGH)
ENDDF:PIC

DEF:PROC(PROC1)
  STREAKS(1)
  STARS(0)
  SIGNATURES(NO)
ENDDF:PROC( PROC1)

DEF:DATA-COLLECTION(DC_CRUISE-MODE)
  SBV-MODE(CRUISE-MODE)
ENDDF:DATA-COLLECTION()

```

Figure 8

The first roll law minimizes the thermal input into the SPIRIT 3 telescope from the earth and thus conserves its cryogen. The second roll law enables the solar panels to be rotated about the Z-axis for maximum solar illumination and power generation. These are the type of soft constraints that an analyst examines to optimize the resource usage of the experiment.

Figures 9 and 10 are examples of the output of the PROGRAPH process for the first roll law. Typically a 28 day simulation is run but for illustration purposes a 24 hour time period is shown here. Fig. 11 is the annotated task file for the GOOD\_TIMES processor. Output of the GOOD\_TIMES processor is a "Surveillance Opportunity File" that tabulates when the experiment can be conducted for the required length of time while satisfying all the constraints.

Figures 12 and 13 are examples of the output of the PROGRAPH processor for the second roll law. Figure 14 is the surveillance opportunity file corresponding.

Once the opportunities are chosen, APL/MOC schedules the surveillance events.

## 4.2. Weekly and Daily Planning

The predominant work of choosing the opportunities is achieved at the monthly planning level. The weekly and daily planning process merely handles perturbations to the scheduled events because of spacecraft orbit or configuration changes, uplink and downlink contact opportunity changes, etc. At this stage, the feasibility analysis is rerun merely to verify that these perturbations have not affected the valid time interval chosen for the surveillance experiments in any way; and to recompute the cost of the event.

## 5.0 Summary

A successful Feasibility Analysis System has been developed in SPOCC to facilitate the scheduling of the Surveillance Principal Investigator's experiments on the MSX. The System uses knowledge of relevant geometries and spacecraft and instruments constraints to model the cost of conducting an experiment. The System has been tested extensively and fully supports the long experiment planning process associated with the MSX.

## REFERENCES

1. Ted Fishman, private communication.
2. PVWAVE reference manual.
3. Applied Physics Laboratory: "The MSX Operations Constraints and Requirements Handbook (MOCARH), Ver. 1".

GEO BELT SEARCH EXPERIMENT

— Solar Array Output  
 ..... Battery Power  
 - - - Battery Depth Of Discharge

Start Time : 1994/07/28 23:14:00.000  
 End Time : 1994/07/29 23:19:00.000

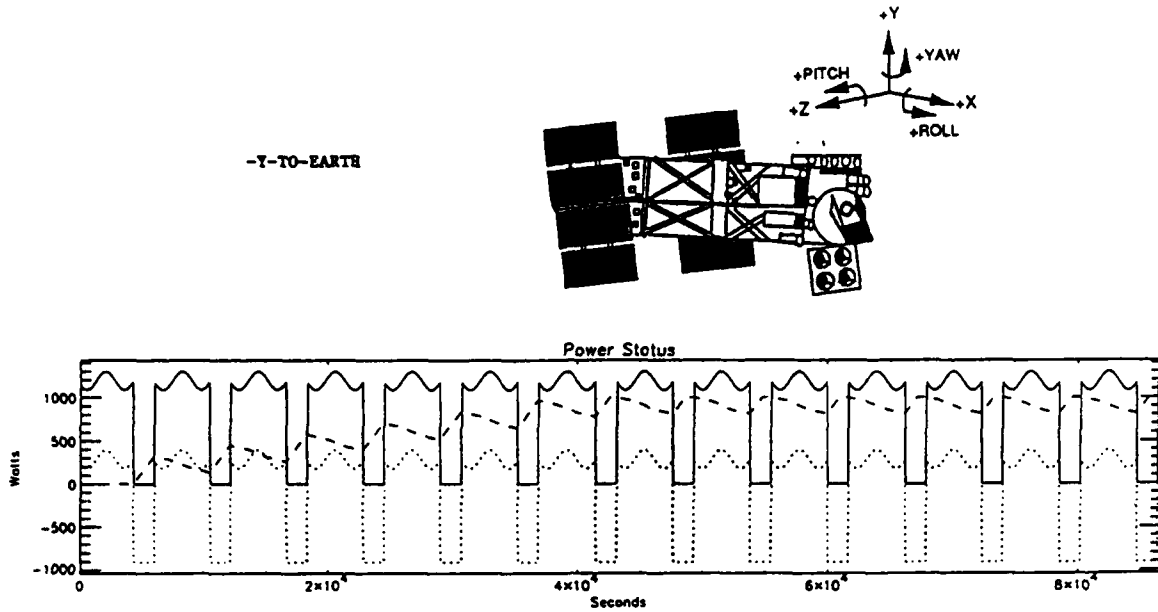


FIGURE 9

GEO BELT SEARCH EXPERIMENT

— Y-Axis to Sun  
 ..... Y-Axis to Earth Tangent

Start Time : 1994/07/28 23:14:00.000  
 End Time : 1994/07/29 23:19:00.000

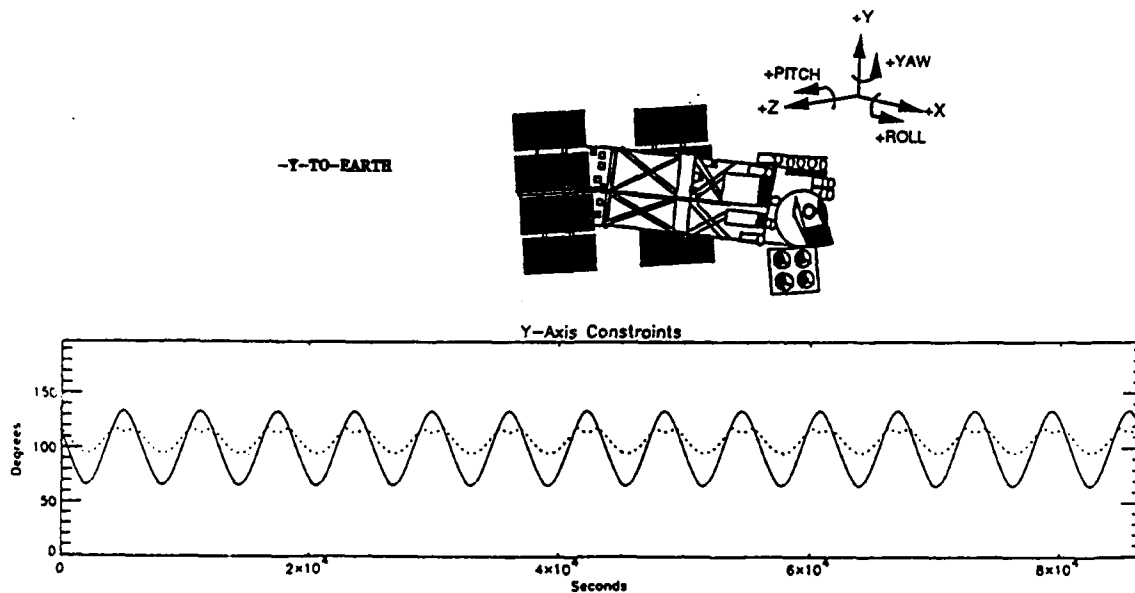


FIGURE 10

## SAMPLE TASK FILE

dur\_min 180  
dur\_max 1440  
xsun\_max 180  
xsun\_min 30  
xearth\_max 180  
xearth\_min 1.17  
xmoon\_max 180  
xmoon\_min -180  
xvel\_max 180  
xvel\_min 30  
ysun\_max 180  
ysun\_min 45  
yearth\_max 180  
yearth\_min 30  
ymoon\_max 180  
ymoon\_min 0  
shadesun\_max 180  
shadesun\_min 60  
shadeearth\_max 180  
shadeearth\_min -180  
arraysun\_max 180  
arraysun\_min -180  
smephase\_max 180  
smephase\_min -180  
stephase\_max 180  
stephase\_min -180  
stmphase\_max 180  
stmphase\_min -180  
saa\_max 180  
saa\_min -180  
output\_max 10000  
output\_min -10000  
load\_max 10000  
load\_min -10000  
power\_max 10000  
power\_min -1000  
state\_max 10000  
state\_min 70  
gyro\_max 10000  
gyro\_min -10000  
btemp\_max 10000  
btemp\_min -10000

FIGURE 11

GEO BELT SEARCH EXPERIMENT

— X-Axis to Sun  
 ..... X-Axis to Earth Tangent

Start Time : 1994/07/28 23:14:00.000  
 End Time : 1994/07/29 23:19:00.000

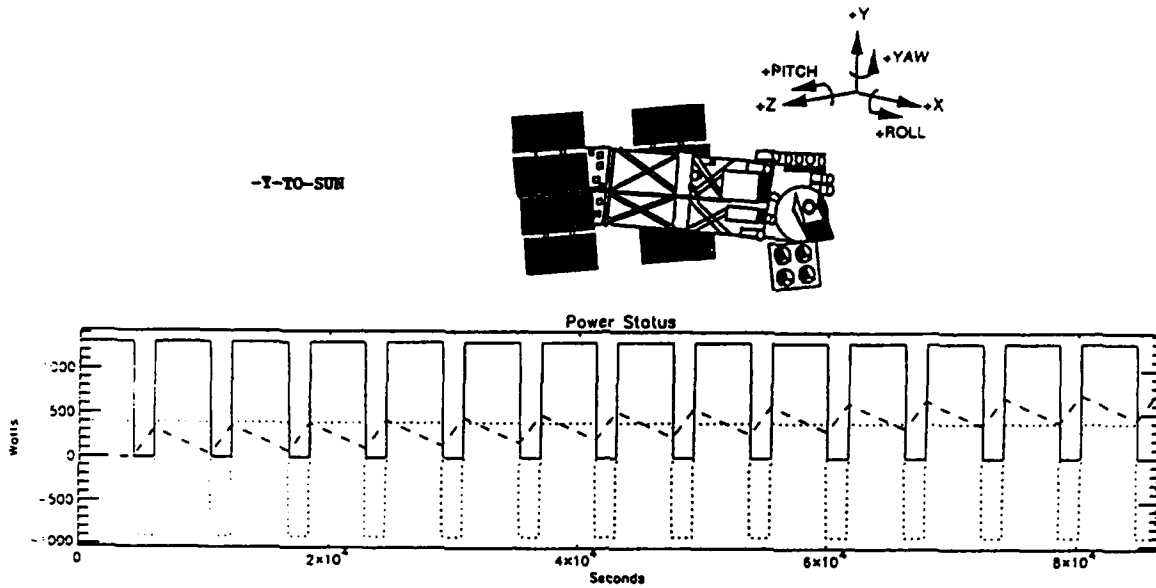


FIGURE 12

GEO BELT SEARCH EXPERIMENT

— Y-Axis to Sun  
 ..... Y-Axis to Earth Tangent

Start Time : 1994/07/28 23:14:00.000  
 End Time : 1994/07/29 23:19:00.000

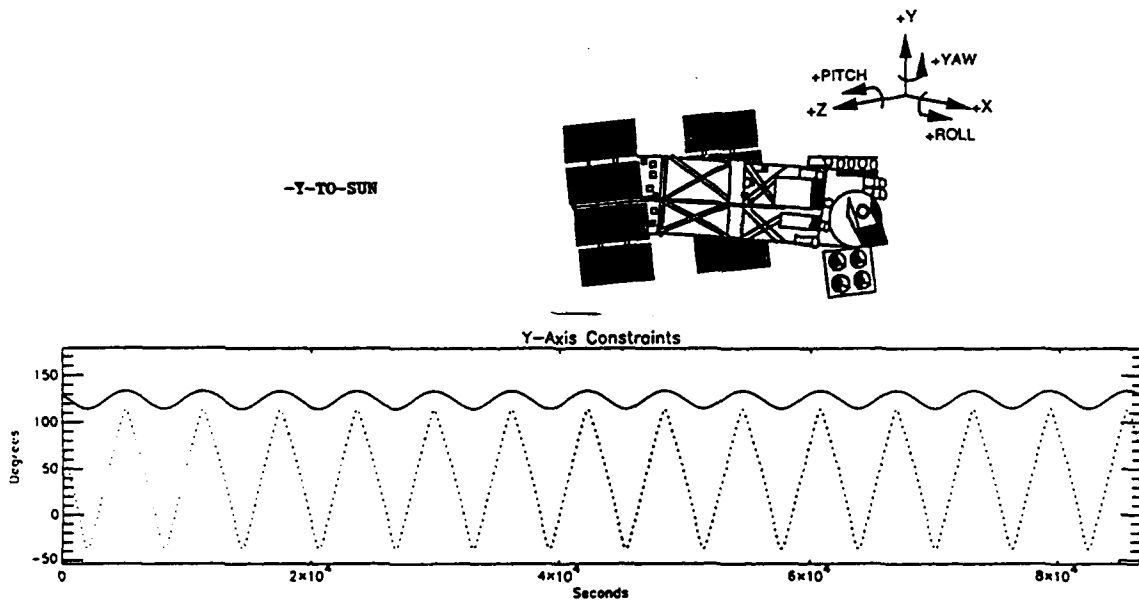


FIGURE 13





## MSX Reference Sphere Detection And Tracking

J.M. Rumreich, R. Sridharan (MIT Lincoln Laboratory)

### I. INTRODUCTION

The Midcourse Space Experiment (MSX) satellite is a Ballistic Missile Defense Organization (formerly Strategic Defense Initiative Organization) sponsored experimental spacecraft. The MSX satellite, due for launch in late 1994, is shown in Figure 1.

The MSX satellite's primary missions are to collect phenomenology data of backgrounds, of missile targets and plumes, and of resident space objects (RSOs). Secondary missions are functional demonstrations of detection, acquisition, and tracking of ballistic missiles and space-based surveillance of RSOs.

Three primary instruments will be located on-board the spacecraft: the SPIRIT 3, a long-wave infrared sensor; the SBV, a broad-band visible sensor; and the UVISI, a visible and ultraviolet wavelength sensor.

The MSX satellite will also carry six reference spheres to be used for the on-orbit calibration of the SPIRIT 3 sensor. In addition to calibration, these spheres will provide the opportunity to perform a number of useful studies related to their orbital propagation and detectability. The success of such experiments, as well as the SPIRIT 3 calibration, depend on obtaining accurate metric and orbital data on the spheres. Although the MSX sensors themselves may be able to provide some data, it will be necessary to employ ground-based sensors as well.

It is the purpose of this paper to address the issues of detection and tracking of the MSX reference spheres using ground-based sensors. In particular, it will be shown that the MIT Lincoln Laboratory's Haystack radar is the only operationally available sensor capable of reliably detecting, acquiring, and tracking the spheres. This result will be born out through the consideration of other available sensors and through the use of computer simulation.

### II. PLANNED STUDIES

The main purpose for deploying the MSX reference spheres will be for the precise radiometric calibration of the SPIRIT 3 sensor. Also planned are studies on the effects of earthshine in the infrared band. In addition to these, however, there a number of other interesting and potentially useful studies that could be pursued with the reference spheres.

The development of new techniques in space surveillance, be it for detection, acquisition, tracking, or calibration, is assisted immensely by the availability of orbiting spheres that can be used as reference targets. The six reference spheres are no exception; in fact, because of their controlled injections into orbit, they represent nearly ideal control objects for study and experimentation. For example, they could be used as calibration objects for debris data collection instruments, including the MSX itself, or to assess debris detection and discrimination techniques.

The reference spheres could also be utilized in the study of the effects of radiation pressure and atmospheric drag on orbiting debris. Currently there are significant uncertainties in the

atmospheric density parameters at the MSX altitudes. Short and long term studies of orbiting spheres, especially those with high area-to-mass ratios such that drag perturbations are increased, could provide greater understanding in this area.

### **III. MSX REFERENCE SPHERES**

The design of the MSX reference spheres and their deployment necessarily focusses on optimizing calibration of the SPIRIT 3 sensor. Secondary considerations, however, are given toward benefitting other studies utilizing the spheres.

#### **3.1. Physical Characteristics**

Precise orbit determination requires that the spheres be detectable and trackable by the on-board sensors as well as by ground-based sensors. The size and surface composition of the spheres are the crucial factors affecting these properties.

Five of the reference spheres will be 2 cm in diameter and made of aluminum to provide a conductive surface for radar tracking. These spheres will be coated with Martin Black to enhance thermal emissivity to approximately 0.99. (The effect of the coating on the radar-cross-section (RCS) of the spheres is not expected to be significant.) These spheres will be solid, resulting in a cross-sectional area-to-mass ratio of about 0.3 cm<sup>2</sup>/gm.

The sixth sphere will also be 2 cm in diameter and made of aluminum but will be gold-coated to enhance thermal reflectivity to aid in the study of earthshine effects. Furthermore, this sphere will be hollow and have a wall thickness of only 1.5 mm, resulting in an area-to-mass ratio of nearly 0.6 cm<sup>2</sup>/gm. (Note that conventional satellites tend to have an area-to-mass ratio of about 0.1 cm<sup>2</sup>/gm.) This relatively high area-to-mass ratio will increase orbital drag on the sphere, thus aiding in the study of atmospheric density.

#### **3.2. Injection Scenario**

The MSX satellite will be in a circular orbit at approximately 900 km in altitude with an orbital inclination of 99°. Each sphere will be ejected from the spacecraft either prior to or following a major MSX target experiment. Furthermore, each will be ejected with a relative velocity of 13 m/sec and in a direction selected to optimize the SPIRIT 3 calibration.

### **IV. DETECTABILITY OF THE REFERENCE SPHERES**

A necessary condition for the success of all planned experiments utilizing the MSX reference spheres, including the SPIRIT 3 calibration itself, is that accurate metric and orbital data on the spheres be available. The MSX sensors, however, are not expected to be able to collect data on the spheres except immediately after deployment and on other infrequent close approaches. Success, therefore, requires that the spheres be detectable and trackable by ground-based sensors.

#### **4.1. Ground-Based Sensors**

An earlier report [1] analyzed the detection and tracking of the reference spheres by the MSX itself and by ground-based optics and radars. Some of the sensors considered were the AMOS IR

sensor, the GEODSS and ETS visible light optical systems, and the Haystack, Millstone, TRADEX, and MMW radars. The principle conclusion was that the only ground-based instrument that could reliably detect the spheres, particularly soon after deployment, is the sensitive Haystack radar. The report concluded further that the ground-based optical satellite tracking instruments and the on-board SBV sensor could be used as backups to provide metric data.

#### 4.2. Haystack

The Haystack radar, operated by MIT's Lincoln Laboratory, is a narrow beamwidth, high resolution radar operating at 10 GHz. Its pulse widths range from 5 msec down to 256  $\mu$ sec, with frequency bandwidths from 200 kHz to 1 GHz. Detection parameters of relevance to the detection and tracking of the reference spheres are given in Table 1.

At 10 GHz, the radar-cross-section of the 2 cm diameter spheres will be approximately -35 dBsm. Published data indicate that using a single 1 msec long pulse, the Haystack radar will achieve signal-to-noise ratios (S/Ns) on the spheres of:

<u>range (km)</u>	<u>S/N (dB)</u>
1000	23
2000	11
3000	7.

Using coherent integration of 25 pulses would be adequate to achieve a S/N of 20 dB even at 3000 km. Note also that the radar is capable of detecting multiple scatterers simultaneously, but can only track one at a time.

The recommended mode of operation of the Haystack radar during the reference sphere searches will be the 1 msec / 10 MHz mode (see Table 1). This mode provides high energy-per-pulse, thus enhancing its detection capability. A coherent integration of 5-10 pulses would provide additional detection sensitivity.

The Haystack radar is capable of producing data with a calibrated accuracy of 0.5 m in range, 10-50 mm/sec in range rate, and 0.005° in angle at a S/N of over 20 dB. Further, the quality of these tracking data are adequate to support an orbit determination accuracy, based on multiple passes, with a maximum error of 15 m.

The 256  $\mu$ sec / 1 GHz mode (see Table 1) will be the preferred mode for reference sphere tracking by the Haystack radar.

**TABLE 1: HAYSTACK RADAR PARAMETERS**

<u>PARAMETER</u>	<u>OPERATING MODE</u>	
	<u>1 msec / 10 MHz</u>	<u>256 <math>\mu</math>sec / 1 GHz</u>
pulse width	1 msec	256 $\mu$ sec
peak power / duty cycle	320 kW / 35 %	320 kW / 35 %

bandwidth	10 MHz	1 GHz
pulse repetition frequency	300 / sec	up to 1200 / sec
range window	3.7 km	40, 60, or 150 m
range resolution	18.75 m	25 cm
S/N per pulse at 2000 km range	11 dB	5 dB
coherent integration	100 pulses	100 pulses
angle beamwidth	0.05°	0.05°
first range sidelobe (dB relative to peak)	-38 dB (TE weighting)	-38 dB (TE weighting)
range sidelobe falloff (beyond first sidelobe)	6 dB / 120 m	6 dB / 1.2 m
Doppler sidelobe (dB relative to peak)	-28 dB	-28 dB
angle sidelobe (first) (dB relative to peak)	-22 dB	-22 dB
Doppler resolution	15 m/sec	
dynamic range in RCS	60 dB	60 dB

#### 4.3. Factors Affecting Detectability

The ability of the Haystack radar to detect and acquire the reference spheres in the presence of the parent MSX is a function of its ability to discriminate between them. This would not be a problem but for the fact that the radar-cross-section of the MSX is expected to be of the order of 30 dBsm, while that of the spheres will be only -35 dBsm.

The uncertainties in the ejection velocities also affect the radar's ability to detect the reference spheres. Specifically, because the MSX has no real-time communication capability to collect and process data, near-real-time acquisition of the spheres will require the use of the *a priori* uncertainty values to bound the radar's search space.

The expected uncertainties in the reference sphere ejections may be specified in terms of the three components below:

<u>component of ejection velocity</u>	<u>uncertainty</u>
time of ejection	<< 1 sec
speed (relative to parent)	$\pm 0.5$ m/sec
direction (relative to parent)	$\pm 0.5^\circ$ .

Of these, the uncertainty in ejection speed will have the greatest effect on the ability of the Haystack radar to detect the reference spheres. Analysis has shown that after only 20 minutes an error of 0.5 m/sec would translate into a positional error of 600 m, which in turn could translate into a S/N degradation of 3 dB per pulse at close ranges ( $\approx 1000$  km). Note also that this error grows linearly with time.

On the other hand, an error of  $0.5^\circ$  in ejection direction would translate into a positional error of only about 100 m after 20 minutes. It follows that the effect of this error is not significant for the Haystack radar over short time intervals. Likewise, so long as the error in ejection time is much less than one second, its effects will be negligible.

The discussion above exemplifies the problem of sphere detection using the Haystack radar. If a sphere is ejected just prior to or during a pass over the radar, then the backscattered signal returned from the MSX could dominate that from the sphere. Conversely, if the sphere ejection occurs a substantial amount of time prior to the pass, then the radar, with its narrow beamwidth, will confront a large search problem. In either case, detection and acquisition of the reference sphere could be difficult.

## V. SIMULATION

A software simulation package was created for the purpose of investigating the detectability of the MSX reference spheres using the Haystack radar. Following is a description of the software and of the results obtained from simulation.

### 5.1. Software

The crucial discriminants available between the MSX satellite and its reference spheres will be their metric positions in radar space and their radar-cross-sections. It follows that in order for the simulation package to be useful, it was required to:

1. model the relative displacement between the MSX and the spheres, for a few orbital revolutions after ejection;
2. model the Haystack radar in terms of its sensitivity and acquisition window; and
3. assess the discrimination between the MSX and the spheres in radar parameters so that a strategy which maximizes the probability of sphere acquisition by the radar can be derived.

Following is a description of the models employed by the simulator for meeting requirements 1 and 2 above. Graphical output from the simulator and the analysis of that output was used in satisfying requirement 3.

### 5.1.1. Relative Displacement Between MSX and Sphere

The position ( $r$ ) and velocity ( $r'$ ) of the MSX at some time  $t$  is specified using earth-centered inertial (ECI) coordinates. Each sphere ejection is then specified by the time of ejection, the ejection speed relative to the MSX, and ejection direction given in local orbital coordinates (azimuth and elevation). Uncertainties in the ejection speeds and directions may also be specified, resulting in bounds on the output.

Orbit propagation of the MSX and the spheres after their ejection is accomplished using a simple two-body model based on a closed-form solution to the traditional  $f$  and  $g$  "series". This model, although it ignores the effects of perturbations on the satellites, was deemed satisfactory. In particular, it has been assumed that while the effects of perturbations can be significant on the orbits, their differential effects on the spheres relative to the MSX will be insignificant over the relatively short duration of interest.

### 5.1.2. Radar Model

Because an absolute measure of the radar-cross-sections will not be available in real-time and because the discriminant will be reflected in signal-to-noise ratios at the radar, it is vital to model the radar performance in terms of expected S/N.

The expected S/N received on an object at the Haystack radar can be modelled as:

$$S/N = S_{1000} + \sigma - 40 \log_{10}(R/1000) - \delta_{\text{ANGLE}} - \delta_{\text{RANGE}}$$

where

$S_{1000}$	=	S/N on a 0 dBsm object at 1000 km and centered in the radar beam (58 dB for Haystack)
$\sigma$	=	RCS of the object (dBsm)
$R$	=	range to the object (km)
$\delta_{\text{ANGLE}}$	=	angle offset correction (dB), and
$\delta_{\text{RANGE}}$	=	range offset correction (dB).

The angle and range offset corrections are used to correct for the object's calculated offset from the center of the beam's angle and range windows, respectively. The angle offset correction, or equivalently the reduction in S/N as the object goes away from the center of the beam, has been measured for the Haystack radar by scanning around object 5398, which is one of the Lincoln Calibration Spheres in orbit. The beam shape is shown in Figure 2. Similarly, the range offset correction has been estimated for Haystack based on published numbers and discussions with Haystack personnel. The beam shape is shown in Figure 3 for the recommended radar mode, which is using a 1 msec pulse and a 10 MHz bandwidth.

## 5.2. Results

The simulation package was used to explore the ability of the Haystack radar to detect and track the reference spheres soon after their deployment from the MSX. Following is a description of the simulation and the results obtained.

### **5.2.1. Simulation Description**

Three spheres were deployed from the MSX each with a relative velocity of 13 m/sec along the minus velocity vector of the spacecraft (i.e. retrograde). To account for uncertainties in the ejection velocities, errors in speed of  $\pm 0.5$  m/sec and in direction of  $\pm 0.5^\circ$  were specified.

In order to investigate the effect of deployment time on detectability, different ejection times were specified for each sphere. In particular, spheres 1, 2, and 3 were ejected 30, 20, and 10 minutes prior to the MSX's visibility at Haystack, respectively. (Specifying ejection times relative to the parent spacecraft's initial visibility is within the functionality of the simulation software.)

The radar-cross-section of each sphere was set at -35 dBsm and that of the MSX was specified to be 30 dBsm.

The simulation was performed over the first pass of the deployed spheres over the Haystack radar.

### **5.2.2. Output and Analysis**

The relative positions of each sphere with respect to the MSX are shown in Figures 4-6 for their first pass over the Haystack radar:

- Figure 4: Delta Angle vs Time,
- Figure 5: Delta Range vs Time, and
- Figure 6: Delta Angle vs Delta Range.

These plots depict the differences in angles and ranges between each of the spheres and the MSX as seen from the Haystack radar. It is evident that reasonable discrimination exists in terms of angle and range separation between the parent and spheres, even for the sphere ejected only 10 minutes prior to apparition (sphere 3).

The signal-to-noise ratios expected at the Haystack radar for each of the spheres as well as the parent MSX are shown in Figures 7-9:

- Figure 7: S/N On All Objects with Radar Pointing at Sphere 1, Ejected 30 Minutes Prior to Pass,
- Figure 8: S/N On All Objects with Radar Pointing at Sphere 2, Ejected 20 Minutes Prior to Pass, and
- Figure 9: S/N On All Objects with Radar Pointing at Sphere 3, Ejected 10 Minutes Prior to Pass.

These curves show that the narrow beamwidth and low range sidelobes of the Haystack radar allow a small sphere to be detected in the presence of the parent MSX so long as the radar is pointing at the expected position of the sphere.

## **VI. Conclusions**

This study provides evidence that if the MSX reference spheres are ejected between 10 and 30 minutes prior to an MSX pass over the Haystack radar, then substantial signal-to-noise ratio discrimination between them and the parent MSX will be available; that is, it is likely that the radar will be able to detect, acquire, and track the spheres in the presence of the parent. It is also evident that coherent integration of the radar received pulses would be useful for near-horizon acquisition of the spheres.

Although this report has only explored a single ejection strategy, various other strategies have been tested which support the stated conclusions. The results of this study now await practical verification. Plans are under discussion with the MSX Program to implement the results of this study on the Haystack Radar.

## **References**

- [ 1 ] R. Sridharan, Private Communication
- [ 2 ] Skolnik, "Radar Handbook," McGraw-Hill Book Company, 1970.



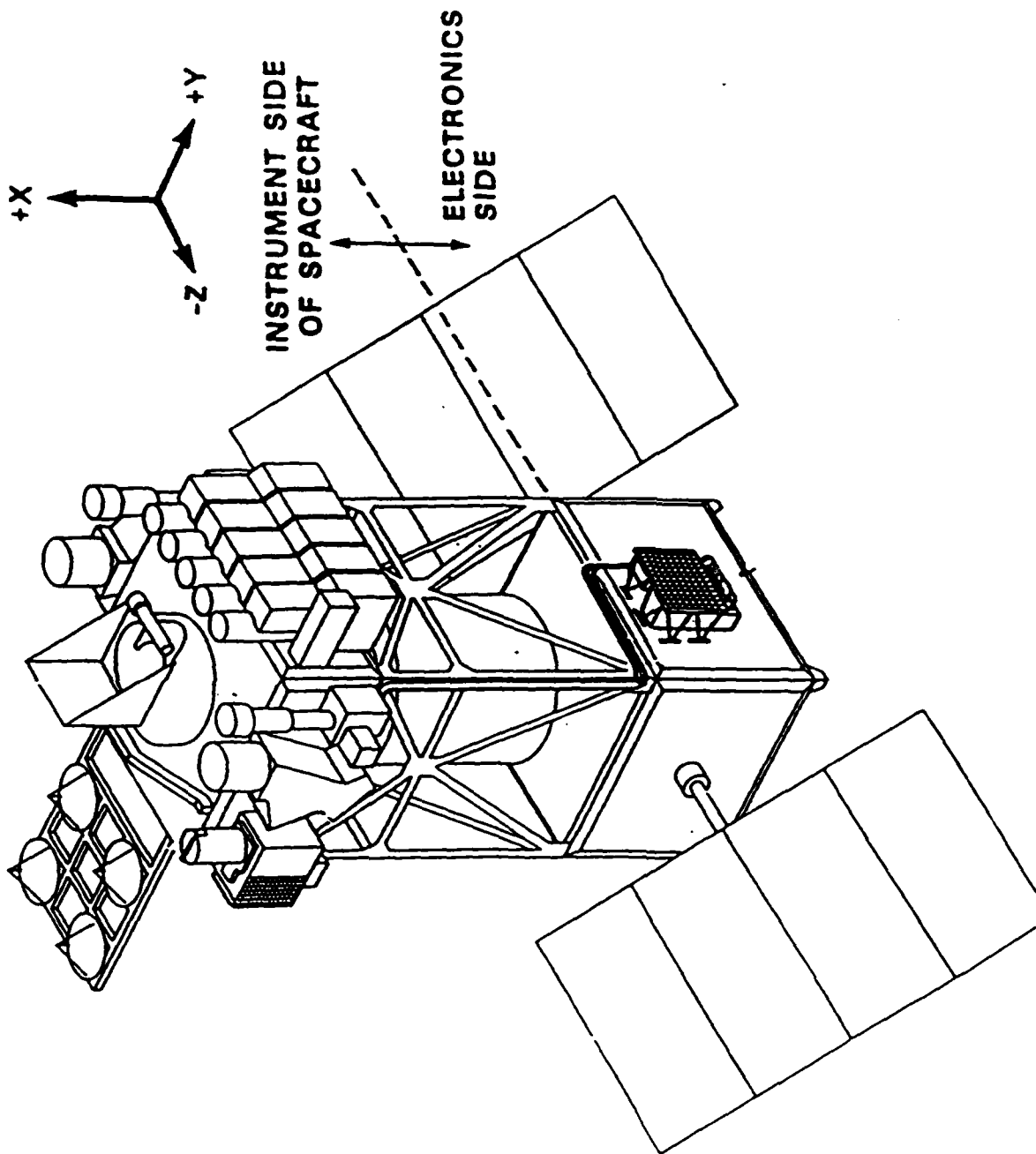
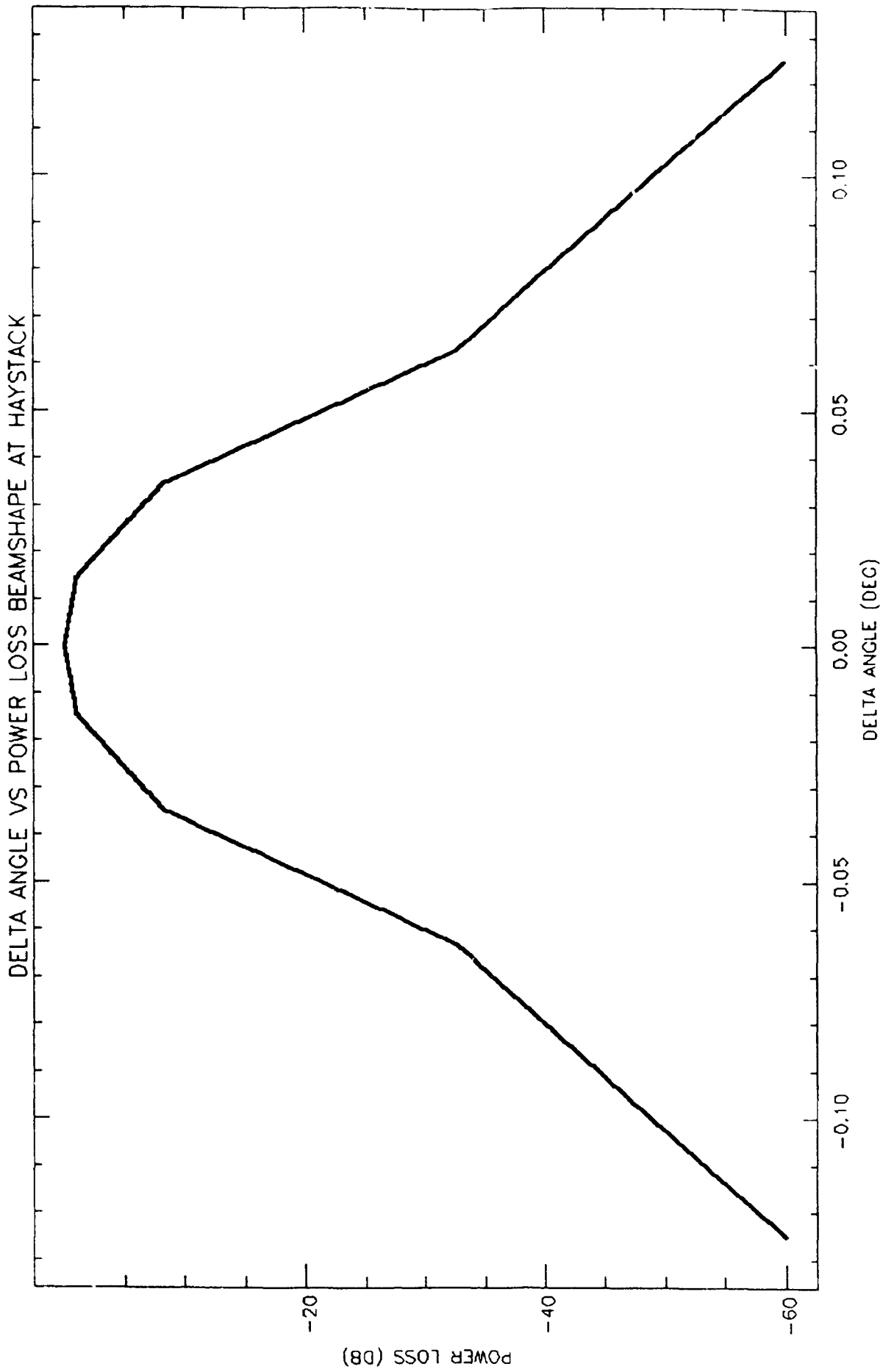
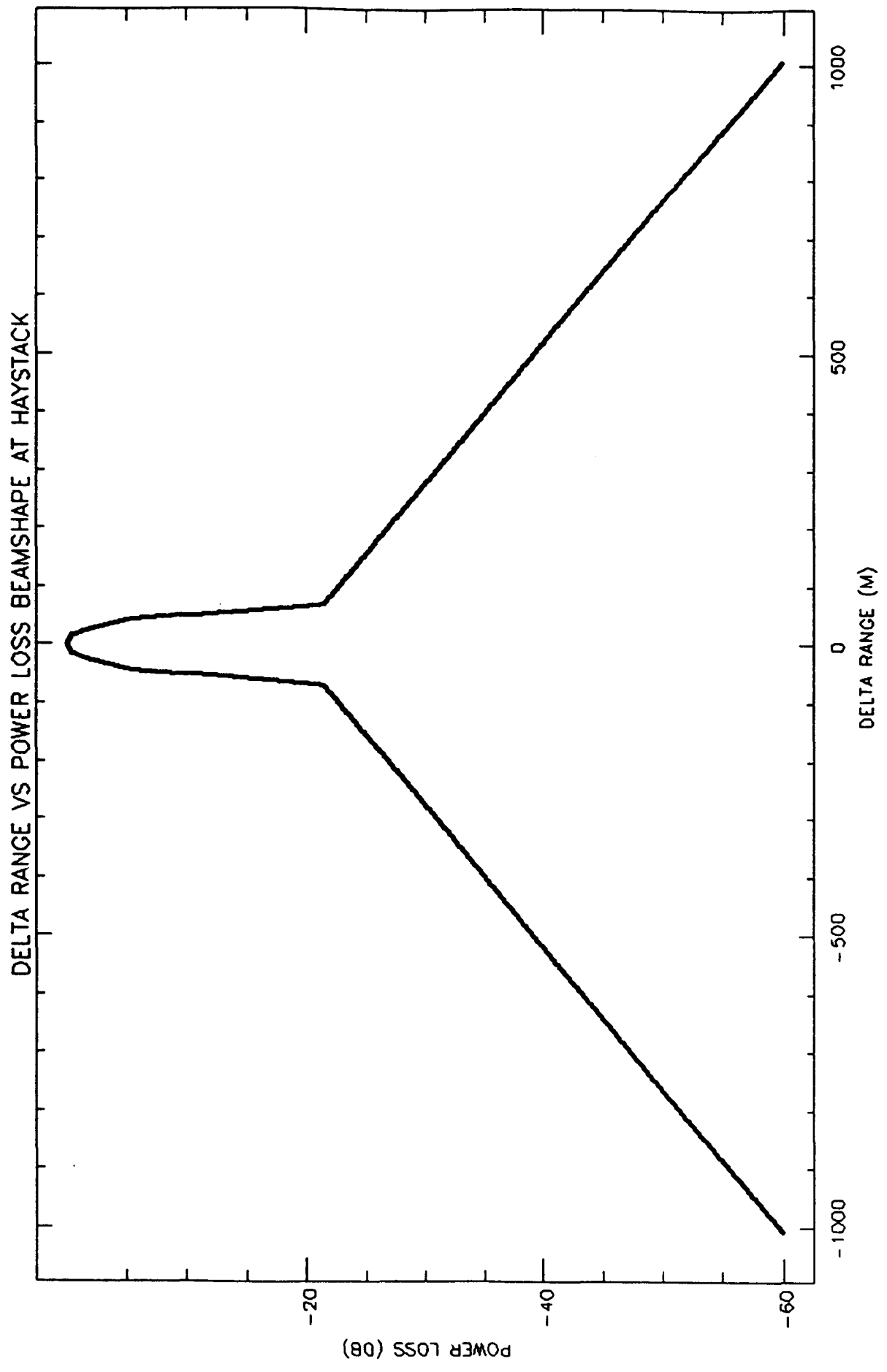
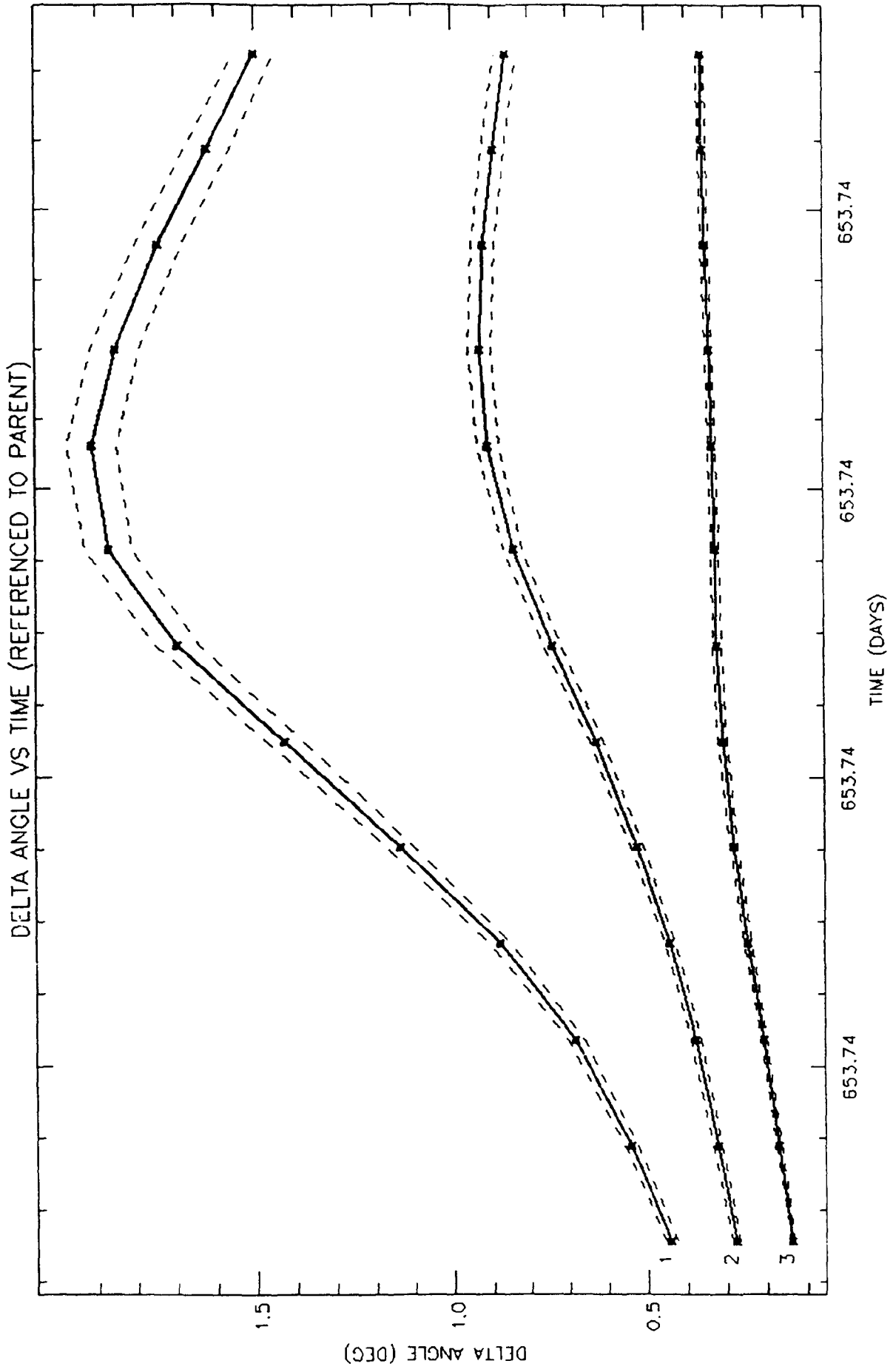
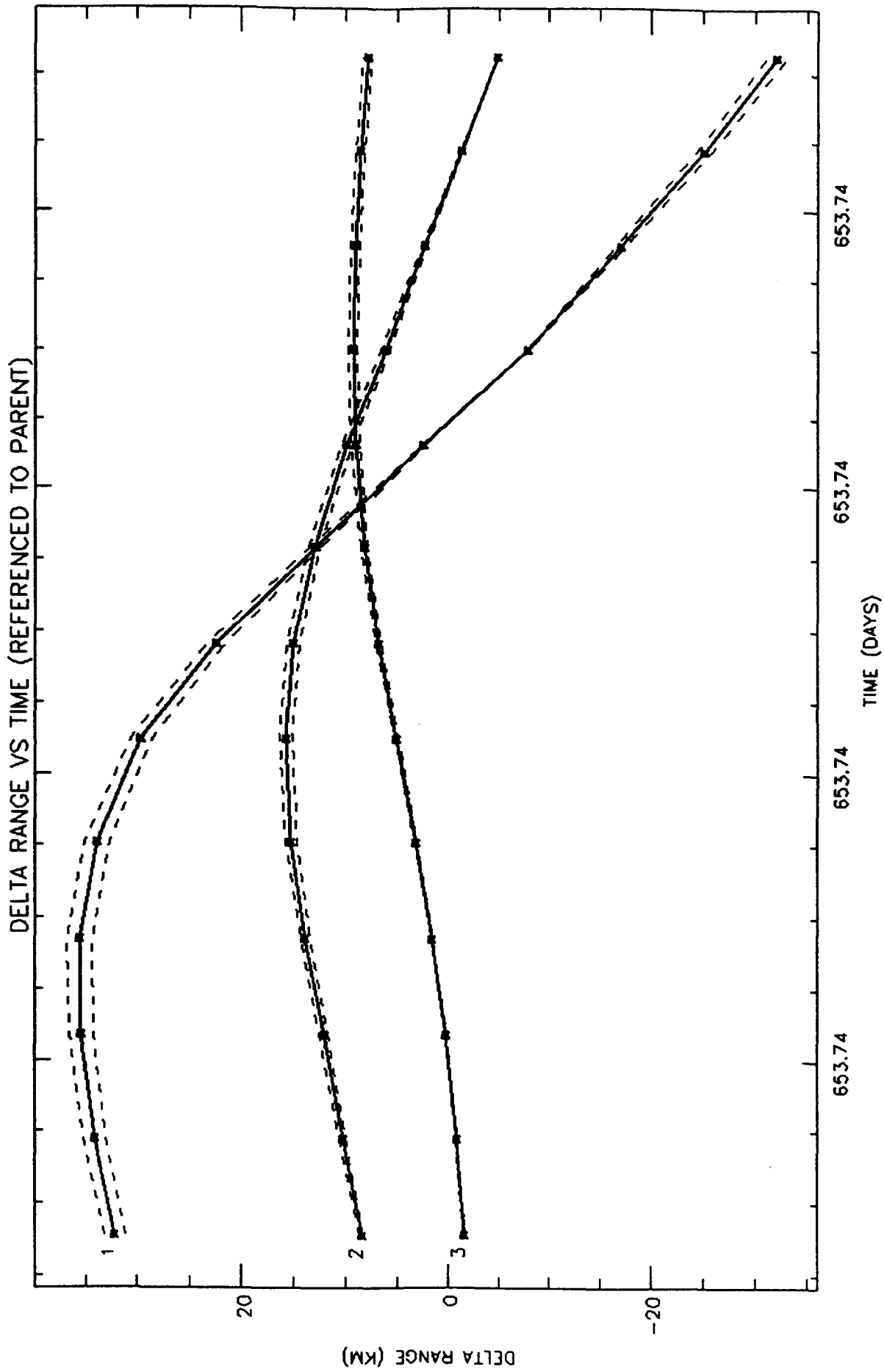


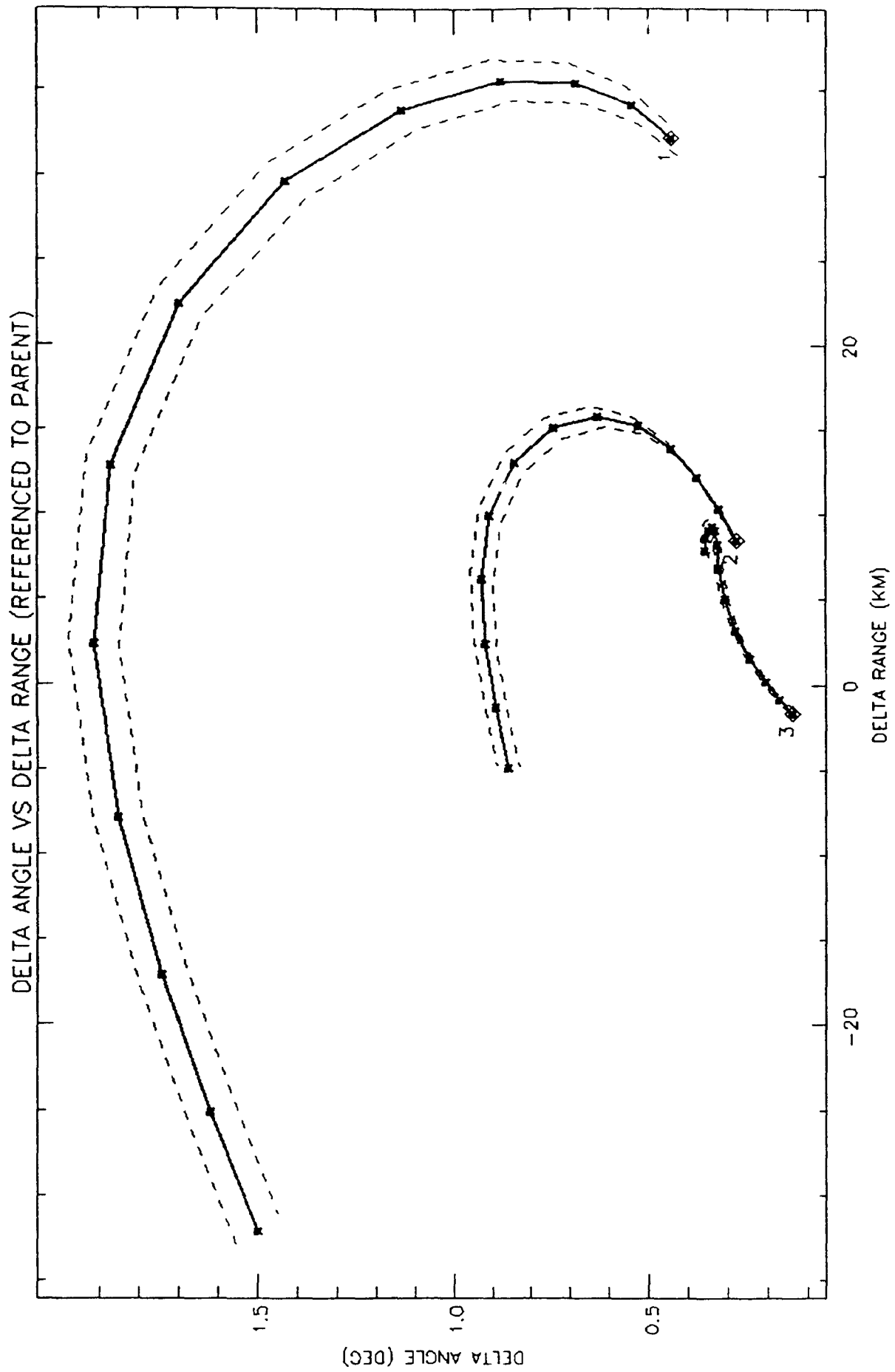
FIGURE 1 MSX SPACECRAFT

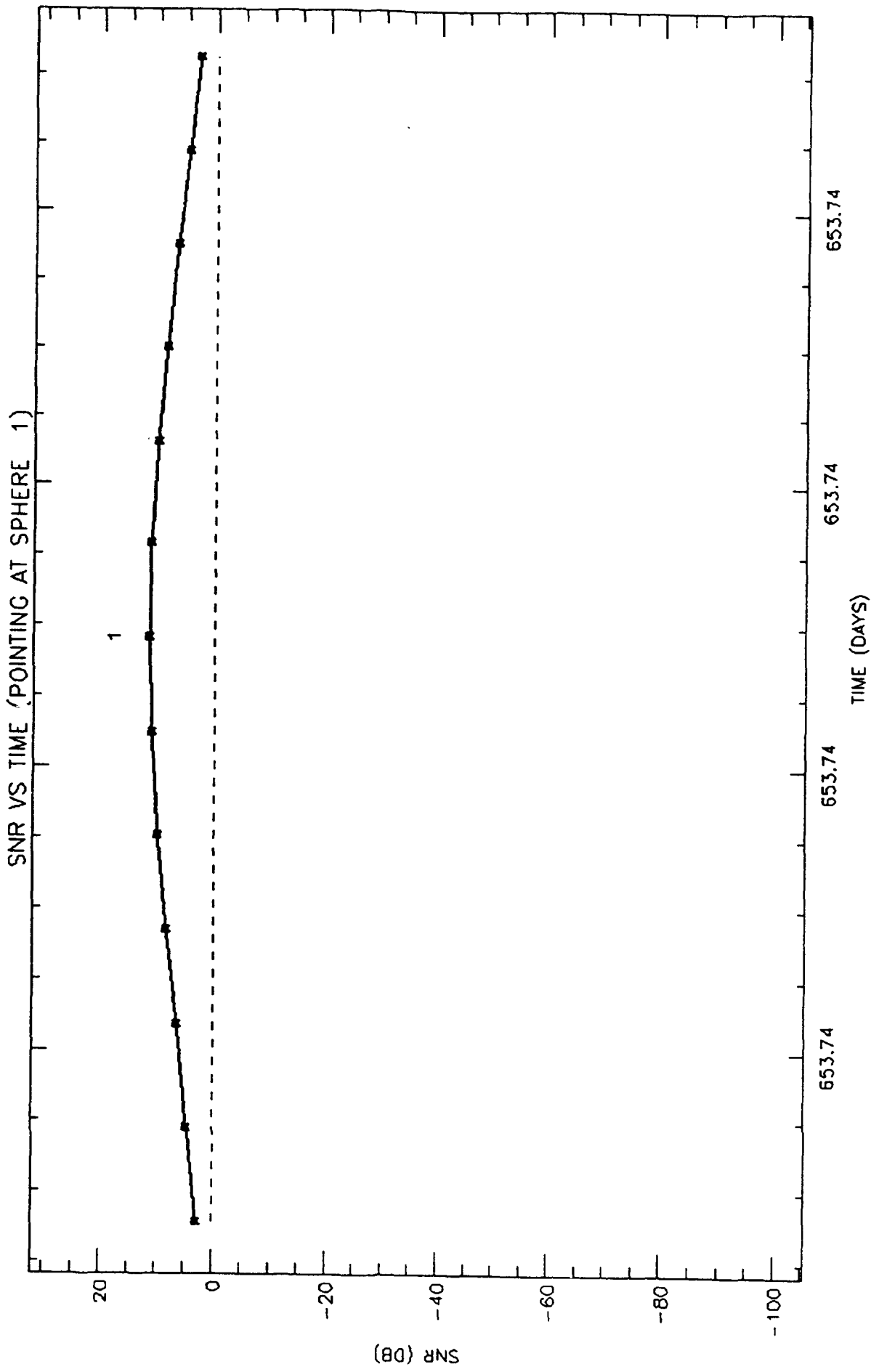




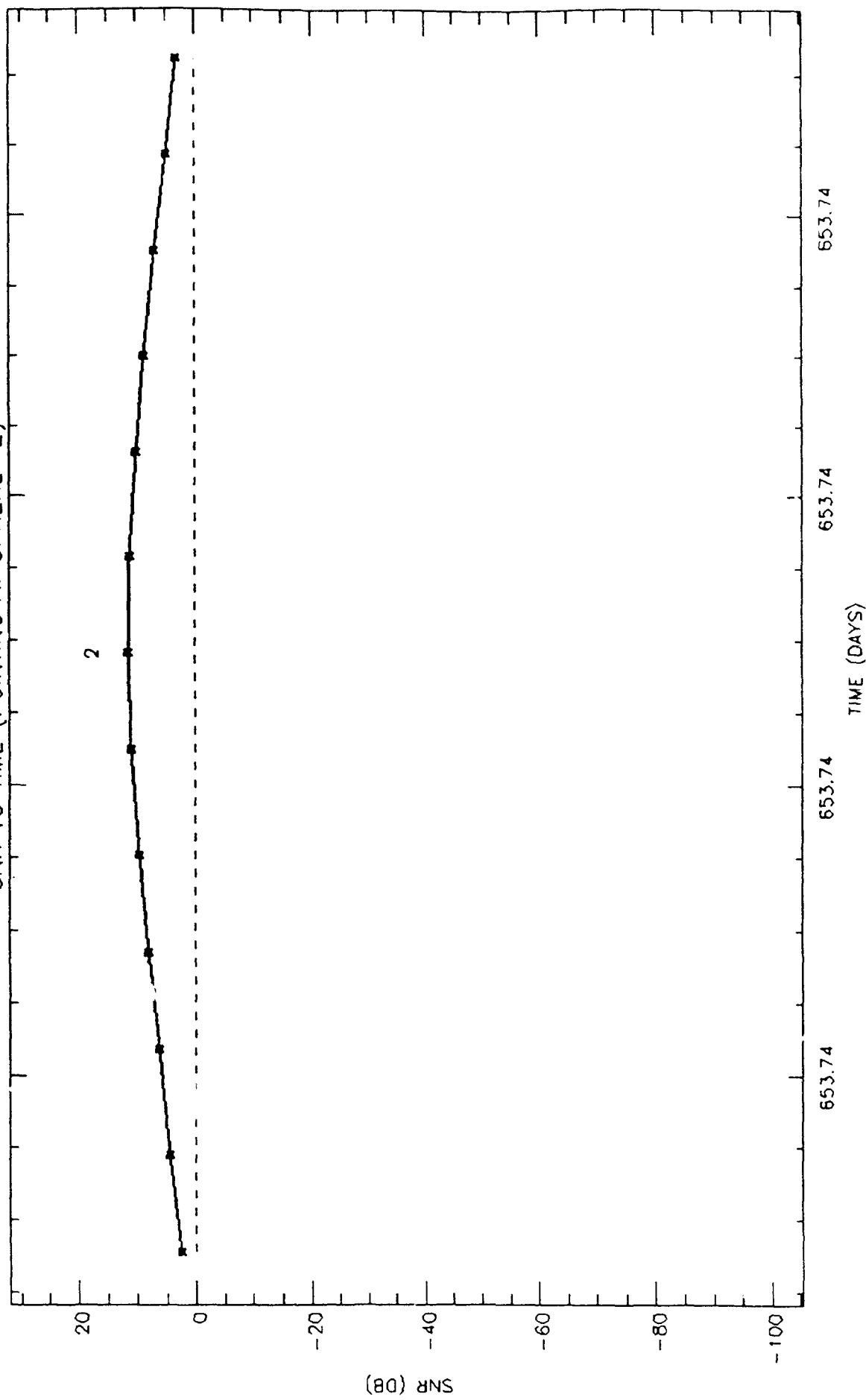






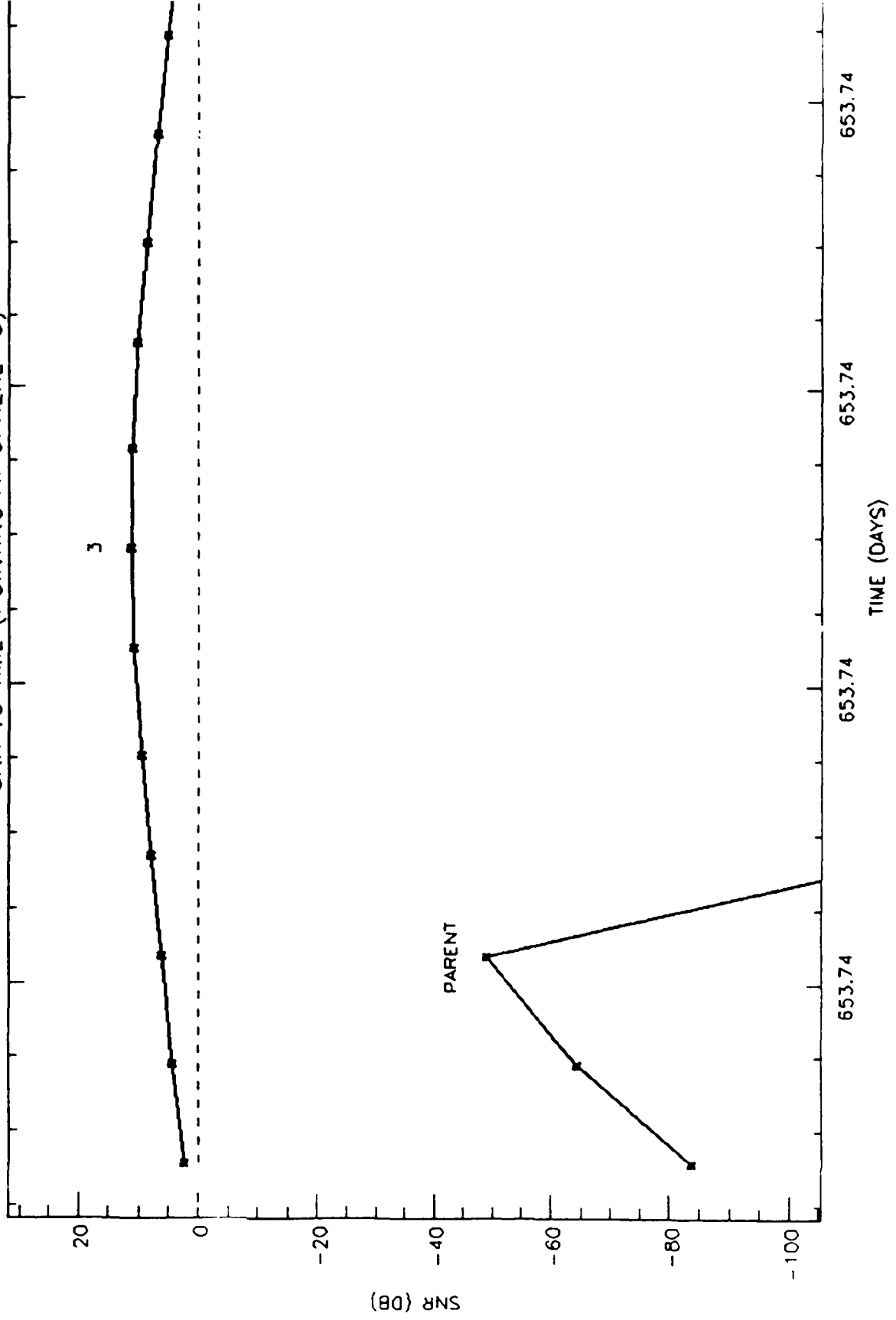


SNR VS TIME (POINTING AT SPHERE 2)





SNR VS TIME (POINTING AT SPHERE 3)



### Space Based Space Surveillance Cost and Performance Study Results

Maj. R.E. Firpo (USAF, SMC/XRF), A.O. Morse (Aerospace Corp.), Capt. G.G. Peredo (USAF, SMC/XRF)

Surveillance of space by space based optical sensors has been the subject of study since the early '70s. These studies have established the desirability and feasibility of the medium, but the risks and costs of space basing were apparently too high to warrant relieving the ground based Space Surveillance Network (SSN) of its space surveillance role. After all, space surveillance picks up only a small portion of the operating cost of the surveillance sites, whereas it utilizes the lion's share of their day to day operations. In the intervening period since the studies began, technology advancement has greatly reduced many of the risks. In addition, spacecraft and ground station costs also appear to be decreasing, and the introduction of low cost boosters such as Pegasus and Taurus will have the same effect on launch cost. These trends, coupled with the concurrent waning of tensions between the world's major powers, and the growing desire to reduce the number of US bases on foreign soil, have made the space based option appear more attractive.

This is not to say that space basing will eliminate the need for ground sensors - it won't, because the simple, low cost system Visible Light Surveillance (VLS) systems envisioned here cannot perform imaging and have limited capability for the tracking of small space debris objects. However, our study has shown that the bulk of the work of the SSN, the tracking and cataloging of spacecraft sized objects, can be done better and faster by the VLS, especially for objects in deep space.

When examination of space based optical concepts began in the '70s, the emphasis was on long wave infrared (LWIR) as the space surveillance medium. Continual analysis and technology development during the 80's resulted in a consensus (ca 1983) that LWIR technology was about ready, so preparation for the acquisition of a Space Based Space Surveillance system (SBSS) began. By direction from OUSDRE, SBSS was to utilize only the LWIR medium. Before the acquisition process could be completed, however, the program was transferred into the Strategic Defense Initiative (SDI) and absorbed by the Space Surveillance and Tracking System (SSTS) program where space surveillance was defined to be a secondary objective. Eventually, Brilliant Eyes (BE) replaced SSTS as the SDI space based space surveillance system, although at first there was concern that this function would severely impact BE spacecraft design. With the evolution of BE came the realization that it could readily perform the space surveillance mission with little adverse impact.

Recent studies have shown that a large constellation of multispectral satellites such as BE is indeed a superior concept for the purpose of obtaining metric space surveillance data. With so many sensors available, only the three or four best situated for detecting and tracking a given object would be selected to do it, thus assuring that only the best viewing angles would be used.

This study was commissioned by AFSPACECOM/DR, to examine dedicated visible light sensing approaches as an interim solution to space surveillance needs, because of the possibility that a robust multispectral surveillance constellation will not be fielded in the foreseeable future. A dedicated VLS constellation of light weight, relatively low cost satellites, if equal or superior to the SSN in satisfying the metric space surveillance requirements for spacecraft sized objects, would give the USAF the flexibility to trim the network without waiting for the ultimate system.

Some of the good news from this study is that a small, low cost dedicated VLS constellation can provide better coverage and tracking accuracy than the SSN under realistic and representative conditions. Additional good news is that evolution in the state-of-the art of focal planes, data processors, small satellite design, ground station design, and even boosters has resulted in lowered cost and risk projections. It appears that the criteria for an effective, low cost interim solution to space based space surveillance can now be satisfied.

In this study, we show the results of coverage and accuracy analyses where we compare the performance of visible light constellations with that of the SSN. We also show cost estimates for two constellations, one in low earth orbit at 880 km, and one positioned in the upper reaches of the Van Allen belt at 10,400 km.

The purpose of a space surveillance system is to view orbit space, report the orbit parameters of every object it is tasked to find in this space, and provide the data which will be used to predict each object's position at a later time, to warn about potential collisions, and to detect maneuvers. In some cases it must also provide the data needed to identify each object and its purpose. In this report we consider only the metric aspects of space surveillance. Clearly, to be detected and tracked, an object must appear in the coverage region of one or more of the sensors. The accuracy of the predicted path of a tracked object depends on a number of factors, primarily sensor pointing knowledge accuracy (assuming a perfect mathematical orbit model), and the number and duration of viewing opportunities.

The configurations which are treated in this study are more or less competitive with the SSN in meeting requirements for spacecraft detection and tracking. They are:

**Dedicated: VLS High** - A three satellite constellation at 10,400 km altitude and 28.5 deg inclination.

**VLS Low** - A four satellite constellation at 880 km altitude and 28.5 deg inclination.

In both of the above constellations the orbits are circular and the satellites are equally spaced.

**Adjunct: VLS/GPS** - VLS sensors as adjunct payloads on three coplanar GPS satellites.

Other potential host systems were also examined briefly but discarded for further study because of major deficiencies. The most notable of these was the Defense Meteorological Satellite Program (DMSP). When this study began the DMSP constellation consisted of two satellites. With only two satellites, data report timeliness would be inadequate, and there would be no opportunity for simultaneous (stereo) tracking of low altitude objects. Because of the timeliness problems and decreased coverage, VLS/DMSP would be useful only to augment the SSN or another dedicated space surveillance constellation.

The altitude and number of satellites for the VLS low constellation were chosen as a compromise among the competing effects of the Van Allen belt, the South Atlantic anomaly, the desire to minimize launch costs, the desire for good near earth coverage, and the desire to have cross link communication. The VLS/GPS option takes advantage of the potential availability of piggy-backing on GPS satellites. The VLS high constellation is a compromise between the other two to help explore the trade space.

In this report we compare performance of the listed VLS system candidates with the SSN, and examine other issues which impact system selection and design.

A 20-cm telescope aperture was selected, which for an off-axis optical design (required to permit operation near the earth limb), results in a telescope and gimbal weight of about 150 lb if Beryllium is used for the telescope and gimbal structure. However, beryllium may not be necessary if payload weight is not severely constrained.

The telescope focal length is a trade between available detector pixel sizes, the pixel instantaneous field of view (IFOV), and the optical design. The required pixel IFOV is determined by LOS angular speeds of the targets of interest, the attainable frame rate, the estimated background levels, and the estimated platform jitter. The chosen CCD array design is readily available from a number of vendors. It can be read out at a reasonably fast frame rate (the 5 Hz frame rate implies a sampling rate of about 1.3 MHz (if four output nodes are included in the design)). This array results in a good FOV and pixel IFOV for the selected  $f/4$  optical design. The risks associated with the producibility and alignment sensitivity of such an off-axis telescope, while higher than those of a simpler on-axis design, are moderate. However, for this design the pointing jitter amplitude should be less than 7  $\mu$ radian rms to avoid loss of signal.

**VLS Telescope--3-mirror, f/4, off axis design:**

Effective Aperture	20 cm
Focal Length	80 cm
Field-of-View (FOV)	1.3 deg x 1.3 deg
Pixel IFOV	22.5 microradians
Optics Throughput	50%
PSF Ensquared Energy per Pixel	80%
Target Straddle Factor	50%
Filter Bandpass	0.4-0.9 micrometers
Mirror BRDF @ 1 deg & 300 Level Contamination	$2.0E^{-2} \text{ sr}^{-1}$
Baffle L/D	4

The optical layout of the VLS telescope is a folded, 3-mirror, off-axis design with a 20 cm aperture. Except for its larger size it is similar to the Lincoln Laboratory Space Based Visible (SBV) sensor (15 cm). In this study's design, mirrors M1 and M3 have concave ellipsoid surfaces, and M2 has a convex hyperboloid surface. A flat folding mirror, F1, is used to direct the image to the focal plane.

Focal plane design is frequently a compromise between sensitivity and dynamic range. The use of a backside-illuminated, buried-channel charge coupled device (CCD) operating in the MPP (multi-phase pinned) mode yields a focal plane with the proper balance of these two qualities. The CCD has high quantum efficiency (QE) and charge transfer efficiency (CTE) as well as negligible dark current levels at near ambient operating temperatures (10 deg C to 20 deg C). The MPP mode, while suppressing surface state dark current, does tend to limit the full-well capacity of the CCD, but a minimum level of 80,000 electrons ( $e^-$ ) is readily attainable. A dynamic range of 12 bits with a full-well capacity of 80,000  $e^-$  requires a readnoise floor of  $\leq 20 e^-$  rms. To achieve this level of detector read noise at the quoted sampling rate, the sensitivity of the on-chip amplifier nodes should be somewhat higher than the typical  $1 \mu\text{V}/e^-$ . CCD arrays built by Lincoln Laboratory have node sensitivities of  $9 \mu\text{V}/e^-$  or higher and provide  $6 e^-$  rms noise floors at 1 MHz sampling rates. Commercial sources have manufactured chips with node sensitivities as high as  $15 \mu\text{V}/e^-$ , and with claimed low noise operation at even higher sampling rates.

One of the problems of CCD focal plane design is radiation sensitivity. However, at the selected altitudes (880 or 10,400 km or higher), the radiation environment is not extreme and can be alleviated by moderate shielding of the focal plane.

**VLS Focal Plane--3-Phase, Backside-Illuminated CCD**

Array Size	1024 x 1024
Pixel Size	18 micrometers
Quantum Efficiency (Solar Weighted)	63%
Operating Temperature	0 deg C
Dark Current (MPP Mode)	58 rms $e^-$ per frame
Frame Time	0.2-2.0 sec
Max Sampling Rate	5.25 MHz
Readout Noise	12 rms $e^-$
Signal-to-Noise Ratio Per Pixel	6
Minimum Streak	1 Pixel/Frame

We used the following assumptions and constraints for this study: the sensor is used in a step-stare mode; above-the-horizon (ATH) viewing only; 110 km is the minimum tangent height; the solar exclusion angle is greater than 20 degrees; and the jitter is less than half of a pixel IFOV (p-p).

When a space sensor is tasked to start its search for an orbiting target, that object may or may not be in the sensor's region of detectability. After a period of time - the "gap time" - the target will enter this region and

the sensor can detect it. This chart compares the gap time performance of the SSN and the VLS High in tracking the following four LEO targets (which have been of interest in recent years). LEO targets are considered here because they are more stressing for coverage.

Target A - 185 Km Altitude, 65 deg inclination
Target B - 260 " " 65 " "
Target C - 440 " " 65 " "
Target D - 640 " " 82.5 " "

Target A is a small, realistic, "worst case" target. The targets get less stressing and more easy-to-detect as the letters progress.

In the analysis of the VLS we consider all conditions that affect detectability: illumination, target reflectance, sensor characteristics, and the sensor to target geometry (coverage). For simplicity, we make the assumption that the detection region of the SSN radars coincides with the coverage region.

When we compared the gap time statistics for VLS High and the SSN, we found that for any given probability of success, the gap time increases as the target altitude decreases. The increase is especially large for VLS in going from target B to target A. This comes about not only because coverage decreases as altitude decreases, but also because target A is much smaller than target B, and because non rejected earth limb radiance (which reduces the signal-to-noise ratio) increases rapidly as the sensor axis points closer and closer to the earth limb.

Only for satellite A (which has a very low orbit altitude) does the SSN have shorter gap times than does VLS. In reality, the assumption we made for the SSN, that the detection region coincides with the coverage region, makes the SSN data somewhat optimistic. The comparison for satellite A may be closer than is indicated by this chart.

When we compared VLS Low and the SSN, we found that the probabilities of success for VLS Low are greater than those for VLS high for any given gap time. The most significant improvement was for target A. This comes about for three reasons: first, non-rejected earth limb radiance affects the sensor signal-to-noise ratio of VLS Low less than VLS High; second, VLS Low is closer to the targets and third, VLS Low has one more satellite to the constellation than VLS high.

The VLS/GPS gap time statistics for the three higher targets are very close to those of VLS High. However, Target A has become undetectable because the signal-to-noise ratio has dropped below threshold even for the best viewing conditions. Signal loss due to the greater range to the target, and noise increase due to the greater effect of earth limb radiance on the higher sensor are the causes of this condition. Consequently, for the remainder of this study, VLS/GPS has been deleted as a candidate constellation. This does not rule out the use of VLS/GPS in a mixed constellation or in combination with a degraded SSN.

Once a target has been detected and tracked, orbit determination and prediction can begin. The accuracy of the resulting orbit and position data depends primarily on tracking accuracy, which for "angles only" sensors, is dominated by the accuracy of sensor pointing knowledge. We compared the accuracy of the SSN and VLS High (10,400 km; 28.5 deg) for five representative cases shown below.

**Case:**

- 1: Target 1 is in a very elliptical, supersynchronous orbit, such as might be performed by a deep space ASAT on a fast transfer. Position and velocity are predicted ahead 6 hours after 75 minutes of track.
- 2: Target 2 is in a Hohmann transfer to GEO. Position and velocity are calculated after 15 minutes of track following initiation of the transfer maneuver.
- 3: Target 3 is in geosynchronous orbit. Position and velocity are predicted ahead 30 minutes after 15 minutes of track.

- 4: Target 4 is in very low earth orbit. Position and velocity are calculated after 45 and 90 minutes of track.
- 5: Target 4 is tracked for an extended period. Position and velocity predictions are made 24 hours ahead. Errors are calculated as a function of track time.

In all cases, errors are 95% SEP (i.e., spherical radius that includes 95% of cases), 95% confidence.

**Orbit Parameters:**

Target	Type	Semi-major Axis (km)	Inclination (deg)	Eccentricity	Mean Anom (deg)	Rt Ascension (deg)	Arg of Perigee (deg)
1	DS ASAT	456627	16.8	0.98592	0.0	0.0	286.0
2	Transf to GEO	24402	65.0	0.73110	180.0	0.0	0.0
3	GEO	42240	0.0	0.0	0.0	250.0	0.0
4	Parking	6596	51.0	0.003	169.0	339.0	80.0

VLS accuracy was found to be better than SSN accuracy (sometimes by more than an order of magnitude), largely because the postulated VLS pointing knowledge errors (30 microradians random, 25 microradians bias), are much smaller than most of the SSN radar azimuth and elevation errors.

For the five cases mentioned above, the accuracy of VLS High is appreciably better than that of the SSN. When we compare VLS High (3 VLS @ 10,400 km; 28.5 deg) with VLS low (4 VLS @ 880 km, 28.5 deg) and see that VLS High is somewhat better than VLS low for high altitudes targets, and VLS Low is appreciably better than VLS High for low altitude targets.

The poorer performance of VLS High for low altitude targets comes about for two reasons - first, when viewing low altitude targets, the high sensor is very much further from the targets. Second, background noise caused by the earth limb radiance is greater for the high sensor. As a consequence the very low altitude target signal-to-noise ratio for the high sensor is much worse than that of the low sensor. This was also noticed earlier in the comparison of gap times, where the performance of VLS High was worse than VLS Low for target A. The latter is a small, very low altitude satellite.

The cost figures for VLS constellations are updates from an earlier study which was completed in 1990. The combined payload weight (telescope and gimbal) of 150 lbs is based on the assumption that the structure will be beryllium. If the weight constraint is relaxed other materials can be used and the payload cost should come down appreciably.

The spacecraft cost was derived using the Aerospace Small Satellite Cost Model (V 5.0) for a spacecraft weight of 700 lbs. The spacecraft weight was derived using the following assumptions:

- Constellations ~ Five satellites for VLS Low and four for VLS High
- Orbit altitude ~ 880 km for VLS Low and 10400 km for VLS High
- Average power consumption ~ 300 watts
- Communications ~ cross links(2) and down link
- Predicted life in orbit ~ 10 years
- Pointing accuracy (spacecraft) ~ 0.1 deg, three axes

The constellation sizes include one spare each. Launch costs are estimates for the Taurus XL booster (28.5 deg inclination from CCAFS) and include range operations and support. Three launches (two spacecraft on each of the first two launches, and one spare eventually on the third) were priced for VLS Low and four for VLS High. VLS High also requires a fifth stage and an apogee kick motor.

Ground station cost is based on the cost of recently developed low cost ground stations for ARPA, DOD, and DOE.

Operations cost is based on the following assumptions:

- Two dedicated small ground stations
- Two person crew; three shift, 24 hour operation
- Three man year/year contractor support

(Note that these are significantly lower than operations costs for ground sites.)

Other costs (20% of subtotal) include special software, reserves, and miscellaneous.

VLS Cost (in Millions of Dollars):

ITEM	1ST UNIT	2ND UNIT	VLS LOW	VLS HIGH
Payload	20	15.0	80.0	65.0
Spacecraft	26	15.0	86.0	71.0
Launch	25	20.0	65.0	110.0
Ground Station	1	0.5	1.5	1.5
Operations	---	---	9.9	9.9
Other Costs	---	---	48.5	51.5
Total	---	---	290.9	308.9

Space based VLS constellations could have the following payoffs:

- Allow closure of foreign bases if desired
- Allow closure of GEODDS
- Improve catalog accuracy
- Eliminate weather effects on GEO coverage
- Greatly improved survivability
- Reduced O & M cost

The conclusions of our study are as follows:

- A space based visible light surveillance system can provide better metric accuracy than the current SSN for spacecraft sized objects
- Except for small targets in very low (<200 km) circular orbit, most LEO targets can be detected and tracked by VLS in less time than the SSN
- An effective VLS constellation can be cost competitive with the SSN, and can be readily augmented in times of political stress
- More study is needed to identify the most cost-effective VLS constellation

## **Analyzing and Modelling Debris in the Geostationary Transfer Orbit**

**R. Jehn (ESOC, Darmstadt, Germany)**

### **Abstract**

As of today little is known about space debris in the Geostationary Transfer Orbit (GTO). In this study emphasis is put on debris in GTO with inclination around 7 degrees, an orbit which is used by the European launcher Ariane. Observation campaigns between 1985 and 1987 revealed more than 250 objects in this orbital region. Many of them are still tracked by U.S. Space Command on a random basis, but data are not publicly available.

The breakup of an Ariane third stage (Spot-1 rocket body) in a sun-synchronous low-Earth orbit in November 1986 revealed information, that might be of help when analysing the debris creation process in GTO. Most of the fragments of this breakup have very high ballistic coefficients (up to several  $m^2/kg$ ). The calculated ballistic coefficients can be explained by lightweight objects such as insulation material.

In Europe efforts are made to investigate the particular problem of space debris in GTO, which is caused by Ariane upper stages. The high power radar system of the German Research Establishment FGAN tracked eight spent Ariane third stages. No evidence exists to support the hypothesis that they exploded, though for four upper stages no final assessment was possible.

It is assumed that some debris in the 7-deg geostationary transfer orbit is insulation material that comes off the cylindrical structure of the upper stages with low delta velocity. This process is modelled, the dispersion of the debris is studied and observation strategies are suggested to maximise the number of debris observations in GTO either with optical or radar systems.

A least squares fit of orbital elements was performed for 19 objects contained in the U.S. Space Command Analyst Satellite Catalogue possessing Ariane GTO-type characteristics. The derived ballistic coefficients were very high, again an indication that many of the debris in GTO are insulation material.

### **Introduction**

The official U.S. Space Command catalogue contains just a small portion of the total number of debris in the geostationary transfer orbit (GTO). Usually only large objects like satellites and upper stages have their elements maintained in the catalogue. Although 17 breakups have been reported in highly eccentric orbits only 64 fragments were catalogued (Ref. 1). However, there is plenty of evidence that space debris also populates this orbital region. Analysis of LDEF's trailing surface indicated that the relative number of catalogued objects with highly elliptical, low inclination orbits must be increased by a factor of 20 to explain the number of impacts (Ref. 2).



Several optical searches for objects in high altitude orbits were conducted with the Ground-based Electro-Optical Deep Space Surveillance (GEODSS) network between October 1985 and June 1987. Together with various radars, such as the FPS-85 at Eglin, Florida, data of more than 250 objects in Ariane-type GTO (mean motion  $\approx 2$  rev/day, eccentricity  $\approx 0.7$  and inclination  $\approx 7^\circ$ ) could be accumulated (Ref. 3). Taff assumed that these fragments are the results of breakups of Ariane upper stages launched in 1985 (Giotto rocket body, 1985-056 B) and in 1986 (Brasilsat 2 rocket body, 1986-026 C).

A dedicated effort was made at the Research Establishment for Applied Science (FGAN) in Wachtberg-Werthhoven to verify the assumption that the latter rocket body has broken up. However, radar images taken in the Ku-Band using a 34-m parabolic antenna, did not support this theory. Also, the L-band signature was very bright (17.2 dBsm on average, Ref. 4). In total FGAN examined eight Ariane upper stages. None of them seemed to have experienced an explosion. Four of them show characteristic specular returns of the main cylinder body and the calculated dimensions coincide with data from the manufacturer. Therefore, an explosion breaking up the whole structure can be ruled out. For the other four upper stages including Brasilsat 2 rocket body, a definite assessment could not be made.

The Giotto rocket body (SSC 15876) remains a mystery. No Two-Line Elements (TLE) were available after August 1988. Therefore it was considered a major candidate for a breakup. However, in July 1993 TLE distribution started again. Strange enough, after five years the Giotto rocket body reappears with a semi-major axis increased by 800 km. To raise the semimajor axis by 800 km the orbital velocity has to be increased by a delta velocity  $\Delta V$  depending on the position in the orbit:

$$\Delta V = \frac{\mu}{2 V a^2} \Delta a \quad (1)$$

where  $\mu$  is the Earth's gravitational constant, and  $a$  the semimajor axis.

If the impulse was applied at perigee (orbital velocity  $V = 10.0$  km/s) then  $\Delta V = 37$  m/s. If the event took place at apogee (orbital velocity  $V = 1.9$  km/s) then  $\Delta V = 194$  m/s. However, whether a fragmentation actually took place, is still unclear. It is possible that SSC 15876 is misidentified with SSC 17325 (1985-056 D); based on L-band signature data obtained as recent as January 1994, the mean radar cross section (RCS) of SSC 15876 and 17325 are, respectively, -4 and +9 dBsm (Ref.5).

Another plausible mechanism to explain the numerous debris in GTO is the non-catastrophic separation of insulation material. Adverse conditions in the space environment (UV-radiation, atomic oxygen, thermal effects) may result in the disintegration, or detachment from the upper stage, of the insulation and its adhesive materials, as well as the attaching pins. Air Liquide (France), the manufacturer of the tank of the Ariane upper stage, provided some information about the thermal insulation to enable Battelle (Germany) to perform realistic explosion tests of a scaled down model (Ref. 6): 20 - 25 mm PVC-foam plates are glued to the outer surface of the tank. Additionally, the plates are fixed with small pins which are carried by a disk glued to the tank wall.

The ripping off of insulation material is also considered to be a possible source of the COBE debris. Between January and July, 1993, COBE spawned numerous objects on more than a dozen separate occasions (Ref. 7). Although such detached objects meet the very high ballistic coefficient observations, their absence should be apparent in the spacecraft temperatures, which to date are normal.

Hence, there are two possible mechanism for debris generation that could explain the large number of debris in GTO: explosions and gradual degradation of the thermal insulation. The purpose of this paper is to analyse which mechanism is more likely. By modelling the two scenarios it becomes evident, that the debris clouds behave differently. If enough observation data is available it will be possible to determine the debris source, which is an important step for starting mitigation measures.

## Calibration of Breakup Models

To model the dispersion of a cloud of fragments it is essential to know the distribution of the area-to-mass ratios of the fragments. One explosion in LEO was well observed and many data were collected: the breakup on 13 November 1986 of the Ariane V-16 upper stage (Spot 1 rocket body) in a 820-km, sun-synchronous orbit. Therefore this example provides the opportunity to calibrate and test the theoretical explosion models.

A widely accepted model for the mass distribution of fragments created during a low-intensity explosion is the exponential distribution by Su and Kessler (Ref. 8):

$$N = \begin{cases} 1.71 \times 10^{-4} M_s \exp(-0.02056\sqrt{m}), & \text{for } m > 1936 \text{ g} \\ 8.69 \times 10^{-4} M_s \exp(-0.05756\sqrt{m}), & \text{for } m < 1936 \text{ g} \end{cases} \quad (2)$$

where  $N$  is the number of fragments with mass larger than  $m$  and  $M_s$  is the mass of the satellite in gramme.

To model the ballistic coefficients (or an equivalent value, the area-to-mass ratio), for each fragment mass a fragment size has to be determined. Quite diverging models are available:

$$m = \begin{cases} 63.8 A_{eff}^{1.13} & \text{if } A_{eff} \geq 2.0 \cdot 10^{-5} \text{ m}^2 \\ 3536 A_{eff}^{1.5} & \text{if } A_{eff} < 2.0 \cdot 10^{-5} \text{ m}^2 \end{cases} \quad (3)$$

where mass  $m$  is in kg and effective cross-section area  $A_{eff}$  is in square metres.

This widely used relation is based on the assumption, that small objects (below 5mm) are spherical with a density of  $4.7 \text{ g/cm}^3$ . Therefore very low area-to-mass ratios are rendered. Based on an analysis by Badhwar (Ref. 9) of 196 well known objects, the following relation was established, which gives much higher area-to-mass ratios:

$$m = \begin{cases} 37.97 A_{eff}^{1.86} & \text{if } A_{eff} \geq 0.01 \text{ m}^2 \\ 7.24 A_{eff}^{1.5} & \text{if } A_{eff} < 0.01 \text{ m}^2 \end{cases} \quad (4)$$

Since eq. 3 predicts area-to-mass ratios 500 times less than those given by eq. 4, the author proposes a relation between the two extremes (Ref. 10):

$$m = 52.67 A_{eff}^{1.42}. \quad (5)$$

Equations 2 to 5 were used to simulate the breakup of a 1000-kg upper stage. The distributions of the area-to-mass ratios of the fragments can be seen in Figure 1: Low area-to-mass ratios for eq. 3 (88 % of the fragments below  $0.1 \text{ m}^2/\text{kg}$ ), higher values for eq. 4 (45 % larger than  $0.3 \text{ m}^2/\text{kg}$ ), whereas eq. 5 has its peak at  $0.1 \text{ m}^2/\text{kg}$ .

But none of these equations are suitable to simulate the area-to-mass ratios of the fragments of the Spot-1 rocket body. In order to derive the *observed* area-to-mass ratio of a fragment the first and last available TLEs were used. The time "TDECAY" was calculated which an object with an area-to-mass ratio of  $1 \text{ m}^2/\text{kg}$  takes to decay from the altitude given by the first TLE to the altitude given by the last TLE during average solar activity ( $F_{10.7} = 150$ ). Applying a correction factor that takes into account the observed solar flux, the area-to-mass ratio can be estimated by the ratio of TDECAY to the actually elapsed time between the two

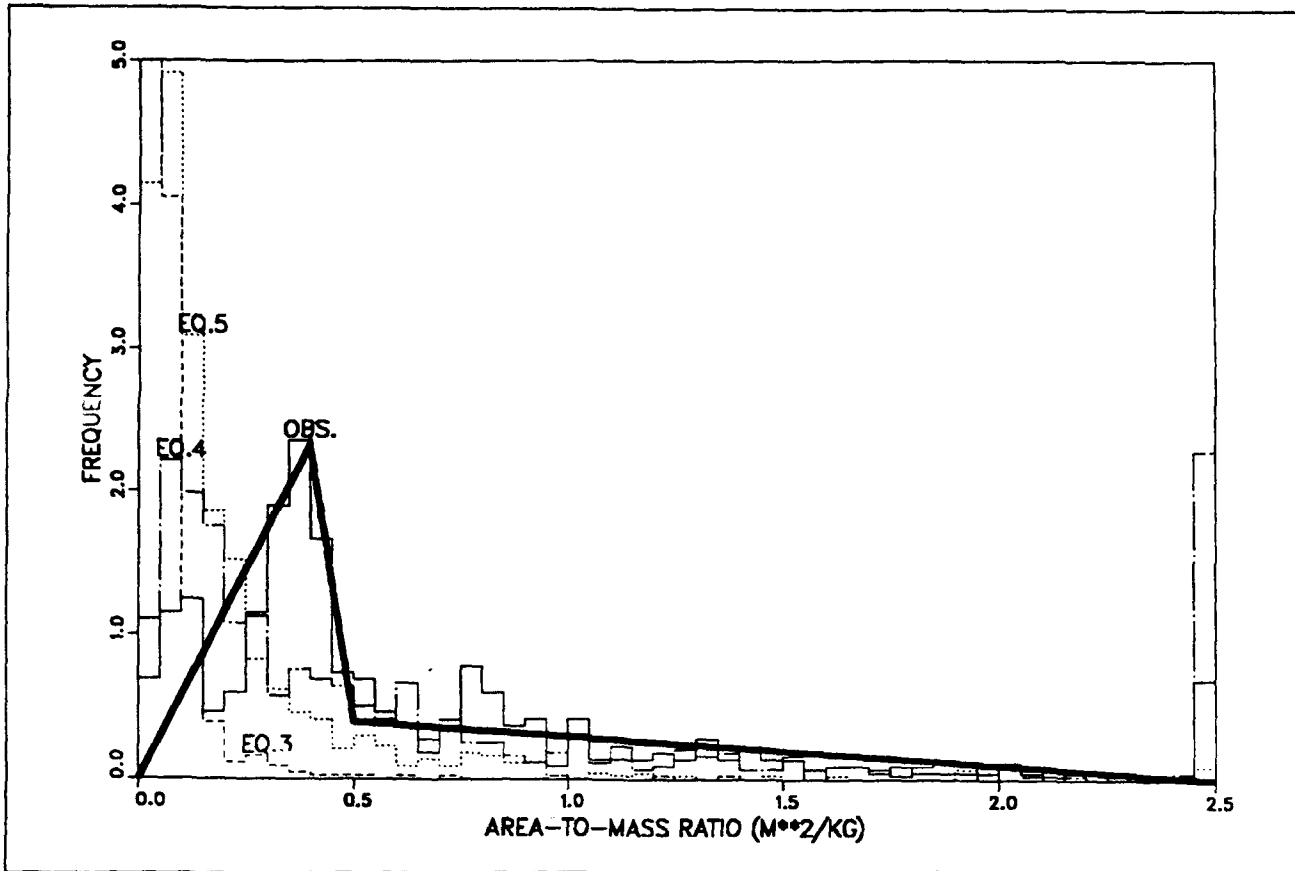


Figure 1. Simulated and observed area-to-mass ratios of the fragments of the Spot 1 rocket body. The bold solid line shows the model proposed in equation 6.

sets of the TLEs (Ref. 11). This procedure was applied to 433 fragments of the Ariane V-16 fragmentation, for which sufficient TLE data were available. (In Table 1, results of this method are in the column "Decay Time".)

In Figure 1, the observed distribution is shown by a solid line. The peak is at  $0.4 \text{ m}^2/\text{kg}$  and 40 % of the fragments have area-to-mass ratios larger than  $0.5 \text{ m}^2/\text{kg}$ !

These high values of area-to-mass ratios can be explained by thin, lightweight pieces of insulation created during the explosion. Therefore the following density distribution function for area-to-mass ratios is suggested for fragmentations where insulation material is involved:

$$f(x) = \begin{cases} 5.8 x, & \text{for } 0 < x < 0.4 \\ 10 - 19.2 x, & \text{for } 0.4 < x < 0.5 \\ 0.5 - 0.2 x, & \text{for } 0.5 < x < 2.5 \end{cases} \quad (6)$$

Eq. 6 is plotted in Figure 1 by a bold line.

To check the accuracy of this simple but very fast procedure for area-to-mass ratio determination, some more sophisticated methods were applied for a couple of test cases. Cour-Palais et al. (Ref. 12) have published radar cross-section and estimated mass for a number of fragments. Using these values and applying

$$A_{eff} = 0.5712 RCS^{0.7666}$$

for the relation between effective cross-section area and RCS, the area-to-mass ratios of five objects are given in Table 1. Four of these objects were also observed by FGAN (Ref. 13), however they used the relation

$$m = 62 RCS^{1.13}$$

to derive the masses of the fragments. Although the RCS-values were in good agreement with the American radar data, this approach resulted in very low area-to-mass ratios.

The author also used a least squares fit algorithm to derive the area-to-mass ratios. Fitting five to seven TLEs within a time period of about two weeks, the ballistic coefficients were iteratively optimized (Ref. 14). Because the orbits are propagated numerically and all perturbing forces are modelled very accurately, these results are quite reliable. They are listed in the first column of area-to-mass ratios in Table 1. The values derived from the decay time are in column 2. They are always smaller (between 16 to 70%). The results of Cour-Palais are in column 3. Except for large fragments they are about a factor of 2 larger than the least squares fit results. The FGAN estimates are in good agreement for the large objects "S" and "Y" (RCS of 12.9 and 6.5 square metres), but they are too small for the small objects "L" and "Z" (RCS about 1 square metre).

Area-to-mass ratios of Spot 1 rocket body fragments					
Fragment	Least Squares	Decay Time	Cour-Palais	FGAN	B* × 11.58
17116 "L"	0.1888	0.1331	0.5207	0.0162	0.0371
17122 "S"	0.0166	0.0116	0.0075	0.0115	0.0028
17129 "Y"	0.0357	0.0110	0.0102	0.0127	0.0027
17130 "Z"	0.0825	0.0764	0.2079	0.0163	0.0214
17472 "HK"	0.7821	0.4495	1.1204		0.1664

Table 1. Area-to-mass ratios of five Ariane V-16 fragments according to different methods of determination.

Finally another method to estimate the area-to-mass ratio of an object was tested. In the first line of a TLE set, there is a drag term B\* which is related to the area-to-mass ratio by (Ref. 15)

$$\frac{1}{2} c_D \frac{A}{m} = \frac{2B^*}{\rho}$$

$\rho$  is the atmospheric density at 120 km altitude at 1100 K exospheric temperature multiplied by the Earth radius and  $c_D$  is the drag coefficient. Inserting  $\rho = 0.15696615$  and  $c_D = 2.2$  yields

$$\frac{A}{m} = 11.5832 B^* \quad (7)$$

For 403 fragments of the Ariane upper stage breakup in November .986, where enough TLE data were available, the average value of B\* was determined and converted to area-to-mass ratio by eq. 7. In Figure 2 these values are plotted versus the area-to-mass ratios derived with the decay-time-method. A good correlation is only discernible for low values. For larger area-to-mass ratios the author regards the correlation as statistically too insignificant as to use the B\* term for further analysis. The values for the 5 fragments mentioned above, are given in the last column of Table 1.

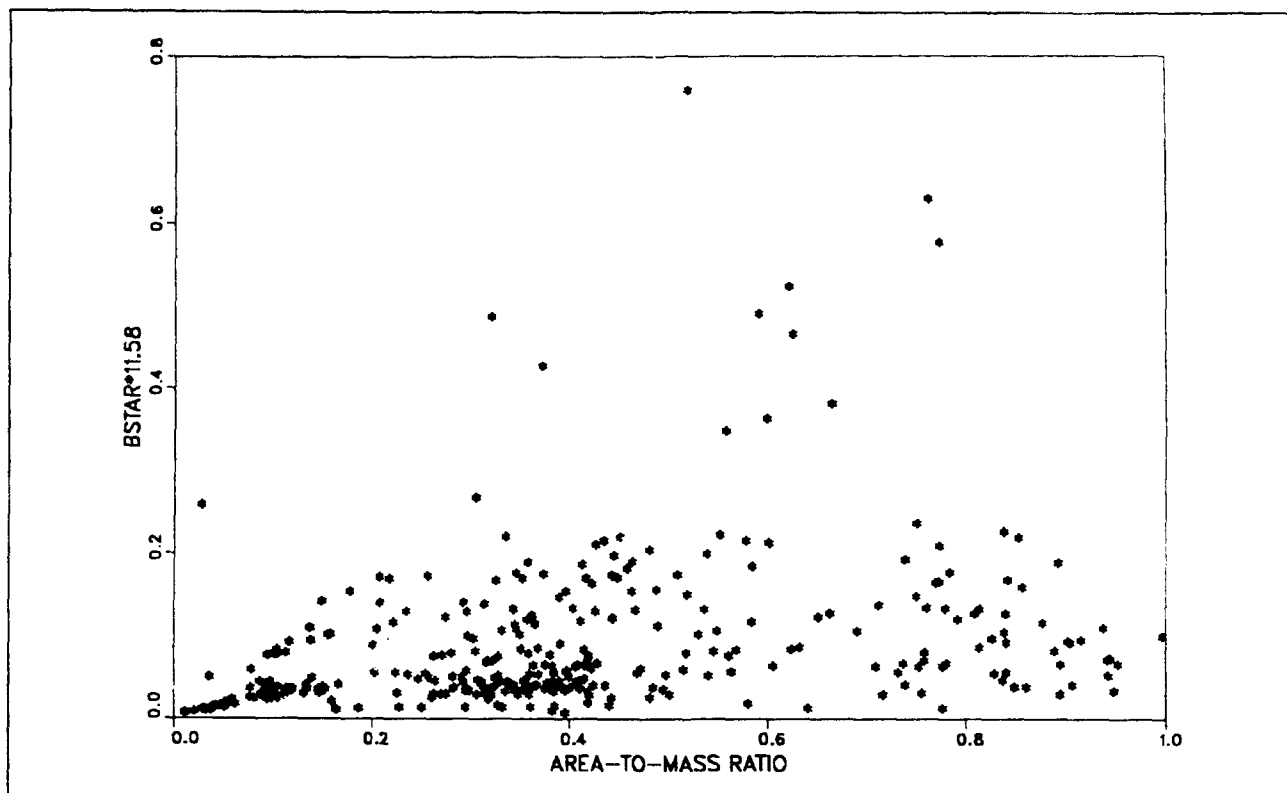


Figure 2. There is little correlation between  $B^*$  and area-to-mass ratio. 403 fragments of the Spot 1 R/B were analysed.

### Ariane Upper Stage Fragmentations in GTO?

In a report by TU Braunschweig six Ariane upper stages in GTO are mentioned which might have broken up (Ref. 16). One source of information was the Teledyne Brown Engineering report "History of On-Orbit Satellite Fragmentations" (Ref. 17). There, two Ariane upper stages in GTO are listed: the rocket body of CAT, the first payload of the Ariane 1 launcher (1979-104 B, SSC 11659) and the AUSSAT/ECS rocket body (1987-078 C, SSC 18352). For the CAT rocket body a Gabbard diagram with seven fragments is plotted. Many debris had high decay rates, another hint that insulation material has come off the third stage. Twelve fragments were observed from the AUSSAT/ECS rocket body event in September 1987, just after the launch. The TBE-report (Ref. 17) says "debris may be operational in nature". In Table 2 the six breakup candidates are listed.

The observation of additional objects like "E" and "F" could be a hint that a breakup had happened. To investigate this assumption FGAN concentrated on object 86-026 C (SSC 16657), the rocket body of Brasilsat 2 and Gstar 2 (GTE Spacenet Corporation domestic communications). On six occasions FGAN tracked this rocket body: 9 Jan 1992, 20 and 29 Oct 1992, 28 Jan 1993, 16 and 26 Mar 1993 (Ref. 4). The measured L-Band signature of this stage shows a fluctuating RCS (17.2 dBms on average), but no specular returns. Thus, the intrinsic motion can not be assessed and it is not possible to tell whether it is intact or fragmented.

With the FGAN radar data and TLE data, the ballistic coefficient of this upper stage was determined. A least squares fit of the observations obtained from October 1989 through December 1993 rendered a ballistic coefficient of  $0.0168 \text{ m}^2/\text{kg}$ . Using this value and starting with the first available TLE of October 1989, it is possible to reconstruct the orbital evolution of 1986-026 C very precisely. To propagate the orbit FOCUS, a semi analytic orbit generator, was used taking into account all major perturbations (atmospheric drag, Earth oblateness, luni-solar gravitation and solar radiation pressure, Ref. 18).

Candidates for Fragmented Ariane Third Stages			
Upper stage	USSpaceCom Catalog Objects	Objects mentioned in RAE-table	Comments
Ariane L01 (79-104 B)	-	-	Event in Apr 80 Decay of R/B in Nov 82
Ariane L04 (81-122 C)	-	-	Decay of R/B in Nov 88
Ariane V14 (85-056 B)	<b>C, D, E</b>	<b>C, D, E</b>	R/B still tracked
Ariane V17 (86-026 C)	<b>E, F</b>	<b>D*, E, F</b>	R/B still tracked
Ariane V19 (87-078 C)	<b>D, E</b>	<b>D*, E</b>	Event in Sep 87 Decay of R/B in Jun 91
Ariane V20 (87-095 B)	-	-	Decay of R/B at first perigee

Table 2. Several Ariane third stages in GTO could have experienced a breakup. \* indicates a part of Sylda, Ariane's dual launch system. Bold letters indicate that the fragment is still tracked (as of February 1994).

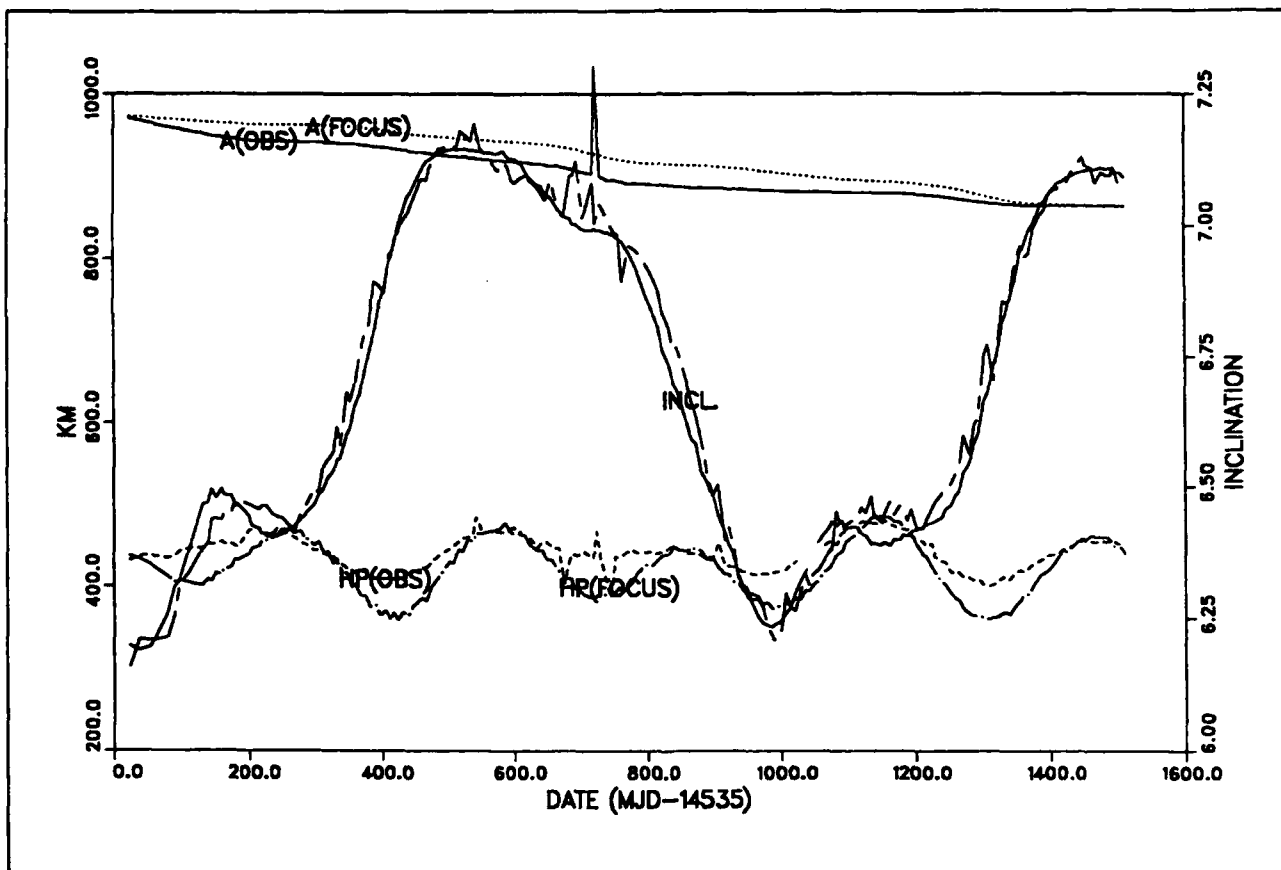


Figure 3. Observed and propagated orbital elements of 1986-026 C. 24000 km have to be added to semimajor axis A. The observed values (OBS) are more jagged than the propagations (FOCUS).

In Figure 3, the time history of semimajor axis, perigee altitude and inclination are plotted. The agreement between the observed (FGAN and TLE) data and the propagated orbit is extraordinary good. This proves that even satellites in GTO can be propagated over several years with high accuracy if the ballistic coefficient is known. This is especially important when observed fragments are propagated backwards in time to ascertain their origin.

## Modelling Debris Sources in GTO

At this point the two possible debris generation mechanisms will be simulated in order to show that the debris clouds behave differently when created by an explosion or via a low- $\Delta V$  separation of insulation pieces. By analysing the debris clouds it will be possible to discern of which nature they are.

Scenario 1: A 1000-kg rocket body explodes in the orbit of 1986-026 C (semimajor axis: 24973 km, eccentricity: 0.7271, inclination: 6.23°). The mass distribution of the fragments follows eq. 2, the area-to-mass ratios are given by eq. 5. The fragments are propagated with FOCUS over five years. (To have about the same number of objects as in scenario 2, only every second fragment is considered. Thus, in total 434 fragments are simulated.)

Scenario 2: A rocket body in the same orbit separates insulation material. Every two days (over a period of 800 days) one fragment is released with a delta velocity of 0.1 m/s in a random direction. The area-to-mass ratios are determined by a random number following the distribution given by eq. 6. Again, the fragments are propagated for five years.

The  $J_2$  term in the Earth's gravitational potential accounts for the Earth's oblateness and causes secular orbit perturbations in the right ascension of the ascending node  $\Omega$  and in the argument of perigee  $\omega$ :

$$\dot{\Omega} = -\frac{3}{2} n J_2 \left( \frac{R_e}{p} \right)^2 \cos i \quad \dot{\omega} = \frac{3}{4} n J_2 \left( \frac{R_e}{p} \right)^2 (4 - 5 \sin^2 i) \quad (8)$$

with mean motion  $n$  and semi latus rectum  $p$ . For the 1986-026 C orbit, the daily precession rates are  $-0.38^\circ$  and  $0.74^\circ$  for node and argument of perigee, respectively. In Figure 4, the early behaviour of a debris cloud in GTO is shown.

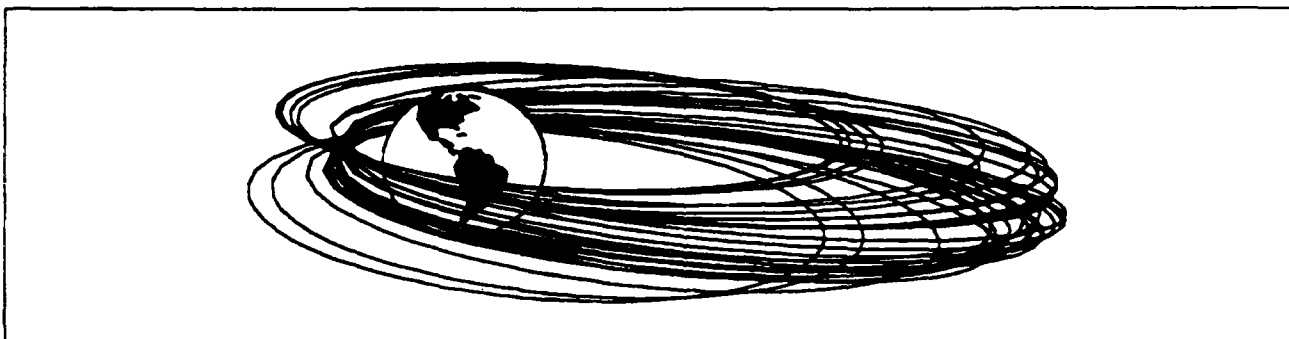


Figure 4. Dispersion of a debris cloud in GTO after 6 months (Ref. 1).

Since the fragments are in low-inclination orbit, the best way to describe the dispersion of the debris cloud is to show the distribution of right ascension of the fragments' apogees. To this end, the apogee is projected onto the equatorial plane:

$$\cos \omega' = \frac{\cos \omega}{\sqrt{1 - \sin^2 i \sin^2 \omega}} \quad (9)$$

where  $\omega'$  is the angle in the equatorial plane from right ascension of ascending node to right ascension of the apogee. For an inclination of  $7^\circ$  the maximum difference between  $\omega$  and  $\omega'$  is only  $0.22^\circ$  and the right ascension of apogee  $\Omega + \omega'$  is nearly identical with the sidereal longitude  $\Omega + \omega$ . In Figure 5, the distributions of right ascension of apogee are shown in yearly intervals.

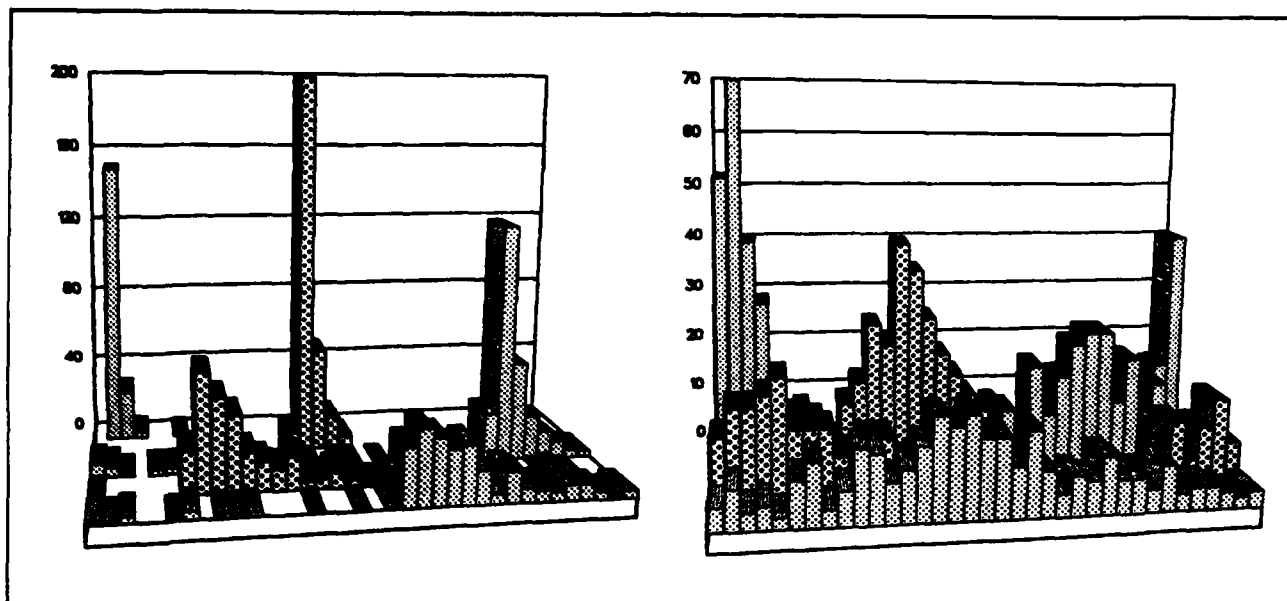


Figure 5. Right Ascension of apogee of fragments after periodic separation of fragments every two days (left) and after an explosion in GTO (right). Distributions are given after 1 year (background) 2,3,4 and 5 years (front).

On the left-hand side the distributions of the fragments separated with low  $\Delta V$  are given. After two years the apogees of 198 of 281 objects (70%) are between  $150^\circ$  and  $160^\circ$  right ascension (in the constellation Leo). The daily drift of the apogees,  $\dot{\Omega} + \dot{\omega}$ , is  $0.36^\circ$  which is 135 degrees per year. This drift (to the right) is evident in Figure 5. Since the mean motion of a fragment is increasing faster than the mean motion of the upper stage due to a higher ballistic coefficient, also the precession rate becomes faster (see eq. 8). Therefore, the right ascension of apogee of the upper stage will always be left of the peak. After five years it is  $205^\circ$  whereas most of the fragment apogees are crowded together between  $200^\circ$  and  $260^\circ$ .

On the right, the yearly distributions of the exploded fragments are shown. The peaks after one and two years are also quite distinct though lower, but after 5 years the dispersion is nearly completed. A concentration from  $90^\circ$  to  $210^\circ$  is still existing.

### Simulation of Detection Rates

The difference in the two distributions influence the observations of both a radar station or an optical observatory. If insulation material splits off the upper stage there must be a considerable concentration of fragments along the orbit of the upper stage. In case of an explosion the concentration is much less obvious. The simulated observation rates after two years for the two scenarios confirm the difference. The detection rates of an observatory at  $50^\circ N$  latitude and  $7^\circ E$  longitude (approximate position of the FGAN radar) with a field-of-view of 1 degree were calculated. For both scenarios 281 objects were assumed to be in orbit.

At beam park mode (fixed staring direction) the maximum number of sightings two years after an explosion will be 25 objects during a ten hour observation campaign ( $22^\circ$  elevation,  $152^\circ$  azimuth, 20460 km mean slant range). In case of scenario 2, 54 sightings of 46 different objects are recorded at  $22^\circ$  elevation and  $162^\circ$  azimuth (mean slant range of 13700 km). However, beam park mode is not the best method to observe the maximum number of fragments. All the 54 sightings will happen during a period of 5 hours, whereas there will not be a single observation during the 5 hours when the orbital plane of the upper stage has moved away from the observation cone. If the beam is moved in such a way that it follows the orbital plane of the upper stage it can detect up to 105 different objects (in total 221 observations, most objects are tracked twice or more). If the fragments were created by an explosion, the moved beam could observe 104 passes of 67 dif-



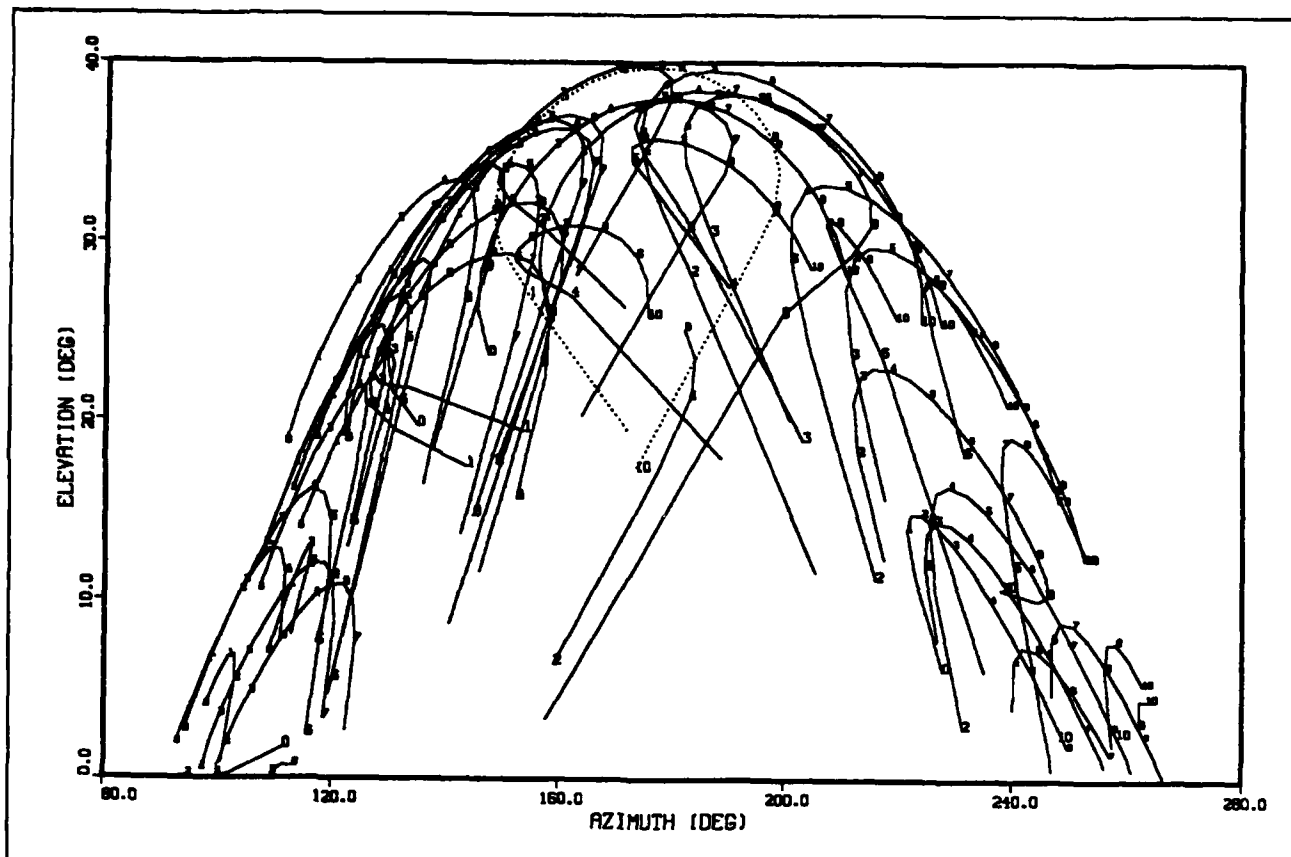


Figure 6. Tracks (azimuth and elevation as seen from 50-deg latitude) of 40 fragments that came off an Ariane upper stage. The numbers give the observation time and the size of the numbers indicate the range.

ferent objects. (Moved beam means the beam is in park mode for one hour, then moved and then in park mode again for one hour.)

In Figure 6, azimuth and elevation of 40 fragments are shown for an observation site at  $50.6^\circ$  latitude. The numbers in the figure indicate the hour of observation. At the beginning (hour 0) the telescope must be directed to the east, whereas later towards the end of the 10-h observation campaign more objects can be found in the west (180 degree azimuth is south).

ESA plans to install a telescope on Tenerife (Canary Islands) at  $28^\circ$  latitude ( $16.5^\circ W$  longitude, 2400 m altitude). The geographical as well as the weather conditions would be optimum for space debris observation in GTO. In beam park mode with a field-of-view of 1 degree the maximum number of detections in case of scenario 2 (insulation material) will be 52. These detections would be made at  $55^\circ$  elevation and  $137^\circ$  azimuth during three hours (no object is seen twice). During seven hours there will be no detections at all. The average slant range of the detected object is 34700 km, i.e. the objects are tracked at their apogee. A much better situation is given at  $42^\circ$  elevation and  $140^\circ$  azimuth. There, 51 sightings of 46 objects are possible with an average distance of only 11900 km. However, even in this favourable case there will be five hours without a single observation.

The ideal observation strategy is to move the beam along the orbital plane of the upper stage from which insulation material rips off. Rather than looking at the apogee, nearly as many objects can be seen at much closer distances. Ignoring objects which are more than 16000 km away, 156 detections of 139 different objects are possible with the optimum search strategy within ten hours. The average radial distance of the fragments is 13375 km.

## Orbital Elements from the Analyst Satellite Catalogue

The U.S. Space Command Analyst Satellite Catalogue contains a significant amount of orbital elements of debris objects in GTO; a subset of this database is provided to ESOC. The format is the same as the Two-Line Elements, but the satellite number is between 80000 and 90000. The field for the COSPAR identifier is empty because it was not yet possible to correlate the object to a launch. 458 Analyst Elsets of 58 different objects in GTO with inclination between 3° and 8° were available (as of 8 Feb 1994).

To answer the question what these 58 objects are, an effort was made to determine the ballistic coefficients. For this analysis, each object needed to fulfill two criteria: (1.) A minimum of five sets of orbital elements spanning five weeks and (2.) the perigee altitude below 1200 km, because sufficient atmospheric drag is necessary to determine the area-to-mass ratio. 19 objects met these criteria. An iterative least squares algorithm was used to fit the observation data consisting of semimajor axis and perigee altitude. (In order to have consistent data the TLEs are propagated to the perigee, before they are fitted. The angular information of the TLEs was not used.) The solve-for-vector had three components, the initial semimajor axis, initial perigee altitude and ballistic coefficient. In Ref. 19 this method was tested and verified for the reentry predictions of Ariane GTO upper stages where highly accurate ballistic coefficients are required. For orbit propagation FOCUS (Ref. 18) is used.

In five cases the root-mean-square (RMS) error of the fit was so high, that the results were discarded. In these cases the orbital elements from the analyst satellite catalogue had too large uncertainties and a reliable determination of the ballistic coefficient was impossible. The average RMS-error in the remaining 14 cases was about 2 km in semimajor axis and 4 km in perigee altitude. The results of the determination of the ballistic coefficient are presented in Table 3. Only 4 objects (29%) have a ballistic coefficient below 0.1  $m^2/kg$  whereas 5 objects are beyond 0.2  $m^2/kg$ , which could imply that they consist of insulation material of an Ariane upper stage.

Ballistic Coefficients from Analyst Elsets					
SSC No	No of Analyst Elsets	First Date	Last Date	Perigee Altitude	Ballistic Coefficient
81035	46	24-Oct-93	04-Feb-94	327	0.0042
88135	8	29-Nov-93	20-Jan-94	628	0.2189
88162	25	22-Oct-93	06-Feb-94	1066	0.1167
88205	5	22-Oct-93	24-Nov-93	840	0.1783
88231	16	25-Aug-93	16-Jan-94	1130	0.1264
88353	47	21-Oct-93	05-Feb-94	546	0.1018
88412	9	12-Oct-93	13-Jan-94	1025	0.0248
88543	8	25-Oct-93	25-Jan-94	650	0.3681
88553	11	11-Dec-93	04-Feb-94	621	0.4750
88638	9	14-Nov-93	19-Jan-94	648	0.3781
88641	7	29-Nov-93	21-Jan-94	868	0.3807
88651	45	24-Oct-93	06-Feb-94	291	0.0087
88748	43	25-Oct-93	05-Feb-94	377	0.0500
88897	11	30-Sep-93	04-Feb-94	680	0.1431

Table 3. Ballistic coefficients were determined by a least squares fit of available Analyst Elsets.

## **Conclusions**

Analysis of debris in Ariane-type GTO orbits supports the theory that some of the observed fragments are insulation material rather than fragments created by an explosion. However, pertinent data were available only for 14 objects, which is not sufficient to prove that assumption. More observational data is needed to allow more consolidated studies. It was shown in this paper, that a single telescope or radar would track many fragments during a short observation period, if it looks in the wake of spent Ariane upper stages. It is planned that Europe will soon contribute measurements either by FGAN or by a new observation site in Tenerife.

The next step must be to unambiguously correlate the observed fragments to one launch. To this end the fragments must be propagated backward in time until they match a parent body. The software at ESOC shows that accurate orbit prediction is possible even over some years (see Figure 3). If it is possible to show that an upper stage produces lightweight debris at many different times, then this would prove that the observed debris are not the result of explosions as it is assumed today.

The fuel-venting of the Ariane third stage, which is carried out since flight 59 (Spot 3 launch on 26 Sep 1993) regardless of the target orbit, will prevent future explosions (Ref. 20). But, if the main source of debris is insulation material - and the analysis made in this paper corroborates this conjecture - it will be necessary to review the design of the thermal insulation. The conservation of a sustainable GTO environment is especially important, because debris in GTO interfere with satellites both in LEO and in GEO.

## **Acknowledgements**

The author expresses his thanks to those who contributed data for the analyses in this paper: namely to François Nouel (CNES) for sending the data of the Spot 1 rocket body fragments, to Dr. Dieter Mehrholz and Dr. Ludger Leushacke (FGAN) for providing radar data of Ariane upper stages in GTO and last but not least to Scott Wacker (MIT Lincoln Lab) for Millstone radar data and innumerable comments during the last two years.

## **References**

1. Flury, W., Janin, G., Jehn, R., Klinkrad, H., "Space Debris in Elliptical Orbits", 18th Int. Symposium on Space Technology and Science, Kagoshima, Japan, 19-22 May 1992.
2. Kessler, D. J., "Origin of Orbital Debris Impacts on LDEF's Trailing Surface", Proc. of the 2nd LDEF Post-Retrieval Symposium, NASA CP-1394, 1993.
3. Taff, L. G., "Ariane-Related Debris in Deep Space Orbit", Progress in Astronautics and Aeronautics, Vol. 121, p. 157-162, 1989.
4. Leushacke, L., "Radar Measurement and Analysis of Spent Ariane Rocket Bodies in Geostationary Transfer Orbits", First European Conference on Space Debris, Darmstadt, Germany, 5-7 April, 1993.
5. Wacker, S., personal communication.
6. Fucke, W., "Fragmentation Experiments for the Evaluation of the Small Size Debris Population", First European Conference on Space Debris, Darmstadt, Germany, 5-7 April, 1993.
7. Johnson, N., Orbital Debris Monitor, p. 16-18, Vol. 6, Nr. 4, 1993.

8. Su, S.-Y. and Kessler, D. J., "Contribution of Explosions and Future Collision Fragments to the Orbital Debris Environment", *Advances in Space Research*, Vol. 5, Nr. 2, p. 25-34, 1985.
9. Badhwar, G. D., and Anz-Meador, P. D., "Determination of the Area and Mass Distribution of Orbital Debris Fragments", *Earth, Moon and Planets* 45, p. 29-51, 1989.
10. Jehn, R., "Fragmentation Models", MAS WP Nr. 312, ESA/ESOC, Darmstadt, Germany, December 1990.
11. Jehn, R., "Propagator for Debris Clouds in Low Earth Orbit", MAS WP Nr. 331, ESA/ESOC, Darmstadt, Germany, July 1992.
12. Cour-Palais, B. G., and Crews, J. L., "Hypervelocity Impact and Upper-Stage Breakups", *Progress in Astronautics and Aeronautics*, Vol. 121, p. 25-38, 1989.
13. Leushacke, L., Liewehr, W., Magura, K., Mehrholz, D., "Determination of Physical Characteristics of Space Debris", Research Establishment for Applied Science (FGAN), DARA No. 50 ST 9003, Wachtberg-Werthhoven, Germany, May 1992.
14. Jehn, R., "Salyut-7 / Kosmos-1686 Orbit Determination from Radar Data", Proc. Internat. Workshop on Salyut-7 / Kosmos-1686 Reentry, ESA SP-345, p. 73-77, Darmstadt, Germany, 1991.
15. Hoots, F. R., and Roehrich, R. L., "Models for Propagation of NORAD Element Sets", Project Space Track Report No. 3, Aerospace Defense Command, Peterson AFB, Colorado, December 1980.
16. Eichler, P., Zhang, J., Bendisch, J., Rex, D., "Weiterentwicklung des Modells aller Raumflugobjekte und Trümmer auf Erdumlaufbahnen, sowie Untersuchung der Auswirkungen auf Abschirmung und Ausweichmanöver bei bemannten Missionen", Report R9027, Technical University Braunschweig, Sept. 1990.
17. Johnson, N. L., and Nauer, D. J., "History of On-Orbit Satellite Fragmentations", 4th edition, Teledyne-Brown Engineering, CS90-TR-JSC-002, Jan. 1990. 16. "History of On-Orbit Satellite Fragmentations"
18. Gonzales-Laguna, E., and Klinkrad, H. H., "FOCUS-1 Fast Orbit Computation Utility Software", MAS WP 305, ESA/ESOC, Darmstadt, Germany, Sept. 1989.
19. Martinot, V., "Decay Prediction of Ariane Third Stages on Geostationary Transfer Orbit", Technical Report at MAS/ESOC, Darmstadt, Germany, Sept. 1993.
20. Laporte-Weywada, H. J., "ARIANE Launchers Design for Space Debris Mitigation", 44nd Congress of IAF, IAA-93-632, Graz, Austria, Oct. 16-22, 1993.

## The Use of Radar Cross Section Measurements to Characterize the Space Debris Environment

M.J. Matney (Lockheed Engineering & Sciences Company), D.J. Kessler (NASA Johnson Space Center)

One of the primary tools available to characterize the orbital debris environment is ground-based radar. The primary purpose of the US Department of Defense's radar network is to obtain accurate tracking information for orbiting objects. It is also possible, however, to measure the brightness of the return signal and compute the radar cross section (RCS) of the object. To a simple approximation, the measured RCS value is proportional to the relative size of the illuminated object. Because RCS is in units of area, it has become standard to speak of an equivalent size, defined by the size of a sphere with a cross sectional area ( $\pi r^2$ ) equal to the object's RCS. In order to accurately characterize the debris environment, however, there needs to be an improvement on that approximation.

From ground tests of violent fragmentations (both from explosions and hypervelocity collisions) it is apparent that much of the orbiting debris is not at all sphere-like. They consist mostly of twisted, irregular shards of metal; primarily steel and Aluminum (although there is a substantial amount of other material). The RCSs of these irregular shapes are extremely complex and vary according to the object's aspect angle, size, material composition, and the wavelength of the radar beam. For instance, a particular irregular object may have widely varying RCS values depending on the angle from which it is illuminated. The computation of these RCSs, even when we know the shapes, is not a simple matter. When we observe a random debris piece in orbit, where we have no *a priori* knowledge of its shape and size, the exact details of its RCS are impossible to describe. Fortunately, we do not need to enumerate an object's RCS behavior in detail in order to obtain information on the overall nature of the orbital debris environment. If we accept that we will never know the exact size and shape of a particular piece of debris from radar observations alone, we can then concentrate on trying to describe the environment statistically.

In order to assign an irregular object a size, we define a three-axis size as the average of three lengths. The first length is the longest length of the object, the second length is the longest length perpendicular to the first, and the third is the length perpendicular to the other two. For the purposes of this study, RCSs and sizes are given in dimensionless units based on the observing radar's wavelength  $\lambda$ . The dimensionless RCS unit is

$$z = \text{RCS} / \lambda^2$$

and the dimensionless size is

$$x = (\text{three-axis size}) / \lambda.$$

A sample set of pieces from hypervelocity impact ground tests were measured in a radar range at various angles and wavelengths. From this data, an average Size Estimation Model (SEM) was obtained to compute a characteristic average size for a particular RCS measurement. Figure 1 shows the experimental data points and the SEM fit. For comparison, the theoretical RCS for conducting spheres is included. Note that for large objects ( $x \gg \lambda$ ), the RCS derived from the SEM is the  $\pi r^2$  area approximation for a sphere described above. This region is often referred to as the optical region. For smaller objects ( $x \ll \lambda$ ), the RCS value falls off much more quickly with size than in the optical region. This region is often referred to as the Rayleigh region. For objects slightly smaller than  $x = 1$ , the SEM RCS value is higher than that expected from the  $\pi r^2$  area approximation, and corresponds to the Mie or resonance region for spheres.

From the individual data points in figure 1, it is apparent that there is a great deal of variation from the mean values fit by the SEM curve. For instance, a particular measured RCS could correspond to two objects that differ in size by a factor of 2 or more. In addition, these data points represent the average values for the RCS, after the contributions dependent on orientation are averaged out. Consequently, for any single radar pulse on a single object, the variation from the mean is potentially quite high. In an

effort to quantify these variations, a series of density functions were fit to the laboratory test data that give the probability of detecting a particular RCS value  $z$  given the size  $x$ . Examples of these functions are shown in figures 2-5 [Bohannon, 1992]. The functions are divided into two types; random object / random orientation (RORO), and random object / averaged orientation (ROAO).

In order to understand the use of these two functions, assume we have a box of random irregular objects all of size  $x$ . One object is drawn randomly, and we make a single RCS measurement (with wavelength  $\lambda$ ) at a single random orientation. The object is then put back in the box, and the box is shaken to randomize the collection. The procedure is then repeated with another object from the box. The resulting distribution of RCS values would be approximated by the RORO function. For the ROAO function, the objects are drawn from the box as before, but now they are measured by the radar multiple times at all different angles, and only the final average RCS is recorded. The RORO function is for use when a radar is in a staring mode and the object is only in the beam for a short time. There are not enough pulses on the target to be sure if the effects of orientation have been removed. The ROAO function should be used to describe what is seen from a tracking radar, where an object has been illuminated by many radar pulses at different orientations and then averaged. Note that there is a limit to how accurately we can measure a given object's size; no matter how many measurements we make of it. Without further information about the object's shape, there is a limit to our knowledge of the object's size. The probability distributions for each of the two models

$$P_{\text{RORO}}(z,x) dz$$

$$P_{\text{ROAO}}(z,x) dz$$

represent the probability that an object of size  $x$  will be seen with RCS between  $z$  and  $z + dz$ .

Using these functions, it is possible to estimate how completely a particular radar system will detect all objects in a given size range. Assume a tracking radar (we will use the ROAO function) can only detect objects with an RCS greater than  $z_0$ . The fraction of objects of size  $x$  the radar will be able to detect will be given by

$$\frac{\int_{z_0}^{\infty} P_{\text{ROAO}}(z,x) dz}{\int_0^{\infty} P_{\text{ROAO}}(z,x) dz}$$

A graph of this function is presented in figure 6. As an example, for a 10 cm wavelength radar to adequately catalog most objects down to 1 cm in size ( $x = 0.1$ ), the radar would have to "see" down to -57 dB square meters ( $z = -37$  dB).

The next step is to use these functions to improve our knowledge of the actual orbital debris environment. If one of these debris objects is measured by a radar with RCS  $z$ , we do not know if it is a small object that appears large, or a large object that appears small. From modeling and experiments involving breakups, however, we know that in the orbital debris environment there are many more small objects than large ones. Consequently, it is more likely that it is a smaller object that looks large, simply because there are so many more small objects. If we knew the size distribution in the environment *a priori*, we could compute the relative probability of the particular detection being a particular sized object. Unfortunately, the actual size distribution is the very information we would like to obtain from our radars. What we do have is the distribution of RCS measurements from the radars. The distribution of RCS values that the radar sees is directly related to the size distribution in orbit by the following formulae.

If the differential size distribution in orbit is given by

$$D(x) dx ,$$

then the cumulative distribution of RCS values the radar should see (the number of objects seen with RCS greater than or equal to  $z$ ) is

$$C(z) = \int_z^{\infty} dz' \int_0^{\infty} dx' D(x') P(x',z') ,$$

where  $P$  is chosen from the distribution functions to correspond to the particular radar system as outlined above. This represents a weighted numerical model "radar", where the effects of different size distribution functions may be examined. In previous analyses of debris and meteor populations, a power law has generally provided good fits to the observed size distributions. By a method of trial and error, different power laws can be run through the computer "radar", and the results compared with what is actually seen by the radar.

An example is shown in figure 7, where a composite RCS distribution from the Haystack observations has been fit with a model size distribution. Note that the conspicuous "hump" in the data is due to the radar response in the resonance region. The size distribution that best fit the Haystack observations was

$$D(\text{size in meters}) = (3.24 \times 10^{-4}) * (\text{size in meters})^{-3} + (1.30 \times 10^{-2}) * (\text{size in meters})^{-1.5}$$

where the units are in detections per hour for the Haystack radar [Stansbery et al., 1993]. This model closely resembles size distributions from EVOLVE and other models for determining debris populations. Figure 8 shows a comparison of three different size distribution calculations of the Haystack data: assuming that the RCS equals the area of an equivalent sphere, assuming the size is given by the SEM model, and the weighted fit described above. While the SEM fit is not bad, the weighted model probably describes the distribution most accurately. Note that the data begins to break down for large objects. This is due to the fact that large object sizes are mostly due to human construction activity, while the smaller objects are predominantly created by randomizing breakup phenomena. The size distribution given above will only hold true for smaller objects.

Figure 9 shows an RCS distribution for the Eglin radar (down to objects with RCS = -20 dB square meters), and a fit using the size distribution from the Haystack data. Because the units here are actual numbers of objects in orbit, the size distribution had to be multiplied by a factor of 63,000 in order to scale the results. Figure 10 show the results of the different size estimation methods. Note that a similar "hump" like that in the Haystack data appears, and is due to the behavior of the radar for objects in its resonance region.

For future work, there are other physical parameters that can be modeled using similar methods. If an object's average physical cross-sectional area as a function of RCS can be determined, then measurements of the decay rate and area-to-mass ratio can be converted into mass measurements. There is also the possibility of characterizing the simple shape of an object by looking at it in a tracking radar and obtaining multiple measurements at various angles. In addition, the statistical behavior of the polarization of the reflected radar beam can also be used to help determine material and shape properties of orbital debris.

In this paper, we have presented several methods of determining debris sizes from their radar cross sections. We have shown that the method of assuming an equivalent sphere to determine sizes is inadequate for objects in the resonance region of the radar. Either the SEM or a more detailed weighted size distribution model gives much more reasonable results. The statistical methods will be expanded in the future to describe other physical properties of orbital debris.

Bohannon, G.E., "Comparisons of Orbital Debris Size Estimation Methods Based on Radar Data", NASA Report No. 920123-BE-2048, February, 1992.

Stansbery, E.G., J.F. Stanley, D.J. Kessler, T. Tracy, M. Matney, L. Hock, K. McIntyre, "Orbital Debris Environment Characteristics Obtained by Means of the Haystack Radar", Proceedings of the First European Conference on Space Debris, Darmstadt, Germany, 5-7 April 1993.

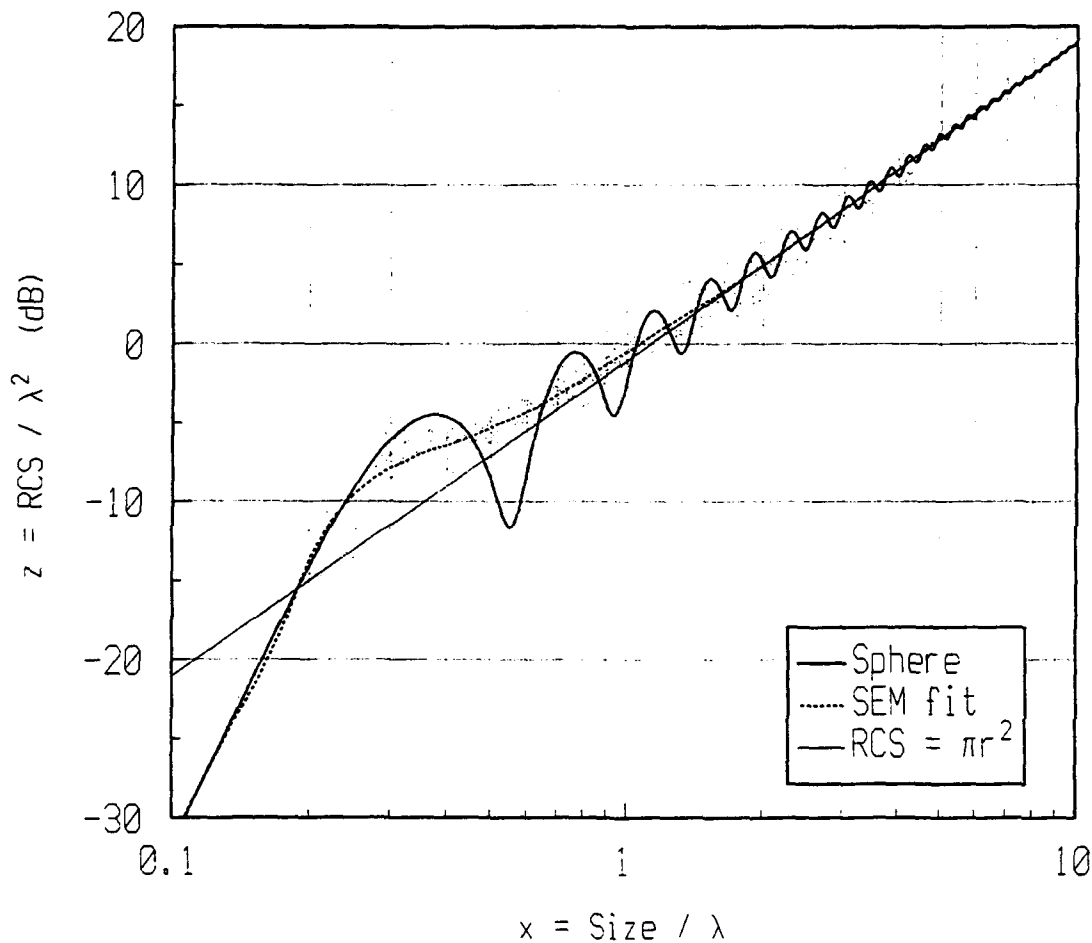


Figure 1. By measuring the Radar Cross Section (RCS) of irregular fragments in the laboratory (data shown as points) an approximate Size Estimation Model (SEM) is fit as a tool in translating RCS into object size. Shown for comparison are the size/RCS functions for an equivalent sphere (with area  $\pi r^2$  equal to the RCS) and the exact solution for a sphere. The bulge in the SEM model between  $x = 0.1$  and  $x = 1.0$  corresponds to the Mie or resonance region for a sphere.



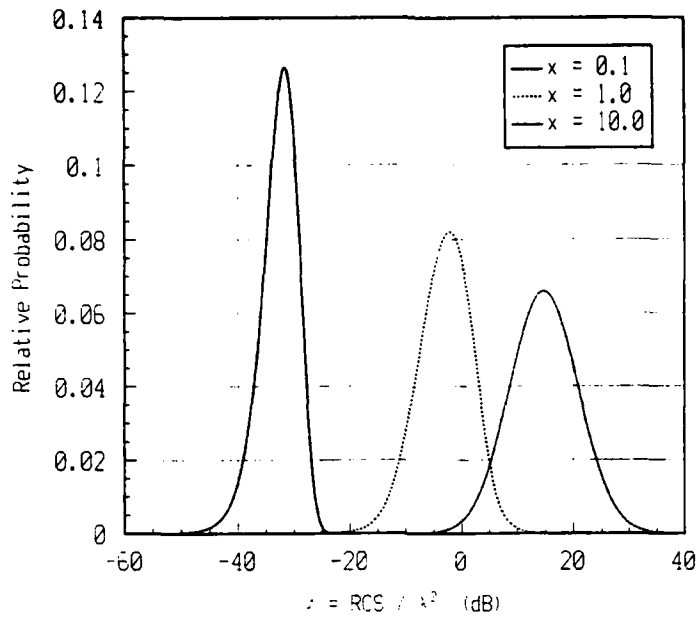


Figure 2. These examples of the RORO probability distribution functions are for random irregular objects measured at one orientation.

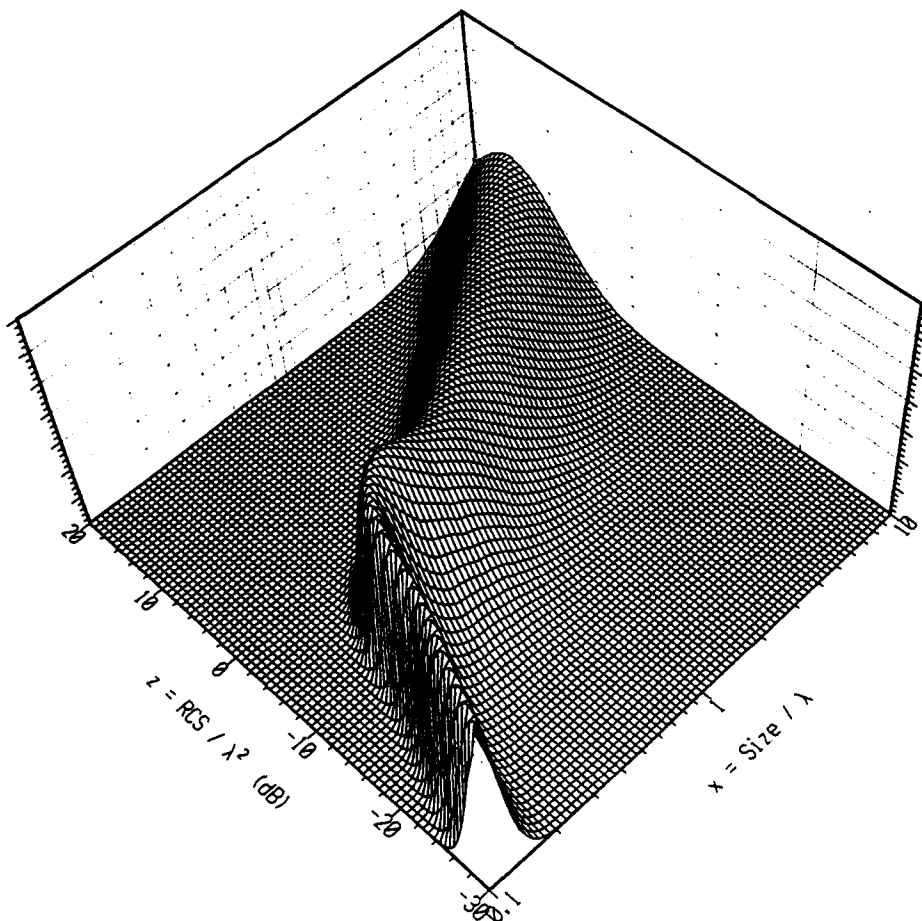


Figure 3. The RORO functions for a range of  $x$  values represent a spread from the SEM function from shown in figure 1.

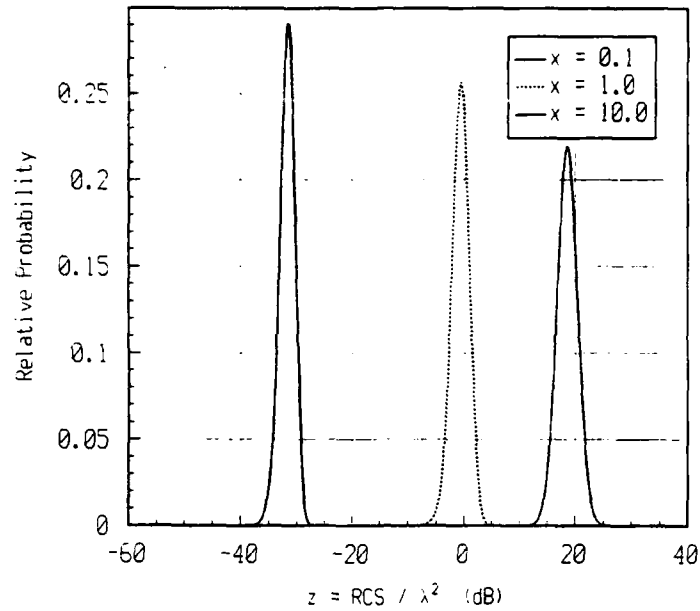


Figure 4. The ROAO probability distribution function are thinner than their counterparts in figure 2 because the dependence on orientation has been averaged out.

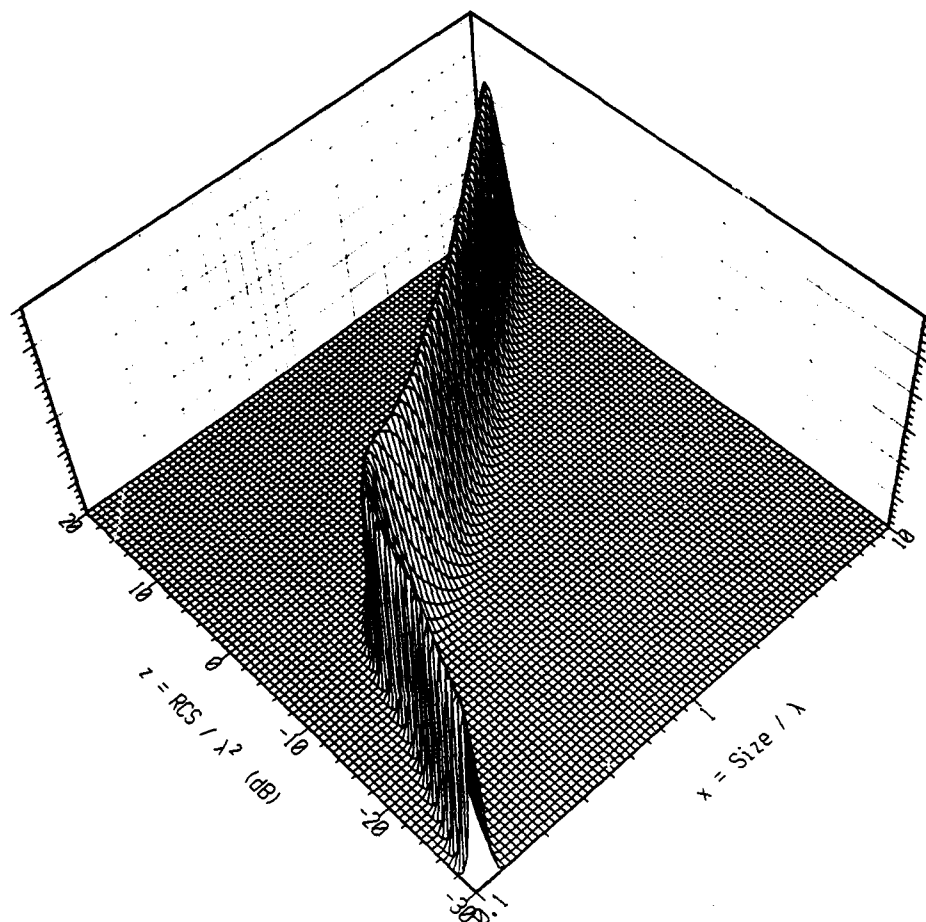


Figure 5. As in the figure 3, the ROAO functions represent a spread from the the SEM function shown in figure 1.

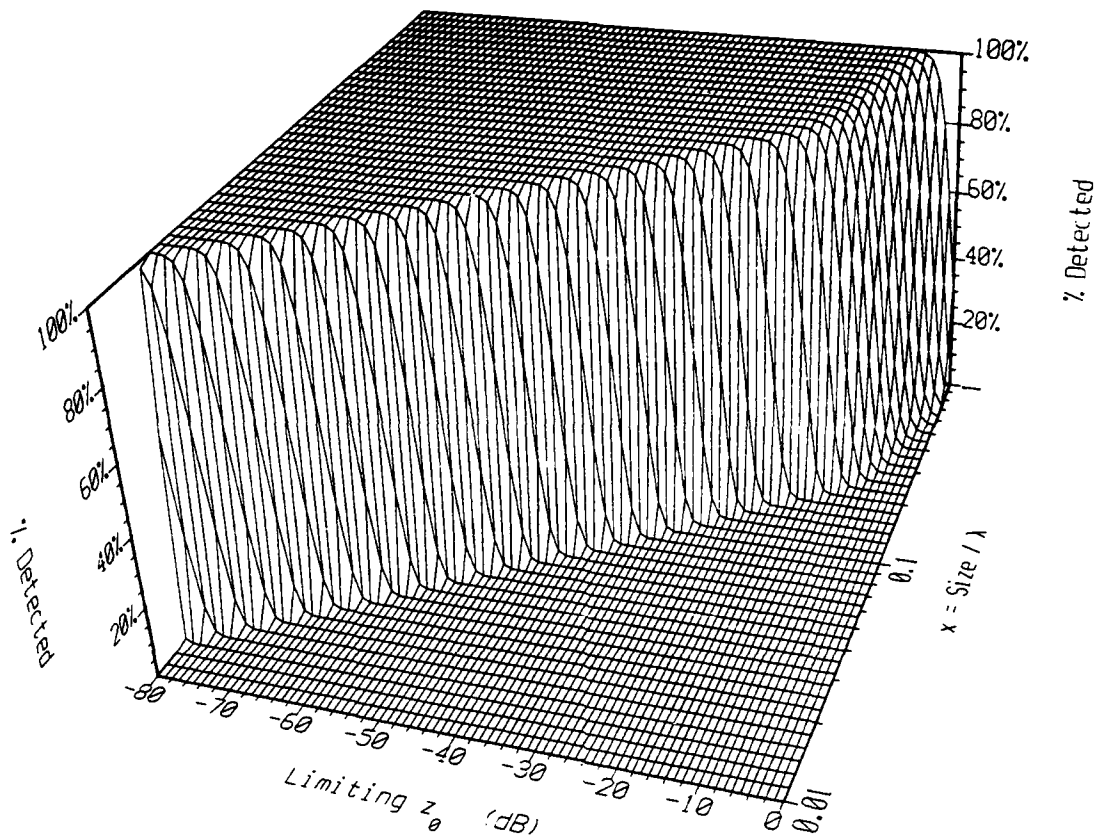


Figure 6. This graph can be used to determine how many objects of size  $x$  in the environment a radar with a noise floor of  $z_0$  will be able to detect.

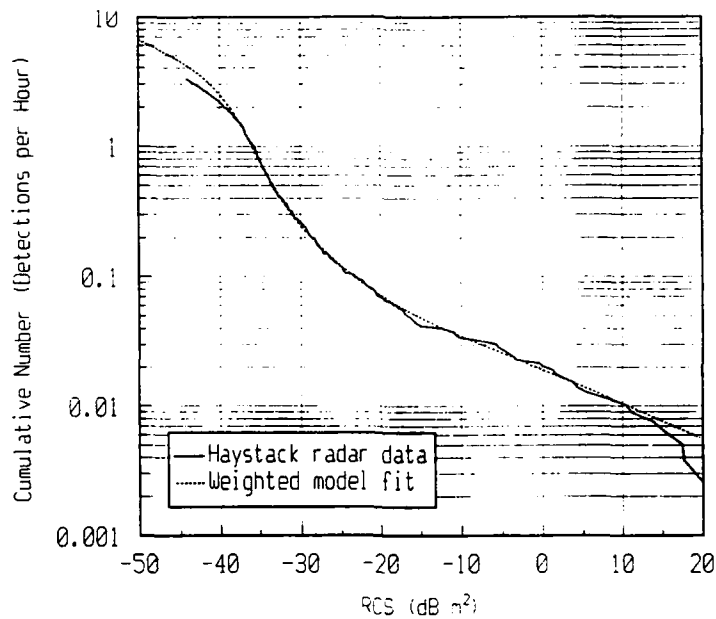


Figure 7. A composite set of RCS measurements from the Haystack radar has been fit by the size distribution in the text. The divergence of the fit below  $-40 \text{ dB m}^2$  is in the sub-cm region near the limit of Haystack's sensitivity.

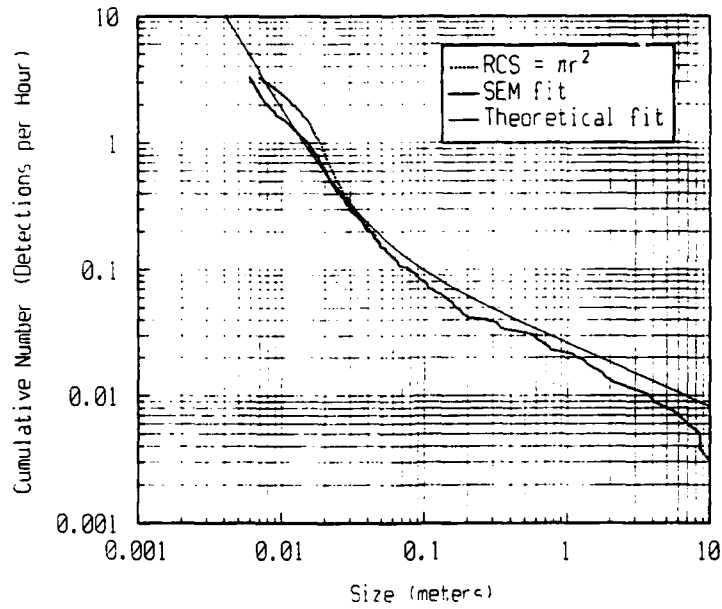


Figure 8. The size distribution for the Haystack radar observations has been approximated by the three methods discussed in the text. The theoretical fit is probably the most accurate.

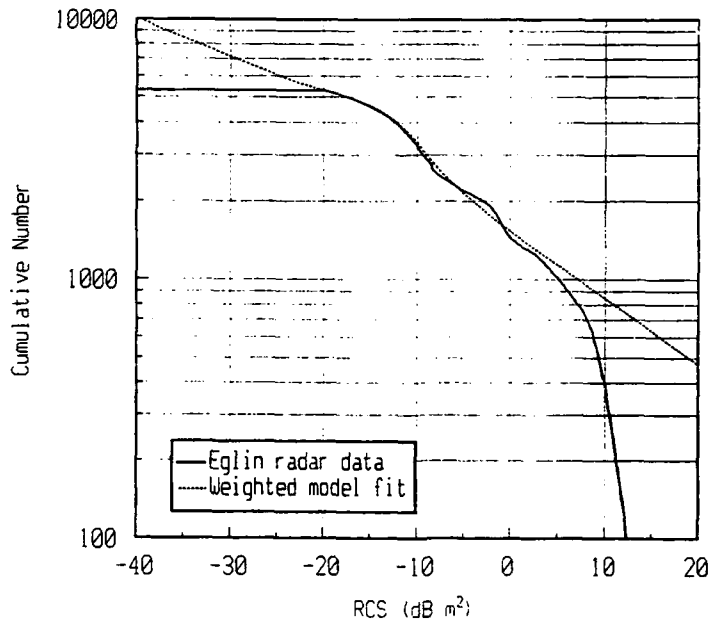


Figure 9. The Eglin radar data has been fit by the size distribution used for Haystack. The cutoff value for the Eglin data is set at -20 dB m<sup>2</sup>.

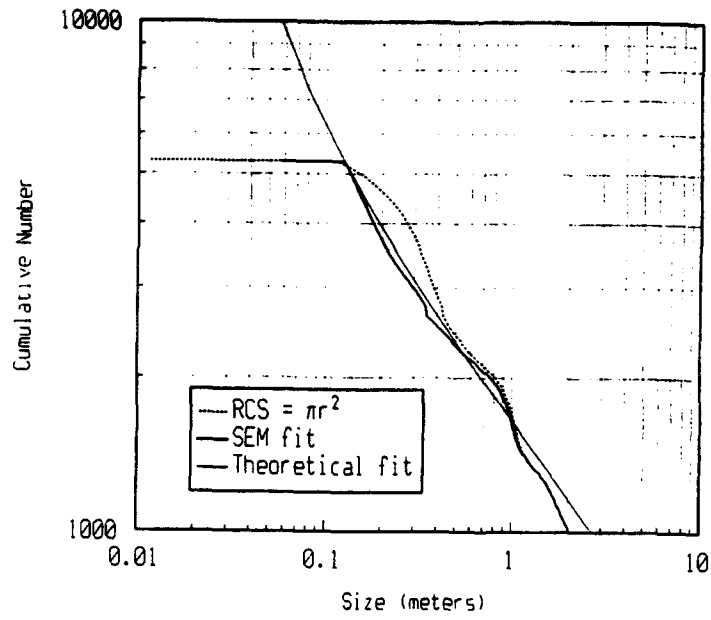


Figure 10. Three size distribution have been approximated for the Eglin data as in figure 8. The theoretical fit is probably the most accurate.

## ANALYSIS OF ORBITAL DEBRIS DATA COLLECTED USING THE HAYSTACK RADAR

Thomas E. Tracy (NASA/LESC), Eugene G. Stansbery (NASA), John F. Stanley (NASA)

### ABSTRACT

Beginning in October 1990 and continuing to the present over 2300 observation hours have been achieved by the Haystack radar for the purpose of defining the space debris environment. This paper describes collection methods and provides analysis of the data. Physical size estimations are presented based upon principal and orthogonal radar cross sections (RCS). Orbital debris flux calculations are derived from the probability of detections within the Haystack half-power beam volume. Inclination and altitude trends are established and temporal changes in the debris populations are examined.

### 1. GENERAL

Although it is doubtful that a single satellite fragmentation would today cause an instantaneous 400% increase in the total Earth satellite population, as happened in 1961 (Ref. 1), there can still be a significant statistical effect. The powerful 1.023 milli-second pulswidth waveform of the X-band Haystack radar is capable of detecting orbital debris just under 0.5 cm in diameter. Most Space Surveillance Network (SSN) radars do not track objects below 10 cm to 20 cm in size. Because the amount of space debris is known to increase geometrically with smaller sizes (Ref. 2) this means that there are 50 to 100 times more fragments (down to 0.5 cm) than are recorded in the standard catalogs. An estimate of 400,00 such objects has been computed based upon Haystack findings.

Using this yardstick, a single high intensity fragmentation is capable of producing tens of thousands of new mini-satellites. Depending upon their altitude and orbital eccentricity the debris can stay in orbit for just a few days or up to hundreds of years. During periods of high solar flux the atmosphere expands upward to higher than normal altitudes and the resultant drag has a "cleansing effect" on the debris within its increased regime. The first two years of Haystack measurements were taken during a period of near-record high solar flux. Future measurements may reveal a higher density of fragments for altitudes up to 600 km.

Much of the above discussion points to the conclusion that the space debris situation has not yet become static but rather continues to evolve. If, as seems apparent, tens of thousands of particles down to the size of 0.5 cm diameter can result from one violent fragmentation then sudden statistical change can still take place. It may be worth bearing in mind that just over 7000 objects

are currently being maintained in the (NORAD) satellite catalog. Further, while the general pattern of small debris particles may generally mirror the inclinations and altitudes of the larger cataloged population it need not do so. Should a solitary satellite in a lightly used orbital plane undergo a high intensity breakup then the resulting thousands of small particles could cause a noticeable departure from the catalog within that regime.

The orbital area from 900 km to 1000 km has been referred to as a "storage altitude" (Ref. 3). Haystack results in Fig. 1 and subsequent figures would seem to confirm this. In fact, twice as many small debris objects have been detected here than were predicted by the NASA model (Fig. 2; Ref. 2). Each dot on figure 1 represents a single object detection having an integrated signal-to-noise (S/N) greater than 10.0 dB and a maximum principal polarization S/N greater than its maximum orthogonal polarization S/N. (The reason for these criteria is that better quality inclination values are thereby derived). Data for this plot was gathered from the entire database spanning from October 1990 through September 1993. The area on figure 1 from approximately 50 deg to 70 deg inclination and from 900 km to 1000 km altitude is quite obviously denser than surrounding regions. Subtler areas of density can be seen elsewhere such as the lower altitudes between 60 deg and 70 deg inclination and centered above the 30 deg inclination mark.

The lower dashed line of Fig. 2 represents the cumulative detection rate of known cataloged objects while the solid line represents the cumulative detection rate of objects as small as 0.4 cm in diameter as detected by the Haystack radar. A factor of 100 can be seen between the two lines.

Figs. 3 through 5 show cumulative inclination values for individual yearly periods of debris gathering. The first one (Fig. 3) is for the period October 1990 through calendar year 1991. This one shows a spread of inclination "centers" from the lower 50s, lower-to-mid 60s, and lower 70 degree inclinations. Inclinations from calendar year 1992 are more condensed with the majority of inclinations seemingly centered around 63 - 64 degrees. Also 90 degrees inclination stands out from the other high inclination values in 1992. The trend toward a condensed center of inclinations is seen to continue in 1993. The majority of values again centers around the mid-60 degrees. Figure 6 is a compilation of these three plots.

The estimated sizes of the objects contributing to the inclination plots of the above figures are shown in Fig. 7. A line has been drawn through the eight centimeter diameter size to indicate the smallest size generally observed by Space Surveillance Network radars. Although this line is somewhat arbitrary it suffices to show that the vast majority of these detections are not recorded in the standard catalogs. The centimeter-sized population between 50 deg and 70 deg inclination and between 900 km and 1000 km altitude is essentially invisible to the UHF and VHF radars currently being used.

There is some evidence (Ref. 4) that high intensity breakups can be statistically observed by Haystack when in the passive beam

staring mode. On September 5, 1992 an engine unit (Cosmos 1603) which had been previously released from its parent ship, fragmented. Residual hypergolic propellants on board are thought to have caused the explosion. The approximate altitude at time of fragmentation was 835 km. Orbital inclination was 66.6 degrees. NAVSPASUR observed 62 objects associated with this breakup; 15 of these appeared in the satellite catalog. (Ref. 5)

A Haystack radar debris gathering mission began as scheduled on 15 September 1992 and continued for seven days. The resultant inclination values from 90 degree beam staring are shown in Fig. 8. The most prominent values appear to be centered about -66.5 degrees. For contrast the inclination values from the previous Haystack mission in JUL/AUG 1992 are shown in Fig. 9. These show a much more diffuse number of inclination contributors. Further, although the 90 degree beam staring hours in September were half of those in JUL/AUG the peak number of inclination occurrences centered around 66 degrees are almost identical. This indicates a significant flux increase at that inclination for the September mission. Also altitude related debris flux increases in September were quite comparable to the altitudes shown in the Gabbard diagram of reference 5.

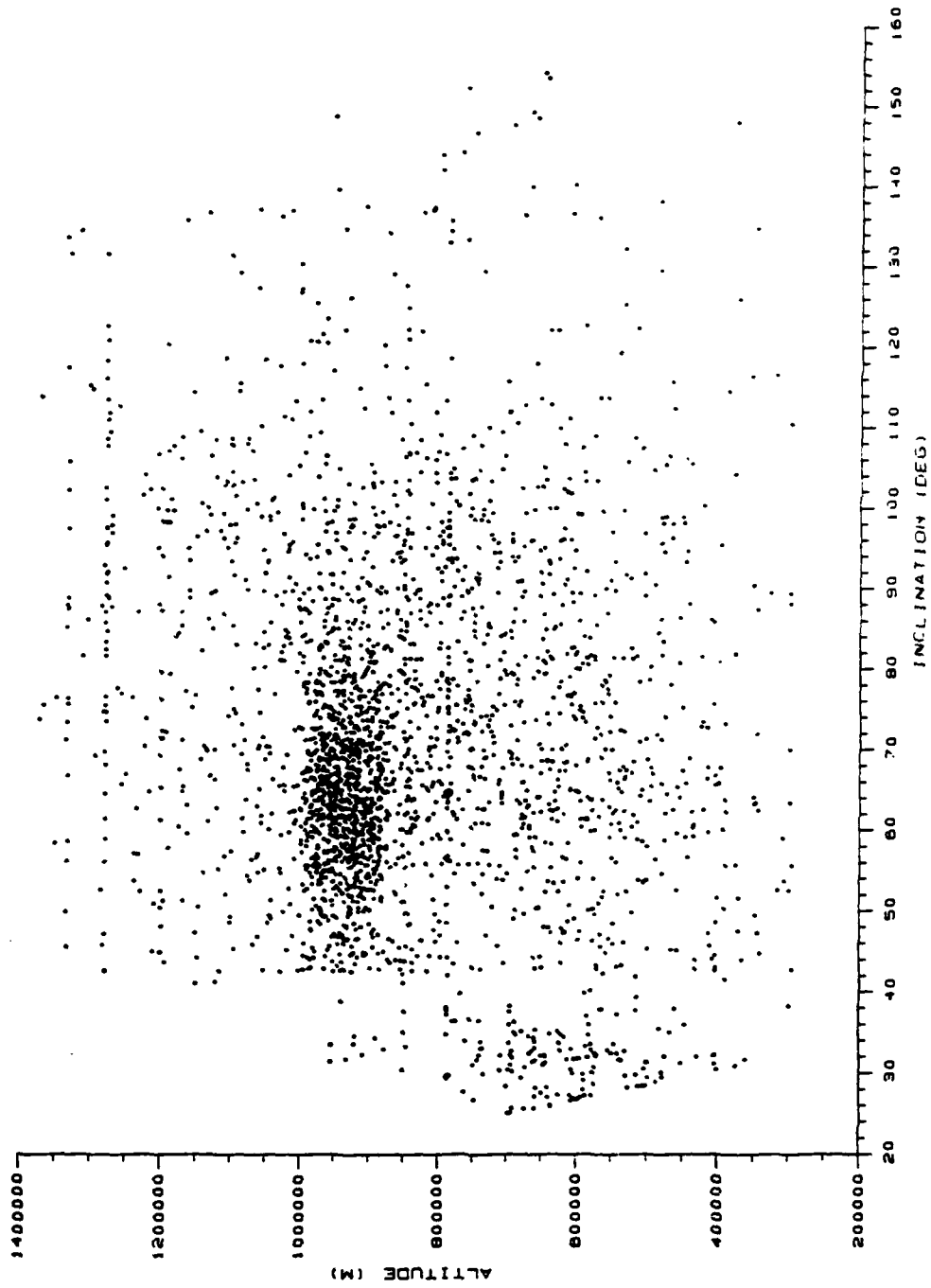
#### REFERENCES

1. Johnson, N., and Nauer, D., "History of On-Orbit Satellite Fragmentations", Fourth Edition, Teledyne Brown Engineering, January 1990.
2. Stansbery, E., Tracy, T., Stanley, J., Kessler, D., Matney, M., Hock, L., and McIntyre, K., "Characterization of the Orbital Debris Environment Using the Haystack Radar", NASA publication JSC-32213, Appendix A, March 1993.
3. Johnson, N., and McKnight, D., ARTIFICIAL SPACE DEBRIS, Orbit Book Company, Malabar, Florida, 1987.
4. Tracy, T., "Haystack Observance of Cosmos 1603 (Sat # 15338) Engine Breakup", Lockheed/JSC internal memo, September 1993.
5. Nauer, D. "History of On-Orbit Satellite Fragmentations", Sixth Edition, Teledyne Brown Engineering, January 1993.



Fig. 1 Haystack Detections from Oct. 1990 through Sept. 1993.

OCT 1990 THRU SEP 1993  
ALL DEG S/N > 10.0 DB



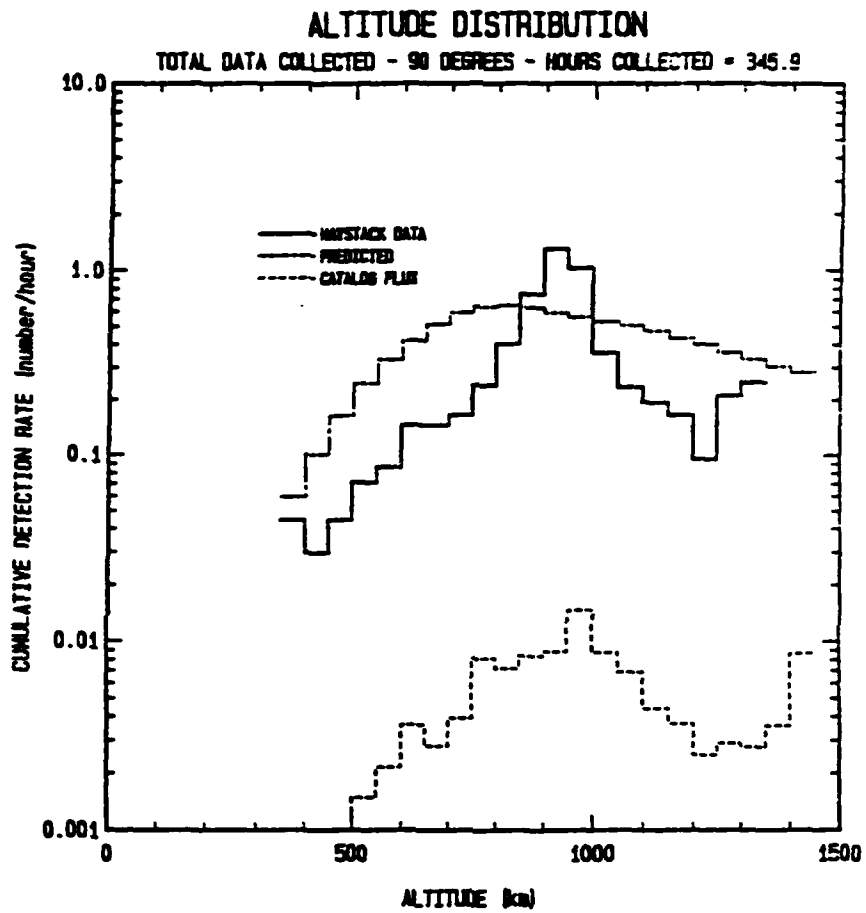


Fig. 2 Measured and predicted altitude distribution for objects detected by Haystack at 90 degree elevation.

Fig. 3 Inclination distribution Oct. 1990 through calendar year 1991.

OCT 1990 THRU DEC 1991  
INCLINATIONS ALL DEG S/II > 10.0

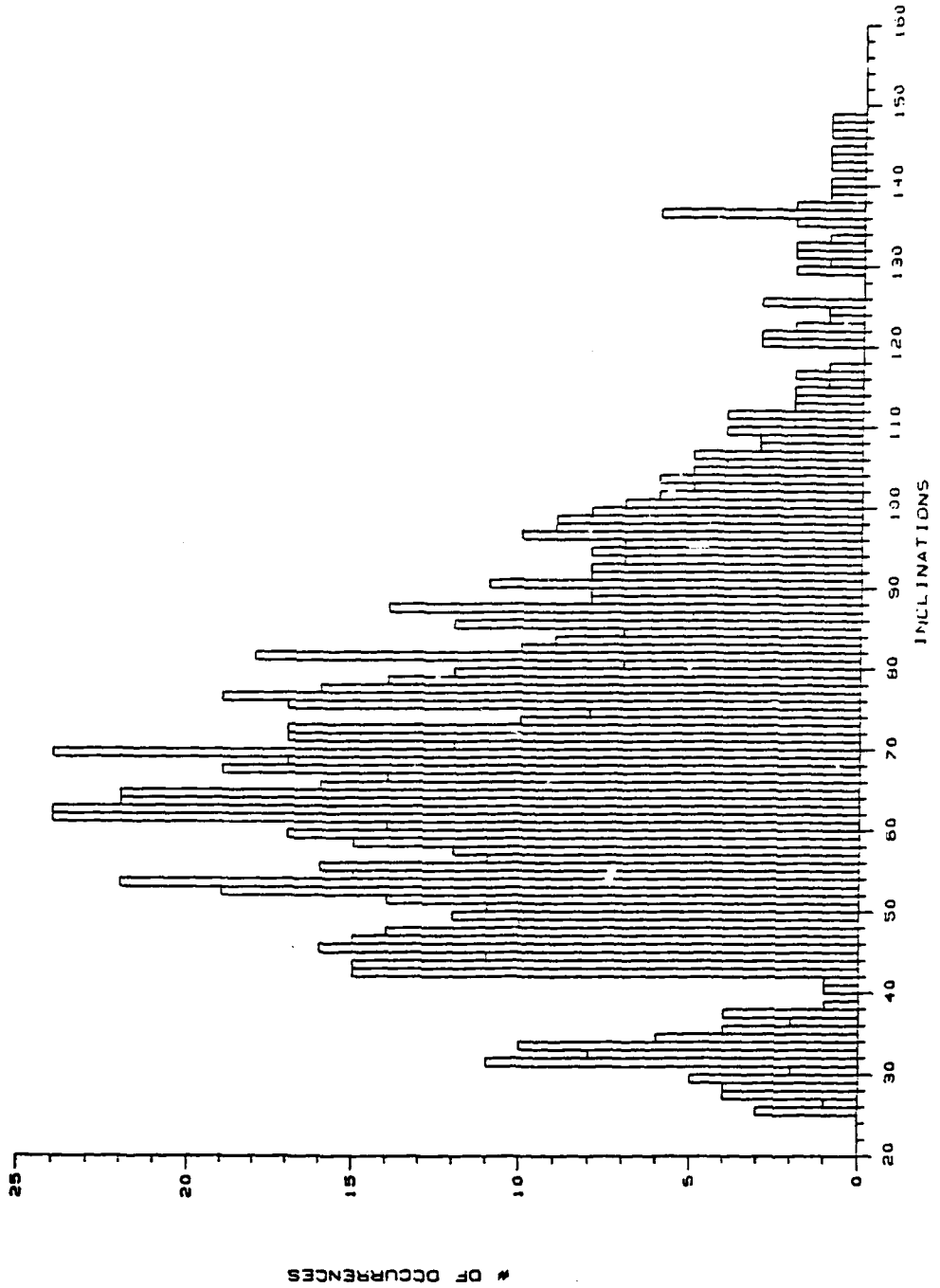


Fig. 4 Inclination Distribution calendar year 1992.

1992 INCLINATIONS  
ALL DEG S/N > 10.0

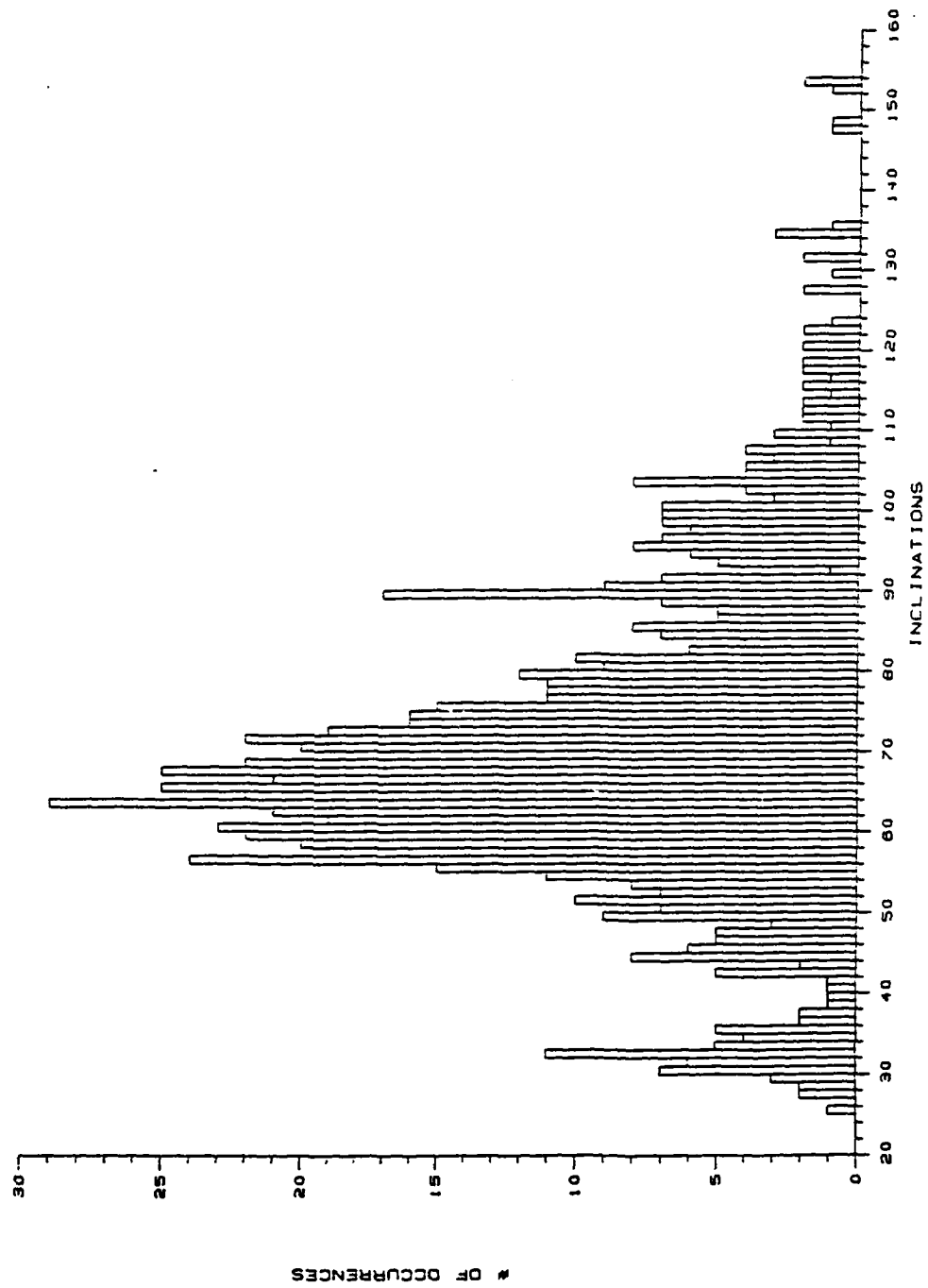


Fig. 5 Inclination Distribution calendar year 1993.

1993 (THRU SEP) INCLINATIONS  
ALL DEG S/N > 10.0

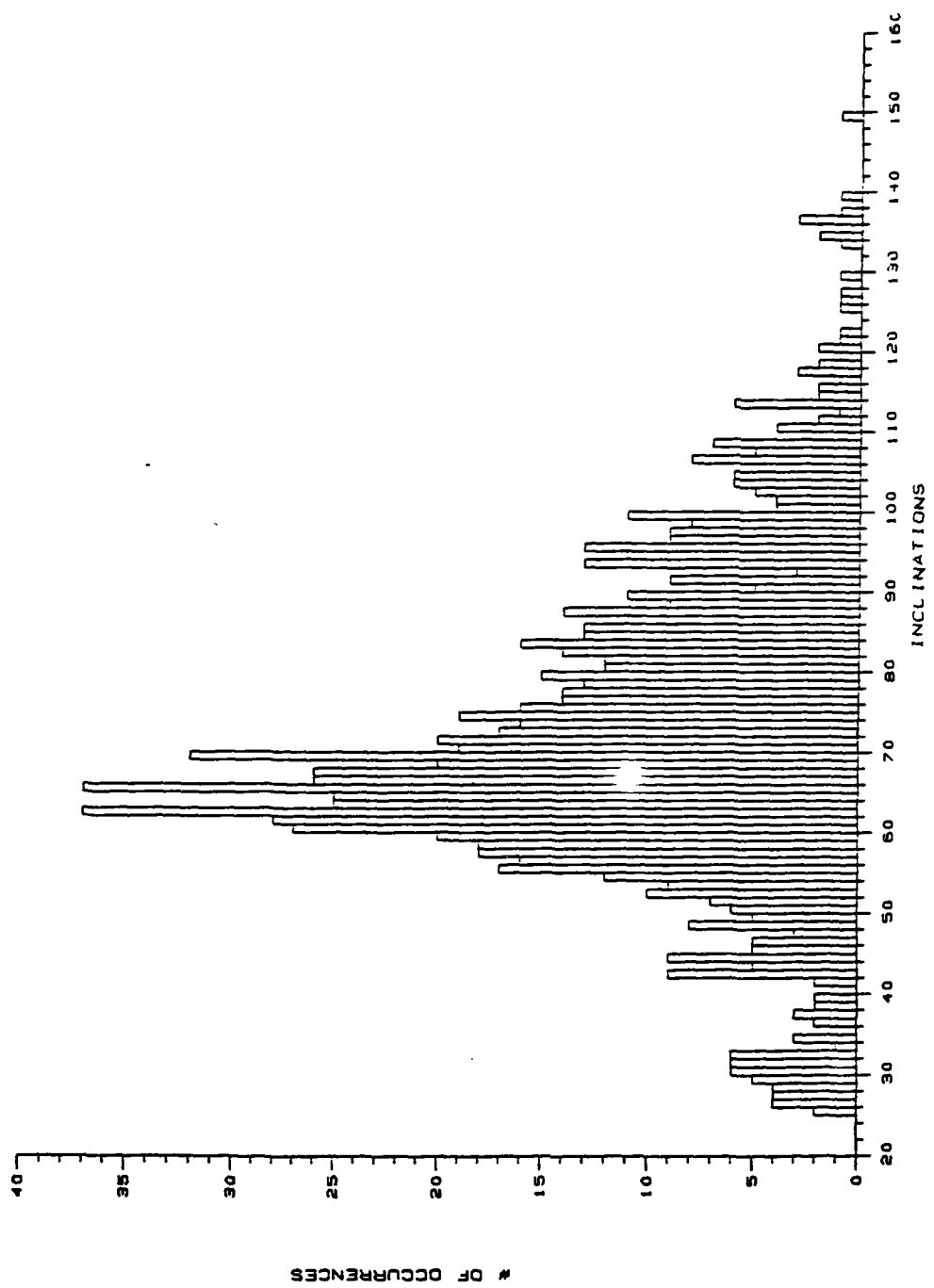


Fig. 6 Cumulative inclination distribution Oct. 1990 through Sep. 1993.

OCT 1990 THRU SEP 1993  
INCLINATIONS ALL DEG S/11 > 10.0

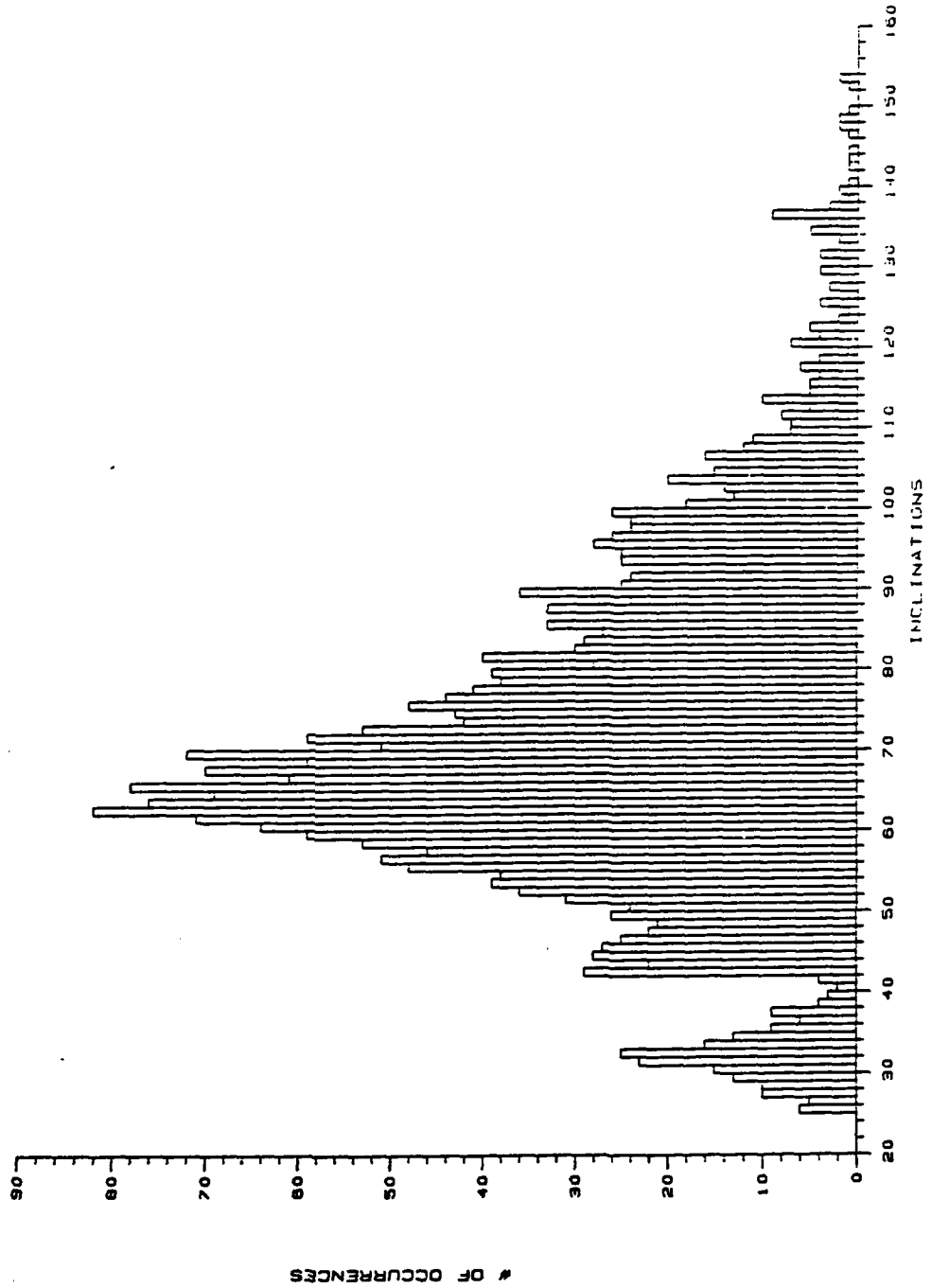
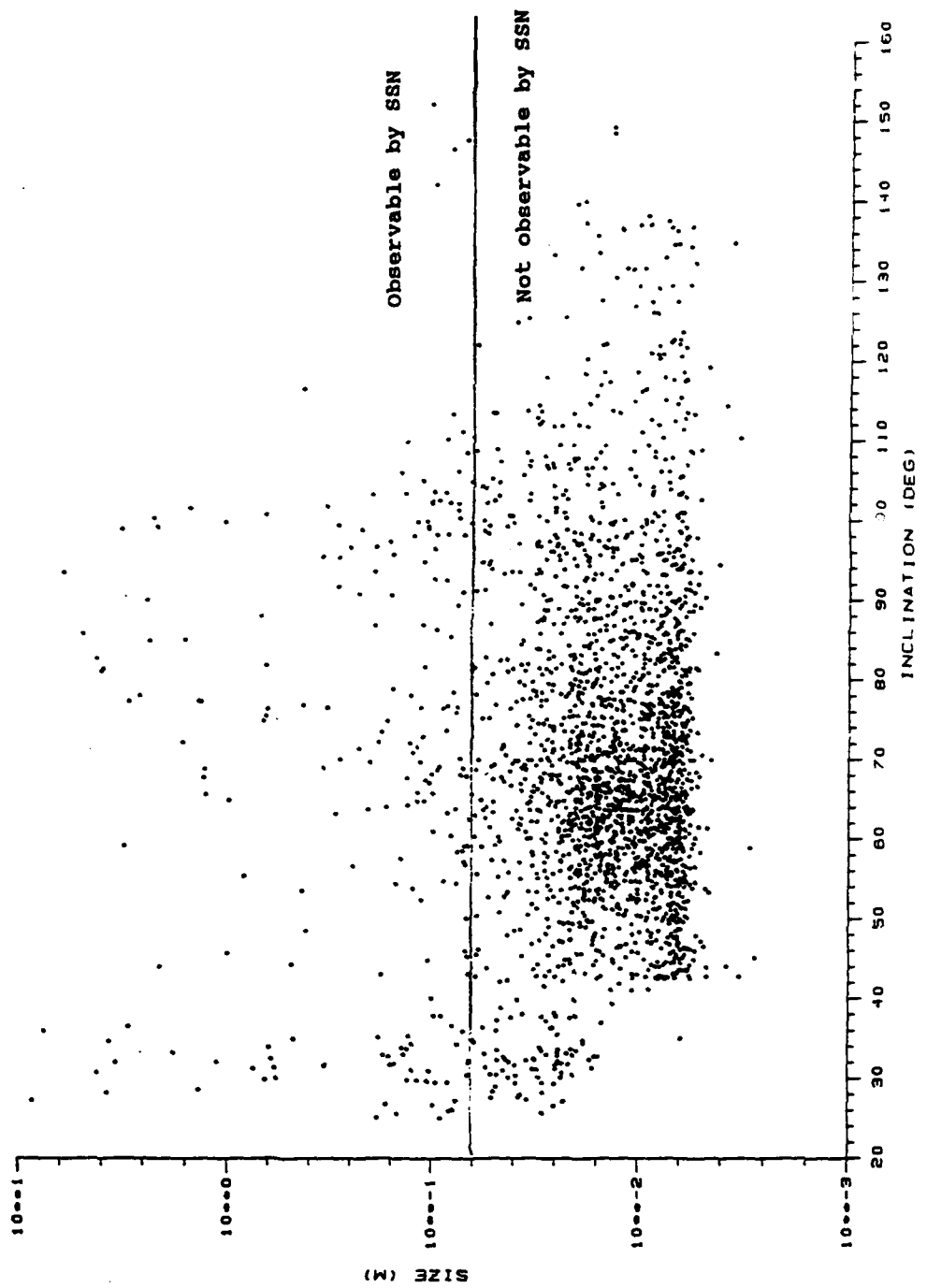
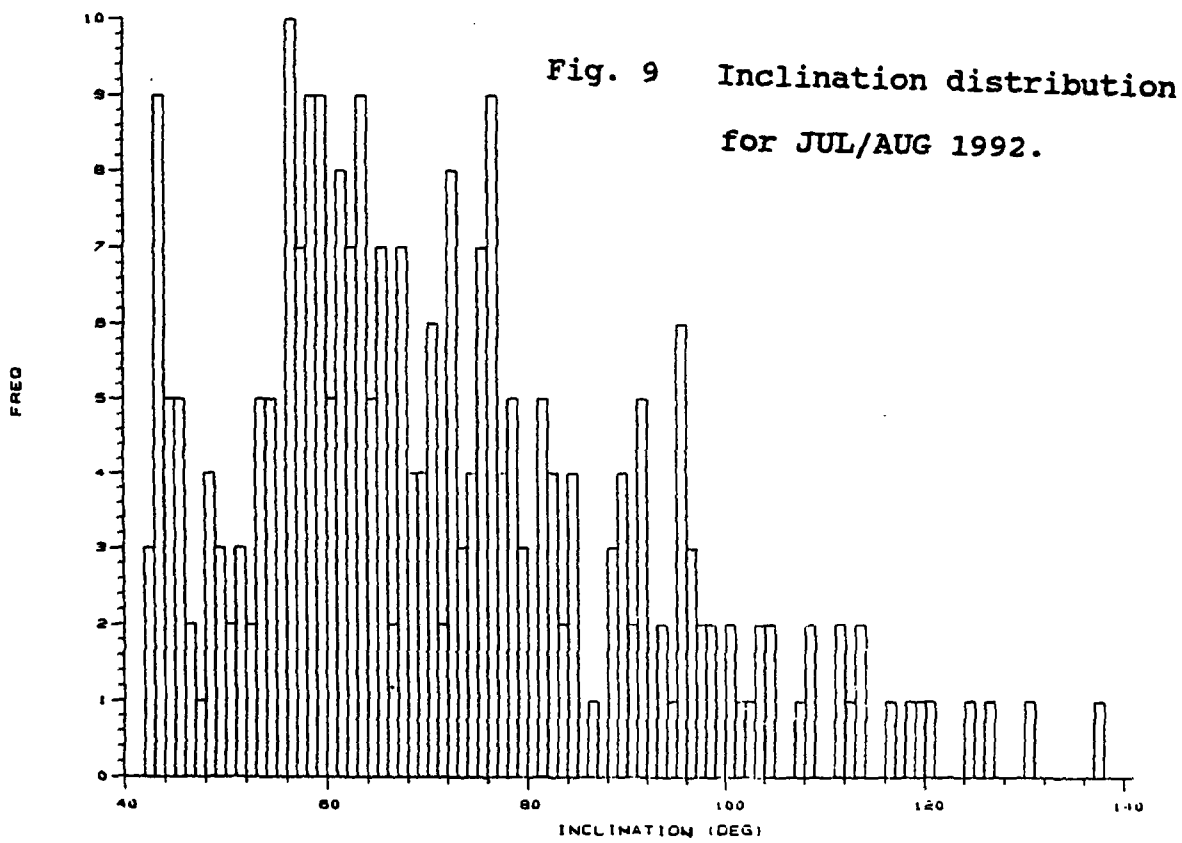
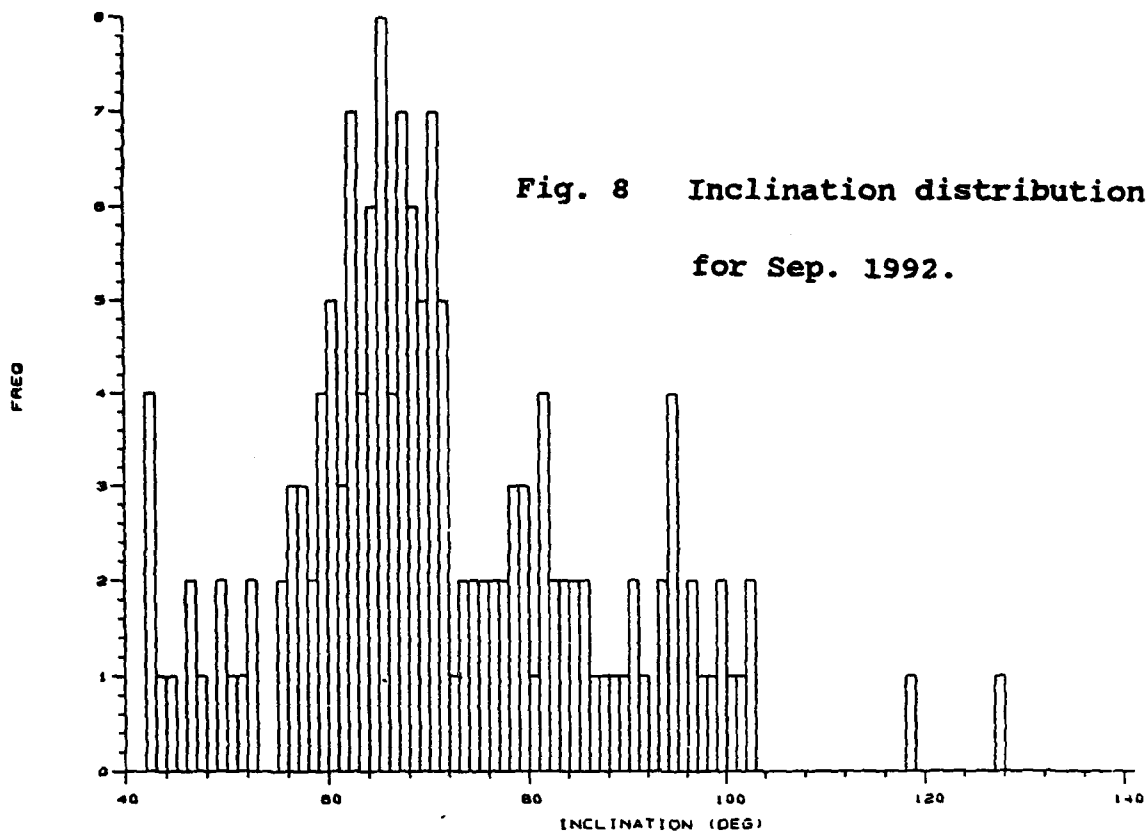


Fig. 7 Size vs. Inclination for Oct. 1990 through Sep. 1993.  
S/N > 10.0 dB.

OCT 1990 THRU SEP 1993  
INC V. SIZE ALL DEG S/N > 10.0







## **Modelling of satellite breakup and fragment detection.**

*J. Dick (Royal Greenwich Observatory, UK),*

*R. Crowther (Defence Research Agency, UK)*

### **1. Introduction**

It is important for satellite design engineers and mission planners to have a good knowledge of the in-orbit debris environment that their satellite will encounter. Such knowledge affects not only the choice of orbit and appropriate shielding technology, but also the fundamental viability of the project. Although we have a good catalogue of large objects ( $>0.5$  m), from SSN radar observations, and a good statistical knowledge of the LEO small-object ( $<1$  mm) population from the study of retrieved surfaces, we remain relatively ignorant of the intermediate-size debris population in all orbital regions. Our knowledge of the GEO debris environment is especially poor because of its range and the absence of retrieved surfaces.

Considerable effort has been expended on computer modelling of the risk from debris impact[1,2]. Models, of course, rely on observational data to tie them to reality. Observational techniques using ground-based optical instruments are well established, both for LEO[3-5] and for GEO[6-8], but data are still scarce because observation of the debris population is nontrivial in terms of the telescope time and information-processing facilities required. It is also important to understand that the topocentric orbital motion of debris can reduce the probability of detection, that collisions between large and small objects can result in an unnoticeable change in the large object's orbit (both effects leading to incorrect (low) predictions of population density) and that the operational problems of a debris-detecting global network might differ from the existing SSN facilities.

In this paper we model the breakup of a satellite in GEO and examine the problem of detecting break-up from changes in the large-object orbit and the resultant debris, using sensor sensitivity models. We also discuss the application of our sensitivity model to debris in other orbits and to debris-surveillance network tasking.

### **2. Breakup model and fragment generation**

We have simulated the collision of a satellite of mass 2000 kg in geostationary orbit ( $a=42240$  km,  $e=0.0$ ,  $i=0.0$ ) with a 1 kg piece of debris initially in geostationary transfer orbit ( $a=24610$  km,  $e=0.717$ ,  $i=0.0$ ). The debris approaches the satellite with a closing velocity of the order of 1.4 km/s and strikes its front surface. The impact produces a partial fragmentation of the satellite leaving 98% of the original satellite mass intact. Our breakup model is based on theory presented by McKnight[9].

The predicted trajectories (in terms of  $a$ ,  $e$  and  $i$ ) of the fragments produced, assuming an isotropic breakup, are shown in Figure 1. We can see that there is a relative small spread of trajectories about the nominal geostationary orbit. The small spread is due to the relatively low impulse velocities imparted to the fragments; velocity values are driven by the impact energy (and therefore the closing velocity) of the projectile, which, in a GEO/GTO encounter, is relatively low compared with collisions in LEO. The  $a$ - $e$  diagram for fragments shows a constrained distribution that we can use to limit the extent of our later calculations. Note that, in general, it is the smaller fragments that occupy the most-changed orbits (see Figure 2).

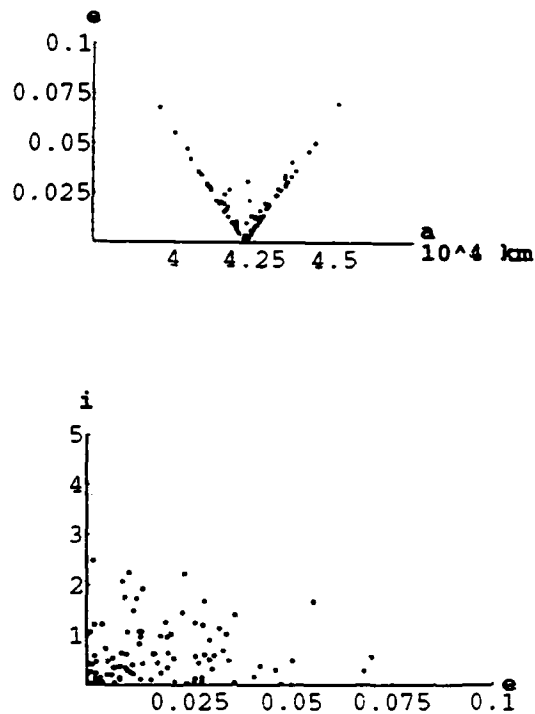
The trajectory of the large (target) object would not be expected to change following a hypervelocity impact with a smaller impactor object; the target object would continue to follow its nominal orbit as observed by the SSN. Hence, large inactive objects can suffer impacts and generate debris without themselves showing symptoms.

### 3. Detection model

Once we know the types of orbits into which debris are injected, we then need to determine how successfully we will be able to detect them, given that we know the type of sensor system that we will use. This detectability information will tell us, for a given orbit or class of orbits, how complete any survey will be and will also indicate optimal search strategies.

The detectability of a debris particle is a function of the sensor system, the debris intrinsic brightness (dependent on albedo, range and solar phase angle) and of its angular speed. The angular speed is important — the faster a particle traverses the sensor's field of view, the smaller the amount of signal deposited into each of the sensor's pixels, so the larger the minimum diameter detectable.

**Figure 1** Distribution of debris orbital eccentricity, inclination ( $^{\circ}$ ), and semi-major axis ( $10^4$  km).



Crowther *et al.* [7] discussed a signal-environment model for ground-based telescopes that they used to determine the minimum detectable diameter ( $\phi_{\min}$ ) for their trial debris survey of a small region of the GEO ring. For this paper, we have extended that model, in *Mathematica*, to include the effects of range, position in the observer's sky, and angular velocity in the detector's field of view.

This extended model is no longer restricted to GEO debris and now predicts minimum detectable diameter at any position along an arbitrary orbit when that position is observed from an arbitrary ground-based site: the position in orbit and position of the observer are two fundamental variables in the detectability problem.

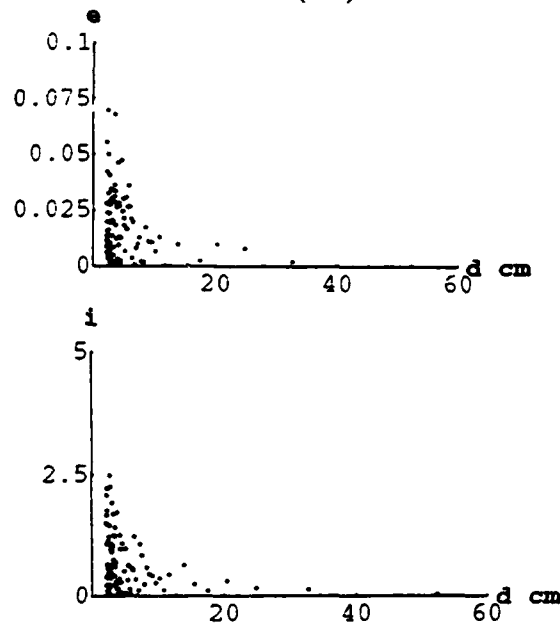
Using this model, we can calculate  $\phi_{\min}$  as a function of position-in-orbit ( $m$ ) and the hour-angle ( $h$ ) of the debris orbit's ascending node at the observer's site. These two variables allow us to predict the  $\phi_{\min}$  for an orbit-site combination at any time, assuming, of course, that the sky is dark at the site; when the object is below the observer's horizon, we set  $\phi_{\min}$  to an arbitrary large value. If  $\phi_{\min}$  is plotted with  $m$  along the  $x$ -axis and  $h$  along the  $y$ -axis, we can find various parameters from the plot.

A cut parallel with the  $x$ -axis shows how  $\phi_{\min}$  varies during the day for a set position in the orbit (*not* a set sky position as defined by a constant sensor altitude and azimuth). Because the site will be sunlit at some part of the day, only a subsection of the  $x$ -axis will have a dark sky during any day. The position of the dark-sky subsection will move along the  $x$ -axis and will complete a cycle of the  $x$ -axis during one year; the duration of the subsection is dependent on the site location and solar declination. If two sites observe the same position along an orbit then their respective  $\phi_{\min}$  performance will be represented by two points along a line of common  $m$  with the difference in site longitudes equating to the  $x$  separations of the points. (Both sites must be in their night zone.)

A cut parallel with the  $y$ -axis shows how  $\phi_{\min}$  varies at an instant at different positions along the orbit as viewed from one site.

It is also possible to make cuts at a slope of 1 second per second (unit gradient) that

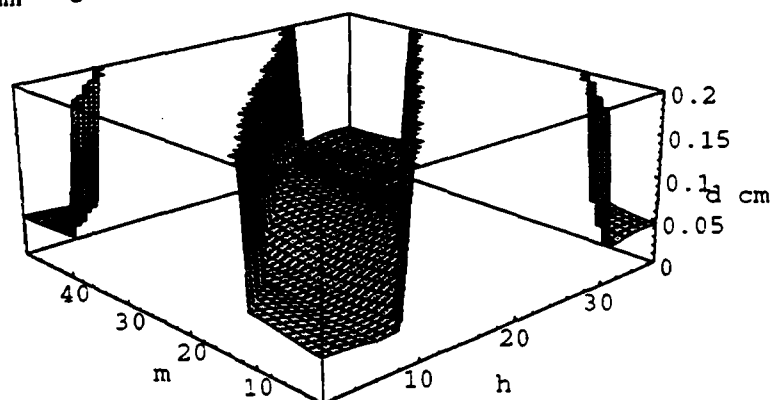
**Figure 2** Distribution of debris orbital eccentricity and inclination ( $^{\circ}$ ), as a function of diameter (cm)



show how  $\phi_{\min}$  varies as a site takes snap-shots (the sensor is static during the exposure) of an object as it progresses along its orbit. For unit-gradient cuts, different y-axis intercepts represent objects in the same orbit but with different epochs.

In all cases,  $\phi_{\min}$  is also dependent on the sensor's parameters (*e.g.* aperture, pixel field of view, detector noise, etc.) and can be developed to model more accurately sky background effects and, by specifying the sensor motion, to determine the detection thresholds in blind tracking (where the sensor tracks a hypothetical object in some orbit). Figure 3 shows an  $h$ - $m$ - $\phi_{\min}$  diagram for an object in a near-GEO orbit: we have used an orbit of a fragment generated by our modelling, with  $a=43800$  km,  $e=0.04^\circ$ , and  $i=2^\circ$ . In the diagrams,  $h$  is in  $10^\circ$  steps and  $m$  is in  $10^3$  s steps. The z-axis is used to plot  $\phi_{\min}$ . The surface of  $\phi_{\min}$  in Figure 3 is reminiscent of a canyon: the variations in height along the canyon floor (more visible in a contour plot) show that  $\phi_{\min}$  varies depending on  $h$  and  $m$ . The steep walls represent the rapid increase in  $\phi_{\min}$  as the object sets in the observer's sky; no value is plotted for objects that have set. The small sections of visibility at the extreme right and left of the diagram are caused by the modulo nature of both axes.

Figure 3  $h$ - $m$ - $\phi_{\min}$  diagram

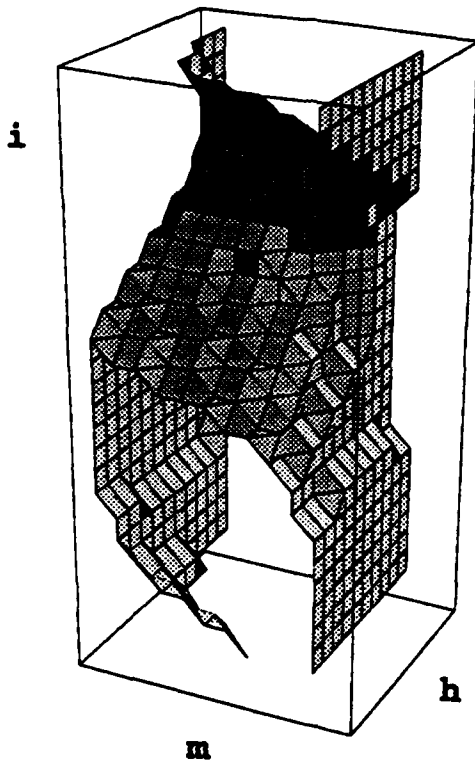


We can also display, as a three-dimensional contour plot, the effect of a third parameter (*e.g.* eccentricity, inclination, or argument of perigee) by plotting a surface of constant  $\phi_{\min}$ . Figure 4 shows a surface of constant  $\phi_{\min}$  for a high eccentricity orbit ( $e \sim 0.74$ ), with inclination plotted as the third variable, along the z-axis.

#### 4. Selection effects and optimal sensor tasking

An  $h$ - $m$ - $\phi_{\min}$  diagram is a good way to show the selection effects applicable to a particular observation. For the fragment whose visibility is plotted in Figure 3, some part of its orbit is visible during any day but the choice of  $h$  (a function of date and time) determines  $\phi_{\min}$ . The actual value of the debris' ascending node ( $\Omega$ ) and argument of

**Figure 4** Surface of constant detectable diameter as a function of  $h$ ,  $m$ , and  $i$ .



still there are preferred values of  $h$  in terms of both detectable size and duration of observing window (Figure 6). Such information affects the tasking strategy for a debris-surveillance network.

Indeed, the tasking strategy for a debris-surveillance network must overcome problems that are different from those encountered by a network that is designed to track large objects that principally occupy circular orbits and whose orbital evolution history is available.

- The weak signal levels returned from small (but still damaging) debris present a greater challenge to sensors.
- Observations suffer from more severe selection effects.
- The orbits of small debris change more rapidly than those of large objects, so the network's orbit-maintenance load is far greater.
- The eccentricity distribution will be different.

perigee ( $\varpi$ ) will affect the phasing of the diagram and the exact value of  $\phi_{\min}$ .

But these phasing effects will not affect the general conclusions: for a GEO-like orbit, most of the fragments are below the typical visibility threshold ( $\sim 5$  cm) of our mock sensor — a high-efficiency, 1.5m aperture, CCD-equipped telescope — but  $\phi_{\min}$  is a relatively flat function of  $m$  and  $h$ ; objects  $\sim 5$ cm in size and larger potentially are visible at any time of year.

However, if we examine the  $h$ - $m$ - $\phi_{\min}$  diagram (Figure 5) for the particle that caused the fragmentation (viewed from a UK site), we see that there are periods during the year when no particle in that orbit will be visible while at other times  $\phi_{\min}$  is a strong function of  $h$  and  $m$ .

Such effects are site dependent. If we observe the particle from an equatorial site, coverage of the orbit is better but

**Figure 5**  $h-m-\phi_{\min}$  diagram for impactor viewed from a UK site. Contours are at 5 and (outermost) 10 cm.

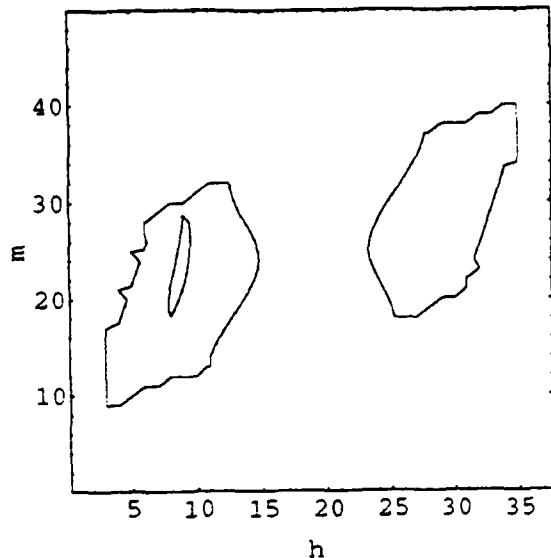
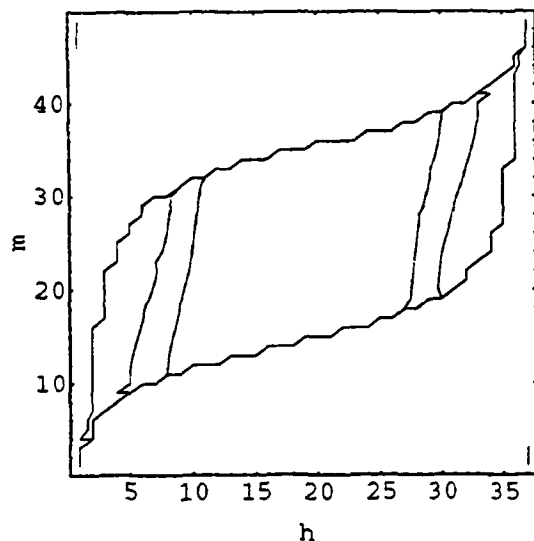


**Figure 6**  $h-m-\phi_{\min}$  diagram for impactor viewed from an equatorial site. Contours are at 5 and (outermost) 10 cm.



Large objects typically have near-zero eccentricities (75% of ~3000+ objects in the NASA Satellite Situation Report have  $e < 0.05$  [5]) which eases orbit computation and lessens orbital-motion selection effects. Small debris particles created as the result of a high kinetic-energy collision or an explosion are predicted (see above and [10]) to have much higher eccentricities.

Detection and determination of eccentricity is difficult during the short time that LEO debris can be tracked from any one site [5]. The resulting limited knowledge about the eccentricity-related orbital elements and the nonapplicability of circular-orbit approximation result in large uncertainties in the location of an object soon after detection. To obtain an approximate orbit, post-detection observations taken shortly after discovery are required: multi-site observations with wide field-of-view sensors are important, thus raising associated issues of sensor network management.

## 5. Commentary

Using a model breakup and an  $h-m-\phi_{\min}$  diagram, we have shown that it is difficult to detect small objects in GTO and debris in GEO: the former suffer from severe selection effects, the latter because large inactive satellites may not show any symptom of having been hit and the debris generated are difficult to detect because of their size and range. These are not insurmountable problems — large-aperture wide-field optics (e.g. [11]) and optimal search strategies can help.

For a discovered object or a sought-after class of objects in a limited range of orbits (perhaps clustered soon after an on-orbit breakup), an  $h-m-\phi_{\min}$  diagram can be used to optimally schedule a network because the diagram indicates the site, time of day and year, and position in orbit that will yield the highest chance of detection (or re-detection). Such information can indicate selection effects in observational surveys and could be used to schedule observations to monitor debris deposition by launch operations, so allowing compliance with future debris mitigation legislation to be checked.

## 6. References

- [1] Reynolds, R.C., Kessler, D.J., Orbital debris environment projections for Space Station Freedom, *First European Conference on Space Debris*, ESOC Darmstadt, Apr. 5-7, 1993.
- [2] Sdunnus, H., Klinkrad, H., An introduction to the ESA reference model for space debris and meteoroids, *First European Conference on Space Debris*, ESOC Darmstadt, Apr. 5-7, 1993.
- [3] Henize, K., Stanley, J., Optical observations of space debris, *AIAA/NASA/DoD Orbital debris conference*, Baltimore, April 16-19, 1990.
- [4] Henize, K.G., O'Neill, C.A., Mulrooney, M.K., CCD observations of orbital debris, *AIAA/NASA/DoD Orbital debris conference*, Baltimore, April 16-19, 1990.
- [5] Lobb, D.R., Dick, J.S.B., Green, S.F., *Study on optical sensors for space debris observation*, ESA Study No. 9267/90/D/MD.
- [6] Gehrels, T., Vilas, F., A CCD search for geosynchronous debris, *Icarus* **68**—412—1986.
- [7] Crowther, R., Dick, J., Edwin, R., Parker, N., Optical sensing of objects in the geostationary ring, *First European Conference on Space Debris*, ESOC Darmstadt, Apr. 5-7, 1993.
- [8] Boehnhardt, H., Photographic observations of the co-located spacecraft at 19° West, *Technical Report*, c/o ESOC, Darmstadt, 1992.
- [9] McKnight, D.S., Determination of breakup initial conditions, *Journal of Spacecraft and Rockets*, **28**—470—477—1991.
- [10] Zhang, J., Kessler, D.J., Rex, D., Interpretation of the distribution of large craters on the Long Duration Exposure Facility (LDEF), *First European Conference on Space Debris*, ESOC Darmstadt, Apr. 5-7, 1993.
- [11] Dick, J.S.B., Bingham, R.G., Walker, D.D., Ground-based telescopes for the observation of space debris, *First European Conference on Space Debris*, ESOC Darmstadt, Apr. 5-7, 1993.

# **A CCD Search for Geosynchronous Debris From the Breakup of SSC 3432**

P. D. Tennyson and G. E. Powell  
MIT / Lincoln Laboratory

## **ABSTRACT**

Debris from the breakup of the LES-6 Titan 3C trans-stage rocket body, SSC 3432, was observed by the MAUI GEODSS less than one hour after it fragmented on 21 February 1992. A Search of the "pinch" point was undertaken in May of 1993 at the Experimental Test System (ETS) Site in Socorro, NM. The "pinch" point search exploited advanced Electro-Optical surveillance techniques and technologies developed at Lincoln Laboratory.

## **I. INTRODUCTION**

The Advanced Electro-Optical Space Surveillance (EOSS) Technology Program at MIT / Lincoln Laboratory develops Visible and Mid-Wave Infrared staring imager technology and optimal signal processing technology for space and missile surveillance applications. The program emphasizes system studies to determine requirements and perform design trades, and laboratory and field testing and demonstrations of the technology. The transfer of technology to the user community and the resulting interaction is a key goal of the program.

## **II. THE FRAGMENTATION OF 3432**

### *The Maui-GEODSS Video Tape*

At about UTC 10:00 on 21 Feb., 1992, the operators at the Maui-GEODSS Site detected a cluster of objects near the nominal position of the LES-6 Transtage Rocket Body. At the time, this satellite, SSC 3432, which is located in the equatorial geosynchronous belt, was being searched for routine position measurement.

When the operators saw the unusual cluster of images, they started the tape recorder. The tape showed the images as a cluster of dashes or streaks in a video frame, which was an accumulation of 12 "and" frames, each with an integration time of 0.3 s. The telescope was driven at the sidereal rate for star cancellation with the GEODSS system in the operator assist mode. The camera was zoomed with a 1° circular field of view.

The tape showed 5 accumulated frame sets as follows: First, one accumulated frame is shown with the satellite images near the edge of the FOV, and then 4 subsequent frame accumulations are shown in progress with the group of satellite images approximately centered in the FOV. Each of the 4 latter sets shows the 12 "and" frames accumulating in sequence with evident streaking satellite images.

### *Observations from Still Photographs of the Tape*

Still photographs were made from each of the 5 frame sets to enable relative position measurements of the objects to be made. The illuminated Reseau points in the GEODSS camera, which were visible in some of the photographs, indicated that the plate scale on the photographs was 133.4 mm/1°, and allowed geometric distortion in the camera to be corrected. Figure 1 from [Powell, et al., 1993] shows how the objects moved relative to each other between frames 2 and 5.





Figure 2  
Constructed overlay of Frames 2 and 5

### *The Orbital Parameters*

The orbital elements for 3432 and 81069, respectively, before and after day 52 are presented in Table 5. The semi-major axis of 3432 is decreased by 17.85 km between day 49 and day 53 which leads to a drift rate increase of 0.23 degrees/day, or in other terms, the orbital period is decreased by 54 seconds. A similar change is seen with 81069, where the orbital period of 81069 is 4:48 greater than that of 3432 prior to day 52.

### **III. THE PINCH POINT**

SSC 3432 fragmented on day 52 of 1992 at approximately 9:30 UTC. We developed a search strategy for finding the fragments based on basic concepts of orbital motion. If we were given a fragmentation in the two-body system. Then every fragment would pass through the break-up point once per orbital period. In reality, we do not have a two-body system. We must compensate for luni-solar perturbations, solar radiation pressure effects, non-homogeneous mass distribution in the non-spherical central body, etc. The dominant perturbation to the orbital plane is due to luni-solar effects. Therefore, the orbit of 3432 at break-up is propagated to the observation time, and then we set the true anomaly equal to

what it was at break-up. The "pinch point" is the point in space defined by the break-up true anomaly and the other orbit elements at epoch.

#### **IV. EXPERIMENTAL TEST SYSTEM (ETS) SITE**

The primary field test location for the EOSS program is the Experimental Test System (ETS) Site in Socorro, NM. This site performs a number of space and missile surveillance functions. Sensor technologies and concepts are evaluated and demonstrated. Surveillance techniques are developed and refined in a quasi-operational surrounding. Space object measurements can be performed on objects at all altitudes. The ETS telescope suite includes computer controlled 31 inch and 14 inch telescopes in two domes. Routine observations performed at the ETS site include debris search and White Sands Missile Range launch support.

#### **V. SENSOR DESCRIPTION**

The visible sensor camera system runs a 1024 by 1024 pixel Lincoln Laboratory CCID-10. The camera has a demonstrated total system noise of seven electrons at a 1 MHz pixel rate on each of four read ports. The video signal is digitized to 12 bits. The highest gain yields 2.39 electrons per digital number on average. The dark current of the camera is 0.8 electrons per pixel per second at -60C. The camera has a range of exposure times from 0.4 seconds to 102.4 seconds.

The signal processing and data recording system used for the 1024 field test effort was a commercially available Silicon Graphics VME-Bus based 4D/35 workstation. The processor in the workstation is 36 MHz MIPS R3000 with 96 Mbytes of RAM. The graphics sub-system was the XS-24 option. An IKON 10099 board is the DMA interface to the camera. A bulk memory of 128 Mbytes was used to buffer the data stream for the CPU. The entire system is easily programmable in both C and FORTRAN languages.

The camera was mounted on the 14 inch f/1.7 ETS telescope in the A-dome. The field of view of configuration was 2.6 degrees on a side. This telescope is co-aligned to the ETS 31 inch A main telescope. The telescope was equipped with an EBSICON and was operated in a prime focus configuration giving a 2 degree diagonal field of view when run in a non-zoom mode. The main telescope was controlled by the normal mount and control computers.

#### **V. EXPERIMENTAL TECHNIQUE AND DATA REDUCTION**

As data on unknown or uncorrelated objects (UCT's) is considered CLASSIFIED by USSPACECOM, the camera was run in an isolated mode with no data recording enabled. The ETS main camera system and telescope control was operated in its SECRET configuration. The CCD camera was used for broad area search and the EBSICON telescope was used to perform correlation and metric data gathering.

The telescope was pointed to a preselected line of sight and images gathered. The exposure time was selected to be the Dwell-in-Cell time for geosynchronous objects to maximize sensitivity. The CCD images were presented to the operator as a maximum value projection. This allowed moving objects to appear as growing streaks while the background was suppressed. If a moving object was located, a comparison to the catalog was performed by the ETS main telescope.

If the object did not correlate, the object was brought to boresite of the main telescope and metric observations were gathered. The CCD camera was turned off. The metric observations were used to generate a preliminary element set. [elset fitting technique]. The

element set would be used to re-acquire the object on the next night. The raw observations were sent to the analysts at Millstone Hill for further analysis. The analysts would determine if the object was consistent with the desired breakup and would provide a more accurate element set for the object.

If no object were detected, the field would be observed for a total of 5 minutes. The line of sight would then be shifted to a new field of view to keep the predicted pinch point as close as possible to the boresite of the ETS main telescope.

## **VI. FIELD TEST RESULTS**

As part of 1024 field test in May of 1993, a pinch point search was performed to locate breakup pieces of SSC 3432. The illumination constraints were such that the pinch points was only observable for about 40 minutes after sunset and before it set below our 15 elevation limit. The search was performed and one candidate UCT was detected. An element set was generated for re-acquisition the next night. Millstone later confirmed that the object was consistent with the breakup event.

Early the next morning the anti-pode point was searched for about two hours unsuccessfully. Two objects were detected and tracked. The element sets later turned out to be consistent with two other "known" UCT's not from the desired breakup.

The next night the object was thought to be reacquired and a new set observations were performed. Later analysis indicated that a database error had occurred and the object observed was another known UCT. This was not discovered until Millstone had reduced the observations. The detection rate of 1 object in 40 minutes of search is consistent with the expected detection rate from a 23 piece breakup.

## **VII. FUTURE PLANS**

A future field measurements effort is planned for a time when the illumination angles on the pinch point are more favorable. The sensor system will be enhanced by a higher quantum efficiency back-illuminated CCD and by a new display subsystem with a high performance signal processing chip. The first opportunity for the observations will be in the early 1994. Observations of other breakups and broad area searches of the Geo-belt may also be performed with this sensor system.

## **VIII. SUMMARY**

A search for the break-up of SSC 3432 has been performed successfully with a high performance CCD camera system. The search exploited both the advanced sensor technology developed by Lincoln Laboratory and the techniques developed to enhance knowledge of the orbits of objects in space.

## **IX. ACKNOWLEDGMENTS**

The support of the ETS and particularly the site manager Dave Gibson is greatly appreciated. This work was supported under U. S. Air Force Contract F19628-90-C-0002 to MIT/Lincoln Laboratory.

## SPACE DEBRIS MEASUREMENTS: PHASE ONE FINAL REPORT

E.C. Pearce, M.S. Blythe, D.M. Gibson, and P.J. Trujillo (MIT Lincoln Laboratory)

### ABSTRACT

This Report documents the results of Phase One of the Phillips Laboratory Debris Measurements Program at the Experimental Test System. Observationally, the primary goals of the program were to develop and implement techniques to detect and track small, previously uncataloged space debris. Additionally, techniques were developed to monitor sensor performance and understand observational biases. During the program, a total of 840 objects were detected, with 346 objects being previously uncataloged. An analysis of the orbital distribution of the tracked objects has shown that orbital distribution of the observed space population is significantly more eccentric than the Space Surveillance Catalog. Long term tracking of several pieces has shown that the orbital dynamics of many smaller debris objects are poorly modeled by currently used propagation models. Finally, a lower limit on the space population larger than 10 cm has determined that the catalog is incomplete by at least a factor of 1.6.

### 1. INTRODUCTION

MIT Lincoln Laboratory has a long history of optical debris measurements at the Experimental Test System (ETS) in Socorro, New Mexico. In the mid-1980s, the first optical survey was conducted [1]. This survey was a simple, near-zenith staring debris search. Both 80 cm telescopes were pointed to the same position near the zenith. Objects passing through the field of view were recorded on video tape for later analysis. The ratio of detected but uncataloged debris to cataloged objects was found to be approximately 3 to 1. Moreover, the researchers felt that this ratio would increase by a factor of 2-3 if the observational biases against the smaller uncataloged objects could be removed from the data. Unfortunately, techniques to monitor sensor performance and account for these biases did not exist at the time of this survey.

In May 1991, MIT/LL began the current optical debris measurements program. This program was part of a PL organized task to search for and *track* space debris in support of the DoD effort to characterize the space debris environment [2]. An additional requirement imposed by Air Force Space Command (AFSPACECOM) was to determine debris orbital element sets. New techniques were developed to acquire and track the rapidly streaking objects [3, 4]. Consequently, the new effort was unique from the previously outlined programs. The initial phase of measurements program concentrated on specific sun-synchronous debris clouds from recent breakups. In order to maximize sensitivity, a technique called "pseudo-tracking" was developed and used. When searching in this mode, the telescope tracked along the orbit of previously cataloged cloud members. When an object was detected, the telescope operator would manually acquire and track the object. Once acquired, the object would be tracked to the horizon, generating enough metric data for accurate orbit determination.

Beginning in February 1992, the acquisition and track techniques developed for the pseudo-tracking searches were combined with the original near-zenith stare methodology [5, 6]. For this latest series of observations, the ETS 80 cm telescopes would stare at different selected Guide Star Photometric Catalog (GSPC) fields. However, instead of simply recording and analyzing streaks, objects were actively acquired and tracked. The new "stare and chase" observations combined the best features of both the staring and pseudo-tracking searches. As part of the same program, similar measurements were conducted at the Air Force Maui Optical Station (AMOS) incorporating many of the techniques developed at the Lincoln Laboratory [7].

## 2. ETS INSTRUMENTATION

The Experimental Test System is located on the northwest corner of the White Sands Missile Range in southern New Mexico [8]. The site is blessed with some of the darkest skies in the continental United States, with night sky brightness routinely reaching  $m_v = 22.0$ . The site was originally constructed in 1975 as a prototype for the Ground Based Electro-Optical Deep Space Surveillance (GEODSS) system. The twin 80 cm Boller and Chivens telescopes used in that prototyping effort continue to be the ETS's workhorse instruments.

For the majority of the stare and chase debris search, the first ETS 80 cm telescope, ETS-A, was operated in its  $f/2.87$  prime focus configuration while the second telescope, ETS-B, was operated in its  $f/5$  Cassegrain configuration. With the typical sensor configuration, ETS-A provides a  $2.0^\circ$  field of view while ETS-B provides a  $1.0^\circ$  field of view. The prime focus configuration offers a significantly enhanced search area compared with that in the Cassegrain configuration. However, the corresponding loss of sensitivity negates any expected increase in the debris detection rate.

Each telescope was equipped with a Westinghouse intensified electron-bombarded silicon diode array camera (I-EBSICON) [9]. The I-EBSICON cameras have an unusually large 80 mm fiber optic faceplate, allowing full coverage of the telescope focal plane. While the ETS cameras are similar to the GEODSS cameras, an intensifier stage provides significantly enhanced sensitivity over the unintensified GEODSS counterparts. The ETS cameras are sensitive enough to provide sky background limited performance, even at RS-170 video rates.

## 3. METHODOLOGY

### 3.1 General Observational Considerations

Since the primary altitude of interest in the debris search is between 500 and 1500 km, observing must be scheduled during the twilight hours. During twilight, the objects are illuminated by sunlight, but are observed against a dark sky. However, when devising an optimal search, several complicated trades must be considered. Generally, these trades concern the following: (1) the background sky illumination, (2) the illuminated range of altitudes in the field of view, and (3) the opportunity for reacquisition of discovered objects on the subsequent revolution. All three of these factors are functions of both the time window observed and the stare position of the telescope.

Early in the program, debris observing sessions were conducted during the one hour period boarding on nautical twilight with the telescope in a near-zenith sidereal stare. Later in the program debris reacquisition became an increasingly high priority.<sup>2</sup> In order to successfully reacquire a debris object, it must be observed on the subsequent revolution (typically 100-150 minutes later). Unfortunately, this typically places the object far to the west at an extremely low elevation. The observing conditions of these "rev 1" passes can be improved significantly by moving the initial search field to the east by a modest amount. Although this causes a higher shadow height during the stare period, the cost in sensitivity of looking as much as 15° off zenith is negligible. Thus, evening twilight stare fields were moved approximately 20° east of the zenith beginning in October 1992.

### 3.2 Stare and Chase Debris Search

The stare and chase debris search methodology has grown from a number of techniques developed over the three year program. Basically, the search technique is a "near zenith sidereal stare" search, where the telescope is pointed near the zenith and objects are detected as they streak across the field of view. Several significant enhancements have been added to this basic methodology, including: (1) background astrometric and photometric calibration fields, (2) acquisition, tracking, and subsequent reacquisition of detected objects, and (3) continuous monitoring of the observing conditions and sensor performance. In combination, these techniques have transformed simple zenith stare debris searches from isotropic head-counts, into a technique that can quantify the environment as a function of orbital parameters and catalog new objects.

During the observing sessions, both telescopes were positioned on selected Guide Star Photometric Catalog (GSPC) fields near the zenith or slightly east of the zenith. The GSPC fields were selected to provide an appropriate sequence of both astrometric and photometric calibration stars. Typically, each GSPC field contains 5 to 7 reference stars with  $m_v$  between 12 and 16 magnitude. For most observations, both ETS 80 cm telescopes were positioned on different GSPC fields separated by approximately one half hour in right ascension. The east/west fence provided the maximum cross-section for the predominate near-polar orbiting debris population.

In previous debris searches, the stare data were simply recorded on video tapes which were later analyzed, giving detection counts and perhaps an estimate of inclination and mean motion. In the stare and chase debris search, detected objects are detected in real time and actively chased down, acquired, and tracked for several minutes, allowing accurate orbit determination, subsequent reacquisition, and detailed study. When the telescope operator detected an object crossing the field of view, the operator would use a manual acceleration joystick to establish a coarse track on the object [3]. Once precision tracking was established using the joystick, a DBA Systems automatic video tracker would maintain a precision track during metric data acquisition.

---

<sup>2</sup>Note that debris reacquisition requires evening sessions, since subsequent passes of discovered objects during morning sessions occur in daylight.

Once precision tracking was established, the object's track was correlated against the Space Surveillance Catalog. The correlation was performed against a full database of nearly all SSC SATCAT and analyst satellites. If the object did not correlate to a known object, metric data were acquired on the remainder of the visible track. Typically, this would result in a metric track 3 to 5 minutes in length. Next, an initial orbit determination (IOD) and differential orbit correction (DOC) were performed use the MIT/LL software package ANODER-R version 11.0. For the IOD, the Gauss-Gibbs method was used exclusively. Then, a DOC using the SGP4 force model was performed with all rev zero observations. For the initial DOC, the SGP4 ballistic drag term  $B^*$  was given a null value. Tests using known satellites in sun-synchronous orbits showed that the "rev 0" orbits obtained in this manner would be accurate to better than  $\pm 5$  minutes on the subsequent revolution ("rev 1"). The across-orbit uncertainty is typically less than  $0.1^\circ$ .

The element sets derived for the initial rev 0 pass are more than adequate for orbital distribution studies. Unfortunately, angles only data from a single pass is not sufficient to determine the mean motion,  $n$ , and eccentricity,  $e$ , accurately enough to allow the object to be cataloged. In order to catalog the object, its reacquisition on its post-discovery "rev 1" pass is critical. To reacquire such objects, one must perform a rapid along orbit search typically spanning  $\pm 5$  minutes.

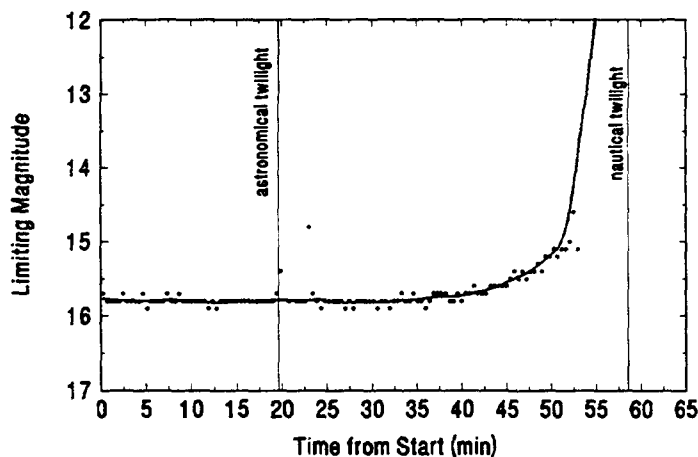


Figure 1. Coverage file from a morning twilight session.

Typically, non-optimal sensor performance causes the population of smaller debris objects to be underestimated unless the bias can be systematically removed. Unfortunately, sensor systems rarely perform at the quoted optimal levels and, as a result, all data collected must be "handicapped" to a mean level of performance. As part of this program, MIT/LL developed techniques to track continuously the sensor performance in terms of limiting magnitude and sky brightness. The limiting magnitude estimates are derived from area photometry of several photometric calibration stars in the GSPC background sequence using a DataCube MAX200 digital image processing system. The system also correctly reconstructs the "on field" and "off field" times by tracking selected guide stars in the background field. Thus, the actual search time can be determined and documented, independent of time spent chasing objects or performing other off-field calibrations. Consequently, the amount of search time at or below a particular limiting magnitude can be calculated, and the bias against the smaller debris objects can be removed.

Figure 1 shows a graphical representation of a typical coverage file for a morning twilight session during June 1993. Local astronomical and nautical twilight are indicated by the vertical lines. The conditions during this session would be considered photometric or near photometric. As twilight approaches, the limiting magnitude decreases with the increasingly bright sky. Near nautical twilight, the sky becomes too bright for safe operation of the EBSICON cameras. It is important to remember that all observations of the lowest orbits occur between astronomical and nautical twilight when the sensor performance is rapidly changing and is generally less than ideal, even on photometric nights. Thus, continuous sensor performance monitoring is critical.

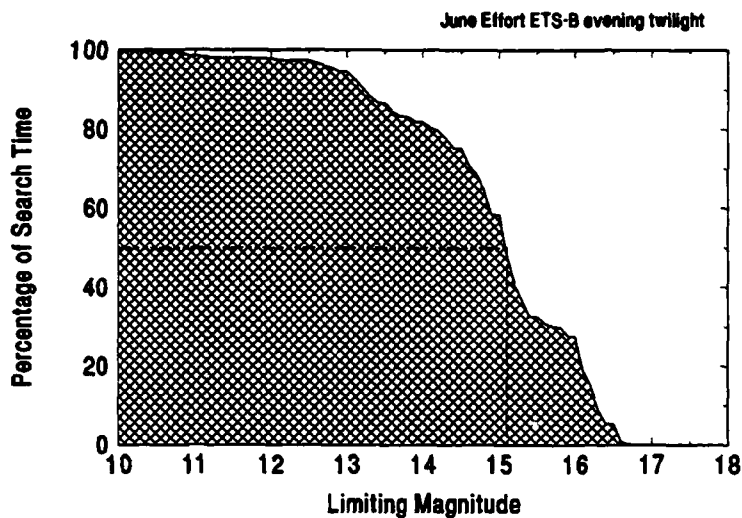


Figure 2. Sensor performance of ETS-B during June 1993.

ous analysis, the sensor performance vs. time must still be convolved with other factors such as shadow height.

## 4. RESULTS

### 4.1 Orbital Distribution of Uncataloged Objects

Perhaps the most significant result of the stare and chase program was the recognition that the orbital distribution of uncataloged debris, and hence the total space population, is considerably more eccentric than the population of cataloged objects. Although a more eccentric debris population had been indicated by impact studies on the Long Duration Exposure Facility (LDEF) and from the range rate distribution of objects detected in the NASA Haystack debris search, this program was the first to directly measure the orbital distribution [10, 11]. Figure 3 shows the eccentricity distribution of the tracked UCTs from the stare and chase program. Although there is a large population of nearly circular orbits, the moderate and high eccentricity peaks at  $e \approx 0.3$  and  $e \approx 0.7$  are considerably higher than the corresponding peaks in the catalog distribution. While the peak near an eccentricity of 0.7 is indicative of geosynchronous transfer orbital debris, the source

Figure 2 shows a compilation of all the coverage files from ETS-B during the June Effort evening twilight sessions. The abscissa shows the limiting magnitude of the sensor while the ordinate shows the percentage of search time for which that magnitude was visible. For this month of observing, ETS-B had a median limiting magnitude of approximately 15.1. From this Figure one can visualize how the bias against the fainter objects, say for example, less than  $m_v = 16$  can be accounted. However, for a rigorous



of the moderate eccentricity peak is not clear. It is speculated that the moderate  $e$  objects are predominately decayed GTO debris, launch hardware from Soviet/CIS early warning and Molniya satellites, and uncataloged Cosmos 862-class debris.

Note that the distribution shown in Figure 3 has not been corrected for the observational bias against the high eccentricity objects. The effect of this bias can be visualized by creating a three dimensional plot as shown in Figure 4. Here, the absolute value of the mean anomaly

at discovery is shown on the y-axis. This is an indication of the distance the object was from its perigee point when first detected in the search. The x-axis shows eccentricity, while the object's estimated size is shown on the z-axis. Clearly, the smallest objects are generally detected

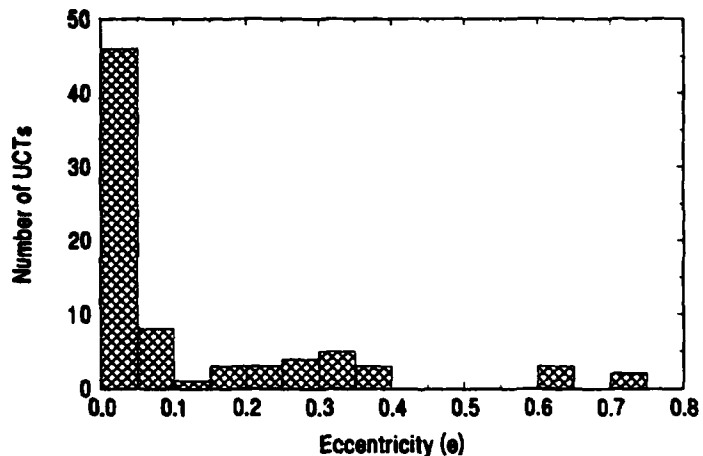


Figure 3. Eccentricity distribution of tracked UCTs.

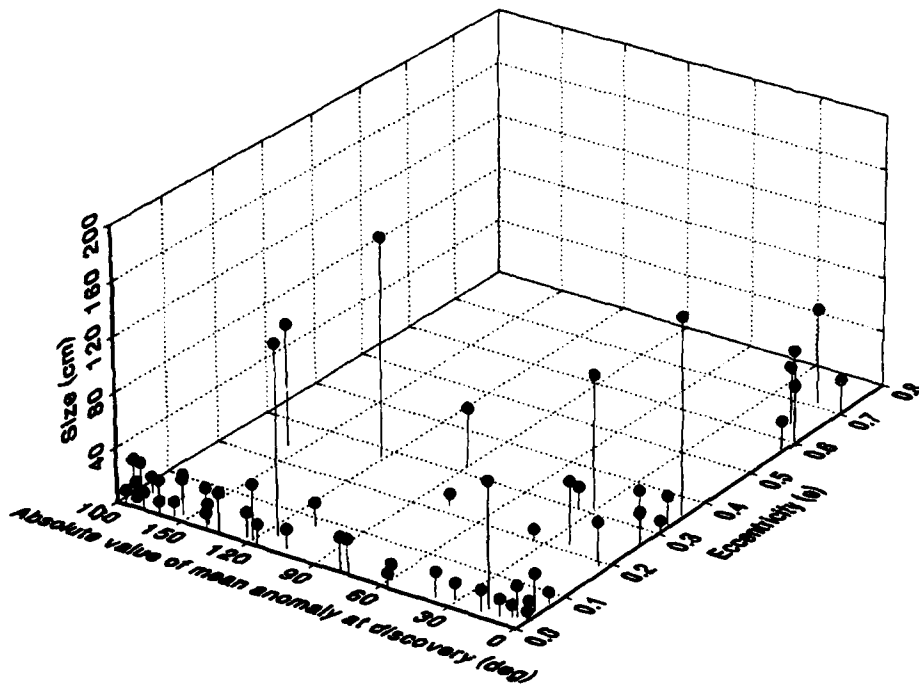


Figure 4. Mean anomaly bias for high- $e$  objects.

only near perigee, particularly if they are in an eccentric orbit ( $e \geq 0.1$ ). At eccentricities typical of GTO, objects are only detectable over a small fraction of the orbit. Thus, an incomplete optical search will have a significant bias against the detection of these objects.

## 4.2 Debris Size Distribution

Figure 5 shows the size distribution of the tracked UCTs. In most cases, the size was estimated by assuming that the object is a Lambertian sphere with an albedo of 0.08. For a few objects with highly specular signatures, a second size estimate was made using a simple model for a specular reflector with an albedo of 0.50. The sun angle and range was reconstructed from the derived element set from the rev 0 pass. The object magnitude was measured directly from the EBSICON using a Quantex QX-7 digital image processor. Comparison stars were obtained from the background GSPC stare fields.

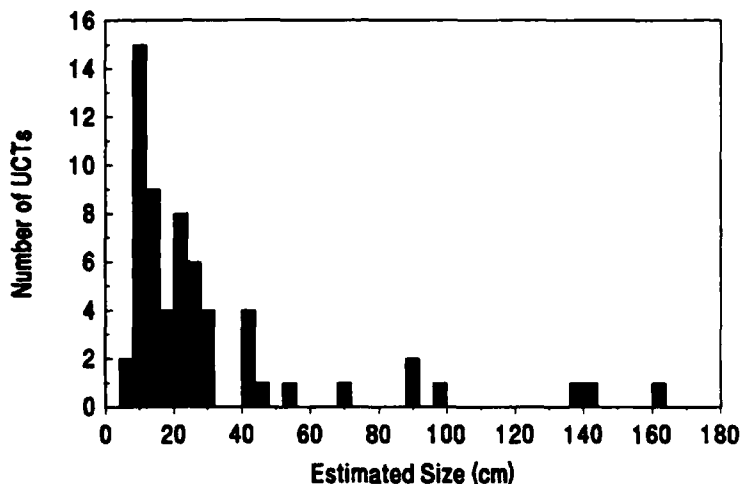


Figure 5. Size distribution of tracked UCTs.

Examination of Figure 5 shows that the majority of the tracked UCTs were in the size range from 10 to 30 cm. This reflects the relative completeness of the SSC catalog at the high end and the sensitivity limit of the ETS sensors at the low end. There are also several large UCTs, some with sizes in excess of one meter. However, comparison with Figure 4 shows that most of the larger UCTs are in highly eccentric orbits. It is also likely that many of these "larger" UCTs have relatively small radar cross sections in comparison to their optical sizes. This study, as well as other previous observations, have shown differences in the size estimates derived from radar and optical observation, indicating an incomplete understanding of the physical properties of debris.

## 4.3 Dynamically Interesting Objects

During the study, six previously uncataloged small UCTs were tracked and studied for an extended period of time. One of the objects, ETS 97034, was tracked by the ETS for 195 days. Five of the six objects exhibited very high drag or other anomalous orbital perturbations. These objects are "dynamically interesting" in the sense that their orbital perturbations are not adequately modeled by traditionally used force models. These objects are initially identified by anomalous

large orbit residuals where differential orbit corrections are made using data taken over multiple revolutions.

The object ETS 97108 was the prototypical object of the class of dynamically interesting objects. This object was tracked by the ETS for 155 revolutions (16 days). The object was later correlated to an object being intermittently maintained by the Naval Space Command (NAVSPACE) as 87736. The unusual perturbations are shown in Figure 6. Clearly, as the size of tracked objects decrease, the effects of solar radiation pressure and atmospheric drag become proportionally larger. With some

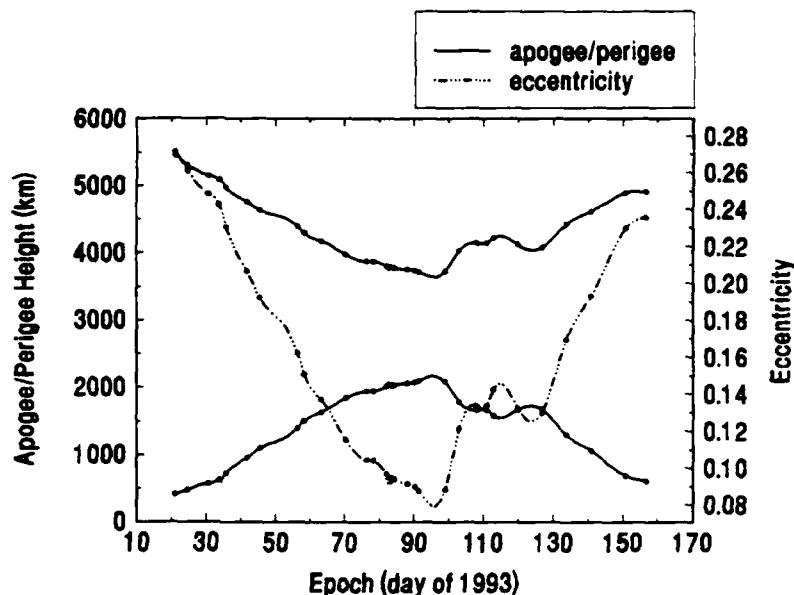


Figure 6. *Orbital perturbations of object ETS 97108.*

of the small, high surface area objects, these perturbations become significant over even a single revolution. In some extreme cases, traditional force models fail to predict these perturbations well enough to maintain the object. Thus, dynamic modeling, as well as detectability, must be considered if these objects are to be cataloged. This is particularly critical with the propagation precision required to allow cost effective collision avoidance maneuvers of large assets such as the Space Station.

#### 4.4 Population Estimate

A preliminary size dependent space population estimate has been made with the collected data. Although this analysis is not as rigorous as that of PL/GPIM nor as rigorous as the data allows, it should provide a firm lower limit for the comparison of the other analyses. This population estimate, shown in Figure 7, has been made by first comparing stare and chase cataloged object detection counts to those from the daily "SATFLUX" predictions.<sup>3</sup> Thus, the fraction of the catalog that was actually observed was obtained. Next, the total number of cataloged and uncataloged detections was used to extrapolate a total space population. Finally, the size distribution of the 71 tracked UCTs was used to produce the population distribution shown in Figure 7. In the Figure, the ETS population estimates in each size bin are indicated by the open-ended error bars. For comparison, the SSC Radar Cross Section (RCS) catalog is also shown. This RCS distribution is based

<sup>3</sup>In addition to the real time correlator, a listing is generated for each session showing all cataloged objects predicted to pass with 3° of the field of view center during the stare period.

on the NASA Catalog of Adjusted U.S. Space Command RCS's and has been adjusted proportionally to match the true cataloged on-orbit total [12]. Also shown for comparison is the population estimate from the MIT/LL "Altair Study." [13]. The line is a power law fit to the right four ETS data points, with the 70% confidence interval of this fit indicated by the dotted lines.

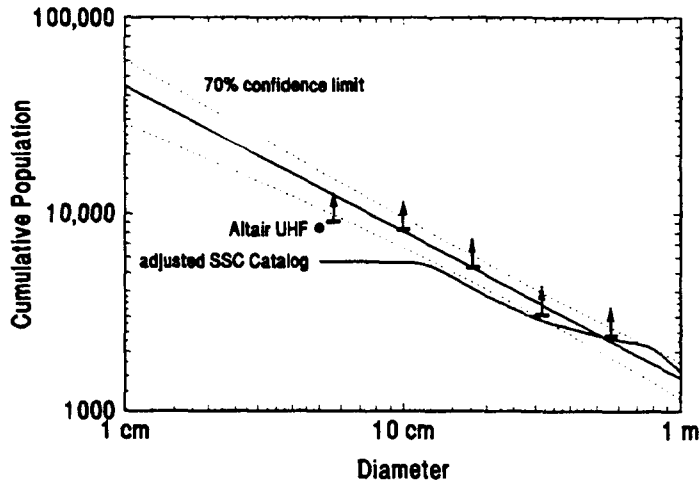


Figure 7. Total space population estimate.

the debris population orbital distribution is similar to the catalog (or is distributed in such a way as to be equally advantageous observationally), (2) the size distribution of the *tracked* UCTs is similar to the entire population of *detected* UCTs, and (3) debris sizes may be estimated by the assumptions outlined in Section 4.2. As we have shown, the first assumption is not correct and accounts for this estimate establishing only a lower limit. The analysis of PL/GPIM has attempted to produce a population estimate without this *a priori* assumption. Nonetheless, the estimate implies that while the catalog is relatively complete to a size of 13 cm, the total population with a size greater than 10 cm is at least a factor of 1.6 larger.

## 5. CONCLUSIONS

From the beginning, MIT/LL has taken an advanced approach to debris measurements. Lincoln has developed important new techniques for measuring and understanding the numerous observational biases that effect optical debris search programs. Additionally, techniques have been developed to allow tracking and cataloging of objects which are currently too small to be tracked and cataloged by the SSN. These techniques have led directly to two significant results. First, and most importantly, the orbital distribution of the uncataloged population is significantly different and more eccentric than that of the catalog. This conclusion, corroborated by both radar and on orbit data, can substantially effect population and threat assessments that assume *a priori* that the space population is orbitally distributed in the same manner as is the catalog. Considerably more data

Examination of Figure 7 clearly shows the effect of sensor and network sensitivity. The SSC catalog begins to roll off at approximately 15 cm. Similarly, the ETS population rolls off between 8 and 10 cm. This is most certainly the consequence of limited sensor performance and not a true characteristic of the debris population. Also note the consistency of the Altair estimate. However, the reader must keep in mind that several assumptions have been made to produce this estimate.

The key assumptions are: (1)

will be required to allow high fidelity determination of the space population and the true orbital distribution, on which current threat assessments are based. Second, a significant fraction of the smaller objects are "dynamically interesting." While that proportion of the sub-10 cm population that may be difficult or impossible to catalog solely because of dynamics is still unknown, it is likely that the dynamics of small objects, as well as their detectability, will impede efforts to catalog these objects in the future.

## 6. REFERENCES

1. L.G. Taff and D.M. Jonuskis, "Results and Analysis of a Bi-Telescopic Survey of Low Altitude Orbital Debris," *Adv. Space Res.* **6**, 7, pp. 131-137 (1986).
2. A.E. Reinhardt, "Potential Effects of the Space Debris Environment on Military Systems," presented at Preservation of Near-Earth Space for Future Generations, University of Chicago (June 1992).
3. E.C. Pearce, private communication.
4. E.C. Pearce, private communication.
5. E.C. Pearce, M.S. Blythe, D.M. Gibson, and P.J. Trujillo, "Results of Stare and Chase Debris Search at the Experimental Test System," in *Proceedings of the 1993 Space Surveillance Workshop*, ed. R.W. Miller and R. Sridharan, MIT Lincoln Laboratory, Lexington, Mass., Project Report STK-206, Volume II, (1993) pp. 99-108.
6. E.C. Pearce, M.S. Blythe, D.M. Gibson, and P.J. Trujillo, "Recent Results of a Reacquisition Debris Search," presented at 31st Aerospace Sciences Meeting and Exhibit, American Institute of Aeronautics and Astronautics, Reno, Nevada (1993) AIAA 93-0161 (also available as MIT Lincoln Laboratory Project Report ETS-123 (10 May 1993))
7. P.W. Kervin *et al.*, "Orbital Debris Characterization Measurements at the Air Force Maui Optical Station (AMOS)," in *Proceedings of the 1993 Space Surveillance Workshop*, ed. R.W. Miller and R. Sridharan, MIT Lincoln Laboratory, Lexington, Mass., Project Report STK-206, Volume II, (1993) pp. 109-119.
8. D.M. Gibson, private communication.
9. R. Weber, "Large-format ebsicon for low light level satellite surveillance," *Optical Engineering* Vol. 20 No. 2, pp. 212-215 (March-April 1981).
10. D.J. Kessler, "Origin of Orbital Debris Impacts on LDEF's Trailing Surfaces," NASA Johnson Space Center, Houston Texas, CR (June 1992).
11. D.J. Kessler, private communication.
12. P.D. Anz-Meador, K.G. Henize, and D.J. Kessler, "The NASA Catalog of Adjusted U.S. Space Command RCS's," NASA Johnson Space Center, Houston Texas (1993).
13. W.P. Seniw, private communication.

## **An Active Imaging Technique that Attains Ultra-High Resolution with Ultra-Low Transmitter Power**

R. B. Holmes, A. MacGovern, A. Bhowmik, P. White, P. Idell  
(Rocketdyne Division, Rockwell International Corporation)

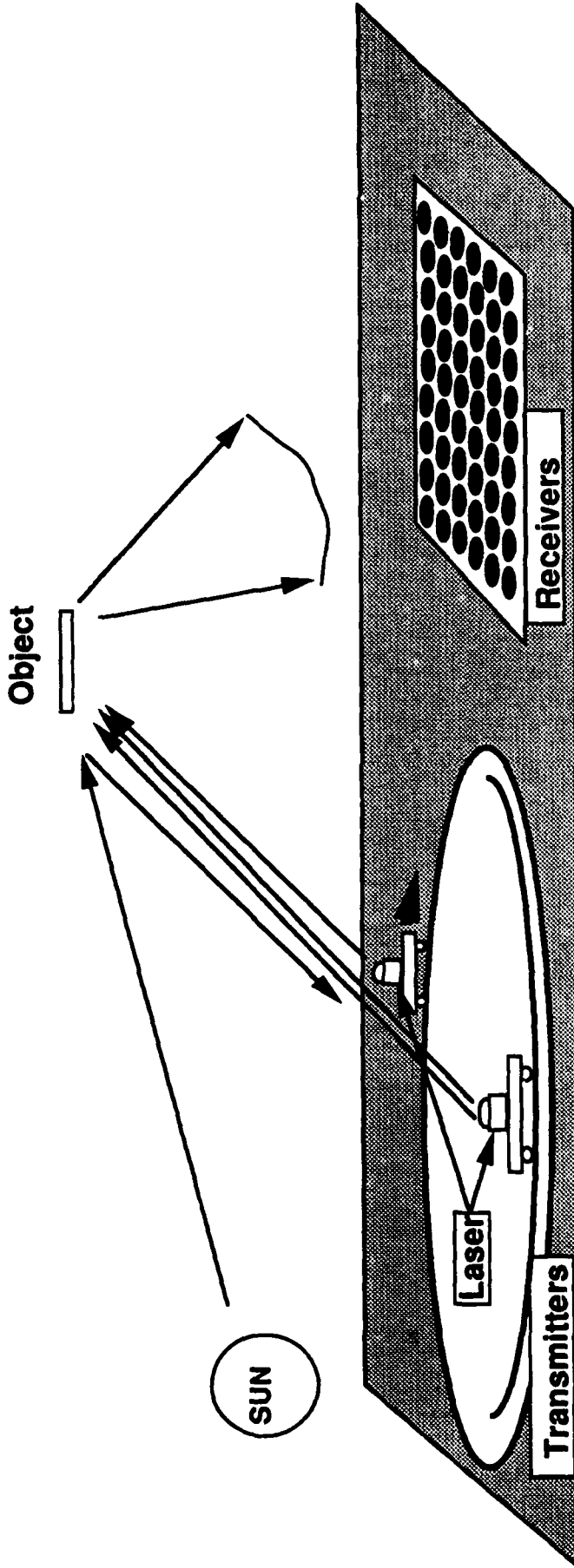
Active imaging techniques offer the promise of improved signal-to-noise ratios for imaging of distant objects. However, this promise has remained unfulfilled for satellite imaging because such techniques typically require relatively high-power illumination. High power is needed in order to obtain adequate signal over relatively small subapertures and short sampling durations; these limitations are set by laser speckle or by atmospheric turbulence. The proposed technique, referred to as Fourier Telescopy, largely overcomes these limitations by encoding the image information in the time domain. The basic approach combines long-baseline interferometry with phase closure to allow sampling at very low temporal frequencies.

This concept is a variant of Fourier microscopy, in which the object is illuminated by two relatively small sources, and the two waves interfere at the object plane to form a grating as shown in Figure 1. The object moves through the grating, or the grating may be made to move across the object by introducing a slight frequency shift on one source relative to the other. The resulting time-varying return signal is just the Fourier component of the object reflectivity, and may be collected by an extremely large receiver or receivers. By illuminating the object with many such pairs of gratings, the Fourier transform of the object is obtained, as illustrated in Figure 2.

Since this technique interferes two electric fields, it is a form of amplitude interferometry, and hence offers superior signal-to-noise properties relative to techniques based on intensity interferometry. The technique is the reverse of long-baseline interferometry, in which a single source illuminates and many apertures receive. Because the transmitters need not be contiguous, very high resolution is obtainable with this approach.

The Fourier Telescopy approach as described above will provide the magnitudes but not the phases of the Fourier components of the object. These phases depend on the phases of the transmitted gratings, which in turn depend on the phases in the atmosphere and the optics. The removal of these aberrations involves two key innovations of the Fourier Telescopy approach.

**FIG. 4. IMAGER INSTALLATION (GEO)**



**Transmitter:**

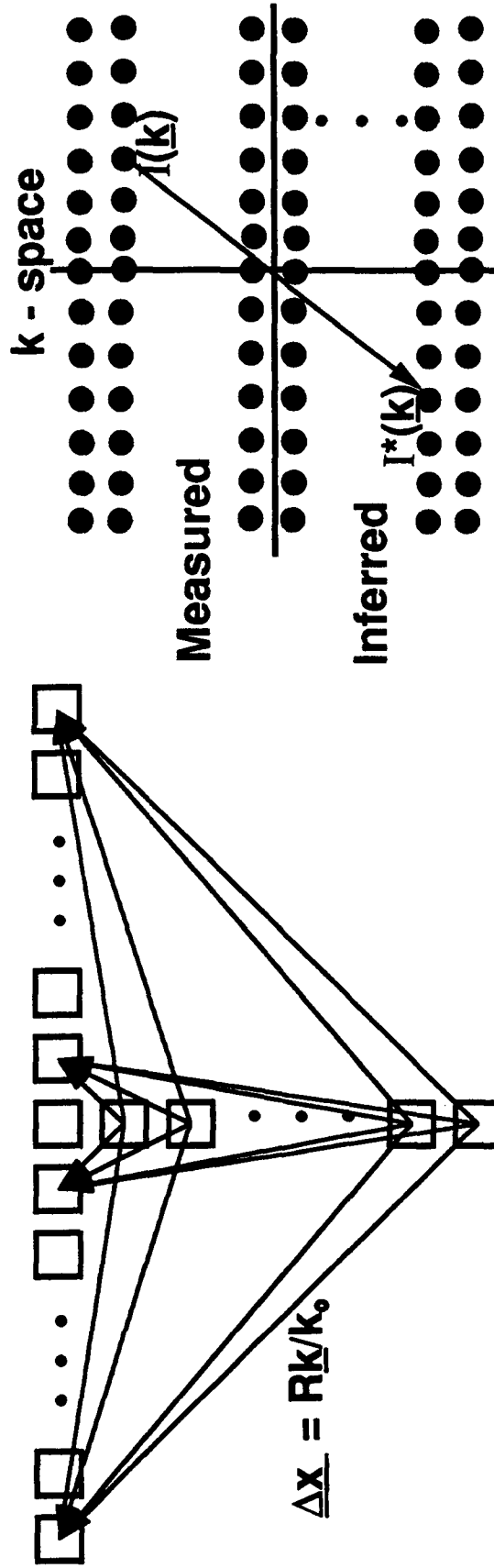
- Illuminator laser (20-1000 Watt ave power)
- Path match / frequency shift ( $\pm 2$  cm /  $\pm 500$  Hz)
- 2-3 Beam directors ( 2-3 apertures,  $\sim 1$  m diam)
- Atm. compensation (solar or AGS signal)
- Beam director translation (1.5 rings, 200 m radius)
- $\approx 50$  Hz track w/ solar signal

**Receiver:**

- $\approx 2400 \times 1 \text{ m}^2$  light buckets
- bucket size set by cost only
- Sum digitized signals
- Post-process
- Pre-run cal + mount model for pointing

**FIG. 2. SIMPLIFIED TRANSMITTER**  
**TWO 1-D TRANSMITTER ARRAYS GIVE FULL 2-D OBJECT SPECTRUM**

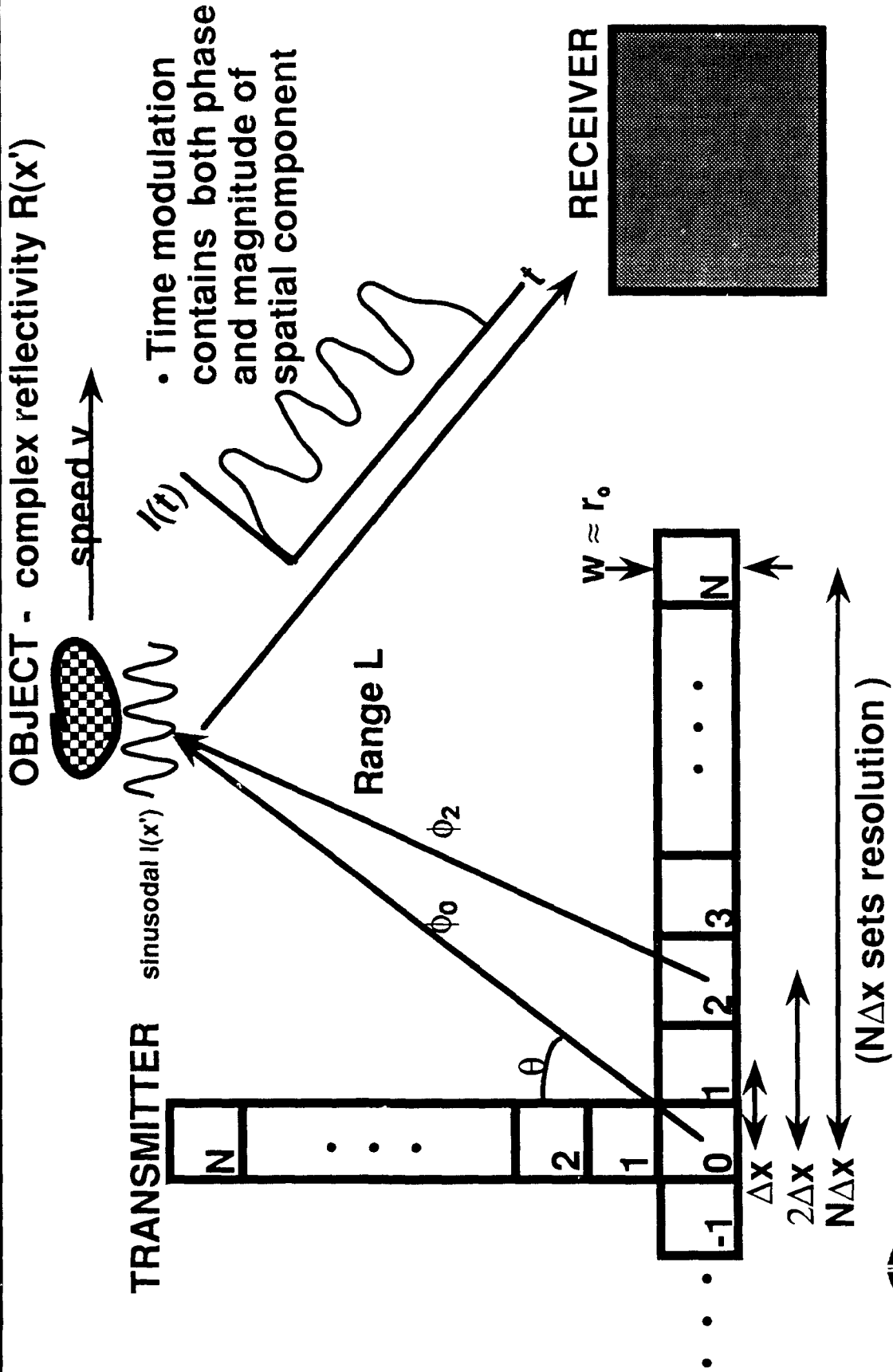
- Need an efficient method of transmitting all wanted gratings
- can use a simple "T" or ring transmitter configuration to get all components



- Fourier component of object radiance =  $I(\underline{k}) \approx M(\underline{\Delta x}) = R\bar{k}/k_0$
- object radiance = pure real, therefore  $I(-\underline{k}) = I^*(\underline{k})$
- therefore need only measure  $M(\underline{\Delta x})$  in half-plane of  $\underline{\Delta x}$
- Need to sequence and frequency-modulate the transmissions



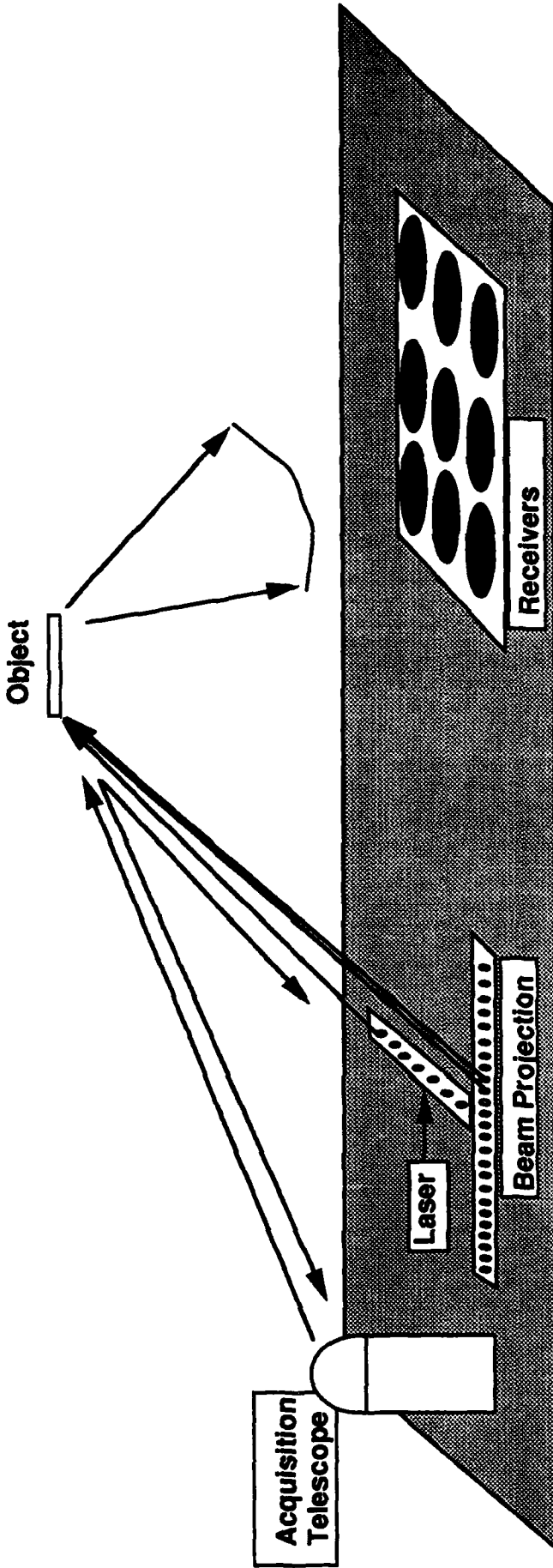
# FIG. 1. FOURIER TELESCOPE - SCHEMATIC



Most significantly, the use of a third, simultaneous transmission may be used to provide phase closure. The use of phase closure eliminates the effect of relative gross piston between the triplet of transmitters. In this way, virtually all phase effects are removed from the transmitters, and the phases of all gratings are relatively fixed. This innovation allows the recovery of the phase of a Fourier component provided the duration of transmission of the triplet is less than the aberrations' time constant. Once a Fourier component is recovered using this triplet, the effects of aberrations are eliminated; hence recovery of Fourier components need not be contiguous in time, and may be recovered at a rate which is convenient for the hardware and limited only by the allowable observation time. This innovation permits extremely low-average-power illumination.

To enable the first innovation, the phase variation across an individual transmitter must be on the order of a wave or less. This can be accomplished in one of two ways: either the transmitters can be made relatively small compared to the scale size of aberrations caused by the atmosphere and optics, or the the aberrations can be compensated. The former approach is well-suited for imaging of LEO objects, and is shown schematically in Figure 3. The latter approach is better for GEO and is shown in Figure 4. If the GEO system is as shown, with 3 x 1 meter transmitters that are compensated, with a 20 J dye laser that operates at 1 Hz, and with a 50 x 50 meter array of photon-bucket receivers, relatively high imaging Strehls may be obtained for realistic objects.

# FIG. 3. IMAGER INSTALLATION (LEO)



**Transmitter subsystems:**  
 Illuminator Laser ( $\leq 1$  kW)  
 Uncompensated, small transmitters ( $\approx 120 \times 10\text{cm}$ )  
 Acq / Coarse Track Telescope  
 Path Match / Frequency Shift ( $\pm 2\text{cm} / 10$  MHz)  
 Beam Switching (kHz rate)

**Receiver:**  
 $\approx 100 \times 1$  m<sup>2</sup> light buckets  
 - bucket size set by cost only  
 Sum digitized signals  
 Post-process  
 Pre-run cal + mount model for pointing



RH545

# Proposal of a Coherent Bistatic Radar Correlated by VLBI Technique

Tadashi Takano and Masanobu Yajima  
Institute of Space and Astronautical Science  
3-1-1 Yoshino-dai, Sagamihara, 229 Japan

## 1. Introduction

Space debris are monitored by USA (SSN), former USSR, ESA and occasionally Japan. Most of radars are monostatic, and dedicated for the detection of unknown objects in space. The new construction of radar stations and the extension of the radar network are quite difficult due to high cost and small operation-benefit in Japan.

This paper proposes a bistatic radar using coherent long pulses or a continuous wave modulated by PN-PSK signals for the purpose of space debris monitoring. The received radio wave is recorded in a VLBI recorder and processed by a VLBI correlator. The proposed system is shown to have several advantages.

The total system is designed and relevant technical problems are investigated. As a preliminary verification step, a satellite in a low-earth-orbit is irradiated, and received at the distance of about 1000 km. The down-converted and recorded radio wave has been successfully detected via VLBI technique.

## 2. Coherent bistatic radar system

### 2.1 System configuration

A bistatic radar system in which radio wave transmission and reception are pursued at different antenna stations is compared with a monostatic radar system in Table 1. In a bistatic system, a dedicated radar station is not needed. On the contrary, we can use a satellite tracking station as a transmission station and a radio observatory with quite a low noise temperature as a reception station. Those stations are more popular than radar stations especially in Japan, and scattered all over the world. Therefore, we can form a space debris monitoring network with much freedom and flexibility.

Table 2 shows the comparison between a short-pulse radar system and a long-pulse (including CW) system. The latter system can be coherent, and enables the synchronous detection of a signal carrier.

For that purpose, a bistatic system needs synchronization of two local

frequencies of a transmission station and reception stations. Nowadays, a broadcasting or a communications satellite can supply the reference frequency for two kinds of stations to generate their own local frequencies.

Down-converted radio wave is sampled by the sampling frequency  $f_s$  and one-bit quantized using VLBI receiver MK- III.

Above-mentioned system (Fig.1) has the following advantages:

- (a) Easy extension of monostatic radar systems to enclose receive-only antennas such as radio observatories or communication stations, because transmission-reception isolation is not needed and VLBI equipment is popular in these stations.
- (b) Easy modification of an originally communications or satellite tracking station to a radar transmission station unless the receiving capability is required.
- (c) Space debris detectability enhancement by means of modern communication technology
- (d) Possibility to obtain the shape information from different view angles of a space debris

## 2.2 Ranging scheme

In a long-pulse or CW radar system, ranging is performed using codes instead of a sharp pulse in a short-pulse radar system. Barker code is preferably used in dedicated radar systems. But in the proposed system., PN codes or tone ranging codes should be considered because of their popularity in satellite tracking stations.

## 2.3 Link calculation

Received radio wave level is calculated by Eq.(1):

$$P_r = P_t \cdot G_t \cdot L_{ot} \cdot L_s \cdot L_{or} \cdot G_r \quad (1)$$

where suffixes t and r represent transmission and reception, respectively,  $L = (\lambda / 4 \pi r)^2$ : free space loss,  $\lambda$ : wavelength, r: slant range,  $G = \eta 4 \pi A / \lambda^2$ : antenna gain,  $\eta$ : aperture efficiency, A: aperture area, and  $L_s = 4 \pi \sigma_s / \lambda^2$ ,  $\sigma_s$ : side-scattering cross section.

Assuming that  $P_t = 20\text{kW}$ ,  $T_r = 50\text{K}$ , Eq.(1) is analyzed for various  $r_{ot}$  ( $=r_{or}$ ) and  $\sigma_s$  to obtain Eb/No. The result is shown in Fig. 2.

## 3. Verification experiments

### 3.1 Objectives and experiment methods

Satellites in orbits are detected instead of actual space debris because the orbits are known in advance. Kagoshima Space Center with 10m and 20m

diameter antennas and Usuda Deep Space Center with a 64m diameter antenna, both of ISAS, are used as a transmission station and a reception station, respectively. The distance between two stations is about 1000 km.

Satellite tracking stations send the up-link radio wave to satellites, and the radio wave is modulated by PN codes in PSK-PM in ranging operation.

### 3.2 Observation of a circular-orbit satellite

Yohkoh is a scientific satellite in a circular orbit of 600 km altitude. Though the visible time is short for 13 to 15 minutes and the angular velocity is critically high to the 64 meter antenna at UDSC. But the satellite scatters back the radio wave at high level and is suitable for the first trial.

Table 3 shows the link budget for the experiment. The scattered wave was successfully received and stored in a magnetic tape using the Mk- III receiver and K-4 recorder. The spectrum of the scattered wave is observed with a spectrum analyzer in the intermediate frequency band.

### 4. Correlation detection using VLBI equipment

In a VLBI correlator, autocorrelation coefficient for a signal  $x_i$  is calculated by

$$R_k = 1/l_{max} \sum_{l=0}^{l_{max}-1} x_l \cdot x_{l+k}, \quad (1)$$

where  $k$ : lag number, and  $l_{max} = f_s \Delta_{pp} n_{pp}$  where  $f_s$ : sampling frequency,  $\Delta_{pp}$ : minimum integration time (1.049sec), and  $n_{pp}$ : the number of  $\Delta_{pp}$ .

The power spectrum is obtained by discrete Fourier transform from  $R_k$  as

$$S_l = \sum_{k=0}^{km} R_k \exp(-j \cdot 2 \pi l k / (km+1)), \quad (2)$$

where  $l$ : a frequency modulu.

Originally the lag number is limited as

$$km \geq k \geq -km-1, \text{ and accordingly, } km \geq l \geq 0, \quad (3)$$

where  $km=255$  in the case of k-4.

The newly designed VLBI recorder K-4 has 16 channels, and each channel has the maximum lag value of 512. We tried to connect all channels in series, and to obtain the maximum lag value of 8192. The off-line analysis of the received data was successful, and Fig. 3 (a) and (b) show the effectiveness of the lag connection. The frequency resolution is improved from 7812 Hz to 488Hz.

The signal-to-noise ratio of an one-bit quantized signal is expressed as

$$\frac{S}{N} = \frac{2}{\pi} \rho \frac{v \sqrt{N}}{\sqrt{b \beta}} \quad (4)$$

where  $\rho$  :correlation coefficient,  $v$ :spectrum line width of a signal,  
N:correlated bit number,  $b$ :frequency resolution,  $B$ :receiving band width.

And using the integration time  $t$ ,

$$N=2Bt. \quad (5)$$

The  $\rho$  is calculated by

$$\rho = \text{signal power/noise power.} \quad (6)$$

If  $v=100\text{Hz}$ ,  $b=7813\text{Hz}$ ,  $S/N > 3$ ,  $T_{\text{sys}}=100\text{K}$ , and  $t=50\text{sec}$ ,

$$\text{signal power} \geq -144\text{dBm} \quad (7)$$

By the lag connection, the detectable signal power is improved to  $-162\text{dBm}$ . The lag connection has been tried first time in this experiment.

Though the VLBI correlator is effective to process the data as stated above, better frequency resolution may be required in some cases. Then, off-line data processing by a large computer is indispensable.

## 5. Conclusions

(1)A bistatic radar with modulation on long pulses or a continuous wave for ranging is proposed for space debris monitoring.

(2)A receiver, a formatter and a recorder, all for VLBI, are used for reception and recording.

(3)A VLBI correlator is used for correlation analysis of a recorded signal, and the lag connection is accomplished to improve frequency resolution up to 488 Hz.

## References

(1)R.M.Goldstein and L.W.Randolph, "Rings of earth", IEEE Trans. MTT, vol.40, no.6, pp.1077-1080, June, 1992

(2)A.R.Thompson, J.M.Moran and G.W.Swenson, Jr., "Interferometry and synthesis in radio astronomy", Wiley-Interscience, 1986.

Table 1 Comparison between two radar systems

Items	Bistatic Radar	Monostatic Radar
Transmission /Reception Isolation	Terrain can be used	T/R switch is indispensable
Networking	Flexible with non-radar stations	Dedicated radar station is needed
Reference Frequency	Stations synchronization is needed	Single clock is sufficient
Reception Level	Weak due to side-scatter	Strong due to back-scatter
Data Processing	Needs data transmission to the center	Can be pursued in the site

Table 2 Comparison between two pulse schemes

Items	Long Pulse	Short Pulse
Detection	Correlation(Coherent)	Envelope (Incoherent)
Noise	Suppressed	Strong
Doppler Measurement	Possible	Impossible
Realtime Detection	Difficult	Easy

Table 3 Link budget of a scattered wave from Yohkoh

Item	Value	Note
Tx Output	50.0dBm	100W
T-Antenna gain	51.0dB	20m diameter
Free space loss	-164.9dB	Altitude 2000km
Scattering loss	27.8dB	RCS 1.0m <sup>2</sup>
Free space loss	-164.9dB	Altitude 2000km
R-Antenna gain	61.8dB	64m diameter
(SUM) Received power level	-139.2dBm	
Receiver noise power density	-179.9dBm/Hz	T <sub>sys</sub> = 75K
Band width	44.0dBHz	25kHz
S/N	-3.3dB	



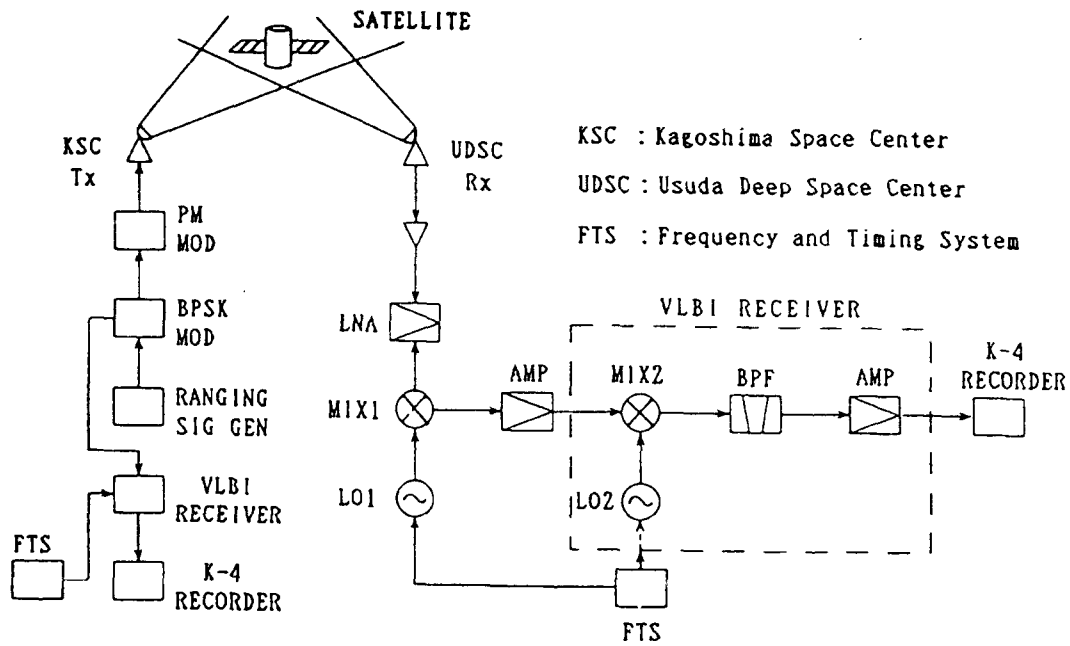


Fig.1 System configuration of the experimental bistatic radar

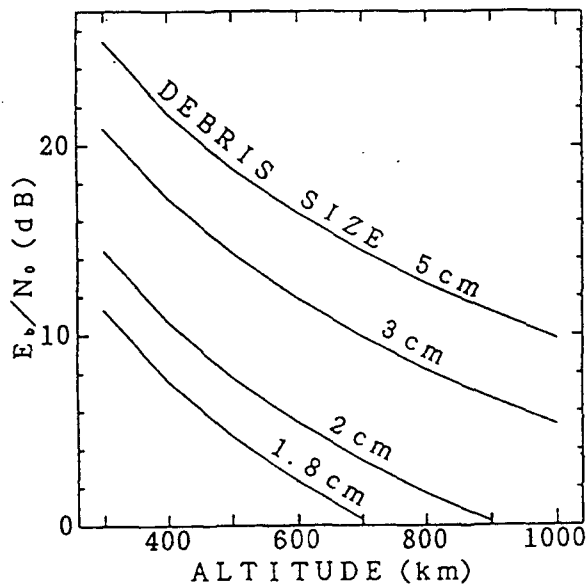
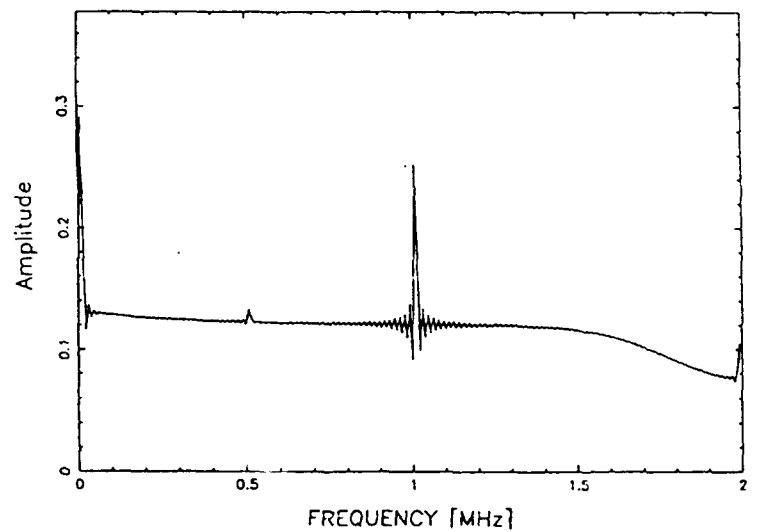
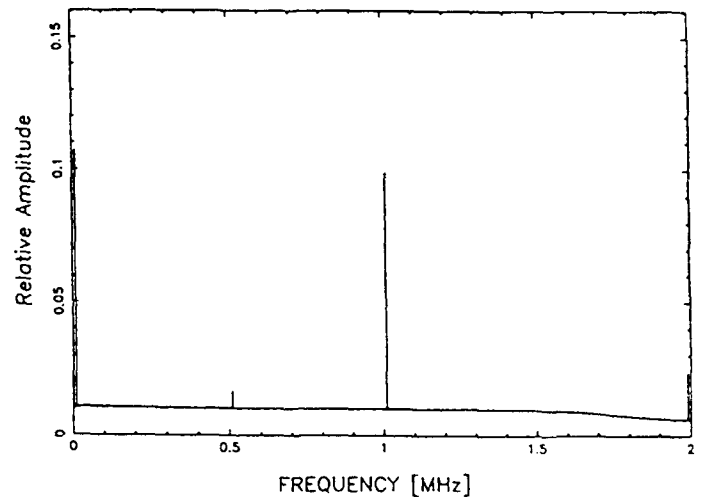


Fig.2 Altitude versus  $E_b/N_0$  for various sizes of a debris



(a) Maximum lag in a single channel (512)



(b) Connected lags of 16 channels (8192)

## Prospects for Observing Space Debris With Solar Coronagraphs

D.F. Neidig (PL/GPSS), E.E. De Luca (SAO/CFA), I.S. Kim (Sternberg State Astr. Inst., Moscow), S. Koutchmy (Inst. d'Astrophys., Paris), R.N. Smartt (NSO)

Solar coronagraphs appear to offer significant advantages over conventional telescopes for observing space debris of small size. By utilizing the albedo-independent, high sensitivity of coronagraphs for detecting particulates angularly close to the sun, it is shown that observed photon fluxes will be many orders of magnitude larger than for observations based on diffuse reflection (backscattering). This may result in signal-to-noise ratios sufficiently large to detect particles an order of magnitude smaller than can be detected via backscattered solar radiation using a conventional telescope with the same aperture as the coronagraph.

The coronagraph's sensitivity advantage becomes apparent by comparing, for a particle of diameter,  $a$ , the solid angles into which solar radiation is backscattered ( $\approx 2\pi$  sr) or forward-scattered ( $\approx \pi\lambda^2/a^2$  sr). The ratio of the photon fluxes observed at some distance, in these two cases, is, to a first approximation, simply the inverse of the ratio of the respective solid angles. Thus, assuming an albedo of 0.1 for the backscattered radiation, the forward-scattered photon flux therefore will be a factor of approximately  $20a^2/\lambda^2 \approx 10^{10}a^2$  larger, at visible wavelengths. The practical advantage of the coronagraph in terms of signal-to-noise ratio, however, is considerably reduced from this impressive value as a result of the bright background against which the coronagraphically-observed debris must be detected. For observations made from the ground at visible wavelengths, the background solar corona, sky brightness, and instrumentally-scattered light combine to produce a background  $10^8$ - $10^9$  brighter than the nighttime sky background. For observations made from space the sky background (the largest of the three contributors in the visible and near-IR) is absent. In the following, we compare signal-to-noise ratios as a function of debris diameter, for coronagraphs observing forward-scattered solar radiation near the solar limb, with conventional telescopes of identical aperture and throughput observing backscattered solar radiation against the night sky. We consider both ground-based and space-based situations.

For the ground-based coronagraph we assume a 2-m aperture and compute the debris signal in stare-mode using (1) the flux of scattered photons in the point diffraction pattern, integrated over the solar disk, at an angular distance 0.3 solar radii (288 arcsec) outside the solar limb, (2) debris orbital altitude and distance 500 km, with corresponding velocity 7.6 km/s which results in a 1-arcsec pixel crossing time  $3 \times 10^{-4}$  s, (3) a 0.1  $\mu$  bandpass centered at 1.6  $\mu$ , which, as compared to visible wavelengths, offers reduced sky background for the coronagraph, and (4) a deep-well near-IR array detector with 1-arcsec pixels and read-out noise  $10^3$  electrons/pixel. We assume the system optical efficiency and the detector quantum efficiency will each be 50%. This instrument will collect a total background signal  $2.7 \times 10^8$  electrons/s/pixel with noise equal to  $[\text{background}]^{1/2}$  plus read-out noise. Relatively short exposure times ( $\leq 0.1$  s) are therefore required in order to avoid detector saturation. Any exposure time shorter than 0.1 s, but longer than the pixel crossing time, will suffice for the space debris observations.

For the conventional telescope we assume a 2-m aperture and compute the debris signal in stare-mode using (1) the flux of backscattered photons from a debris surface with albedo 0.1, (2) a cooled CCD detector with 1 arcsec pixels operating in a band 5500-7500  $\text{\AA}$ , with read-out noise 5 electrons/pixel, and (3) the same debris altitude and velocity as above. The background

signal for this nighttime observation is 38 electrons/s/pixel with noise equal to  $[\text{background}]^{1/2}$  plus read-out noise. For very short exposures the noise will be dominated by read-out noise.

Figure 1 compares the signal/noise ratios for both of the described instruments. The 0.001-s exposure limits the length of the debris tracks to  $\leq 3$  pixels in length. For these very short tracks, it is reasonable to adopt as a detection limit a per-pixel S/N ratio equal to 1. In this case the coronagraph should, in principle, be able to detect debris down to about 0.1 cm in diameter—a factor of about 20 smaller than the conventional telescope's nighttime limit for an identical exposure. The detection limits of both instruments, however, can be lowered by increasing the exposure times to acquire longer tracks. The per-pixel S/N ratio is then somewhat decreased by the increased background signal, although the debris signal, now being deposited on the resulting larger number of pixels, can be used to advantage through application of appropriate extraction algorithms. If, for example, the coronagraph exposure is pushed close to the 0.1 s saturation limit (giving a debris track 100 times longer), the per-pixel S/N detection limit will be reduced by a factor  $100^{1/2}$ , to 0.1, corresponding to debris diameter 0.05 cm. The same procedure works even better with the nighttime observation, where saturation by the background is not a problem. In this case the stare-mode exposure could be increased even to equal the detector field-of-view crossing time ( $\approx 1$  s). This would provide a debris track 1000 times longer, reducing the per-pixel S/N limit to 0.03. The corresponding limit on debris diameter would be 0.5 cm. Of course, with the low background signal, there is nothing to prevent the conventional telescope from realizing further improvements by employing quasi-tracking and even longer exposures. In general, the acquisition of debris tracks of intermediate length, in stare-mode operation, is important as a means of measuring debris angular velocity.

If we make the debris observations from space, we find that both techniques benefit from the absence of sky background. In the following, we compare two instruments of 20-cm aperture, both observing in the 5500-7500 Å range with the same CCD detector as assumed above for the ground-based conventional telescope. The saturating exposure for the coronagraph, assuming a deep CCD well of approximately  $3 \times 10^5$  electrons/pixel, is again 0.1 s, which is determined by the background corona and instrumentally-scattered light. The conventional telescope observing debris via backscattering will encounter no background at all, so that the only noise will be the CCD read-out noise. The assumed debris target is at distance of 100 km and moving at 1 km/s across the line of sight (1-arcsec pixel crossing time  $4.8 \times 10^{-4}$  s). Figure 2 shows the expected S/N ratios for 0.01-s and 0.1-s coronagraph exposures, and, for the conventional telescope, an exposure of any duration greater than the pixel crossing time. The coronagraph's detection limit, based on  $S/N=1$  in each pixel, is 0.03 cm diameter for the 0.01-s exposure, or a factor of 100 smaller than the limit for the backscattering observation. However, this advantage is greatly reduced if the limits are based on track detection instead of per-pixel detection. The 0.1-sec coronagraph exposure provides a debris track  $\leq 200$  pixels, so that, assuming track detection, the per-pixel S/N ratio can be set a factor  $200^{1/2}$  lower; this would result in a limit of 0.02 cm diameter for the observed debris. The backscattering observation, on the other hand, suffering no penalty for increased exposure time, is able to acquire a full 2000-pixel track at no expense of noise. The per-pixel S/N ratio can therefore be set at 0.001, corresponding to a debris diameter 0.1 cm—a factor of 5 larger than the coronagraphic limit.

Several small-aperture coronagraphs have already been flown in space. Although the objectives of these experiments were to observe the solar corona, and the instruments optimized for this application, a number of debris detections were made. Schuerman et al. (1977) reported

numerous such detections, the majority of which were particles in the vicinity of the Skylab module. Additional reports (unpublished) have noted debris detections by the Solar Maximum Mission coronagraph experiment. A somewhat larger aperture (10-cm) space coronagraph is currently under development by the Smithsonian Astrophysical Observatory and the National Solar Observatory, as part of the Space Weather and Terrestrial Hazards (SWATH) mission. The latter experiment, initiated in 1993 under funding by the Ballistic Missile Defense Organization and administered through the Phillips Laboratory, includes several instruments for simultaneous visible light and x-ray/EUV observations of the corona. The SWATH coronagraph, with a sensitivity nearly two orders of magnitude greater than previous space coronagraphs, will be operated in a mode designed to detect orbital debris.

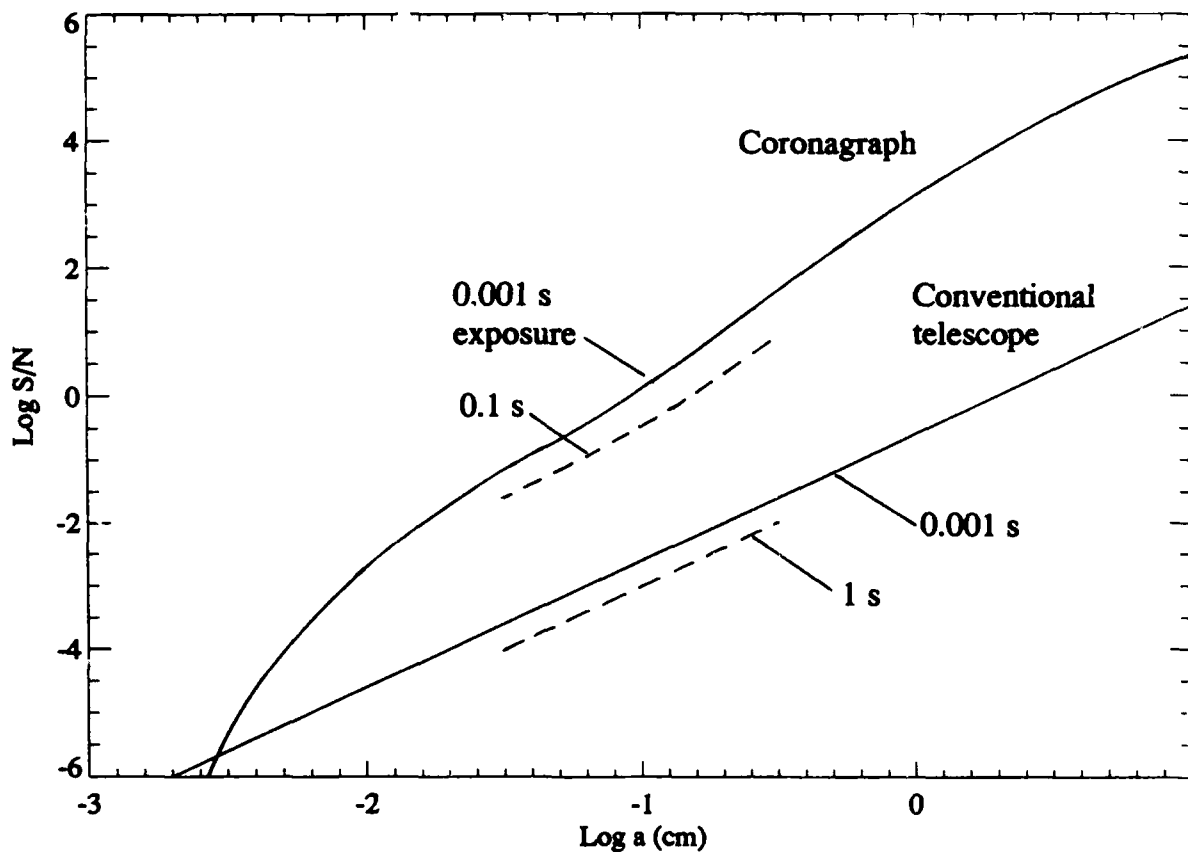


Figure 1. Per-pixel signal/noise ratio as a function of debris diameter. Compared are a 2-m ground-based coronagraph observing debris in 500-km orbit at an angular distance 0.3 solar radii outside the solar limb, and a 2-m ground-based conventional telescope observing the same debris at night.

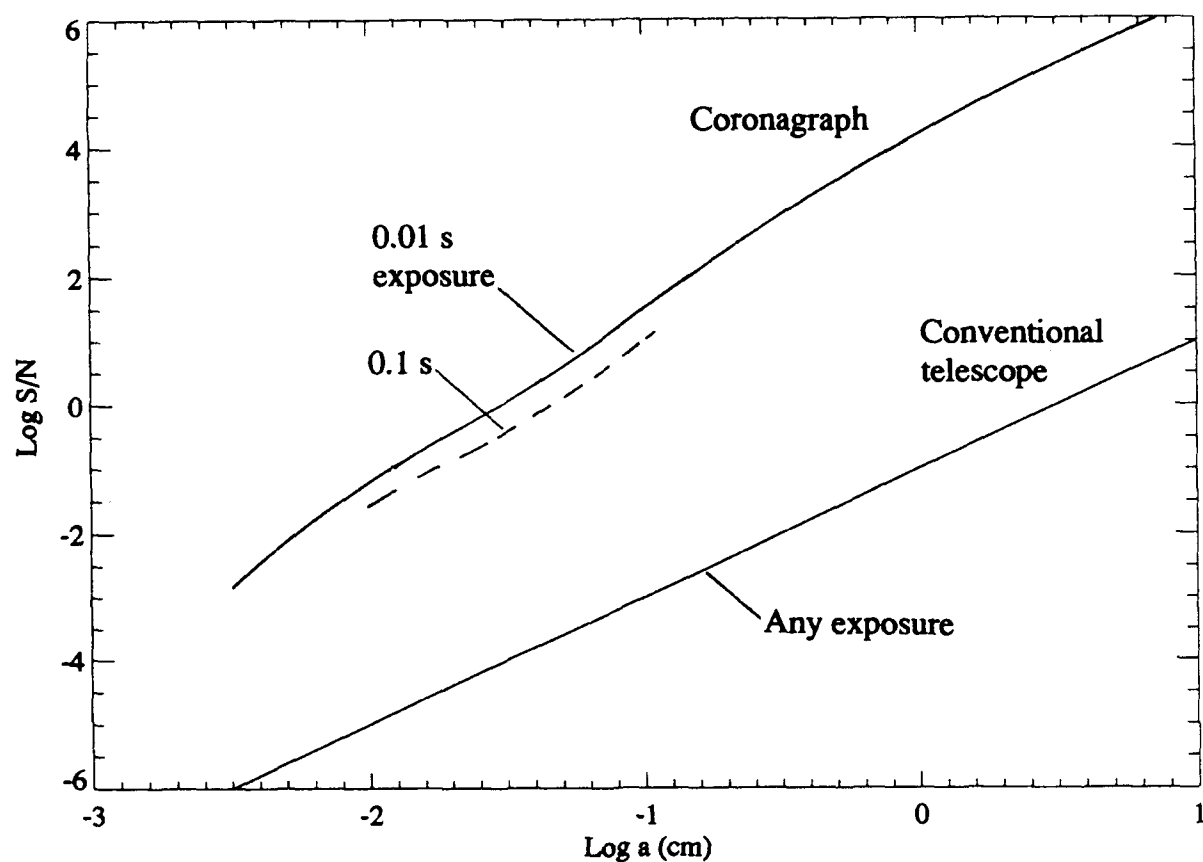


Figure 2. Per-pixel signal/noise ratio as a function of debris diameter. Compared are a 20-cm space-based coronagraph observing debris 0.3 solar radii outside the solar limb at distance 100 km and moving 1 km/s across the line of sight, and a 20-cm space-based conventional telescope observing the same debris via backscattered radiation.

Several important considerations relating to either ground-based or space-based coronagraphic observations of debris are noted here. First, coronagraphs must necessarily operate in a stare-mode, as the instrument must remain pointed at the sun at all times. Some quasi tracking can be achieved, in principle, by effectively moving the focal plane detector. However, because the bright background observed by the coronagraph readily saturates the detector, this focal-plane tracking can be used only to a limited extent, unless there is a vast improvement in detector read-out rates. In any case, orbital elements will not be obtained, and the data would be useful primarily in statistical studies of the debris population. Second, the S/N calculations presented here are based on diffraction from ideal particles (circular disks). Actual debris is more likely to have irregular shapes and rough edges, requiring revised models for the diffraction patterns used in calculating the debris signal. However, periodic glint reflection from plane surfaces on some irregularly-shaped, slowly rotating debris (a likely scenario), could enhance detection probability compared with that of a smooth sphere. Third, subtraction of the sky

background may prove difficult, as the terrestrial atmosphere contains small, moving particulates producing a transient and spatially variable background signal. Reasonable discrimination between such traces and those of debris might be possible on the basis of typical velocities of orbital debris and the typical direction and fast transit times of nearby particles under strong wind conditions, or random and nonlinear traces under quiescent conditions.

In summary, we suggest that the use of coronagraphs, either on the ground or in space, appears to offer an excellent prospect for space debris detection. Any factor,  $F$ , by which the limiting size of observable debris can be reduced will, as a consequence of the power-law distribution of the debris population, result in an increase in debris detection rate by a factor  $\approx F^{1.6}$ . The coronagraph's measurements are independent of albedo, and the advantages that stem from its unique characteristics are manifested in a debris size range not easily observed by other means.

Schuerman, D.W., Beeson, D.E., and Giovane, F.: 1977, *App. Opt.* **16**, 1591.

## The AEOS 3.67 m Telescope and Facility

S. Tapia (LL & PL/LIMA), I. A. De Larue (PL/LIMI), D. Forrester (S Systems Co.), R. A. Frosch (PL/LIMA), T. Jakab (Contraves Inc.), K. Kern (USAF & PL/LIMA), D. Kuo (USAF & PL/LIMM), D. Mooney (Contraves Inc.), R. Richmond (Rockwell Power Systems), S. Smith (Contraves Inc.), K. Zeringue (USAF & PL/LIMA)

### Background

Projected as an upgrade for the Maui Space Surveillance Site (MSSS), the Advance Electro-Optical System (AEOS) telescope is scheduled to start operations in 1997 on the summit of Mt. Haleakala, 3050 m above sea level. Considering only the light gathering power, this new sensor will increase by a factor of 5.8 the existing capabilities of the Air Force Maui Optical Station (AMOS). The program to acquire and install AEOS has been tasked to Phillips Laboratory, Kirtland AFB, by a congressional directive to the Air Force under the Space Track Program Element. The telescope requirements stem from Space Object Identification Statement of Need (SOI SON) 14-89. Generation of the operations concept, the operation requirements document, and the system "A" specification, is the result of continued coordination between Phillips Laboratory and US/AFSPACECOM. Although this new telescope is specialized for space surveillance and atmospheric sciences, observing time will be available to research projects from academia.

### Telescope

Fabrication of the telescope was contracted to the Electro Optical System Division of Contraves Inc. in December 1991. The main design of the telescope, presented in Figure 1, is an elevation over azimuth mount. The primary mirror is a Zerodur pseudo meniscus substrate produced by Schott, Germany, and provided as Government furnished equipment. The pseudo meniscus is 0.16 m thick by 3.67 m in diameter, with a central hole of 47 cm. In order to preserve optical quality the clear aperture has been limited to 3.63 m diameter with a 50 cm central obscuration. The optical figure of the primary mirror will be a paraboloid with F/1.51 focal ratio. Preservation of the optical figure of the primary will depend on 84 active supports placed on the back of the mirror and 48 lateral supports, following the concept developed by Schwesinger (1991). The force commands to the supports will be derived from a front figure model consistent with the image quality, as determined by a wave-front sensor. A data base of periodic re-calibrations of the front figure model will be used to provide frequent updates of the forces applied to the supports.

Two secondary mirrors of 25.0 cm clear aperture will be available to provide two alternative optical systems. The main optical system, in essence a Coudé system, is characterized by F/200, a 0.3 mrad full field of view (FFOV), and a focal plane located at the base of the telescope pier. The second optical system is a Bent Cassegrain system which employs the tertiary mirror centered at the intersection of the elevation and azimuth axes. The Bent Cassegrain system is described by F/32, a 1 mrad FFOV, and a focal plane located 1.15 m outside the trunnion to which the primary mirror cell is attached. The tertiary mirror can direct the beam to any of the two directions of the elevation axis (Nasmyth 1 and 2 locations) as well as any of four symmetric instruments ports located in the trunnion. One of these ports will be used by the wave-front sensor employed in the calibration of the active support of the primary. A key feature of these optical systems is that they can be fully integrated with other subsystems, such as adaptive

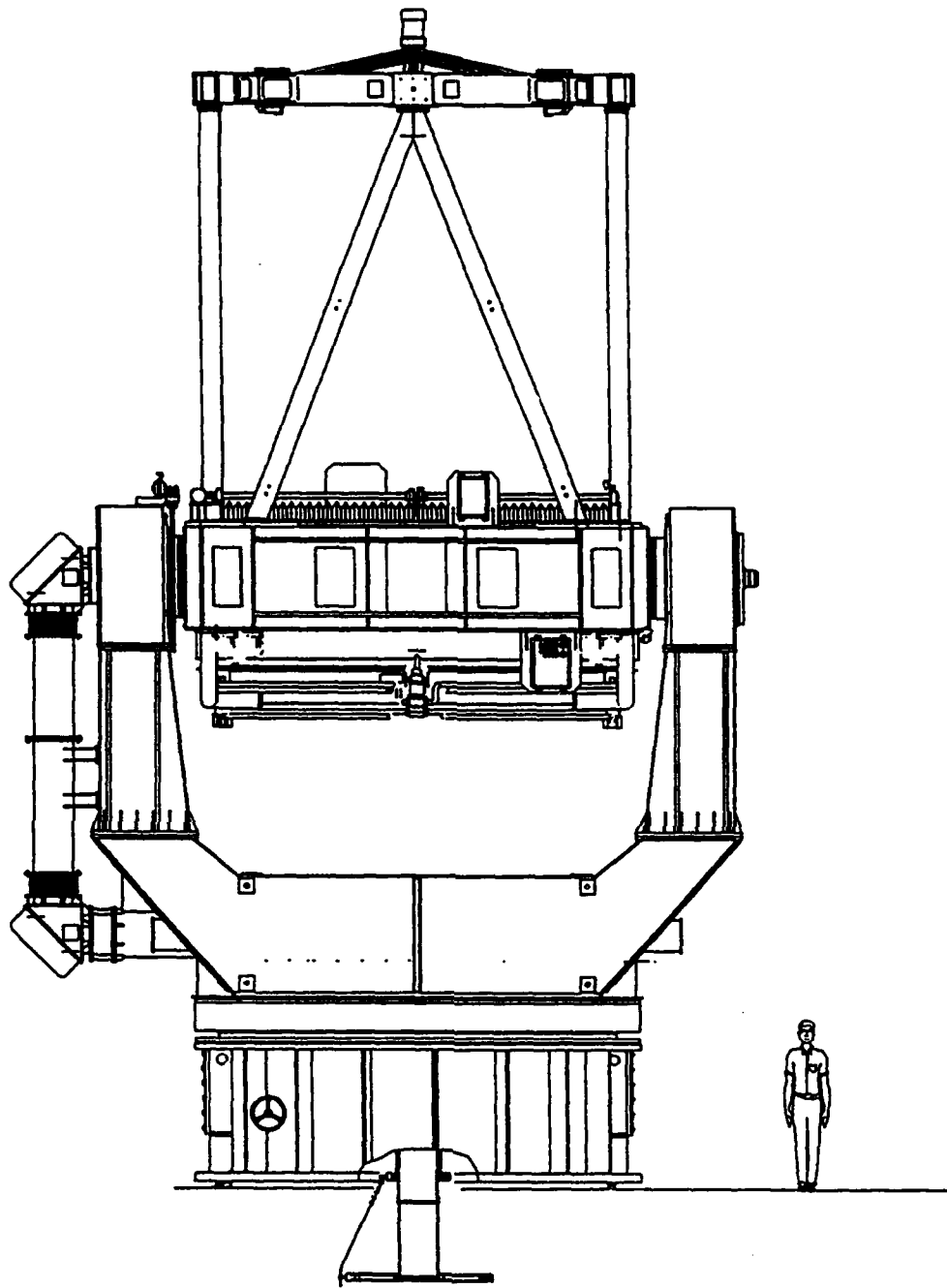


FIGURE 1.



optics (AO). The flexibility of the active primary mirror can be made to work in concert with an AO system.

The schematic drawing of the Bent Cassegrain optical system presented in Figure 2 shows the tertiary mirror sending the beam to one of the six instrument ports available on the telescope mount: the two Nasmyth positions and the four trunnion ports. The distances between the different mirrors are: between the vertex of the primary and the secondary, 5.09 m; between M2 and M3, 4.25 m; between M3 and M4, as well as between M5 and M6, 3.61 m; between M4 and M5, 3.76 m. The beam footprint of the 1 mrad FFOV at the focal plane is 11.63 cm in diameter. Table I provides the calculated aberrations at the edge of the FFOV.

Table I.- Seidel Aberration Coefficients  
for the Bent Cassegrain Focus.

Spherical aberration	none
Coma	-0.11 $\mu\text{m}$
Astigmatism	0.10 $\mu\text{m}$
Field Curvature	1.95 $\mu\text{m}$
Distortion	-0.02 $\mu\text{m}$
Axial color	none
Lateral color	none

The main or Coudé optical system is presented in Figure 3. The distance between M6 and M7 is about 19.48 m. The distance between M6 and M7 was dictated by the need to operate the telescope above the boundary layer. During the local trade winds the boundary layer will be below the telescope for about 80% of the time. The distance between M7 and the focal plane is 14.98 m. The footprint of the 0.3 mrad FFOV at the focal plane is 21.79 cm. At the edge of the field the Seidel coefficient for field curvature amounts to 0.18  $\mu\text{m}$ ; coma, astigmatism, and distortion are less than 0.01  $\mu\text{m}$ ; without spherical aberration and color. Both optical systems were design to preserve the freedom of the user to optimize a particular focal ratio. Consequently, different users can provide their own imaging optics.

Mounted on the sides of the AEOS telescope there will be two acquisition telescopes. A 0.20 m refractor telescope will provide a FFOV of 2.7 degrees, while a 0.58 m reflector will provide two, interchangeable, FFOVs of 0.45 and 0.125 degrees.

The original optical design calls for an aluminum coated primary mirror and M2 to M7 coated with silver under a protective overcoating (one of such coatings is known as Denton FSS-99). Based on the spectral reflectance of these coatings it is estimated that the telescope throughput at the trunnion ports will be about 87% at 500 nm, 83% at 800 nm (wavelength of the depression in the aluminum reflectance), and reach 97% from 2.5 to 40  $\mu\text{m}$ . At the Coudé focus, without adaptive optics, the throughput will be about 82% at 500 nm, 76% at 800 nm, increasing to 94% between 2.5 and 40  $\mu\text{m}$ . Introducing the adaptive optic components and a conservative number of components in the associated optical interface, the upper limit to the throughput will be about 60% at 500 nm, 59% at 800 nm, and 80% between 2.5 and 40  $\mu\text{m}$ . The throughput would increase by about 5 to 10% in the visible and near infrared regions if the primary were coated with silver. For this reason, and since application of silver coating is significantly less expensive than aluminum coating, at the request of Phillips Laboratory, Contraves Inc. is investigating the

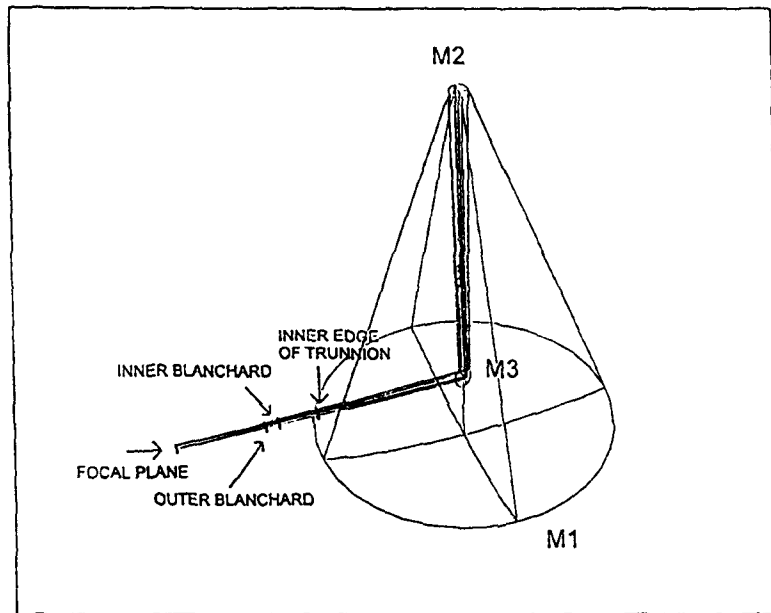


FIGURE 2.

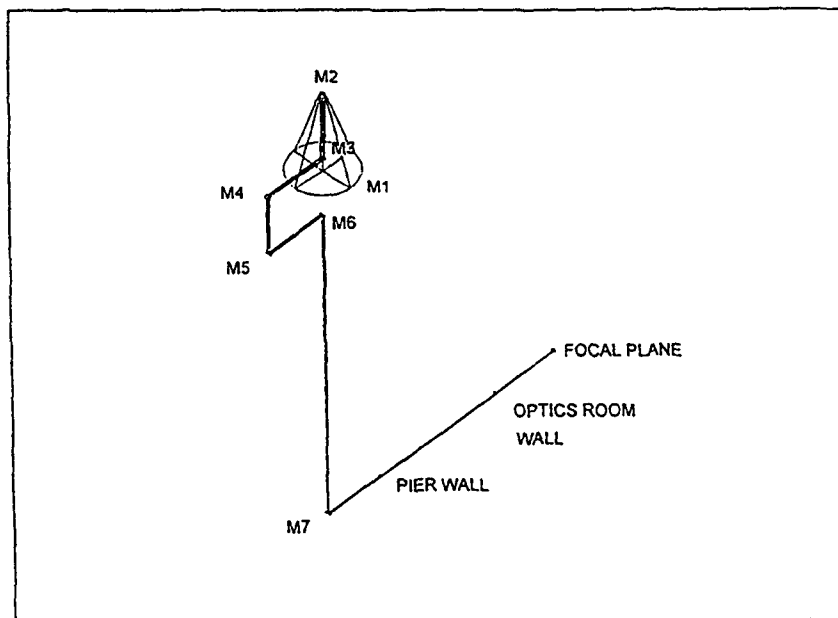


FIGURE 3.

rate of deterioration of silver coating in the environment of the Haleakala summit. A decision on the definitive type of coating for the primary mirror awaits the results of that investigation.

### Facility

Figure 4 displays the elevation profile of the telescope pier and the surrounding building facility. A concrete slab of 36.58 m in diameter will be the foundation of the telescope pier. Under the 1st level of the pier this slab is 2.13 m thick. Its size: complies with structural norms to withstand the type of seismic wave provable on the summit of Mt. Haleakala; it is consistent with the need to provide sufficient mass to resist the inertia of the telescope azimuth motion during an emergency stop; and, it meets the requirements for the stability of the pier. The floor plan of the 1st level is presented in Figure 5. In this figure the 1st level of the pier is represented by the two central octagons connected with radial walls. All the walls at the base of the pier are made of concrete: 45.7 cm thick in the external octagon; 30.5 cm thick in the internal octagon and the radial walls. The space enclosed by the central octagon, or Coudé room, is concentric with the azimuth axis of the telescope and its floor area is circumscribed by a 7 m diameter circle. The last mirror of the Coudé optical system, M7, will be located at the center of the Coudé room, about 1.37 m above the floor. Seven of the surrounding sectors, or optics rooms, have been set aside for installation of observing instrumentation. The beam from M7 to the optics rooms will pass through a 91 cm diameter aperture. This aperture will be fitted with metallic mounts to attach an optical window or components of imaging optics. The floor area of each optics room, as well as the Coudé access room, is about 37.8 m<sup>2</sup>.

Direct support of the telescope is provided by a truncated cone of steel plates resting on the concrete structure of the 1st level. Thus, the pier is formed by the foundation slab, the concrete 1st level, and the cone of steel plates. The entire pier is surrounded by a concentric building. Both structures are completely detached. On the 1st level of the surrounding building there are eight rooms, the experiment rooms, which are a geometric extension of the optics rooms and where additional observing instrumentation can be installed. The optical beam can reach the experiment room through an aperture identical to that placed in the walls of the Coudé room. Experiment rooms 2 to 6 have about 72 m<sup>2</sup> of floor area.

Considerations of security for this facility will follow three main requirements. First, access to the different rooms will be controlled with a card reader system. Second, common areas, as the corridors and the facility entrance, will be generally accessible. Third, it will be possible to perform diverse activities in adjoining rooms.

An optional 2nd level of the surrounding building is under consideration. Its floor plan will be very similar to the floor plan on the 1st level. On top of each experiment room there would be a matching room, or laboratory, suitable for the installation of computers or other electronic equipment. Depending on the availability of the 2nd level, the telescope control room will be located above the assembly area of the 1st level, or in an extension of the assembly area beyond the corridor.

At the height of the 3rd level the structure of the surrounding building is limited to the supports of the dome and the telescope floor, although room to store special equipment will be available between the pier and the dome supports.

Enclosing the AEOS telescope there will be a dome very similar to the dome currently in operation at the Starfire Optical Range of Phillips Laboratory, Kirtland AFB. As shown in Figure

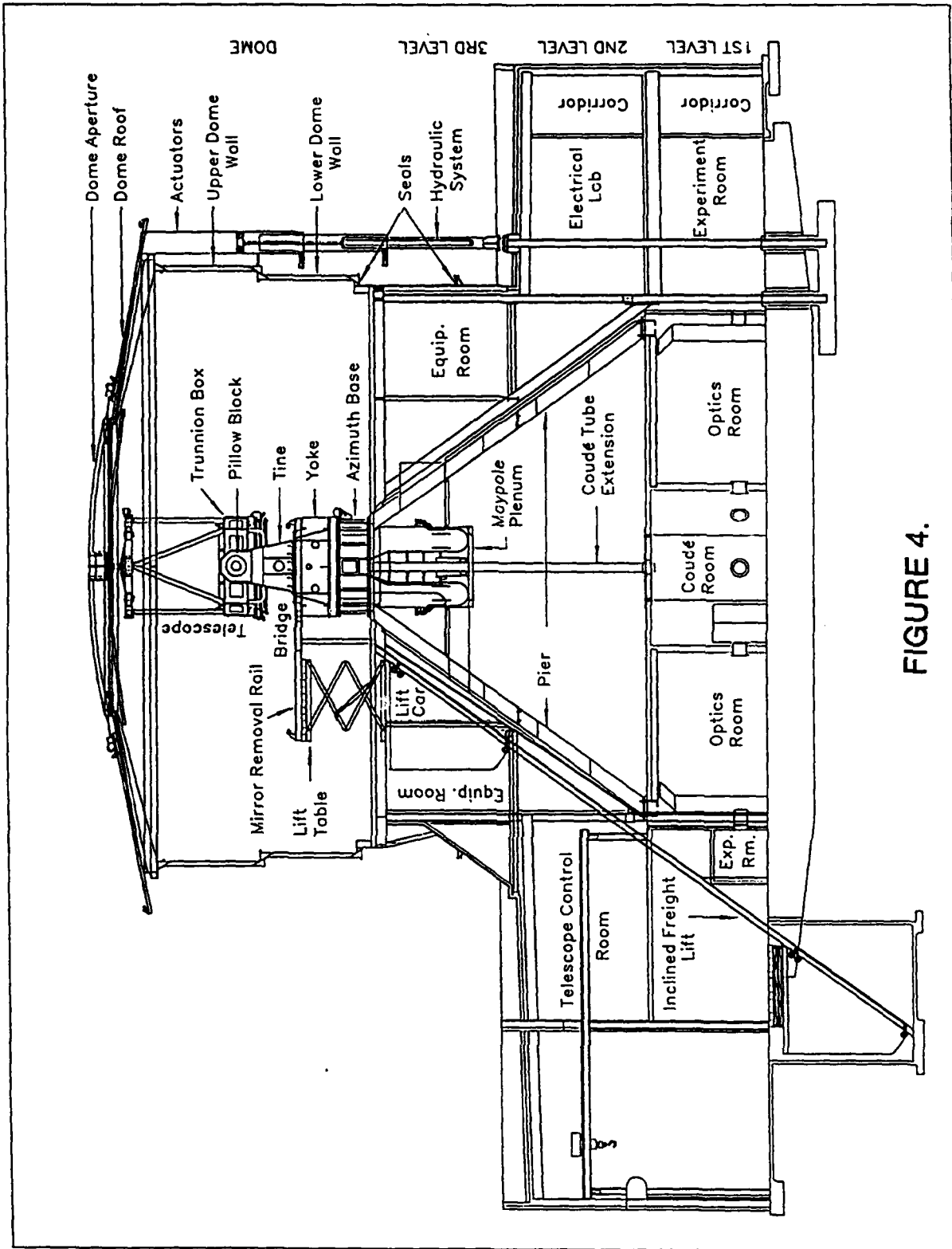


FIGURE 4.

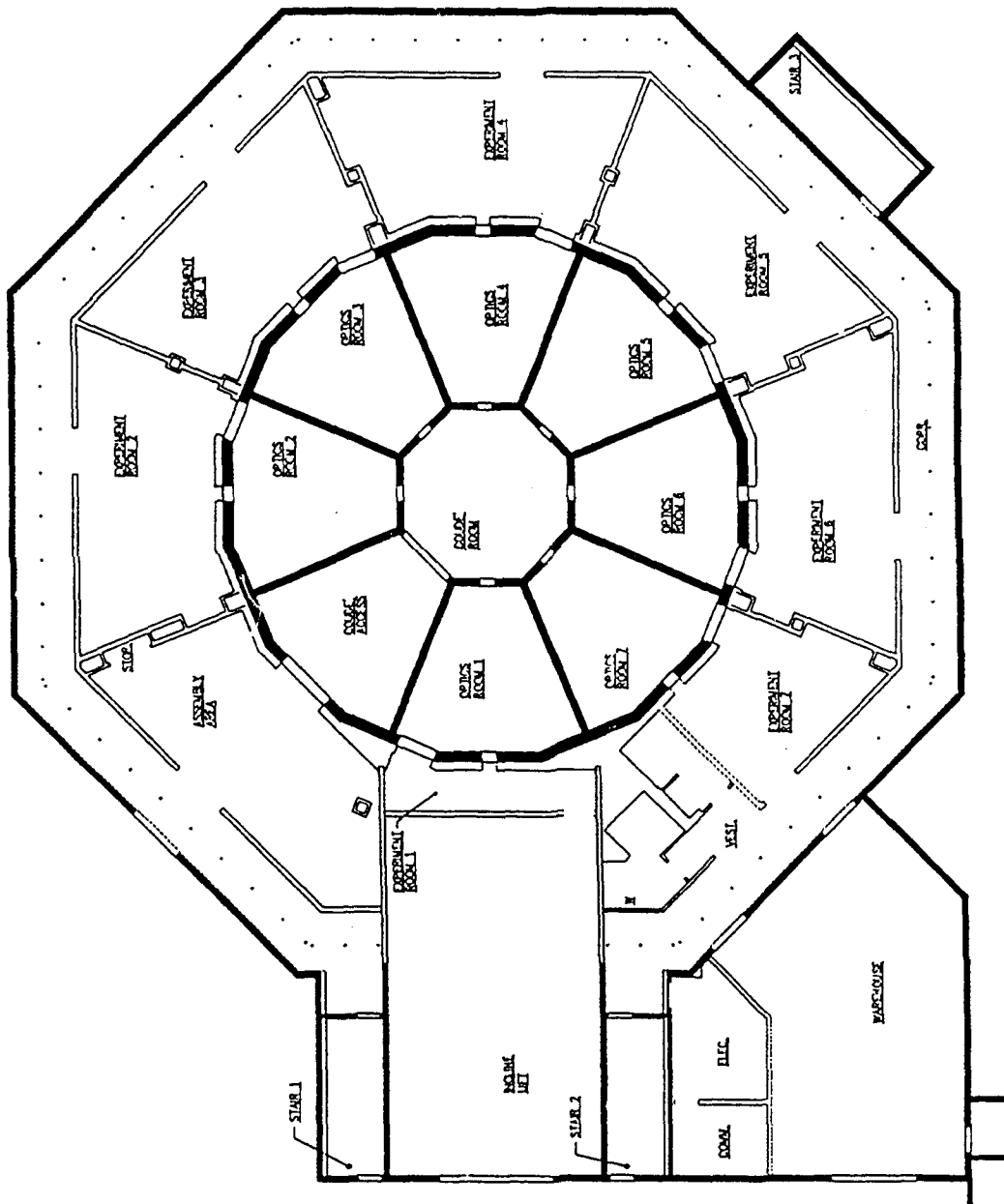


FIGURE 5.

4, the dome will be a retractable structure with a central aperture on the top. The size of the aperture will allow unrestricted retraction even when the telescope is pointing to the horizon. Two shutter halves, provided with sliding motion over the top of the dome, will be used to close the central aperture. During retraction the upper wall of the dome slides down over the lower wall. Eight equidistant hydraulic actuators will move the upper part of the dome during retraction and elevation. A backup pneumatic system will allow emergency operation of the hydraulic actuators in the event of a power system failure. With the dome completely retracted the telescope can point to targets in the full upper hemisphere, and as low as 5 degree below the horizon, without dome rotation and the associated vibration.

In order to provide access of heavy loads to the telescope floor, the surrounding building will have an inclined freight lift. The transporter of this lift was sized to accommodate the primary mirror in its cell in the horizontal position. The inclination angle of the lift matches the angle of the truncated cone of steel planes in the telescope pier. Following stability requirements for the operation of the telescope, both structures will be detached.

### Controls

A block diagram of the AEOS control system is presented in Figure 6. The system will be hosted on several VME crates along with a Sun Workstation serving as a user interface. Major subsystems are: the Gimbal Control Processor (GCP); the Telescope Processor (TP); the Telescope Electronics Control Processor (TECP); and the User Computer (UC). All the subsystems will be tied together through a shared memory network as well as through Ethernet. The GCP is responsible for the movement of the mount with a pair of digital signal processors controlling the azimuth and elevation motor inductosyn with readouts from a 25 bit encoder (corresponding to a resolution of  $0.15 \mu\text{rad}$ ). The TP will contain algorithms to determine the position, velocity, and acceleration of the mount while tracking a satellite pass. The corresponding values are then transferred to the GCP. The TECP will have access to the controls of the chopping secondary, the primary figure system, and the movement of the tertiary. The AO computer, as well as the different sensor computers will be integrated with the AEOS control system by sharing data over the same real time network.

In order to track low earth orbit satellites and suborbital targets, the gimbal will be able to move at 18.3 degree per second in azimuth and 4.75 degree per second in elevation. During a typical satellite track, a NORAD two line elements set is loaded into the TP at the start of the pass. The elements set is converted into an earth center inertial state vector. Upgrades to this vector employ a third order Runge-Kutta two body orbit propagator. The state vector is then transformed into local telescope coordinates accounting for any mount model errors. At this stage, position and velocity coefficients are calculated and sent to the GCP which then moves the gimbal. The tracking system will also operate at sidereal rate as well as from ephemerides tables.

The AEOS control system will be linked with the Observatory Control System (OCS) currently under implementation at the MSSS. Composed of a network of Unix workstations and VME based processors, OCS will be involved in various functions as mount control, sensor operation, data analysis, and mission planning. Multiple operator consoles, in an integrated operations center, will allow a single operator to access various functions throughout the observatory from a single terminal. Command and control will employ a low bandwidth network (Ethernet) and high speed information transfer among various subsystems will use a high bandwidth network (Scramnet). A separate data network will be dedicated to off-loading data from the sensors to the OCS data

# AEOS CONTROL SYSTEM

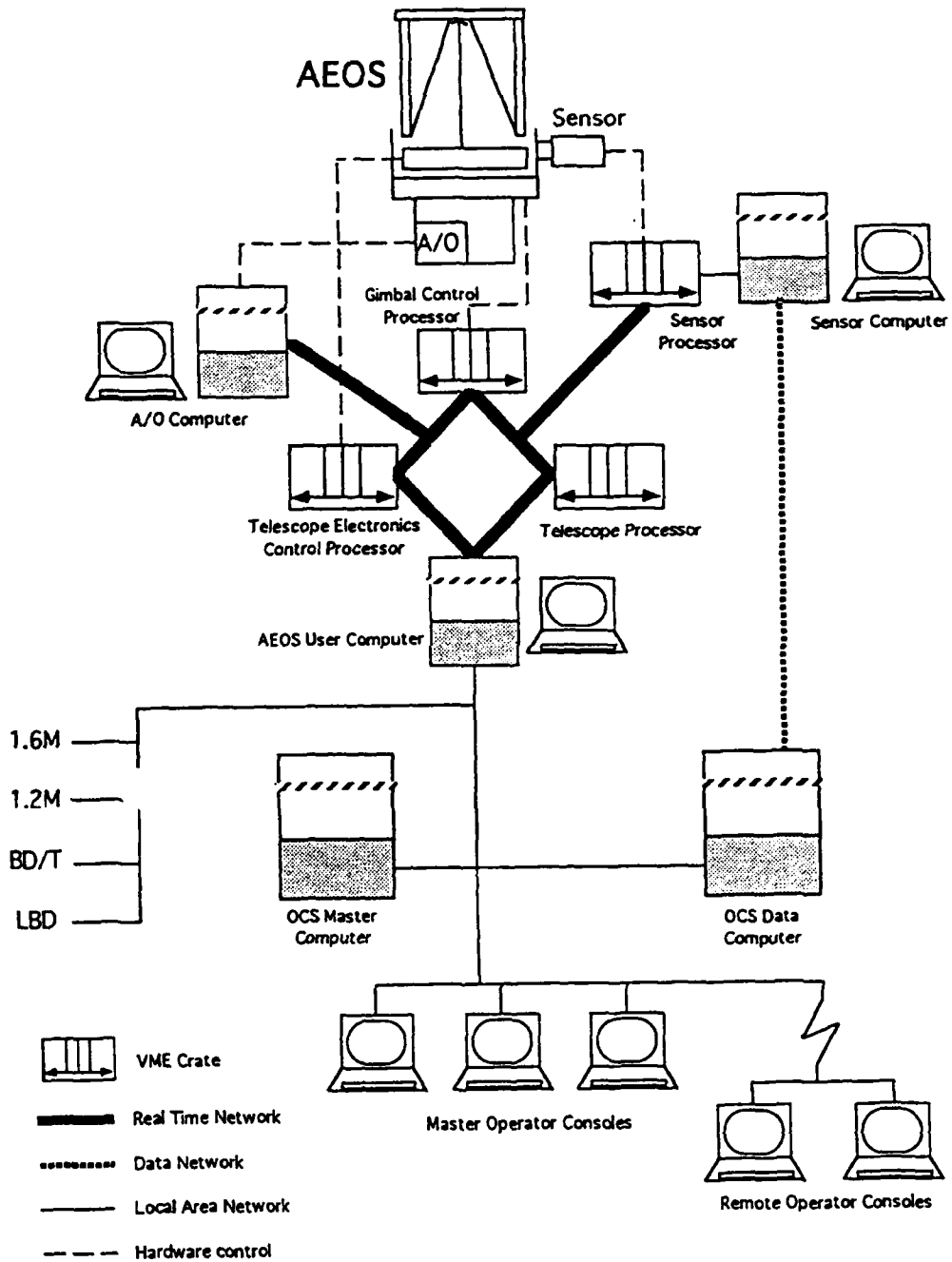


FIGURE 6.

computer. Remote operations capabilities, using a T3 microwave link and identical operation consoles, will allow control of the entire AEOS system from the Phillips Laboratory offices in Kihei.

### Adaptive Optics

An AO system for the AEOS telescope is currently being procured. The system will consist of a high bandwidth tilt correction mirror, a deformable mirror, a real time reconstructor, a wave-front sensor, and the associated pupil relay optics. The tilt correction system will operate between 450 and 650 nm with a variable sampling rate of 10 to 2000 Hz. The level of compensation of atmospheric turbulence will be determined by a set of 300 to 1200 degrees of freedom at variable closed loop bandwidths between 200 to 1000 Hz. The adaptive control loop will have an update rate 10 times faster than the closed loop bandwidth. Operating wavelengths for the wave-front sensor will be between 600 and 700 nm. The entire AO system will be installed at the base of the telescope pier. The optical interface required to deliver the necessary pupils will be located around M7. The AO output will be a compensated, collimated beam which can be directed to anyone of the seven optic rooms shown in Figure 4. This type of optical interface determines that only instruments using the Coudé optical system will have access to compensated images.

### Schedule

At the present time significant progress has been made in the construction of the telescope. Polishing of the primary mirror is expected to be completed in the spring of '94, with major components integration to follow. Meticulous care has been exercised in the facility design and in the environmental impact study required to obtain construction permits. It is expected that the facility will be ready for acceptance of the telescope in the winter '96. Controls and sensors which do not require compensated imaging will be added in '96. The AO capability, which is highly developmental, will be integrated at the close of '96.

### Reference

Schwesinger, G., 1991, *Journal of Modern Optics*, 38, 1507.



## **Hyperspectral Imaging of Near-Earth Space Objects at the Phillips Laboratory**

A. E. Prochko (W. J. Schafer Associates), E. Holbert (Florida Institute of Technology), S. A. Gregory (University of New Mexico), J. B. Rafert (Florida Institute of Technology), T. Payne and S. E. Durham (USAF Phillips Laboratory), and R. F. Horton (SAIC)

### **Abstract**

Hyperspectral imaging is an unconventional imaging technique that is being tested for use in space object identification (SOI) at the Phillips Laboratory (PL). The hyperspectral instrument for application to SOI has low to moderate spectral resolution and low spatial resolution. Preliminary results from the 1993 field experiment have shown that satellites with similar basic structure have similar signatures, and satellites that are structurally different have different signatures. The Phillips Laboratory team is developing methods to extract information from hyperspectral data to uniquely identify space objects and to determine object operational status, material composition and health status.

### **Introduction**

A hyperspectral imager is an imaging spectrometer which captures spatial and spectral information simultaneously. The potential information content of spatial and spectral data together is illustrated in Fig. 1. The hyperspectral imaging technique can be used to obtain a two-dimensional image and a spectrum for each part of the image that is resolved spatially. This results in three dimensions of measured data, called the datacube or "hyper"-cube, from which the image can be reconstructed at any desired wavelength and the spectrum can be extracted from any desired location on the image. Spectral observations alone would aid in SOI; however, obtaining spectral and spatial data simultaneously could offer significantly greater utility. Hyperspectral imaging can contribute new information to understanding space objects. Combined with information from other SOI techniques, hyperspectral data may help determine object operational status, material composition and health status.

In 1992, PL started a program to determine the utility of hyperspectral imaging for SOI. In July 1993, Phillips Laboratory tested two types of hyperspectrometers, dispersive and Fourier transform, for proof of concept. In the initial experiments, spectral information was acquired on near-earth space objects. Most of the data obtained on satellites were spatially unresolved. However, with the dispersive device, the imaging mode was demonstrated on large astronomical objects.

The spectral signature of an object is representative of all the materials reflecting light into the field of view of the hyperspectral imager. Satellite materials can be characterized according to the amplitude and directionality of their reflected spectra.

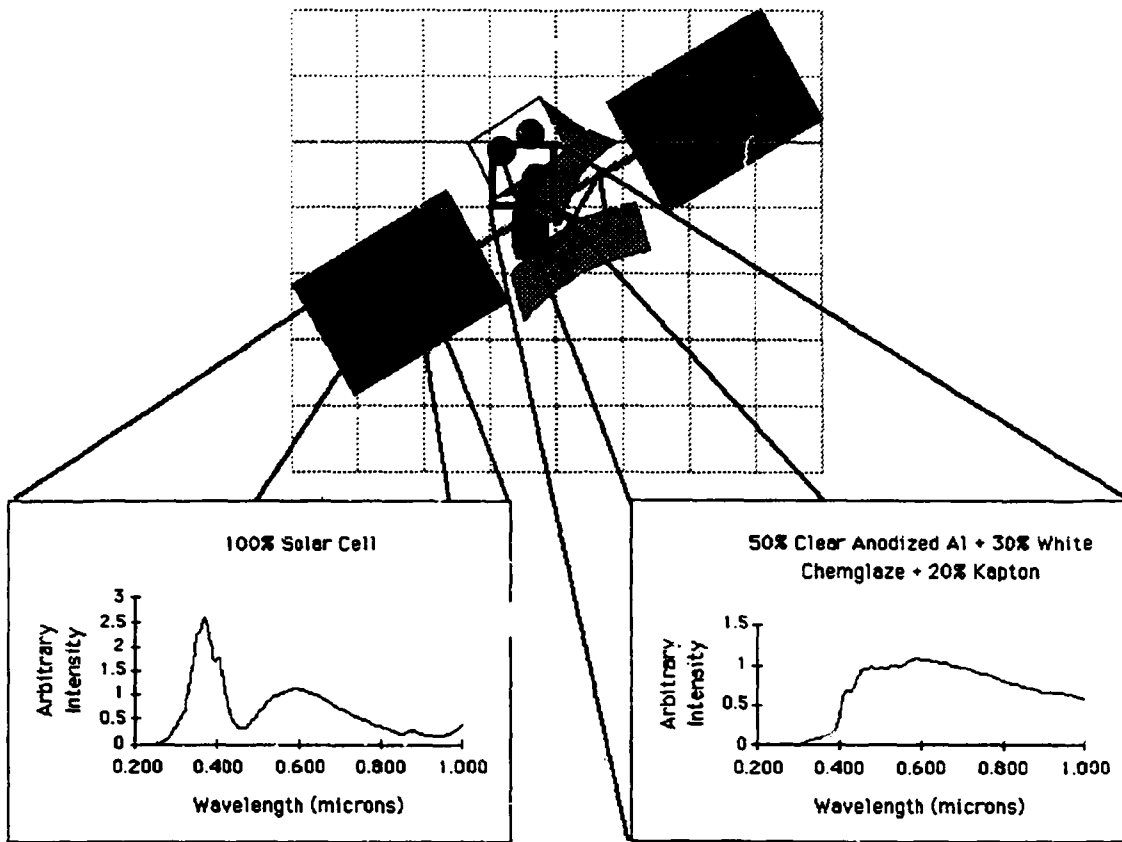


Figure 1: Hyperspectral imaging concept.

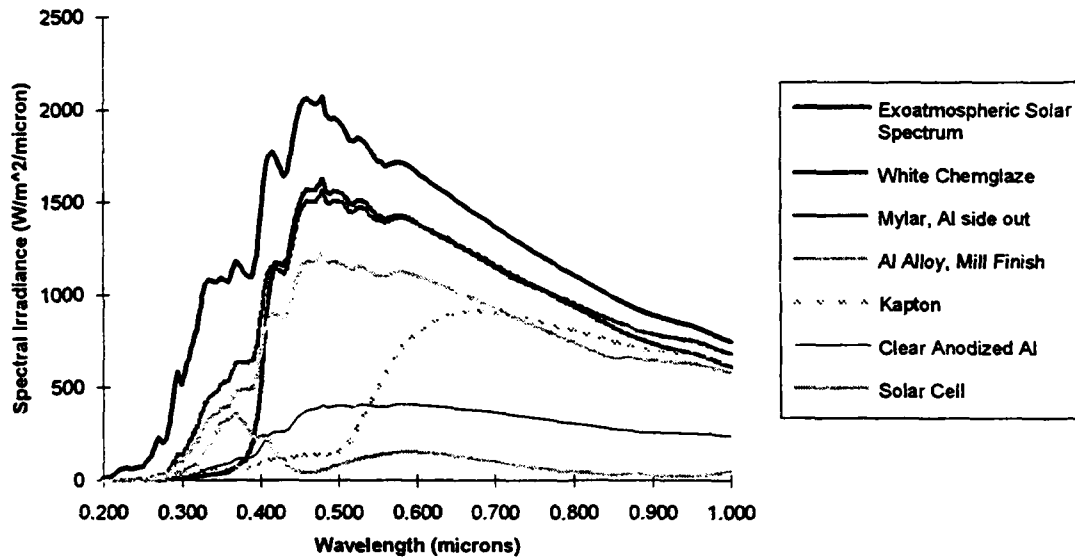


Figure 2: Spectra of solar-illuminated satellite materials.

The reflectivities of the most commonly utilized satellite materials are weakly varying functions of wavelength in the visible region. Figure 2 presents the exoatmospheric solar spectrum and the spectra of several solar-illuminated satellite materials [1]. The signature is expected to vary with orientation, the sun-object-observer angle (solar phase angle) and the age and condition of the surface materials. The variations in signatures will be analyzed by utilizing existing satellite models and by studying selected objects over time. One of the goals of the PL program is to determine whether the signature is unique to an object or to a class of objects.

### **Hyperspectral Instruments**

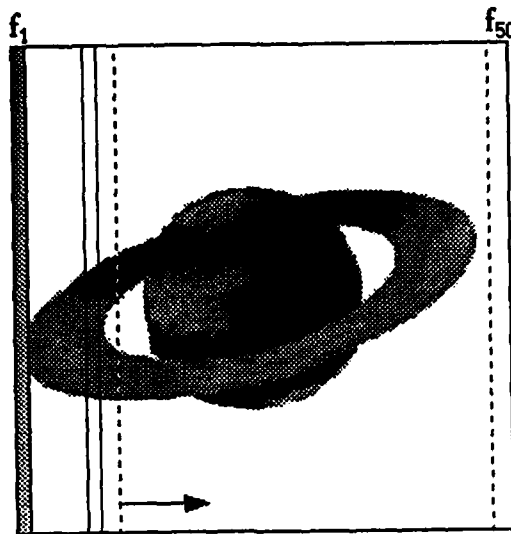
The dispersive spectrometer (grating) was developed by Science Applications International Corporation. The spectral resolution was nominally 4 nm at 550 nm. The instrument used a 512 X 512, 19  $\mu\text{m}$  pixel Thomson CCD (TH7895B) with a UV-sensitive coating. The dispersive imaging spectrometer was used to obtain one dimension of spatial information and one dimension of spectral information simultaneously on the CCD; the second spatial dimension was obtained by scanning the slit across the image to build up spectral information for each spatial slice of the image (see Fig. 3). The resulting ensemble of spatial/spectral frames forms a datacube.

The Fourier transform spectrometer (FTS) was developed at the Florida Institute of Technology using the Sagnac interferometer design [2, 3, 4, 5] and is illustrated in Fig. 4. The resulting data is an interferogram which must be apodized (noise introduced by the finiteness of the signal is minimized) and Fourier transformed to get a spectrum in wavelength space. The spectral resolution was nominally 2.5 nm at 550 nm (apodized). The sensor was a 1024 X 1024, 12  $\mu\text{m}$  pixel CCD (TC 215 chip from Texas Instruments) mounted in a SpectraSource MCD-1000 camera. The FTS can be used with a slit to obtain the second spatial dimension by scanning. However, several slitless designs for an imaging Fourier transform spectrometer (IFTS) are under consideration in order to achieve 2-D spatial and 1-D spectral information simultaneously and thus, more efficiently.

### **Summary of First Hyperspectral SOI Experiment Results**

In the proof-of-concept experiment, both instruments were positioned at the end of the coude path of the 1.5-m telescope at the Starfire Optical Range (SOR) at Kirtland AFB, NM. Because of the low throughput at the assigned experiment location on the telescope, large and bright objects were selected as targets. Observing conditions for near-earth space objects were limited to terminator conditions.

Figures 5, 6 and 7 show spectral signatures of three different satellites obtained by the Fourier transform spectrometer on the same night. The original signals were interferograms that were calibrated (flat fields, darks frames and biases), apodized and Fourier transformed. The optical system and the atmosphere were removed using



50 frames at 3 frames/min  
 Total scan time was 17 min

Figure 3. Dispersive imaging spectrometer scenario for Saturn.

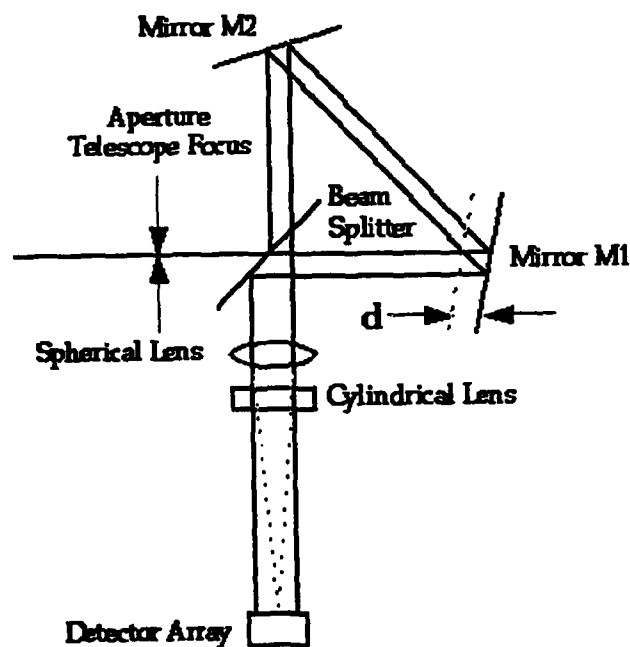


Figure 4. FTS of Sagnac interferometer design.

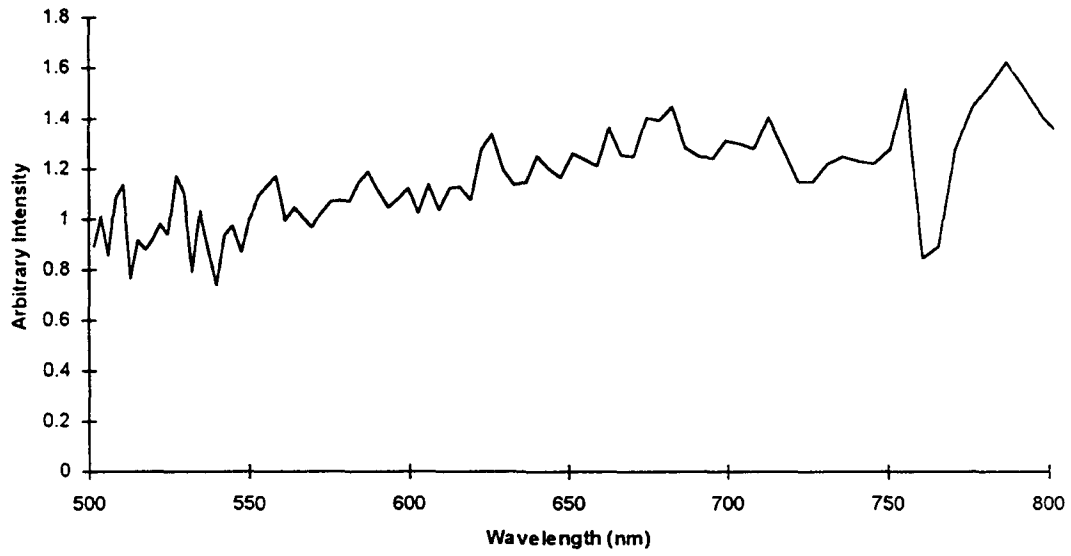


Figure 5. Hyperspectral signature of satellite A.

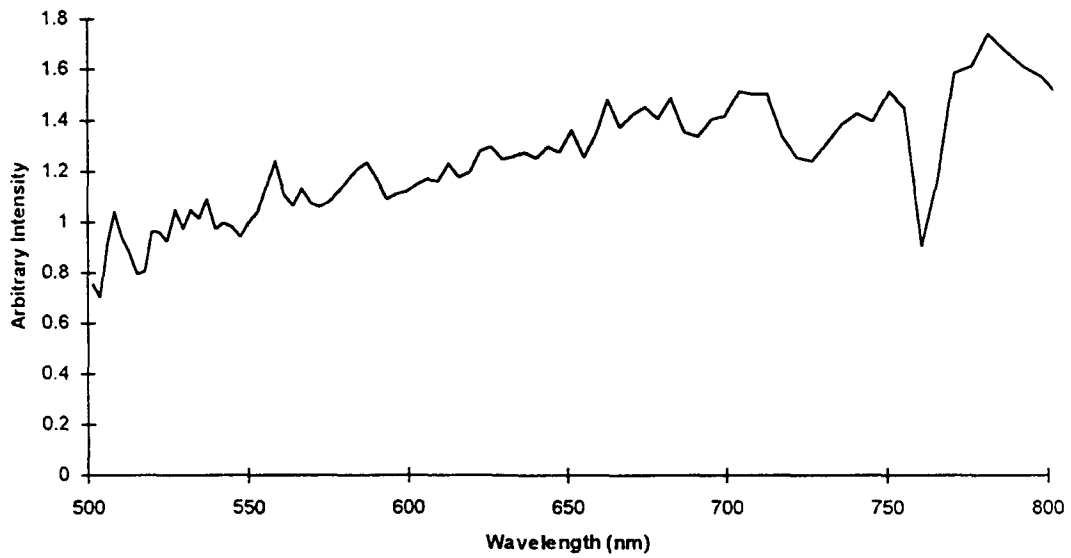


Figure 6. Hyperspectral signature of satellite B.

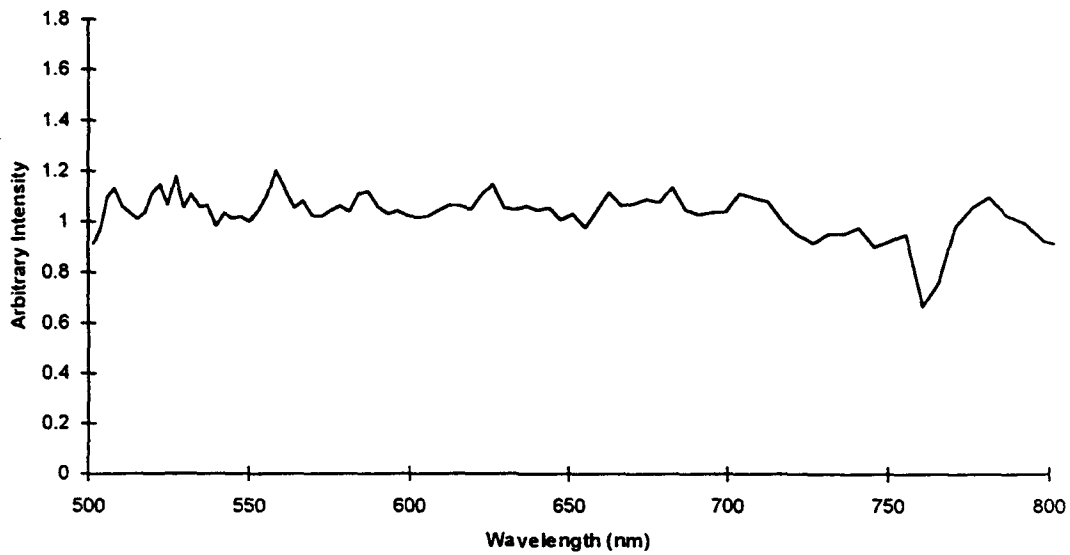


Figure 7. Hyperspectral signature of satellite C.

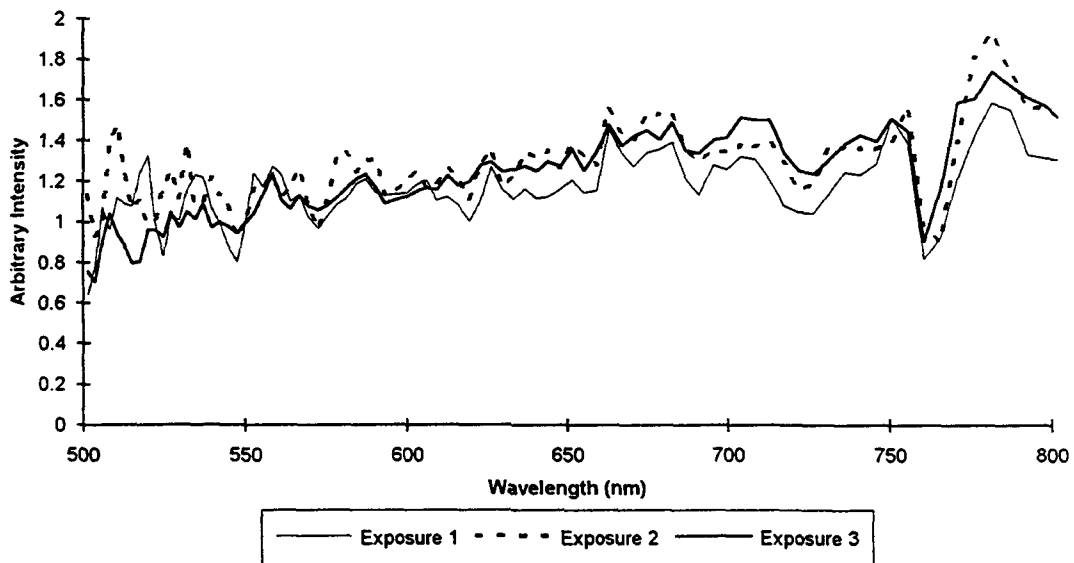


Figure 8. Signatures of satellite B at several locations in the pass.

standard astronomical methods. By observing an A0 type star and dividing the observed spectrum by its known spectrum published by Massey, et al. [6], a correction function was derived and applied to data taken near the same elevation angle [7]. The atmosphere has not been entirely removed which is evident from the O<sub>2</sub> absorption lines at 760 nm, which were not taken out of the published spectrum of the A0 star. Any short-term signature variation within the integration period (10 to 20 sec) was not detected. All signatures are normalized at 550 nm. Satellites A and B, which have the same basic physical components, have similar signatures. Both of these signatures exhibit higher intensity in the red. Satellite C has a very different physical structure than satellites A and B; its signature is more blue and less red than the signatures of satellites A and B. Figure 8 shows the signature of satellite B at several locations in the pass. This variation is most likely due to changes in orientation and residual atmospheric effects.

The PL Hyperspectral Imaging program is a dual-use program benefiting both military and astronomy communities. While it is important to observe standard stars for spectral and atmospheric calibrations, planets, binary stars and galaxies were also observed. By scanning the slit of the dispersive device across Saturn, a datacube was created. Two monochromatic images reconstructed from the datacube are shown in Fig. 9 and 10. Figure 9 is an image of Saturn at 775 nm where methane has high reflectivity. Figure 10 is Saturn at 968 nm where the dust and rings are reflecting sunlight and the planet's atmosphere is absorbing sunlight. Hyperspectral images of large satellites were attempted, but the pointing accuracy of the telescope used for this experiment was not sufficient to register multiple frames and thereby build a satellite datacube. Planned telescope and instrument upgrades will allow the technique to be developed for satellites in the future.

## Conclusions

The results of this experiment have indicated that different satellites show different spectral trends. Preliminary analyses suggest that similar satellites viewed in similar orientations will tend to have similar spectra that may constitute a hyperspectral class of satellites. Identifying a satellite or class of satellites from spectral signatures is only part of the information that can be extracted from a hyperspectral datacube. There are ongoing analyses to extract information on satellite status and material composition.

Analyses to predict signatures for selected objects have begun. These include satellites for which high-fidelity models exist and satellites for which a hyperspectral history is maintained. Modeling is crucial to understanding hyperspectral data. As the satellite orientation changes with respect to the observer, different illuminated materials of the satellite will influence the observed spectrum. Using the PL Satellite Assessment Center's spectral and image rendering codes, the hyperspectral team will compare simulated results from several unclassified satellite models with data obtained in the current experiment at the PL Malabar Test Facility in Florida. Experiments are

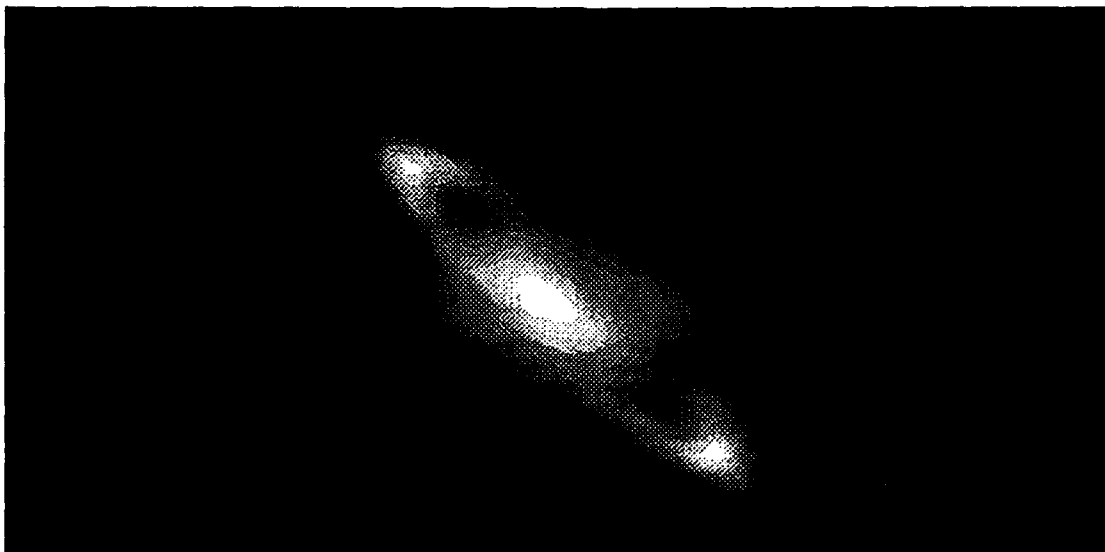


Figure 9. Saturn image at 775 nm.

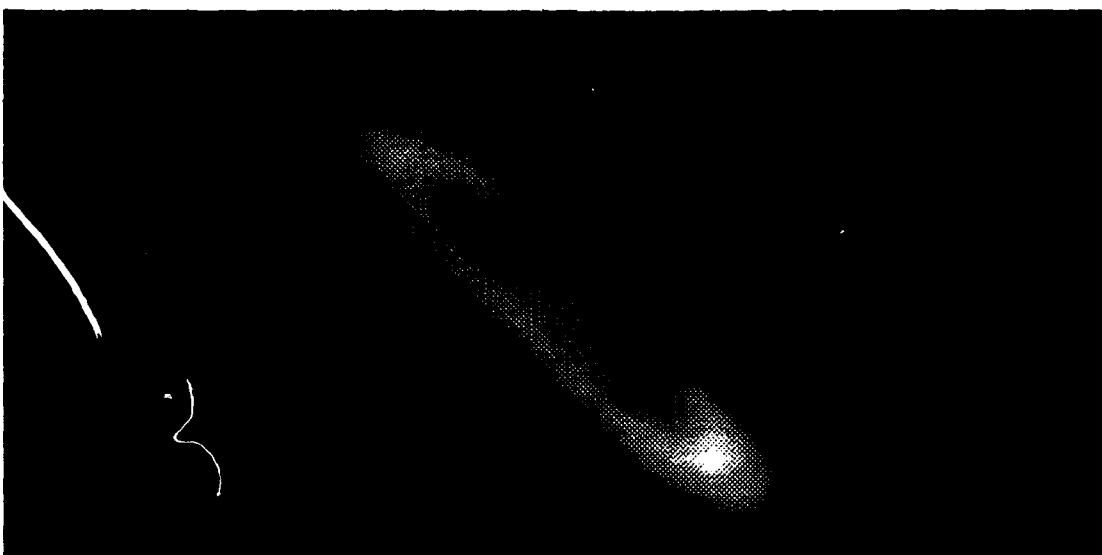


Figure 10. Saturn image at 968 nm.



continuing to improve upon the hyperspectral technique as well as to build a database of satellite signatures. More detailed observations are underway to allow a more complete removal of the atmosphere.

Hyperspectral data has the potential to provide additional information about space objects that cannot be provided by radar or conventional optical imagery alone. If it is proven after further development that hyperspectral imaging can contribute significant information to SOI, it will be added to other operational SOI techniques and integrated into the imaging workstation in development at the Phillips Laboratory Lasers and Imaging Directorate (PL/LI) and the Advanced Weapons and Survivability Directorate (PL/WS). In conjunction with other SOI information, hyperspectral imaging may prove to be of considerable value to multiple users.

### **Acknowledgements**

This work was sponsored by the United States Air Force, Air Force Systems Command, Air Force Weapons Laboratory, Kirtland AFB under Contract No. F29601-88-C-0071. The Hyperspectral Imaging program is led by the Phillips Laboratory. In 1993, the hyperspectral team consisted of the Phillips Laboratory, the Florida Institute of Technology, the University of New Mexico, Science Applications International Corporation, Ball Corporation and W. J. Schafer Associates, Inc. Individual team members deserving specific acknowledgement for their help in the proof-of-concept experiment at SOR include R. Carreras, G. Tarr, D. Holland, J. Wells, C. Coyle, D. Duneman, L. Ackermann, R. Lagarde and R. Sanchez. Thanks also to S. Gonzales for help in preparing some of the figures and to D. Tyler and R. Benedict for their helpful comments during the writing of this summary.

## References

1. "Matter.dat Surface Properties Data Compilation," GIE-TN-92-013, 1992.
2. Rafert, J. B., Holbert, E., Rusk, E. T., Durham, S., Caudill, E., and Keating, D., "The Malabar Spatially-Modulated Imaging Fourier Transform Spectrometer (SMIFTS)," Proceedings of the International Symposium on Spectral Sensing Research, Maui, HI, November 16-20, 1992.
3. Rafert, J. B., Holbert, E., Rusk, E. T., Durham, S., Caudill, E., Keating, D., and Newby, H., "A Visible Spatially Modulated Imaging Fourier Transform Spectrometer for Astronomical Applications," Bulletin of the American Astronomical Society, vol. 25, 1993.
4. Rafert, J. B., Lucey, P. G., Newby, H., "A Spatially-Modulated Imaging Fourier Transform Spectrometer for Astronomical and Booster Plume Observations," Proceedings of the ESO Conference on Progress in Telescope and Instrumentation Technologies, Garching, Germany, April 27-30, 1992.
5. Rafert, J. B., Blatt, J. H., Holbert, E., Sellar, R. G., Newby, H. D., Durham, S. E., "Hyperspectral Imaging Fourier Transform Spectrometers for Astronomical and Remote Sensing Observation," Proceedings of SPIE's 1994 Symposium on Astronomical Telescopes and Instrumentation for the 21st Century, Kona, Hawaii, March 13-18, 1994.
6. Massey, P., Strobel, K., Barnes, J. V., and Anderson, E., "Spectrophotometric Standards," Astrophysical Journal, vol. 328, pp. 315-333, 1988.
7. Holbert, E., "Development and Verification of the Spectral Performance Model of a Spatially Modulated Imaging Fourier Transform Spectrometer," Ph.D. dissertation, Florida Institute of Technology, (Work in Progress).

# Coherent Laser Radiometric Measurements of LEO Satellites

David G. Voelz, William Richard, Douglas B. Rider, David H. Stone (USAF Phillips Laboratory), Kathy J. Schulze (Rockwell Power Systems), David Dean (Hughes Aircraft)

## Introduction

The US Air Force Phillips Laboratory recently completed the Floodbeam Experiment, recording the first ever coherent laser returns from non-augmented, low earth orbit satellites. Illumination was performed during terminator periods (the satellite was sunlit while the experiment site was in darkness). This allowed use of a visible tracking system for good performance against distant and dim targets.

A coherent, pulsed, near-infrared laser was used to illuminate 35 different satellites at the Starfire Optical Range (SOR), near Albuquerque, NM. The 1 meter clear aperture Starfire Beam Director (SBD) was used to transmit pulses at a 1/7 Hz repetition rate. A low-noise IR camera collected speckle returns at a re-imaged pupil plane of the Starfire 1.5 meter telescope. Results include first ever resolved satellite whole-body speckles. Radiometric data are consistent with calculations, and exhibit occasional glinting. Depolarization data were obtained by comparing energy in the returns corresponding to the outgoing linear polarization in addition to the cross polarization. Depolarization data represent losses to a coherent imaging system.

## Laser Illuminator

Laser illuminator requirements included substantial energy per pulse, excellent beam quality, and superb coherence. A 1.3 micron wavelength, photolytic (flashlamp pumped) iodine laser was developed in-house at the Phillips Laboratory that met the requirements. Coherence length was demonstrated to be greater than 45 meters using Mach-Zehnder interferometry. The coherence length had to be substantially longer than the greatest dimension of a typical target so that a fully developed speckle pattern would be produced by reflections from all observable points on a target.

Laser pulse energy exceeded 50 Joules on a routine basis. More energy was available, but the pulse shape deteriorated due to development of an initial gain-switched spike. Additionally, flashlamps would fail as they were driven to excessive voltages. Energy was also somewhat restricted by the necessity to extract useful energy in a minimal pulse length. Many hardware modifications were performed to reduce the pulse length to 7 microseconds. Satellite orbital velocities inherently produce speckle smearing, reducing the quality of the captured speckle patterns. Even at 7 microseconds, our data show these effects.

The laser's pulse repetition rate was 1/7 Hertz. The longitudinal flow design restricts higher repetition rates without severe degradation in beam quality. At 1/7 Hertz, the laser beam quality was better than 1.5 times diffraction-limited. This repetition rate still allowed typically 15 to 20 shots per engagement.

## Transmitter/Tracker System

The transmitter system was required to accurately track satellites as dim as 10th visual magnitude ( $M_V = 10$ ) and place the illumination beam on the target with less than 5  $\mu$ rad rms boresight and jitter error. The system also had to preserve the excellent beam quality and linear polarization of the high power beam. A large variety of satellites and rocket bodies were illuminated during the experiment. In all cases the objects were classified as "dead" and appropriate permission was obtained from the USSPCM Laser Clearing House.

A schematic of the experiment is shown in Figure 1. The 1.3 micron laser beam was directed to the satellite using the Starfire Beam Director. Although the director has a 1 meter clear aperture, tracking and illumination was limited to a 28 cm diameter aperture. The transmitter/tracker system used three different wavelength bands for propagation, tracking, and alignment. The near-infrared band is used for transmitting the high power beam. Care was taken

to maintain the high degree of linear polarization of the outgoing beam through the use of (1) a fully reflective path at near normal incidence, and (2) polarization preserving coatings on the optics.

Sunlight reflected from the target in the wavelength band between 600 nm and 900 nm was used for target fine tracking. The track sensor employed a Gen III intensifier and a Hamamatsu position-sensitive photomultiplier tube (PMT). The signals from the PMT closed the tracker loop around the beam steering mirror (BSM). Three track bandwidths were utilized: 3 Hz for very dim targets, 17 Hz for normal operation, and 75 Hz for bright targets. The target set ranged from approximately  $M_V = 4$  at the brightest, to less than  $M_V = 10$  (which were not trackable). Individual objects varied in brightness over the course of a pass and from night to night due to changing viewing geometry, variable weather conditions, and changing aspect angles.

System alignment, boresight and point-ahead were achieved using a 458 nm wavelength alignment beam that was injected into the iodine laser cavity to mimic the high power beam mode. The alignment beam regurgitated from the cavity was then sensed to estimate the position and pointing of the high power beam. The point-ahead angle necessary to hit the satellite was calculated from the orbit trajectory and digitally added to the point-ahead control loop. The alignment system was one of the limiting factors in determining the laser repetition rate. Approximately five to seven seconds were required for the laser cavity to settle after each laser pulse before the alignment laser was stable enough to accurately predict the path of the high power beam.

An operations summary follows: Targets were selected during pre-mission planning. Ephemeris data and predictive avoidance times were loaded into the mount control computer prior to the pass. Rough pointing was accomplished by the mount controller. The target was normally acquired in the wide field-of-view (FOV) camera which has a FOV of approximately 4 milliradians. The mount operator updated the object's position to center it in the 300 microradian narrow FOV camera. The tracker operator then centered the object in the 60x80 microradian tracker FOV and closed the fine track loop.

Laser firing was initiated once fine track was established and the safety system showed all clear. The safety system consisted of many interlocks to make sure that the laser cannot fire unless all systems are go and all the dangerous areas are clear. The final safety check was an aircraft watch operator holding down a ready-to-fire button.

### **Receiver System**

The receiver system was required to record a pupil-plane image of the returning speckle patterns. The system had to adequately sample the pattern spatially, determine the amount of depolarization of the light induced by the target, and allow accurate radiometry values to be obtained from the data. The polarization measurement was important since depolarization effectively amounts to a loss in return signal when measuring a linearly polarized, coherent speckle pattern.

Referring to Figure 1, the returning 1.3 micron photons were collected by the 1.5 m telescope at the SOR and a low-noise IR camera recorded the speckle patterns. The receiver optical system actually separated the linearly polarized light that was aligned with the transmit beam from the light scattered into the cross polarization. The optical system also employed a zoom lens that adjusted the pupil image magnification to ensure adequate spatial sampling of the return speckle pattern by the camera. The zoom system allowed a 3:1 magnification range. Accurate radiometric calibration of the receiver optical train and camera was completed in the laboratory before the system was fielded.

Coarse pointing was accomplished with the mount control system using an ephemeris model. The open-loop pointing of this mount was sufficient to keep the object within the FOV of the pupil-plane camera. The visible light focal-plane camera viewed an image of the target which was used by the mount operator to center and maintain the open-loop track on the target.

## Results

The Floodbeam experiment was designed to demonstrate the technologies necessary to do acquisition, pointing, tracking, and illumination of low earth orbit satellites. The primary goal of the experiment was to collect accurate radiometric measurements of a set of approved satellites. Additionally, an ambitious objective was to spatially sample the coherent returns to examine the statistical properties of the backscattered coherent laser speckle.

Figure 2 shows an example of the radiometric measurement made on a single satellite pass. The graph shows the total number of returned photons that reached the camera face. The collection aperture was the full 1.5 m diameter. As can be seen, the return varies across the entire pass showing the expected increase in return at the shortest ranges during the middle of the pass. The graph also shows some dramatic pulse to pulse variations which are probably primarily due to pointing and tracking jitter as well as changes in the target aspect.

An example of the speckle patterns collected for one of the larger targets is shown in Figure 3. The figure shows returns from five consecutive laser pulses near the middle of a particular pass. The patterns are all scaled to a common reference shown on the right of the figure. A few of the brightest speckles are slightly saturated in this display in an attempt to show the full detail of the speckle patterns. Visually, the pupil images appear speckled as one would expect for a coherent return. Initial analysis shows that the contrast in the patterns is also very high. The fringing pattern discernible at approximately 45 degrees to the right of vertical indicates that this particular satellite's longest dimension was oriented along that axis. Although not immediately obvious, the patterns are slightly smeared, approximately 1/4 to 1/2 of a pixel, due to the velocity of the speckle pattern and the 7 microsecond laser pulse. Analysis is currently underway to remove the effects of smearing.

Figure 4 shows some initial radiometric results for several classes or types of targets. The vertical axis is the total return reaching the camera face (as in Figure 2). Along the bottom axis, targets are grouped in seven classes that were thought to have similar backscatter cross-sections. The dark bars in the graph are average, maximum returns for a specific satellite. These values were obtained by finding the maximum return (single laser shot) for each pass of the given object and averaging these maximum values over all the engagements for that object. In other words, the dark bars represent the typical "best" shot of a given pass. The lighter bars are values calculated using a radiometric model that incorporates the system transmissions, estimated target cross-sections, laser beam quality, etc. The figure shows that in most cases the "best" shot returns are larger than the predicted returns, which is expected since the "best" shots may include glints or other advantageous phenomena such as momentary good seeing conditions. Only class 6 targets seem to show weaker returns than expected which suggests that the cross-sections of these targets are smaller than those used in our model. Further radiometric data reduction is underway.

## Conclusions

The experiment was extremely successful. Difficult problems were solved in establishing a new experimental facility at the Starfire Optical Range, while conducting an ambitious field experiment. Extensive radiometry and speckle pattern data will be useful in the development of new imaging concepts, especially for the Phillips Laboratory's Active Imaging Testbed, now under development.

## Acknowledgments

The authors would like to acknowledge the many people who were involved with the experiment and its development over the years: from the Phillips Lab Imaging Technology Branch Maj Paul Idell, Lt Col Shawn O'Keefe, Capt Ted Kreifels, Lt Donna Keating, Dr John Gonglewski, MSgt Pat Connolly, and Capt Bill Arrasmith; from the PL Laser Branch Dr. Vern Schlie and Dr Robert Rathge; from the PL Tracking Branch Dr. Sal Cusamano, Lt Ralph Galetti, and Capt John Mileski; from the PL SOR Division Capt Eric Stewart, SSgt Ben Knepper, and Dr Bob Fugate; from Hughes Aircraft Jim Kitchen, Gordon Lukesh, Mike Meline, Dennis Mansell, Joe Paranto, Calvin Barnard, Sylvia Rogers, Carla Neuman, and Terry Shirrod; from Rockwell Power Systems Steve Hanes, Jeff Baker, Bob Wilmot, Joe Blea, Victor Gamiz, Robert Babnick,

Joe Rae, and Bruce Crawford; from BDM Roger Holt, Nils Hochhauser, Charly Tipton, Russ Smith, Jerry James, and Cathy VanBerg; from S Systems Ted Turner and Karl Shrader; from tOSC John Belsher and Glenn Tyler. The authors realize that many more people were indispensable in getting this experiment off the ground. We regret not being able to mention everyone, but offer our sincere thanks to all.

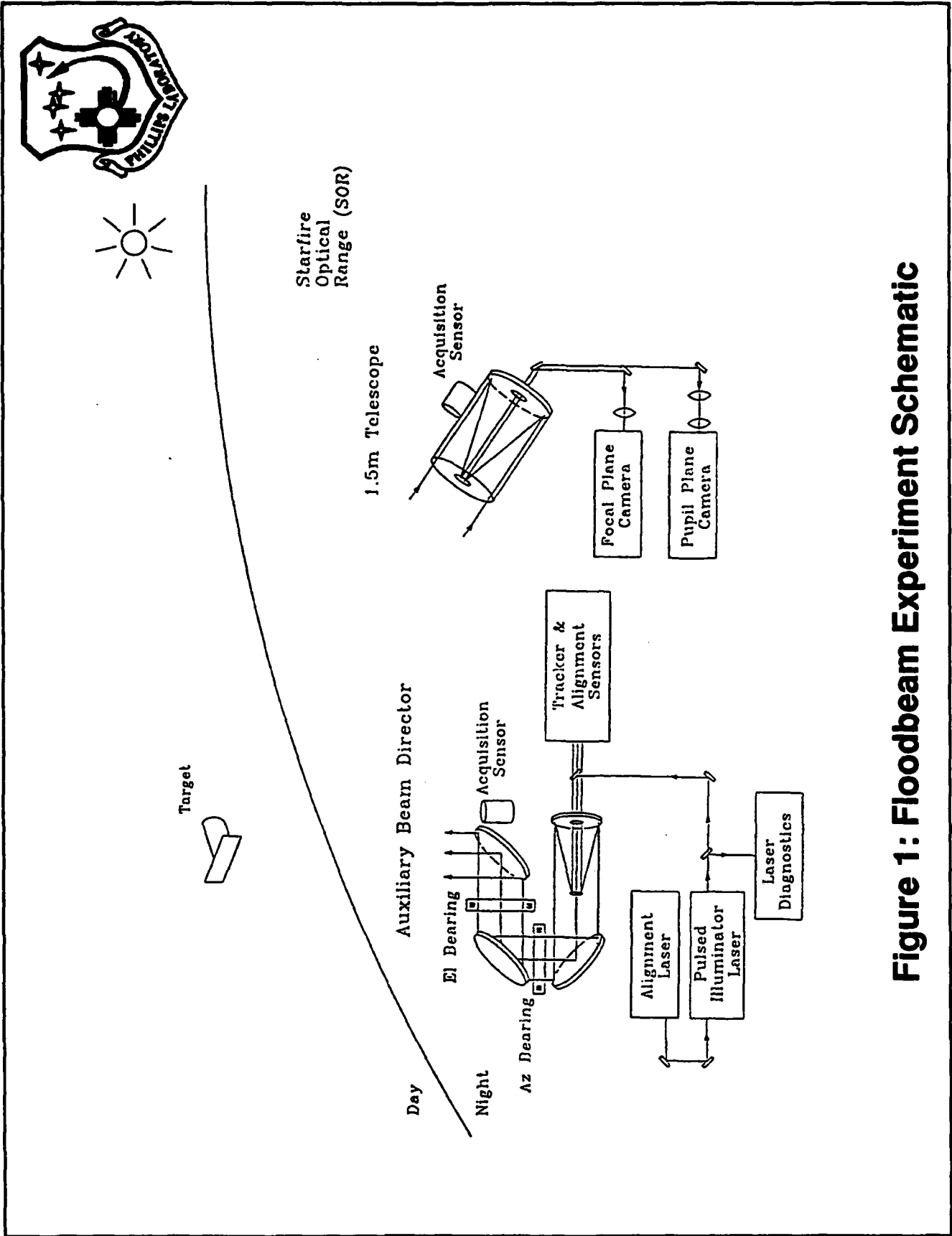
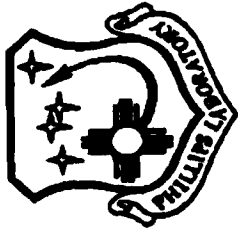


**Figure 1: Floodbeam Experiment Schematic**



Total Return - 9 Sep 93



Figure 2: Total Photon Return from a Single Satellite Pass



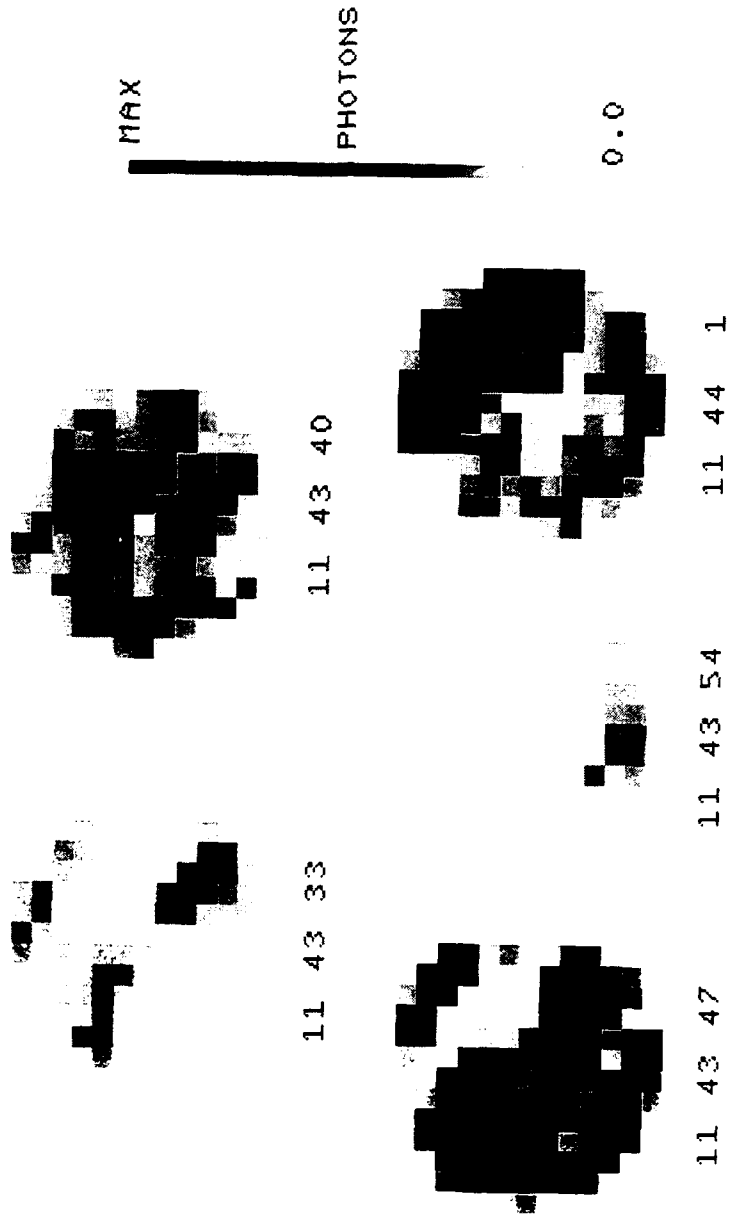
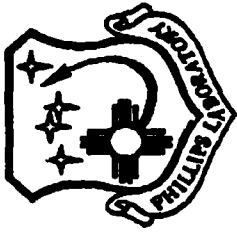


**Figure 3: Five Consecutive Speckle Snapshots**

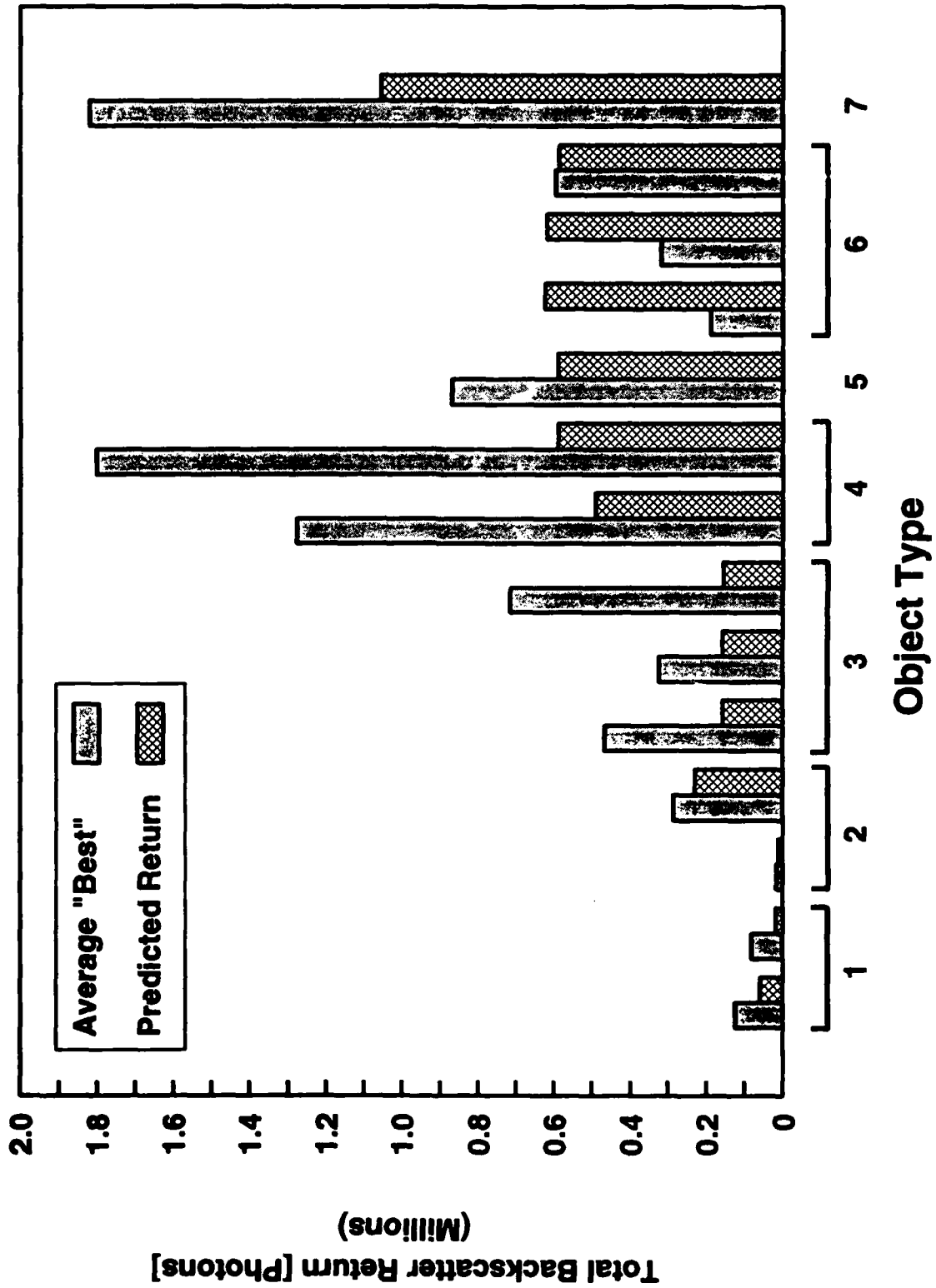


Figure 4 - Averaged "Best" Returns For Multiple Passes Normalized By Prediction

## GEODSS Upgrade Prototype System (GUPS)

Dr. C. Max Williams (TRW), Sam D. Redford (TRW)

### 1. Introduction and Summary

The Ground-based Electro-Optical Deep Space Surveillance (GEODSS) System provides critical metric and SOI observation data on deep space satellites to the Space Surveillance Center (SSC) in Cheyenne Mountain. GEODSS concepts and development occurred in the 1970s and it became operational in the early 1980s. It was based on the 1970s technology including sensor, signal processing algorithms and hardware, and data processors and languages.

The GEODSS Upgrade Prototype System (GUPS) is a 3 year technology insertion program and is a part of the Space Surveillance Network Improvement Program (SSNIP). GUPS was procured by the Air Force Sacramento Air Logistics Center (SM-ALC), will be technically managed by the Electronic Systems Center (ESC) and performed by TRW, Inc. GUPS will demonstrate the applicability of several technological advances to the GEODSS system. The new technologies include high performance Charge-Coupled Device (CCD) sensors, enhanced signal processing and tracking algorithms, and modern data processing equipment and languages. Many of these technological advances are directly attributable to MIT/Lincoln Laboratory (MIT/LL) research programs. The resulting system will have greatly improved sensor performance, with higher sensitivity (higher probability of detection of dim objects, and lower false alarms), higher sensor throughput (both search and track rates), and improved metric observation accuracy.

GUPS will develop an Exclusion Zone Sensor (EVS) which will provide an automated method of determining which areas of the sky are acceptable for observations. The GUPS program will also demonstrate relocatability, and that the GUPS can be transported by land, sea or air, and can be deployed worldwide within months. Figure 1 illustrates the relocatable system.

The GUPS program features numerous demonstrations at the GEODSS Test Site (GTS) highlighting relocatability and improved sensor performance. GUPS is expected to continue as a testbed for new technologies prior to their use in the operational system. Capabilities proven in GUPS can be easily incorporated in the GEODSS Modernization Program (GMP) which will upgrade the existing GEODSS system.

### 2. History and Legacy of GEODSS / GUPS

The anticipated GUPS sensor capabilities and improved sensor performance are attributable to both the GEODSS system and many recent technology developments at MIT/LL. Research for the GEODSS system began in the early 70s, and involved ESC, MIT/LL and TRW. A contract was awarded to TRW in 1978 to develop and install operational sites at Socorro, Maui, Diego Garcia, and Korea (now deactivated). The sites provide both metric observations and Space

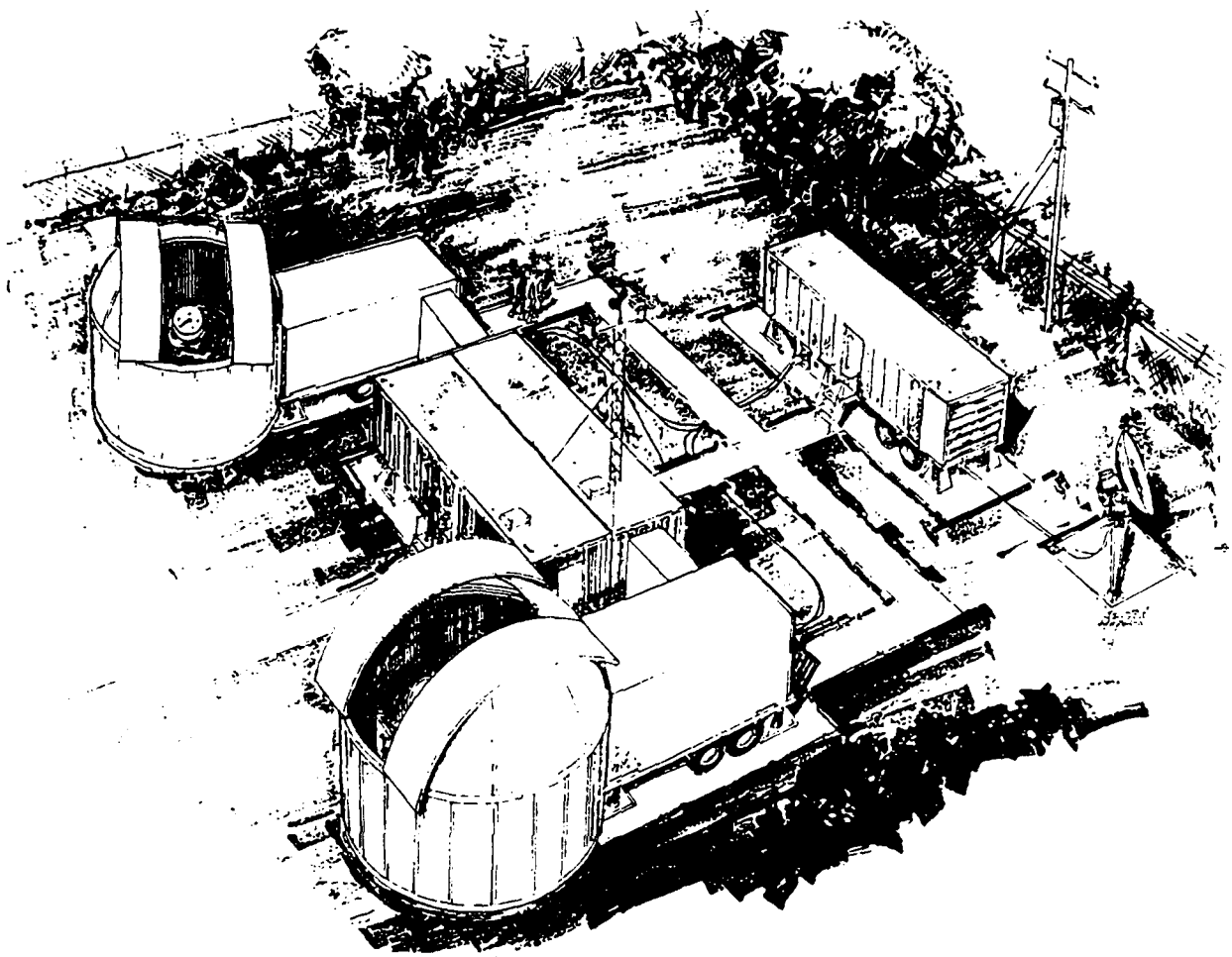


Figure 1. A Deployed - Relocatable GUPS

Object Identification (SOI) data on deep space objects to the SSC. GEODSS uses a 40 inch main telescope and polar mount developed by Contraves; the same telescope will also be used in the GUPS system. GEODSS uses an Ebsicon tube as its sensor, and processes binary data using an elementary sidereal tracking algorithm. Significant improvements have occurred in sensor and signal processing methods since the initial GEODSS development.

During the last 5 years, MIT/LL has made several contributions to electro-optical sensor technology. In addition to the development of the CCD itself (discussed later), MIT/LL has been involved in the development of the Transportable Optical System (TOS) and the Space-Based Visible (SBV) sensor on the MSX satellite. In particular, the TOS program demonstrated improvements in detecting dim objects (using target track methods) and metric observation accuracy (using nearby "guide stars"). The SBV project developed improved sky-background rejection methods (normalized maximum value projection) and developed automatic target acquisition algorithms for target track. Features from both projects will be used in GUPS.

### 3. Relocatable Shelters

The relocatable GUPS, illustrated in figure 1, is being developed such that the complete system can be dismantled, transported by land, sea (as top level container cargo) , or air (Air Force C-141), and deployed to a previously unprepared worldwide site within six months of deployment decision. Upon arrival at a prepared site, the relocatable GUPS can have the telescope mounted and associated mission equipment functioning within one to two weeks. The design of the relocatable GUPS is based upon International Standardization Organization (ISO) transportable shelters and trailers which have an extensive history in mobile and transportable military applications. The GUPS relocatable system incorporates one Telescope Shelter, one Operations Shelter, a custom trailer with hydraulic lifting devices, and an existing GFE GEODSS observation dome and dome base, as illustrated in figure 2. In addition, GUPS has been designed to easily accommodate expanded mission requirements whereby each Operations Shelter can control up to 4 Telescope Shelters.

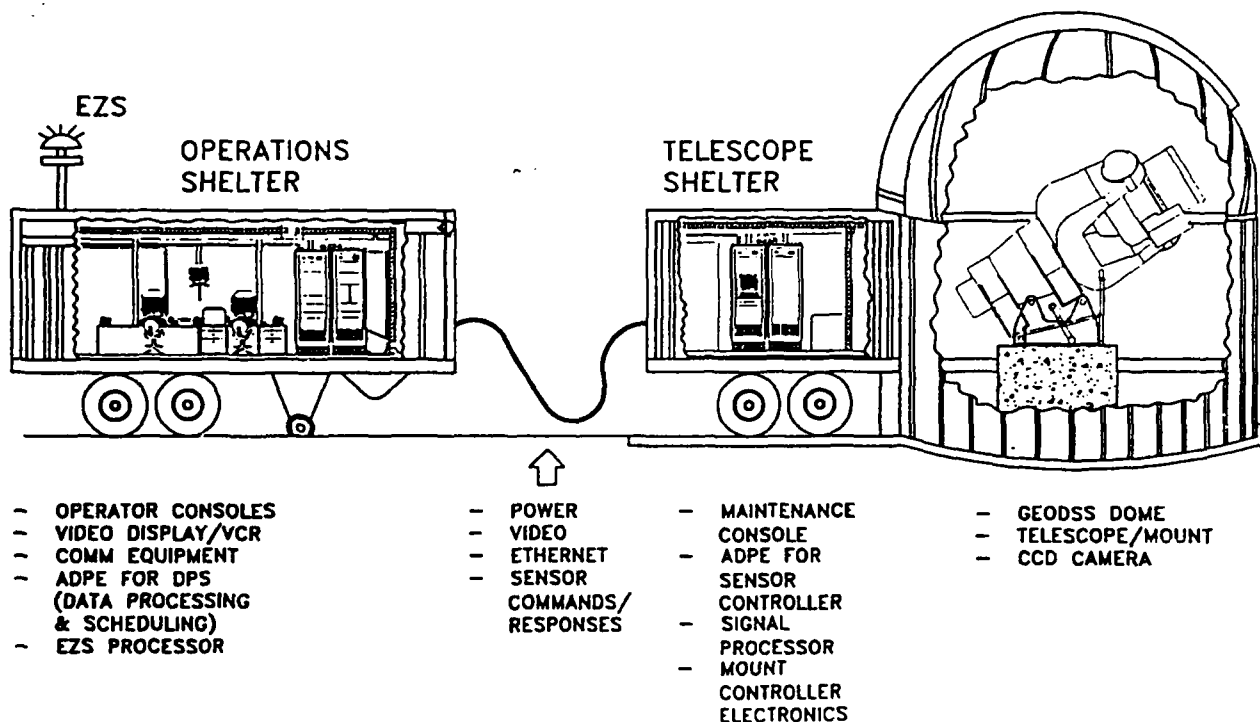


Figure 2. GUPS Operations and Telescope Shelters

The relocatable GUPS is capable of being deployed in both the northern and southern hemispheres at site locations between + or - 45 degrees latitude. The GUPS Telescope Shelter is designed to allow the transfer of the telescope from the shelter to a rigid pedestal without the need for special support equipment at the site. Regardless of site location, full telescope azimuthal coverage above 20 degrees elevation (except where restricted by the mechanical limitations of the mount), and geostationary belt coverage ( + or - 10 degrees on either side of the geostationary equator) down to within five degrees of the horizon is assured because of the unique capabilities of the transportable shelter system.

#### 4. Sensor Controller Subsystem

The most complex element of the GUPS program is the development of the Sensor Controller Subsystem. Figure 2 illustrates the Telescope Shelter which physically contains the Sensor Controller including the general purpose data processor and the signal processor hardware which process image data from the CCD camera. The Operations Shelter houses the Data Processor and Scheduling (DPS) Subsystem which supports the operator displays, communications equipment, catalog maintenance and the task scheduler for the system. A single DPS subsystem is capable of controlling up to 4 sensors.

The DPS software in the Operations Shelter will transmit high level commands to the Sensor Controller, such as:

- Search in given area and report on any observed detections,
- Search for a known object at a predicted location and rates,
- Acquire and track a known object for x seconds, or
- Collect SOI data for x seconds on an object in track.

This simple, straightforward command interface to the Sensor Controller also facilitates remote control of a sensor by a distant site such as the Integrated Space Operations Center (ISOC) which will be developed on GMP. In the remote operations mode, an operator and scheduling software at the ISOC would send Sensor Controller type commands to the communications portion of the local GUPS DPS subsystem. These commands would effectively "pass through" the local DPS to the Sensor Controller; metric and SOI observation data would pass through the local DPS back to the remote ISOC. This remote control capability will be demonstrated on the GUPS program.

Although many of the new GUPS concepts were developed to take advantage of the high performance CCD sensor, the GUPS Sensor Controller and its signal processing architecture and tracking algorithms can be used with the existing Ebsicon tube. GUPS sensor controller capabilities, including both sidereal and target tracking methods, will also be demonstrated on an Ebsicon sensor.

There are many elements in GUPS, but three particularly important elements are the CCD chip and camera, tracking algorithms, and the signal processing architecture to process the large volumes of CCD sensor data.

#### 4.1 CCD Camera

The most important technology insertion element in GUPS is the large-format CCD sensor. It will provide significantly improved sensor performance over the current Ebsicon sensor. The CCD chip is produced by MIT/LL and the CCD camera is being developed by Photometrics according to MIT/LL generated specifications. The CCD chip is a large 1960 x 2560 array having over 5 million pixels. It will have high resolution with each pixel corresponding to a 2x2 arcsecond area. It is back-illuminated and has a quantum efficiency exceeding 0.65. It is a frame transfer device, has 8 output ports and can be readout in 0.3 seconds (readout in less than 0.1 sec for binned data). The CCD device also has a 32x32 photometric subarray which is used for SOI data collection.

The first production CCD camera will be incorporated in GUPS. It will use thermoelectric cooling to minimize thermal noise in the CCD sensor. (See related proceedings paper by Dr. R. Weber for more details on the chip and camera.)

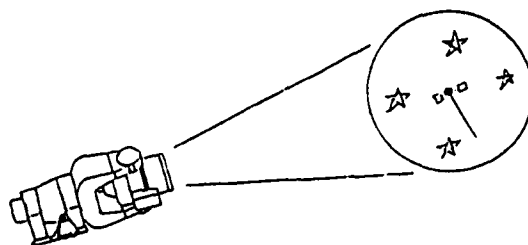
#### 4.2 Tracking Algorithms

GUPS is required to track objects in two modes: Fast Track Mode, wherein objects are detected and observed in a minimum time, and the Dim Object Mode, to detect the dimmest objects possible. GUPS will utilize both sidereal and target tracking methods to meet these requirements. Figure 3 illustrates the two methods and addresses the advantages and disadvantages of each.

An elementary sidereal tracking method was implemented in GEODSS, but there have been many improvements over the years. Figure 4 illustrates the more advanced sidereal method which will be implemented in GUPS. As shown in the figure, sidereal track is basically composed of two processing elements, the star background rejection and the streak detection (these are often referred to as time dependent processing and object dependent processing).

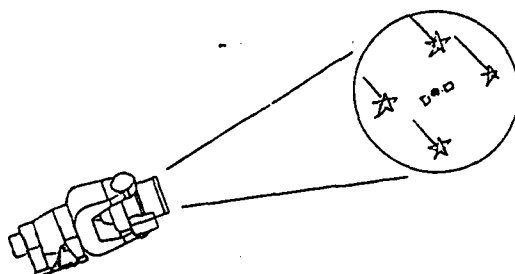
For star background rejection, GUPS will utilize a variant of the normalized maximum value projection method presented in MIT/LL Technical Report # 846 (by P. Chu). This method has been proven at the MIT/LL Experimental Test Site (ETS) and is used on the SBV sensor. The star background rejection algorithm is mathematically very simple, but is computationally demanding. It must be performed on 5 megapixels, 3 times a second, and the resulting signal processor load is estimated to be 500 million floating operations per second (MFLOPs).

### SIDEREAL TRACKING



- **Description:**
  - Telescope "stares" in the direction of fixed stars
  - Satellites leave a "streak" over many pixels
- **Advantages:**
  - Supports Track While Scan
  - Tracks Multiple Objects Simultaneously
  - Can Detect/Track an Object Independent its Angular Rate
- **Disadvantages:**
  - Hard To Detect Dim Objects or Fast Moving Objects  
( Light Spread Over Many Pixels )
  - Longer exposure times may actually lower SNR

### TARGET TRACKING



- **Description:**
  - Telescope slews at the same angular rate as moving satellite
  - Keeps an Object in the same Pixel (at least shorter streaks)
- **Advantages:**
  - Can Detect Much Dimmer Objects (Dwell in Cell yields higher SNR)
  - Can generally increase SNR with longer exposures
  - Excellent for finding Geosynchronous Satellites
- **Disadvantages:**
  - Must Know Objects Angular Rate Fairly Accurately  
(but all Geosyns are 15 arcsec/sec)
  - Requires Translation, Registration for each Image Frame

Figure 3. Characteristics of Sidereal and Target Track



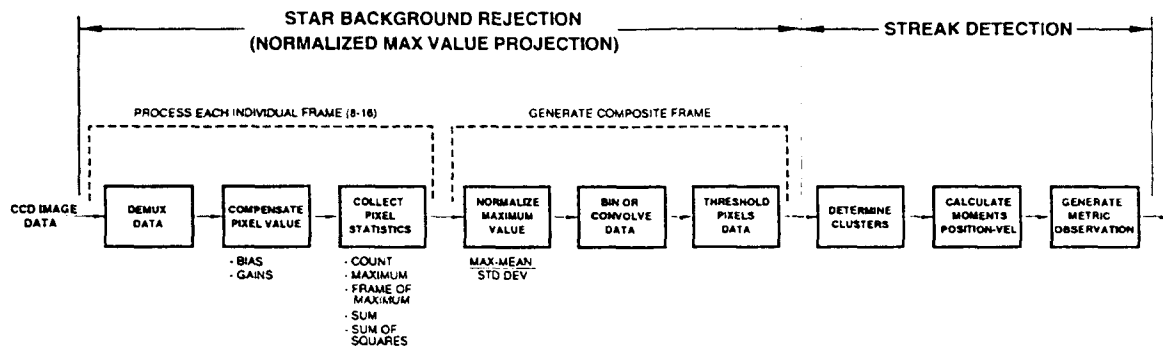


Figure 4. GUPS Processing for Sidereal Track

There are four basic classes of streak detection algorithms which are being evaluated for use in GUPS. These are:

- Cluster / Moments: The GEODSS Link 2 algorithm uses an early version of this technique and advanced versions have been used on various satellite systems. It finds clusters of nearby points which may be part of a streak and then calculates moments to determine if the distribution of the points are consistent with that of a streaking object. Angular positions and rates are then calculated.
- Hough Transform / Moments: Current research efforts are examining the viability of using a Hough transform which maps a streak into a local maximum in the transform space. This may allow the detection of sparse streaks present in low signal to noise environments.
- Chu Method (MIT/LL Technical Report # 846): This technique looks for streaks along 20 angles, and determines the probability that the points along a line are from a streak. It has been implemented for the SBV sensor.
- Maximum likelihood matched velocity filtering (MIT/LL Technical Report # 940 by S. Pohlig). This is the "optimal" method for streak detection but is computationally demanding. It is sometimes referred to as a "step and add" algorithm.

The GUPS requirements essentially demand that it can detect a streak resulting from a signal of noise ratio of 6 (goal is to detect with SNR = 3). Our baseline streak detection method is a cluster/moment method which should easily meet the detection requirements while being the simplest proven method. However, a signal processing architecture has been selected which will support growth to other streak detection methods.

A disadvantage of sidereal tracking is that the object moves across many pixels and the signal to noise on each individual pixel may be too small for detection. The target tracking algorithm (also called rate track) solves this by slewing the telescope and sensor at the same rate as the object, thereby integrating the energy in a small area, achieving a much higher signal to noise ratio and thus providing a higher probability of detection. This method is utilized in the TOS system. The SBV sensor also uses this method along with an automated acquisition method for target track. This method will be used in GUPS. It will allow GUPS to detect much dimmer objects than detectable with other algorithms; this is in addition to the increased sensitivity from the CCD itself.

After an object has been initially acquired using the automated target track algorithm, it can be "autotracked" using methods employed in TOS. Autotracking involves finding the object in each frame, centroiding the intensity data from pixels containing the object, and exercising closed-loop feedback control of the telescope mount to maintain track. This tracking method will allow extended track on an object without relying on an element set.

#### 4.3 Signal Processing Architecture

The GUPS Sensor Controller Subsystem will employ a VME-based data processing architecture. Candidates for the host processor include the Sun Sparc processor and the Motorola 68040 processor. However, these processors cannot perform the estimated 500 MFLOP processing required for the maximum value projection algorithm.

Three image/signal processing architectures are being examined to perform this heavy processing. One approach is to use the Data Cube image processor which MIT/LL will use in early CCD camera testing. A second approach utilizes VME boards with Digital Signal Processing (DSP) chips such as the TI C40 DSP chip. The third approach is to use a VME chassis with Intel i860 processors. Figure 5 depicts a candidate architecture of 13 i860 processors to perform the signal processing functions for sidereal tracking. There are ongoing trade studies to select the final architecture.

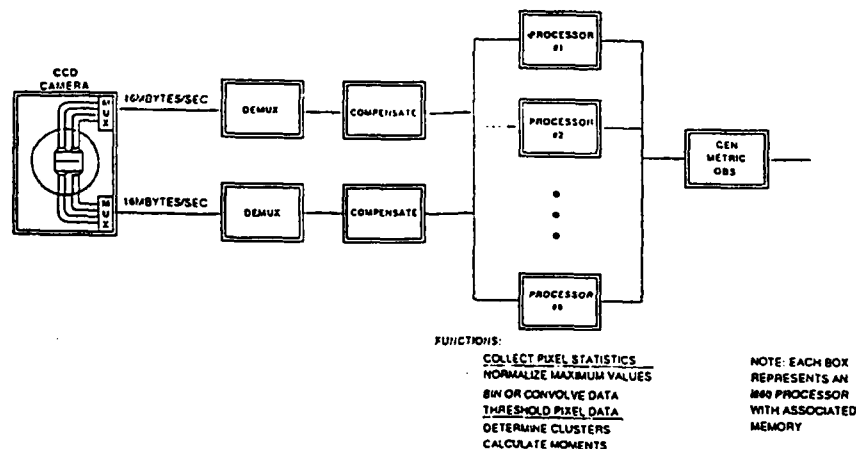


Figure 5. A Candidate GUPS Signal Processing Architecture

#### 4.4 SOI Data Collection

The CCD chip and camera support the collection of Space Object Identification (SOI) data in addition to collecting metric observations. The chip has a 32x32 photometric array for collection of SOI data.

Once an object has been detected and is in autotrack, the Sensor Controller will adjust the mount slewing rates so that the object appears on the 32x32 subarray. Closed-loop autotracking will continue on the subarray during SOI data collecting. Autotracking allows the collection of SOI over extended time intervals.

GUPS will collect SOI data at 100 samples per second and will be able to estimate the intensity of each sample accurately to +/- 0.25 Visual Magnitudes. GUPS will also employ multiple filters over the array allowing collection of multi-spectral SOI data.

#### 5. Exclusion Zone Sensor

The GUPS program will also develop an Exclusion Zone Sensor (EZS) which determines sky visibility data at the local sensor site. The EZS will utilize a CCD sensor but it is functionally similar to the "Pansky" developed by MIT/LL which used a Vidicon tube.

The EZS will generate a map of cloud cover over the sensor site and will also identify an exclusion zone around the moon. This data is transmitted to the scheduler so that it can determine those sky areas where objects can be successfully tracked and areas which should be avoided. For remotely controlled systems, the EZS mapping data can be transmitted to the remote control location for use in its scheduler.

#### 6. Test Simulators

Figure 2 illustrates the GUPS Operations Shelter which will eventually contain a fully operational Data Processing and Scheduling (DPS) Subsystem. The GUPS program is not tasked to develop a full capability DPS system (it will be developed on GMP). However, GUPS is developing a sophisticated test driver, termed the DPS Simulator, which will exercise the complete functionality of the Sensor Controller.

The DPS Simulator will provide a Graphical User Interface (GUI) for the operator. It will be able to receive and manage a space object catalog from the SSC and will have SPG4 orbit propagation software. The DPS Simulator will have a simple scheduling system which can automatically select tasks for metric or SOI data collection and issue the appropriate commands to the Sensor Controller. The DPS simulator will also receive the EZS map and use it in during scheduling. The GUPS DPS Simulator will provide the foundation and infrastructure for an operational DPS.

## Angles-Only Data Association in the Naval Space Surveillance System

P. W. Schumacher, Jr. and D. A. Cooper  
(Naval Space Command, Dahlgren, VA)

### ABSTRACT

The Naval space surveillance system operated by Naval Space Command (NAVSPACECOM) provides redundant, time-coincident, angles-only observations on most of the current satellite catalog. This paper describes the means by which the system associates the observations with cataloged element sets. The catalog maintenance process is, in reality, an exercise in tracking multiple non-cooperative targets with multiple sensors of various type. Such a scenario is known to present potentially severe difficulties in data association, especially when the number of targets rises into the thousands. However, for many years, the NAVSPACECOM system (and the space surveillance network in general) has achieved a high level of reliability in data association, even though more than 8500 targets are currently in track. Some reasons for this success are mentioned.

In addition, a software and computer hardware modernization is now being completed for the NAVSPACECOM system. Among the upgrades is the ability to associate angles-only data from any type of sensor, in particular, optical telescopes. An interesting constraint was imposed on the development of this capability. Because of stringent resource and time limitations, it was required that the validation of the new catalog maintenance software system be complicated only minimally by the inclusion of new data association processing. This requirement led to the development of association gates for the line-of-sight unit vector that are compatible with position-data association gates used elsewhere in the system. The derivation of these gates is described briefly. Association of angles-only data with cataloged element sets does require some kind of comparison against each and every element set. However, it is shown how some simple auxiliary comparisons based on computed range to a nominal plane ("pseudo-range") permit one to filter out many candidate element sets geometrically, leaving only a small fraction of the cataloged element sets to be propagated to the time of the observation.

### INTRODUCTION

In recent years, data association has been recognized as one of the most difficult aspects of multi-target tracking, especially in non-cooperative tracking situations where the kinematic tracking data themselves are the main or only basis for target identification [1,2,3,4]. The association problem always tends to get worse geometrically with the number of targets, so that even the best

association schemes known become computationally unfeasible when the number rises above some threshold. With currently available algorithms, that threshold is usually in the range of several thousand targets. Hence, from this point of view, space surveillance is potentially a very difficult problem: the current catalog of Earth satellites contains more than 8500 objects. All of these are tracked as non-cooperative targets by United States Space Command (USSPACECOM) and its component service commands, using several dozen radar and optical sensors located around the world. Currently, more than 100,000 observations are processed daily to estimate updated orbits for all satellites. But there are some interesting reasons why the data association problem for this tracking scenario did not become unfeasible long ago:

(1) An essentially complete and up-to-date catalog of satellite orbital elements has always been maintained at a central facility (the Space Surveillance Center (SSC) at Cheyenne Mountain AFB and the Alternate SSC (ASSC) at NAVSPACECOM). Moreover, the catalog has always been available to all of the sensors. In other words, we have never had to generate the catalog of more than 8500 objects ab initio. Such a massive data-association task is probably unfeasible with current space surveillance capabilities.

(2) Satellite orbital motion can be modeled rather well compared to the motion of other high-interest targets such as tactical missiles. Moreover, the timescale of orbital motion is such that a tracking network response to an event within tens of minutes is adequate for most surveillance purposes, allowing opportunity for extensive computation.

(3) The vast majority (at least 95%) of currently cataloged objects neither maneuver, split into several distinct satellites, nor use evasive measures to prevent detection.

(4) The space environment provides a relatively low-clutter background for most of the sensors, so the number of false detections reported to the SSC/ASSC is extremely low.

(5) The current catalog size implies a low enough spatial density of objects to prevent frequent confusion of targets. As a result, each sensor can reliably associate individual observations into tracks on a single target.

(6) Since the cataloging operation was started, computer and communication capabilities have continued to grow faster than the catalog size.

An important consequence of these factors is that each individual sensor can, with high probability, associate the correct satellite number with a new observation before the data are forwarded to the SSC/ASSC. Only a small fraction of the associations needed for catalog maintenance have to be made at the central facility. The association processing that is done at the SSC/ASSC consists mainly in verifying the satellite numbers supplied by the sensors (which may involve detecting and correcting the occasional mis-association), plus identifying the relatively small percentage of observations that the sensors could not associate. The latter identification process is the first phase of so-called "uncorrelated target (UCT) processing". Once associated, observations for each satellite are merged into a cumulative central-level track file which is used to update the orbital elements of the satellite. The updated elements are then distributed to all the sensors for use in acquiring future observations.

This two-tiered, sensor-level-plus-central-level approach to data association has always been a fundamental feature of the satellite cataloging operation. In general, it has been very successful. It turns out that, in the current space surveillance network under routine operating conditions, about 90% of the observations are correctly associated by the sensors, making the central-level verification process relatively fast. Of the 10% remaining, about 94% turn out to be already in the catalog after all [5]. Hence, a refined search of the entire catalog is always made at the SSC/ASSC to try to identify the observation before declaring that the data belong to some uncataloged object. The high success rate at the sensor level is what makes it feasible to do this refined search at the central level. Of course, it may happen that a new object has in fact appeared, and that a new element set must be created and examined for inclusion in the permanent catalog. This is the second phase of UCT processing. It involves track-to-track association for an unknown number of targets, and is beyond the scope of the present discussion. In this paper, we are concerned only with the verification and identification steps, with emphasis on the class of angles-only data.

#### THE NAVSPACECOM SPACE SURVEILLANCE SYSTEM

The main angles-only sensors in the current USSPACECOM inventory are the Naval space surveillance (formerly NAVSPASUR) radar interferometer system, operated by Naval Space Command, and the Ground-based Electro-Optical Deep-Space Surveillance (GEODSS) telescopes, operated by Lincoln Laboratory and Air Force Space Command. Because high-altitude objects have relatively low apparent angular motion, the GEODSS association procedures can afford to be rather involved, and may even include some real-time feedback from central level to sensor level. On the other hand, the NAVSPACECOM system was designed to track primarily near-Earth objects, which

are fast-moving and more numerous than high-altitude satellites. Consequently, the simplest possible sensor-level association procedures are preferred in this regime.

The NAVSPACECOM system observes essentially all near-Earth satellites having orbital inclinations of  $30^\circ$  or greater, a majority of the total population. Currently, it records more than 60,000 station-satellite passes, and forwards about 11,000 triangulated satellite positions to the SSC, daily. The system is a continuous-wave multi-static radar interferometer consisting of three transmitters and six receivers located across the southern United States. The transmitters radiate at the single frequency of 216.980 MHz, and the receivers are designed to detect signals that are Doppler-shifted by up to 15 kHz from this value. By design, the transmitter and receiver beams are confined near an Earth-fixed great-circle plane inclined at about  $33^\circ$  to the equator, forming a radar fence. The station locations span a  $35^\circ$  arc of longitude between  $243^\circ$  and  $278^\circ$  east, and coverage of satellite passes between these limits is assured for near-Earth orbits having inclinations above  $33^\circ$ . Over the Atlantic and Pacific Oceans, coverage is altitude-dependent because of horizon limitations, but does extend to orbits of lower inclination. Though its strength is in detection of near-Earth satellites, the system routinely makes detections at slant ranges of more than 25,000 kilometers and occasionally at ranges of more than 40,000 kilometers, giving it wide coverage in both altitude and longitude. The primary system observables are values of east-west and north-south direction cosine measured nearly simultaneously at each of the six receiver stations. The system precision is among the best for high-volume space surveillance sensors: the standard deviation of east-west cosine residuals, reckoned over the entire catalog, is less than 0.0002, and it is known that orbit model errors contribute substantially to the residuals.

The ability of the NAVSPACECOM system to do highly reliable sensor-level data association on a large number of satellites is noteworthy, since it involves an approach that is unique in the current space surveillance network. Because the radar fence has a narrow beamwidth (roughly  $0.2^\circ$ ) in the north-south direction, it is possible to predict, to within nearly the accuracy of the element set itself, when and where a cataloged satellite will be detected by the sensor. This feature, in turn, makes the sensor-level association processing simple and fast: association is declared when the measured time, east-west cosine and Doppler shift are within prescribed gates around predicted values of these parameters. All of the predicted fence-crossings for all satellites and visibility for all six stations for a 36-hour span are pre-computed, stored in a database and supplied to the association software via table-lookup on time values when any of the six stations reports a detection. The association subroutine itself is short and is integrated into the real-time fence observation data reduction software. Subsequently, when an element set is updated,

new fence-crossing predictions for the next 36 hours for that satellite are automatically computed and stored in the prediction database. Experience with this system for more than 30 years has shown that it routinely associates more than 96% of all observations correctly at the sensor level.

#### ASSOCIATION GATES FOR NAVSPACECOM FENCE OBSERVATIONS

The idea of using an a priori gate for association in a multi-target tracking problem has well-known shortcomings. However, it turns out that the concept has been made to work quite well in routine space surveillance operations. This is basically a result of the fortuitous factors listed in the Introduction. Moreover, the association method used for NAVSPACECOM fence observations is tailored to the unique set of observables available with this system [6]. An unassociated fence observation consists of:

- time of observation;
- receiver station index number;
- Doppler shift (relative to any of three transmitters);
- east-west direction cosine.

Each prediction consists of:

- time of fence penetration;
- satellite index number from the catalog;
- list of visible receiver stations;
- time tolerance (orbit-and-time-dependent);
- position components in Earth-fixed Greenwich frame;
- velocity components in Earth-fixed Greenwich frame.

When an observation is received, all predictions within 30 seconds of the observation time are examined. The time tolerance in each prediction has been pre-computed by an empirical formula which represents the uncertainty in time of arrival at the fence as an increasing function of orbital period, magnitude of decay rate, and time from epoch. These trends are designed to accommodate known error trends in the satellite motion model.

Any predicted position which falls within the time tolerance is updated to the actual observation time by a simple rotation transformation accounting for Earth rotation since the predicted time. Of course, this step is highly approximate. It does not produce the same position that a fresh prediction would, but it does remove a large component of the actual position difference and it is simple enough for real-time processing even with relatively slow computers. Then the predicted east-west cosine for the particular station can be calculated straightforwardly in terms of satellite position and station position. The association gate for cosines is defined by relating the difference of cosines to the difference of the angles, to first order, as follows:

$$\Delta(\cos\theta) = (-\sin\theta) \Delta\theta \quad (1)$$



$$[\Delta(\cos\theta)]^2 = \sin^2\theta (\Delta\theta)^2 = (1 - \cos^2\theta) (\Delta\theta)^2 \quad (2)$$

Hence, the prediction is considered further if the cosine residual satisfies the relation

$$[(\cos\theta)_{obs} - (\cos\theta)_{pred}]^2 < 0.001225 [1 - (\cos\theta)_{pred}^2] \quad (3)$$

The numerical constant represents an angle tolerance of about 2°.

Finally, predictions which fall within both the time tolerance and the cosine tolerance are subjected to a Doppler comparison. Even a large Doppler gate will serve the main purpose, which is to screen out the occasional fortuitous alignments of satellite positions with unrelated predictions. Currently, the Doppler tolerance is a fixed value of 310.0 Hz. Predictions which fall within this tolerance of the observed Doppler value, as well as within the time tolerance and cosine tolerance, are accepted for association. Of course, because all predictions within 30 seconds of the observation time are considered, it may happen that more than one prediction meets the association criteria. In that case, a nearest-neighbor strategy is used: that prediction nearest to the observation time is selected. Closeness in cosine or Doppler is not considered. This completes the sensor-level association logic for the NAVSPACECOM fence system.

#### ASSOCIATION GATES FOR POSITION OBSERVATIONS

##### 1. The Verification Step

Most tracking radars in the USSPACECOM inventory supply measurements of satellite position. The position gates used at the ASSC for verification of sensor-level position associations are computed from the element set indicated by the sensor and are reckoned in the familiar radial-intrack-crosstrack frame for the time of observation. The association tolerances in these directions are computed by the following relations:

$$F = 0.01 + 0.0006 \log_{10} \left( \left| \frac{\dot{n}}{2} + 1.0 \times 10^{-21} \right| \right) \quad (4)$$

$$\begin{aligned} \text{radial: } DU &= \text{MAX}(0.003, F) a \\ \text{intrack: } DV &= 5.0 DU \\ \text{crosstrack: } DW &= 0.002 a \end{aligned}$$

Here  $a$  is the mean semimajor axis of the orbit in units of Earth radii and  $\dot{n}$  is the rate of change of the "mean" mean motion in units of radians per CTU<sup>2</sup> (1 Canonical Time Unit = 13.44685108 minutes). The dimensions of the gate reflect the typical situation in which the predicted position uncertainty is greatest in the intrack direction and smallest in the crosstrack direction. For

example, for a near-Earth zero-decay orbit we would obtain roughly  $DU=20$  ,  $DV=100$  and  $DW=13$  , in units of kilometers.

At the ASSC, position observations which appear within their verification gates are passed immediately to the catalog update process. All other observations, regardless of circumstance, are passed to the identification process. Therefore, the possibility of accepting a mis-association does exist, if the sensor has made a mistake with satellites that are very close together. In practice, with the current catalog size, the probability of this type of mis-association turns out to be very low. In any case, mis-associations can usually be detected later as outlying data in the element set update.

## 2. The Identification Step

When position observations fail the verification step, or if the sensor could not associate them in the first place, they are subjected to a comparison against essentially the entire catalog. In the past, when the whole catalog maintenance process was executed in batch mode on a single large computer, the strategy actually was to compare each unidentified observation (or track) against a prediction from each and every element set in the catalog. Currently, however, some screening of the element sets is implemented so that the entire catalog does not have to be retrieved from the database for every unidentified observation. The reason for this change is that the new catalog maintenance system is designed as a real-time process running in a distributed computing environment. In the new environment, retrieving elements from the database takes much more time than the actual association computations. Hence, the best way to shorten the overall processing time is to minimize the number of element sets that have to be retrieved in the first place. Perhaps it should be added that each of the new computers is much faster than the old one, and that the former exhaustive-search identification strategy could meet all system requirements for observation data handling, even in the new distributed environment. But the new strategy greatly improves the association-processing performance margin and makes the whole system more robust.

Since most position observations are associated into single-target tracks at the sensor level, the first step in central-level identification is to attempt initial orbit determination (IOD) based on that single track. The screening of element sets in the database retrieval is done differently, depending on the outcome of the IOD. If a "sufficiently good" element set can be computed from the track, then the IOD process produces both the track element set and a single smoothed position near the middle of the track. Candidates are retrieved from the database only if certain tolerances in mean motion and cosine inclination are satisfied.

Fairly wide tolerances are adopted at this stage of association because the track element set is likely to have large errors and one would prefer to process some possibly unnecessary comparisons than to risk discarding the correct cataloged element set. In a typical near-Earth case, fewer than a hundred element sets are retrieved from the database, perhaps 1% of the current catalog.

On the other hand, if a "sufficiently good" element set cannot be computed from the track, then a measured position near the middle of the track is used. Candidates are retrieved from the database if the geocentric radius of the measured position lies between the epochal perigee and apogee radii, the latter being "padded" with a tolerance of about 20 nautical miles. One slightly worrisome factor to consider here is the decay in apogee and perigee between epoch and observation time. However, it has been found that the 20-mile tolerance essentially always includes the correct orbit up to 1 or 2 days from epoch. In a typical near-Earth case, several hundred element sets are retrieved from the database, noticeably more than when elements are screened on the tolerances in mean motion and inclination.

From here on, the same identification logic is used for each candidate element set, regardless of the one-track IOD results. The only difference is that either a measured position or a smoothed position, both denoted as  $\vec{r}_{obs}$  below, is being compared with predicted positions. Without executing the complete model of satellite motion, it is possible to eliminate some candidate element sets based on a simple plane comparison. In principle, the elements determine the orbital plane directly, and the nominal position must lie sufficiently close to this plane in order for the association to be possible. To make this comparison with a usefully small tolerance, however, it is necessary to update the orbital plane to the observation time to account for the oblateness-induced motion of the ascending node (which is why this test is not used to screen the retrieval of element sets from the database). The nodal regression rate at epoch is stored in the database, so a secularly updated unit vector normal to the orbit plane is easily calculated. If the observed position lies more than  $1.5^\circ$  from the predicted plane, it is rejected for association. If it does satisfy the plane test, a predicted position,  $\vec{r}_{pred}$ , is computed for the observation time using the full orbit model. Then if the cross-track position residual greater than about 25 nautical miles, or if  $\vec{r}_{obs} \cdot \vec{r}_{pred} \leq 0$ , the candidate element set is rejected for association. This test partly duplicates the plane check, but note that it is done after the full propagation of the element set, so that the candidate orbital plane is defined more accurately, and that it provides a tighter association criterion for medium- and high-altitude satellites (those above about 1780 kilometers altitude) than does

the previous plane check. Then the radial-intrack-crosstrack components of the position residual are used to evaluate the following quadratic form:

$$D^2 = (\vec{r}_{obs} - \vec{r}_{pred})^T M (\vec{r}_{obs} - \vec{r}_{pred}) \quad (5)$$

where  $M = \text{diag}\{1/a^2, 1/b^2, 1/c^2\}$ . Currently, a fixed value of the matrix is used with  $a=4$ ,  $b=40$  and  $c=1$ . The quantity  $D^2$  measures the size of the position residual in a way which accounts approximately for the differing prediction error trends expected. In particular, along-track error is allowed to be relatively large before it is penalized by this formula, mainly because drag effects are always poorly modeled. In the end, only the candidate element set with the smallest value of  $D^2$  is retained for possible association. This one is finally accepted if the observed position lies within the following gate:

$$(\vec{r}_{obs} - \vec{r}_{pred}) \leq \begin{cases} 20 \text{ n. mi. radial} \\ 200 \text{ n. mi. intrack} \\ 5 \text{ n. mi. crosstrack} \end{cases} \quad (6)$$

In effect, then, an ellipsoidal gate is used for identification, rather than a rectangular gate as in verification, and greater relative uncertainty is allowed in the intrack direction for identification than for verification. This completes the logic for central-level association of position observations with cataloged element sets, as implemented at NAVSPACECOM.

#### COMPATIBLE ASSOCIATION GATE FOR ANGLES-ONLY OBSERVATIONS

The NAVSPACECOM system is currently completing a modernization of software and computer hardware both at the six receiver stations and at the headquarters facility. Among the central-level enhancements being sought is an improved ability to associate angles-only data from any type of space surveillance sensor. In particular, it is highly desirable for the new system to be able to verify and identify observations from optical telescopes. However, an unusual constraint was placed on the development of this capability. Because of ongoing operations, as well as stringent limitations on resources and schedule, it was required that the validation of the overall catalog maintenance software system be complicated to a minimum extent by the inclusion of new data association processing. This requirement led to the development of association gates for the line-of-sight unit vector which are based on the position gates already discussed.

Briefly, the gates are just the geometrical conditions that the line-of-sight unit vector point within the projection of the 3-dimensional gate box on a plane normal to the predicted line of

sight at the predicted position. Because of the small angle between the observed and predicted line of sight, we accept a first-order approximation of the residual in the line-of-sight unit vector. Then, in algebraic terms, the conditions to be satisfied by the observed line-of-sight unit vector become

$$\begin{aligned} \rho |(\hat{u} \times \hat{\rho}_{pred}) \cdot \hat{\rho}_{obs}| &\leq |(DV) (\hat{w} \cdot \hat{\rho}_{pred}) \pm (DW) (\hat{v} \cdot \hat{\rho}_{pred})| \\ \rho |(\hat{v} \times \hat{\rho}_{pred}) \cdot \hat{\rho}_{obs}| &\leq |(DU) (\hat{w} \cdot \hat{\rho}_{pred}) \pm (DW) (\hat{u} \cdot \hat{\rho}_{pred})| \quad (7) \\ \rho |(\hat{w} \times \hat{\rho}_{pred}) \cdot \hat{\rho}_{obs}| &\leq |(DU) (\hat{v} \cdot \hat{\rho}_{pred}) \pm (DV) (\hat{u} \cdot \hat{\rho}_{pred})| \end{aligned}$$

where  $\rho$  is the predicted range,  $\hat{u}$ ,  $\hat{v}$ ,  $\hat{w}$  are the radial, intrack and crosstrack unit vectors respectively, and  $\hat{\rho}$  is the line-of-sight unit vector, either "observed" or "predicted" as indicated by the subscript. In each expression, the ambiguous sign is chosen to produce the largest absolute value on the right-hand side. This computation has been implemented in the NAVSPACECOM system with all vectors resolved in the Earth-fixed Greenwich (EFG) frame, and it is used for both verification and identification. If, in the identification step, more than one observation satisfies these conditions, the one selected for association is the one that gives the lowest value of the quadratic form

$$d^2 = (\hat{\rho}_{obs} - \hat{\rho}_{pred})^T B^T M B (\hat{\rho}_{obs} - \hat{\rho}_{pred}) \quad (8)$$

Here the matrix  $B$  transforms EFG vector components into radial-intrack-crosstrack components, and the matrix  $M$  is the same one used in the quadratic form for position residuals.

#### THE USE OF PSEUDO-RANGE IN ANGLES-ONLY ASSOCIATION

In order to identify unassociated angles-only observations, it is necessary to make some kind of comparison with every element set in the catalog. For example, given only a line of sight, it is not possible to exclude some element sets a priori based on apogee and perigee heights, as can be done with position data. On the other hand, some gain in overall efficiency can be obtained. In particular, once an element set has been extracted from the database, it may be possible to avoid execution of the entire orbit model needed to predict satellite position at the observation time, using comparisons based on the elements and angle data alone. Such a purely geometrical approach is now being implemented as a processing option at NAVSPACECOM.

The idea is simple. In principle, the orbital elements determine the orbital plane directly. The observed line of sight will intersect this plane in a single point, except in special

circumstances. The signed distance from the station to the point of intersection, called here the "pseudo-range", can be calculated easily. Requiring the pseudo-range to be a positive number screens out many unviable candidate element sets before they have to be propagated with the full orbit model. An optional and simple refinement is to screen additionally on a certain limiting-range condition. Finally, the point of intersection of the observed line of sight and the predicted orbital plane constitutes a "pseudo-position", which also can be readily calculated. Then it is possible to screen candidate element sets further, comparing pseudo-position magnitude with apogee and perigee distances just as in the case of position observations. The only complications arise in specifying suitable numerical values of tolerances within which all these conditions should be satisfied.

Without executing the entire orbit model, the unit normal vector  $\hat{n}_{pred}$  at the observation time can be approximated as before using a secular update. Now if the observation is indeed associated with the candidate element set, the satellite position vector  $\vec{r}$  satisfies the equation of the orbit plane:

$$\hat{n}_{pred} \cdot \vec{r} = 0 \quad (9)$$

Additionally, the observed line-of-sight unit vector  $\hat{p}_{obs}$  satisfies the vector triangle constraint

$$\vec{r} = \vec{R} + \rho \hat{p}_{obs} \quad (10)$$

where  $\vec{R}$  is the station position. Solve for the range as follows:

$$\hat{n}_{pred} \cdot (\vec{R} + \rho \hat{p}_{obs}) = 0 \quad (11)$$

$$\rho = - \frac{(\hat{n}_{pred} \cdot \vec{R})}{(\hat{n}_{pred} \cdot \hat{p}_{obs})} \quad (12)$$

We call this quantity the pseudo-range. Obviously, equation (12) can give meaningless results in cases where the denominator, or both numerator and denominator, are small. Consider now the four possible cases, keeping in mind that the term "small" must be suitably defined later.

- (i) Both numerator and denominator are "small". This case occurs when both the station and the line of sight happen to lie in the candidate orbital plane at the observation time. The pseudo-range is indeterminate, so no screening based on its value can be done. Consequently, the satellite position at observation time will be computed using the

full orbit model, and then angles-only association can be pursued as in the previous section.

(ii) The numerator is not "small", but the denominator is "small". This case occurs when the station is not in the candidate orbital plane but the line of sight is parallel to the plane. This case presents a dilemma.

(a) The pseudo-range is numerically undefined, tending to infinity. A conservative approach would assume that further screening based on this value cannot be done, so the element set must be propagated with the full model.

(b) On the other hand, we might be tempted to conclude that the line of sight must be directed at something other than an object in the candidate plane, just because it does not intersect the candidate plane. On this approach, the candidate element set would be eliminated from further consideration without full propagation.

Both approaches have been tried in preliminary testing, and the choice seems to hinge on assessments of overall system performance, as discussed later.

(iii) The numerator is "small", but the denominator is not "small". This case occurs when the station, but not the line of sight, is in the candidate orbital plane. The pseudo-range is well defined but "small", meaning that if the object is in the candidate plane then it must be "close" to the station. For ground-based sensor data, we ignore the small probability of such a circumstance and assume that the line of sight must be directed at something other than an object in the candidate plane. The candidate element set is eliminated from further consideration without full propagation.

(iv) When neither numerator nor denominator are "small", the pseudo-range is always well defined and further screening of the element set can be done, as described below, without excuting the entire orbit model.

If the pseudo-range turns out to be negative, then the line of sight intersects the candidate plane "behind" the observer. Thus the observation cannot belong to an object in the candidate plane, and the element set can be eliminated from further consideration. This simple "half-space" check is a relatively efficient screen since, on average, it alone can eliminate about half of the remaining candidates.

Situations can arise in which it is helpful to screen on some other limiting value of the pseudo-range. For example, if the pseudo-range is positive but turns out to be so small that the corresponding pseudo-position would lie inside the effective limit of the atmosphere, we might wish to exclude the element set from further consideration. Similarly, for various reasons, we might

wish to exclude all candidate satellites above or below any fixed altitude limit. We can easily accommodate such a condition by calculating the pseudo-range  $\rho_{LIM}$  corresponding to any fixed altitude limit  $h_{LIM}$ . For a satellite position at the given altitude, we have, assuming a spherical Earth of radius  $R_E$ ,

$$|\vec{r}|^2 = (R_E + h_{LIM})^2 = (\vec{R} + \hat{\rho}_{obs} \rho_{LIM}) \cdot (\vec{R} + \hat{\rho}_{obs} \rho_{LIM}) \quad (13)$$

This quadratic is readily solved for  $\rho_{LIM}$ . If an observation passes both the half-space check and the range-limit check, we then calculate the pseudo-position and compare its magnitude with the candidate perigee and apogee radii.

The comparison must take into account the uncertainty in pseudo-position magnitude, and for this purpose the following formula has been derived.

$$\delta r = \frac{\sqrt{5}}{r |(\hat{n}_{pred} \cdot \hat{\rho}_{obs})|} \left[ (R^2 + \rho^2) \delta \alpha + \rho \sqrt{2R^2 + \rho^2} \frac{\delta \beta}{u} \right] \quad (14)$$

where  $R$  is the station position magnitude. The quantity  $u$  is equal to unity for sensors that supply measured angles, and is equal to sine of the elevation angle for NAVSPACECOM direction cosine data. This equation provides a conservative estimate of the uncertainty in pseudo-position magnitude due to uncertainty in the observation, via  $\delta \beta$ , and in the orbital plane, via  $\delta \alpha$ . These two factors are parameters which can be adjusted empirically to make the comparison work well on real data. Nominally,  $\delta \alpha$  should be about the same size as the orbital effects neglected in the secular update of the plane, roughly  $10^{-3}$ . The factor  $\delta \beta$  should

be the same size as the measurement error (standard deviation). Errors in station position are neglected. Additionally, we must consider the uncertainty in the perigee and apogee. First, the perigee and apogee radii are given by

$$r_p = a(1 - e) \quad \text{and} \quad r_A = a(1 + e) \quad (15)$$

where  $a$  is the semimajor axis of the orbit and  $e$  is the eccentricity. Both of these elements are subject to drag-induced decay, modeled as secular effects in the NAVSPACECOM propagator by a very simple scheme [7]. When both elements have been updated in this manner, estimates of the perigee and apogee radii at



observation time are computed from (15) and the uncertainties in the radii are computed by

$$\delta r_p = [R_p(1 - e) + a]\delta\gamma \quad \text{and} \quad \delta r_A = [R_p(1 + e) + a]\delta\gamma \quad (16)$$

The adjustable parameter  $\delta\gamma$  is nominally the same size as the

neglected orbital effects in the decay modeling, roughly  $10^{-3}$ . Now we can summarize the perigee-apogee screening check. If the pseudo-position magnitude satisfies the inequality

$$(r_p - \delta r - \delta r_p) \leq r \leq (r_A + \delta r + \delta r_A) \quad (17)$$

then the element set is a candidate for association, and the full orbit model is used to predict the satellite position. If the inequality is not satisfied, then the element set can be rejected as a candidate without full propagation.

#### PRELIMINARY RESULTS

Preliminary testing has been done for all of the new angles-only association criteria described here, including the position-compatible gate and the pseudo-range screening, for a sample of about 4000 real radar observations (ignoring the range measurements). The usual position-only processing was used as the standard of comparison.

(a) The angles-only verification and identification, without pseudo-range screening, produces association percentages that are essentially identical to those from the usual position-only processing with retrieval of element sets based on IOD and perigee/apogee screening. Of course, the angles-only identification is slower than the position-only identification, by about an order of magnitude, because the whole catalog must be propagated for each observation.

(b) Once the element sets have been retrieved from the database, pseudo-range screening eliminates about 90% of them without full propagation. Requiring the pseudo-range to be positive eliminates about 50%, and the subsequent perigee/apogee check eliminates about another 40%. The other screens, such as the minimum-range criterion, together eliminate several percent. The net result is that, after the database call, the angles-only association processing is about an order of magnitude faster with pseudo-range screening than without, with no penalty in the association percentages.

(c) No rigorous logic has been found which resolves the dilemma mentioned in connection with pseudo-range screening, when the observed line of sight is parallel to, but not in, the candidate orbital plane. If one chooses always to propagate,

processing time is increased. If one chooses always to eliminate the candidate element set, processing time is shorter and the final results are almost always the same. Unfortunately, the possibility of discarding the correct element set is increased, which increases the overall system burden of UCT processing. For this reason, we are concentrating on the conservative approach, requiring more propagations but essentially never rejecting the correct element set. We expect that the dilemma arises only for a small fraction of any real data set, anyway; in our test data set, the fraction was about 0.3%. We also expect that some of these extra propagations can be eliminated by careful tuning of the adjustable parameters.

#### REFERENCES

- [1] Multitarget-Multisensor Tracking: Advanced Applications, Yaakov Bar-Shalom, ed.; Artech House, Inc., Norwood, MA; 1990.
- [2] Multitarget-Multisensor Tracking: Applications and Advances, Volume II, Yaakov Bar-Shalom, ed.; Artech House, Inc., Norwood, MA; 1992.
- [3] Tracking and Data Association, Yaakov Bar-Shalom and Thomas E. Fortmann; Academic Press, Inc., San Diego, CA; 1988.
- [4] Jeffery K. Uhlmann, "Algorithms for Multiple-Target Tracking", *American Scientist*, vol. 80, March-April 1992, pp. 128 - 141.
- [5] S. H. Knowles, C. N. Melson, E. L. Jenkins, D. L. Perini, "Uncorrelated Target (UCT)/Breakup Processing at NAVSPASUR"; NAVSPASUR Technical Report, U. S. Naval Space Surveillance Center (Naval Space Command), Dahlgren, VA; 15 February 1990.
- [6] R. Stephenson, "Identification Procedures in the ADR", NAVSPASUR Internal Memorandum (ca. 1989), U. S. Naval Space Surveillance Center (Naval Space Command), Dahlgren, VA.
- [7] "PPT2: The NAVSPASUR Model of Satellite Motion", NAVSPASUR Technical Report 92-01, July 1992, U. S. Naval Space Surveillance Center (Naval Space Command), Dahlgren, VA.

## **A UNIX-Processor Based High-Altitude Satellite Monitoring Capability That Uses Narrowband Signatures**

R.C. Raup  
Lincoln Laboratory  
Massachusetts Institute of Technology

Lincoln Laboratory has developed a monitoring capability for high-earth-orbit satellites that processes the narrowband radar signatures collected while the Millstone L-band radar tracks satellites for catalogue maintenance. The project reaches a major milestone this year by providing an operational capability at Millstone as a UNIX-processor based software system that could be transferred to other sensors and analysis centers. Detailed descriptions of the signal and data-processing algorithms and examples of data analysis have been presented previously.

In this presentation a chronological overview of the entire project is given - beginning with the collection of the first fixed databases, continuing through the design, testing and development of the algorithmic basis, the implementation of an automated background-processing system attached to the Millstone radar, and concluding with the engineering of a distributed processing system with an analysis interface using the MIT X Window System. Emphasis is on the concepts that were used to connect the results of a series of small efforts over several years of part time activity to bring the project to its present major milestone, and on the novel ideas in the signature processing system and the analysis interface.

We knew that it was difficult to maintain the amplitude calibration of a sensor over a long period of time, or even to determine the state of a sensor's amplitude calibration by examination of its data. For this reason, we chose to investigate the amount of fluctuation within the cross section time series produced during each satellite track, rather than the absolute cross section levels. This approach allowed amplitude calibration biases to vary from track to track without affecting our analysis. We only required that a constant amplitude bias be maintained within a single track. If the measured cross section fluctuation alone provided a useful measure of satellite performance, then our monitoring system would be more robust across the space surveillance network (SSN), and high performance levels for such a monitoring system would be easier to maintain.

We also knew that few cross section histories of high earth orbit (HEO) satellites showed any significant fluctuation at all. But the SSN (even a single sensor within the SSN) produces many signatures, so even if only a few percent of signatures show fluctuation there might be enough fluctuating signatures to analyze. Therefore the first phase of the project involved studying the amount of cross section fluctuation as a function of as many independent variables as possible, to determine if any patterns of satellite behavior emerged. The technical risk that we were accepting involved whether or not we could find such patterns, and whether or not the patterns could be used to monitor satellite performance.

The first phase was implemented by using a software system connected to the radar in 1988 that made several types of measures of cross section fluctuation and stored as many other observed variables,

including an orbital element set for the satellite, as possible. The system that we installed was general enough that individual experiments could be easily attached. About five experiments were eventually attached. One experiment was part of the project presently being discussed. One other experiment eventually lead to implementation of polarimetric processing at the site. We have since lost the capabilities provided by this initial software system, which was not ported when the computer it resided on became obsolete.

Our experiment measured, among other things, the amount of fluctuation in each satellite signature. Figure 1 illustrates the two types of signatures observed from three-axis stable HEO satellites: the common constant cross section type and the more unusual variable cross section type. The basis for measuring the amount of fluctuation depends on the fact that the constant cross section time series is mathematically a stationary random process, while the fluctuating cross section signature is not. Hence a normalized runs statistic computed from the cross section time series provides a real number indicating an amount of cross section fluctuation. This and most of the other technical details of the algorithms can be found in [1].

After waiting almost a year while the software system collected and compressed the required data, we returned to the project and analyzed about 6000 signatures in the data base. Preliminary results from the experiment were presented at [2]. Part of what we observed is illustrated in figure 2, which shows one of the observable patterns in the behavior of satellite cross section. These data are more recent than the experimental data base collected during the first phase of the project, but we observed this and other patterns in that original data base. Each data point on the two graphs result from a single satellite track. The vertical axes of the two graphs indicate the amount of fluctuation within the track, with data points near the bottom of the graph representing tracks with the greatest amount of fluctuation.

The top graph displays the amount of fluctuation as a simple time series. A small fraction of signatures fluctuate, seemingly at random. The second graph represents the same fluctuation data plotted versus the time of day. Now it appears that the fluctuating signatures do not occur randomly, but prefer particular times during the day. Organizing the fluctuation data around certain observation conditions became a key idea in the monitoring system. These ideas, and others, became important in the next phase of the project.

For the second phase, we decided to attach a software system to the radar that would not only collect the fluctuation data that we believed would be required to monitor the satellite status, but also include algorithms for first characterizing the HEO satellites based on their cross section fluctuation, then flagging unusual or changing fluctuation patterns, all based on what we had observed in the fixed data base that was collected and analyzed in the first phase. Most of the basic algorithm ideas could be tried against the fixed database, but additional work remained for which even the 6000 signature data base was too small. Data processing methods used to analyze the fixed data base had to be enhanced to operate with an open ended source of data, that might be collected from satellite birth to death, as the satellite progressed through changing operational phases; in one parlance the algorithms had to be made 'adaptive'. The fixed data base spanned at most a year in the life of any satellite. Would the extended algorithms designed from our small fixed data base work with the signatures collected over the life time of a satellite? That identified the technical risk that we accepted in implementing the second phase of the project. The resulting processing system is shown in figure 3. It uses a variety of statistical methods that have apparently not been applied previously to space object monitoring. These methods, including the treatment of satellite signatures as random processes, are probably novel in this application. It was put in service in March of 1992.

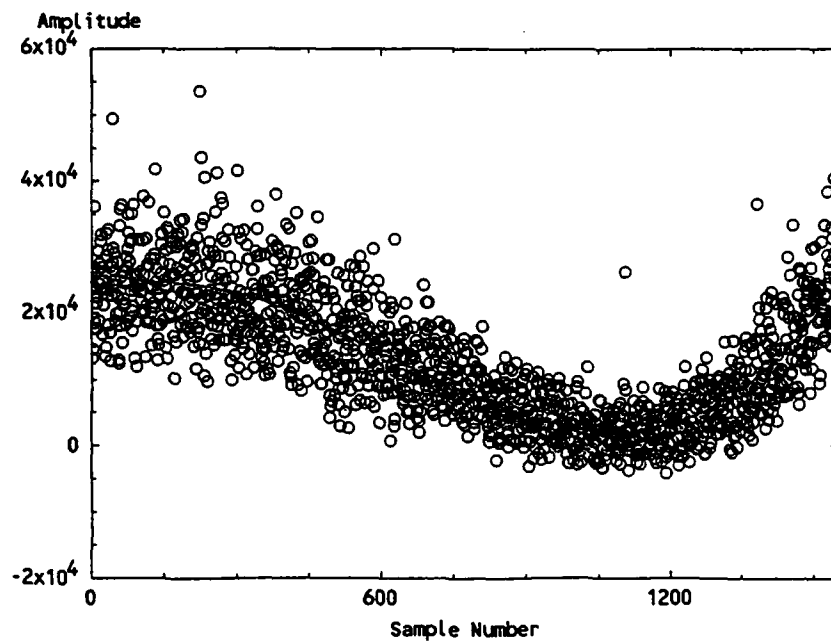
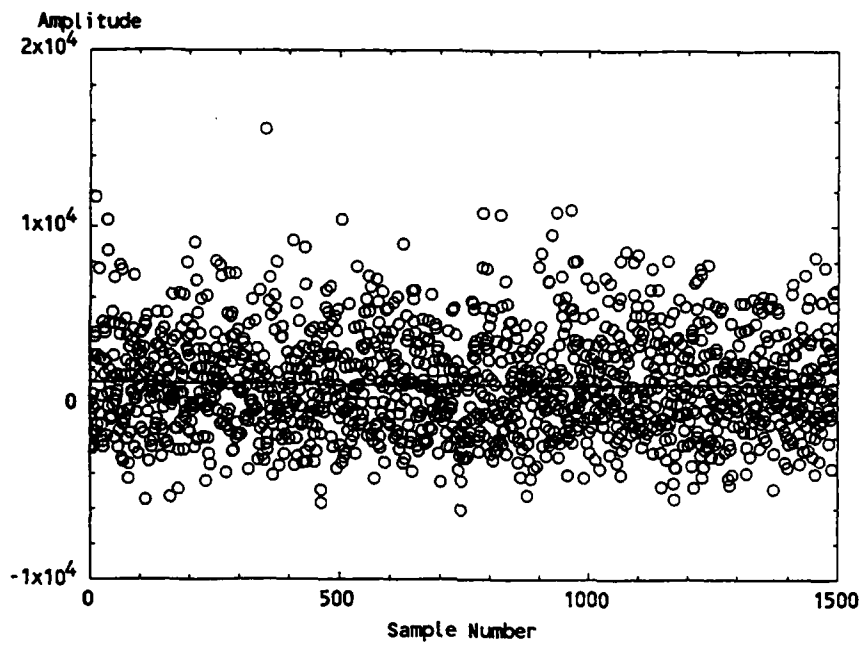


Figure 1: Sampled Satellite Signatures of the Constant and Variable Cross Section Type

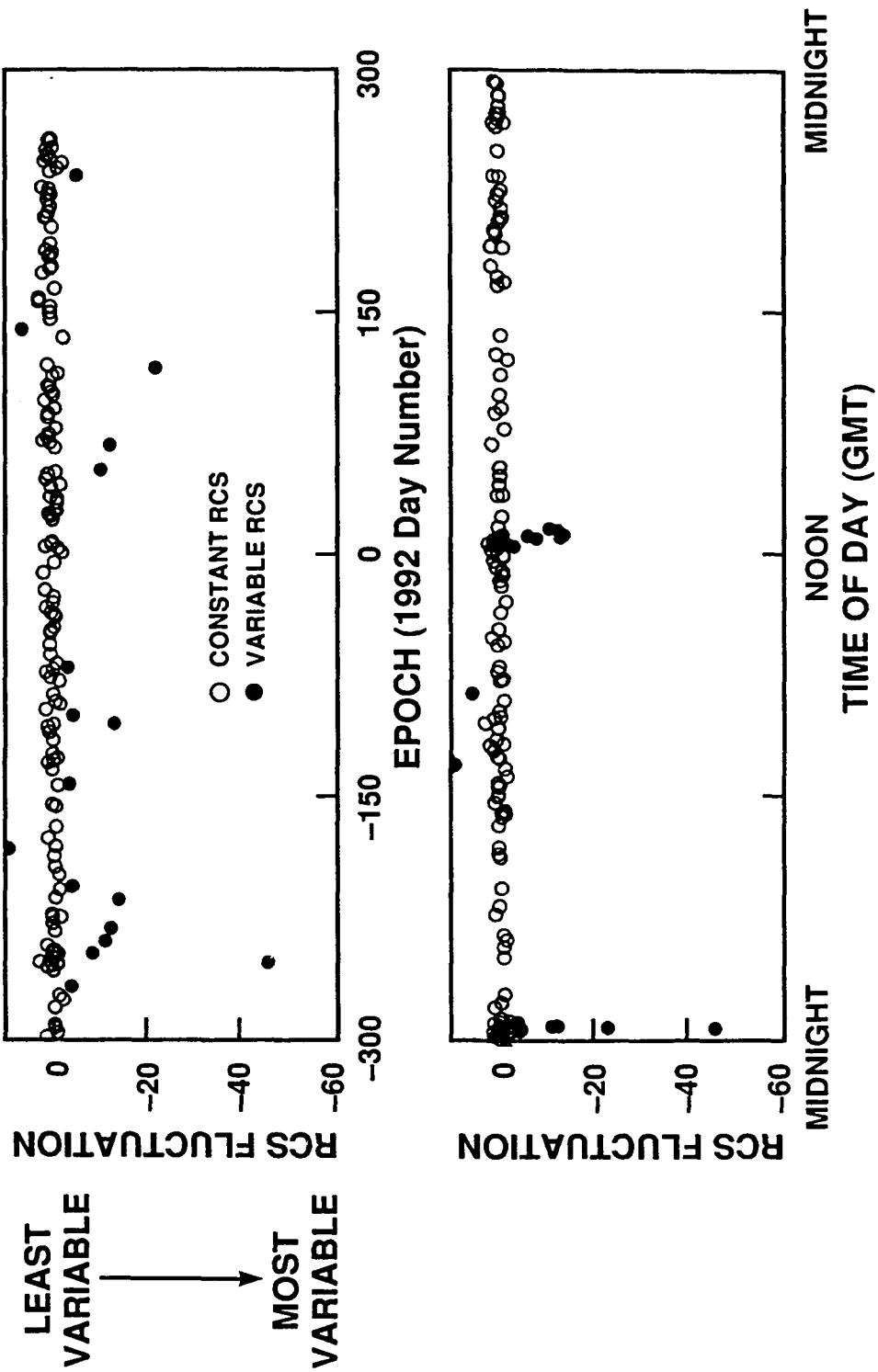
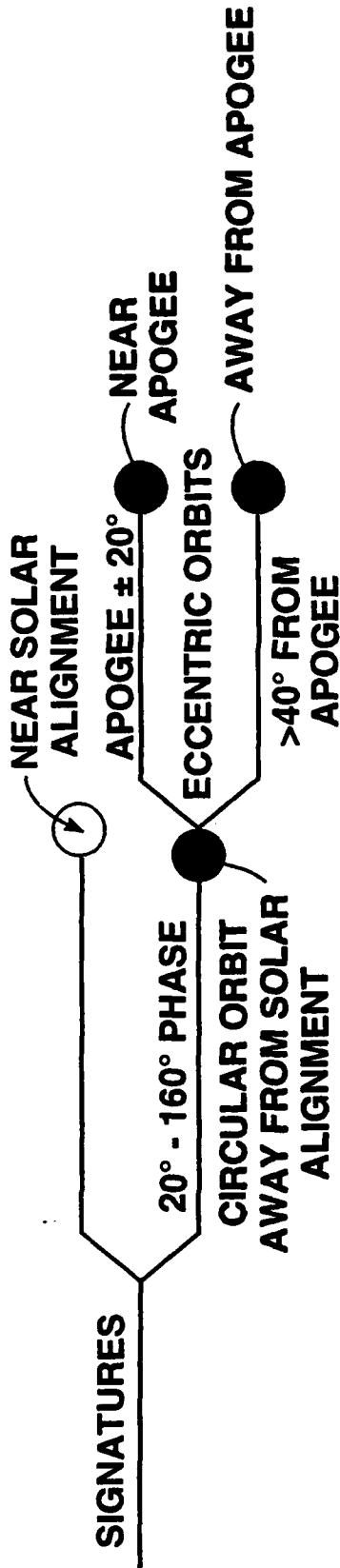
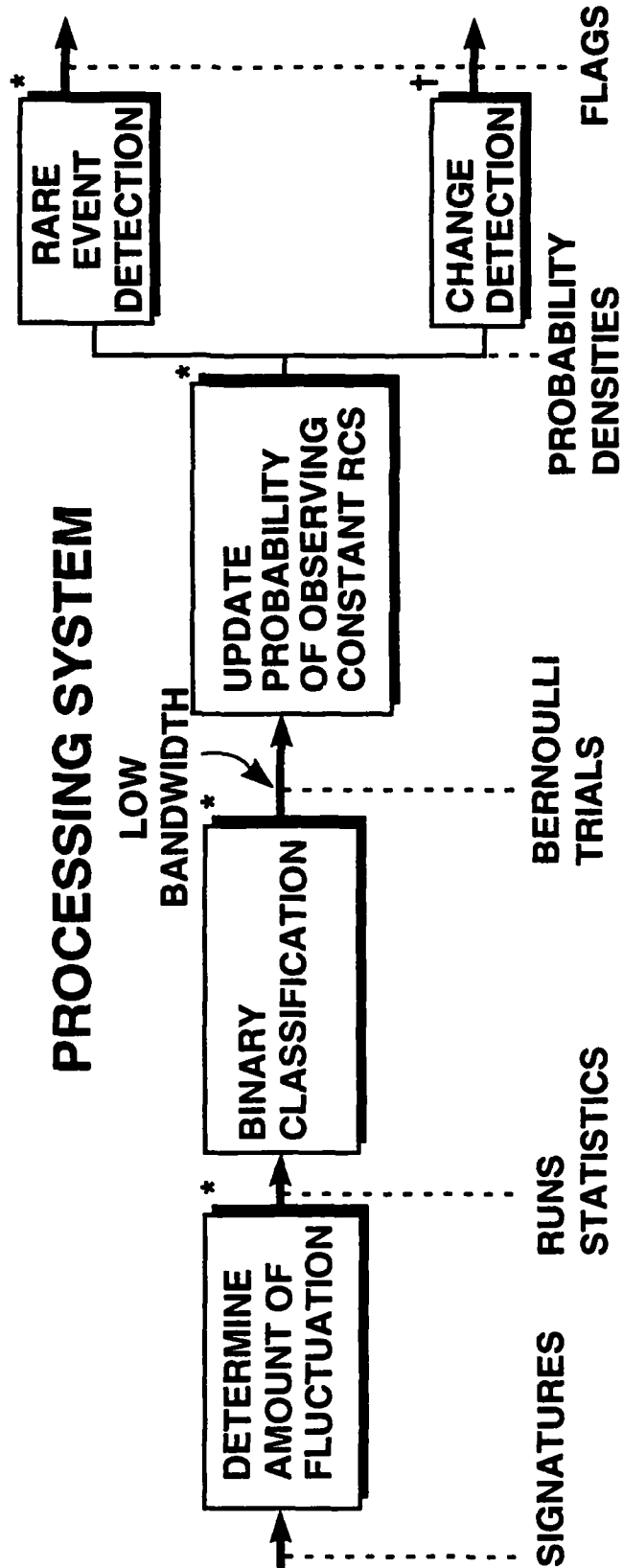


Figure 2: Amount of Satellite Cross Section Fluctuation as a Function of Different Independent Variables

# OBSERVATION CONDITIONS



# PROCESSING SYSTEM



\* TR 876 (1990), PROCEEDINGS 1990 S.S. WORKSHOP

† INTERNAL MEMO (1991)

Figure 3: Signal and Data Processing Overview

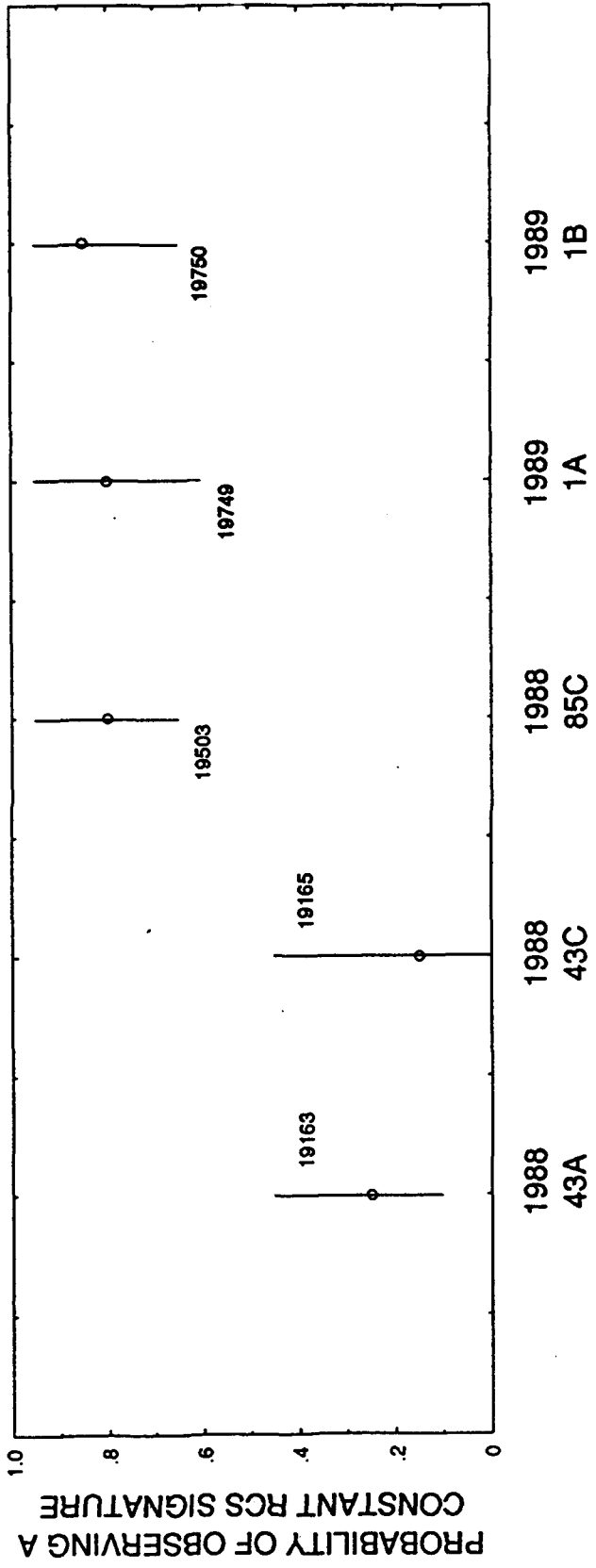
As implemented, the system autonomously processed all of the sensor's signature data, characterized all tracked satellites based on the fluctuation observed in its signatures, and flagged the anomalous signatures. We provided two simple ways to examine the contents of the data bases. First a graphics interface allowed examination of up to seven pre-defined 2-dimensional graphs for any given satellite. This graphics interface had limited interaction with the user, but allowed us the first real time access to the data base. Use of the graphics interface was limited to platforms running the X Window System on our local area net. Where computer-based local access was not possible, we experimented with an ascii summary that was computer generated and could be electronically transmitted, or printed as hard copy. Figure 4 shows one of the graphs that was available through the graphics interface, and an analogous portion of the computer generated ascii summary. Here each data bar represents the characterization of a satellite. All satellites represented are from the same orbital class, arranged from the oldest satellite to the newest. The bar spans the 95 % confidence interval for observing a constant cross section signature from the satellite. The figures illustrate that this class of satellites can be divided into two groups, roughly corresponding to their age. The algorithms autonomously handle such transitions in the characterization of the satellite over its lifetime.

The system performed adequately, but was comprised mostly of experimental software, and experience with the graphics interface suggested that there were many other ways to view and manipulate the data base that would be useful to an analyst. The current phase of the project concentrates on the system engineering and the graphics interface. The system architecture is being configured to make it more useful for transfer to other locations in the SSN. The graphics interface will be more flexible, and more readily extendable if the need for additional analysis tools becomes necessary. The interface can be used simultaneously with any other X Window System clients. There is no significant technical risk associated with this phase of the project, but we are constrained by time and budget to *demonstrate the new architecture later this spring.*

Figure 5 illustrates the distributed architecture. The various components of the system can be operated on different machines at distant locations on a network, or all on the same machine. Each sensor provides a data server that converts its particular data formats to a standard one described by an interface document. A sensor-based component of the system must be operated at the sensor to provide the signal processing for measuring the fluctuation in the signatures and maintaining a data base of results as well as the original signatures. There can be any number of sensors with sensor-based processing in the system. These results are made available to a data-processing component of the system. Only one is needed although multiple data processors could be operated. The data-processing component runs the satellite characterization algorithms and the anomaly detection algorithms. It also supports the analysis interfaces by providing data bases that are converted to graphic form by the interface. One or more analysis interfaces can be operated. The analysis interface is X Window based, and provides formatted text and graphics interactively for the analyst.

One of the novel aspects of the interface is the use of 2-dimensional graphics as an input device for the analyst. This provides some of the functionality of relational data base structures without the explicit use of expensive data base software. Figure 6 shows a typical window set-up. Note the mail and manual page browser - these and any X clients can be used along with the special interface clients, three of which are shown. The two dimensional plot is a modified xgraph client from the University of California that is currently displaying the amount of cross section fluctuation versus time for a satellite. The xgraph client has been modified to allow the user to select a data point with the mouse. An interclient communication system sends information about the selected data point to other clients in the interface system. Here a text-based summary of the satellite observation is automatically updated by the analyst's action. A command utility is also shown for selecting and displaying the various text and graphical information available to the analyst.



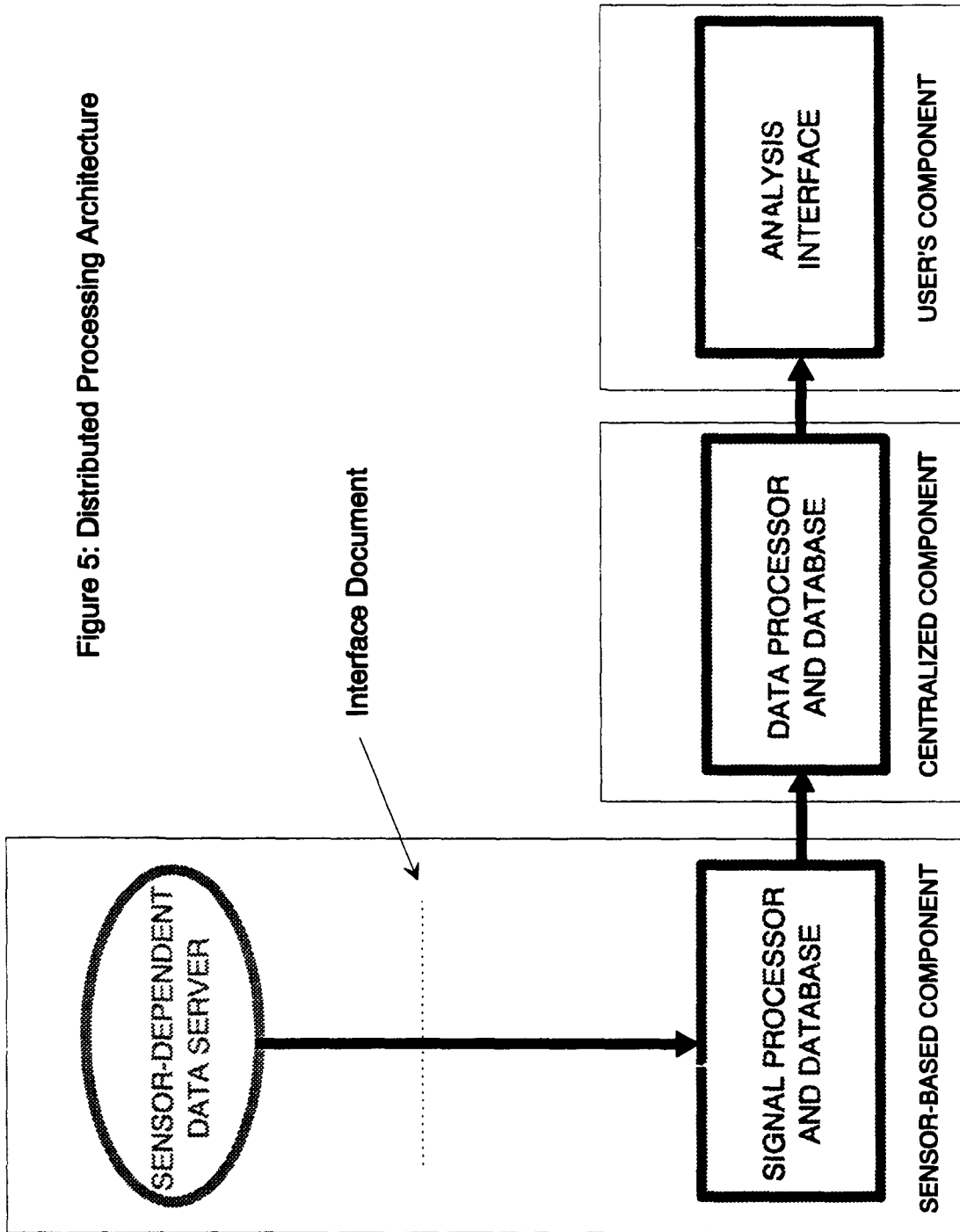


← OLDEST PAYLOAD → NEWEST PAYLOAD

OBJECT NUMBER	SIGNATURE	TRACK DUR	STATS	MEAN	STD	PROB OF OBSERVING CONSTANT RCS	GROUP	DATE/TIME	DUR	MOST RECENT TRACK
19163	43A	43	7	16	185	0	1	91 290/1812Z	217	VAREL
19165	43C	49	12	11	177	0.5	1	91 315/2121Z	122	VAREL
19503	85C	47	26	5	180	0.5	1	91 310/1617Z	145	CONST
19749	1A	60	19	4	167	0.5	1	91 315/2129Z	4	CONST
19750	1B	46	19	3	165	0.5	1	91 315/2153Z	40	CONST

Figure 4: Comparing the Stability of the Members of a Class of Satellites

Figure 5: Distributed Processing Architecture



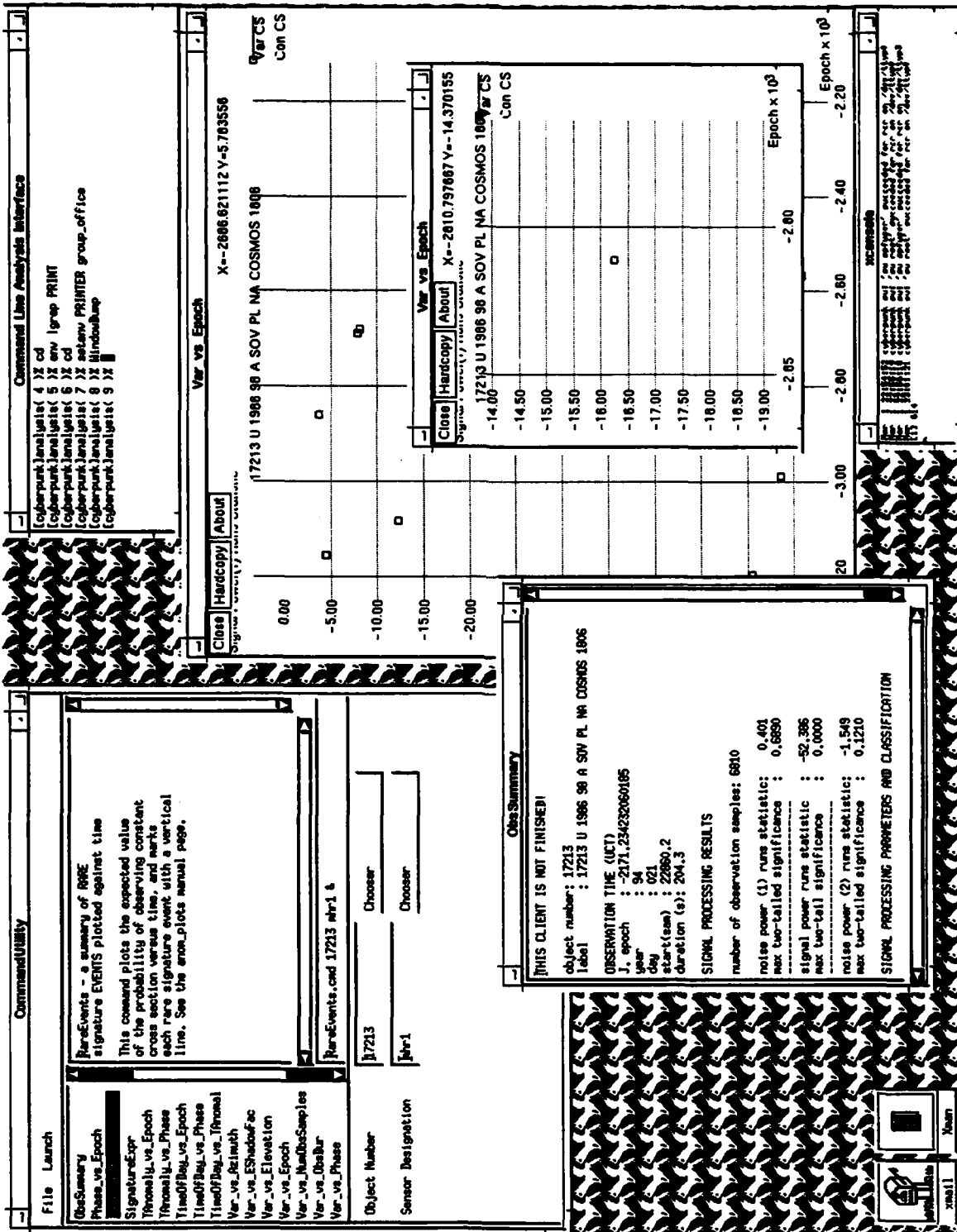


Figure 6: An Interactive Analysis Session with the X/Motif Interface

The project will have met its third major milestone this year. It has arrived at this point over a period of several years of part time effort and a series of decisions based on intermediate results. The advantage to taking such a leisurely approach is probably efficiency. We did very little "throw-away" work in the process of achieving these milestones, and the respite between phases allowed us to think and plan our next course of action.

The heavy utilization of statistical methods appear to be novel applications for satellite monitoring from narrowband signatures. Our X Window based analysis interface uses an unusual input scheme employing graphs to reduce the need for command line and menu inputs from the user. Our system is network transparent and as open as we could make it based on our knowledge of, and the state of UNIX standards.

Problems encountered included the loss of some capabilities achieved along the way due to replacement of computing platforms over the duration of the project; this is more reason to strive for open system implementations. This type of workstation project, for transfer to other sites and centers, never really achieves the economy of scale that can justify proprietary software such as those for graphical rendering and relational data bases. Therefore we did not employ them, working around them or using generously licensed software instead. Our method of using graphs as an input device for the analyst requires an interclient communication package for X. We have no knowledge of the availability of a suitable package, and the one that we developed is still fairly crude. X Windows would benefit from such a package, just as contributed X clients and the MOTIF widgets have made X more useful. We conclude that in spite of these difficulties, there is a role for small low level-of-effort projects such as this one that can provide significant new capabilities for the SSN at reasonable cost.

[1] R.C. Raup, "Bayesian Characterization and Detection of Rare Binary Signature Events," Lincoln Laboratory, MIT, Lexington Mass.: Technical Rep. 876 (15 March 1990).

[2] R.C. Raup and S.M. Hunt, "Background Monitoring of Space Object Status with a Single-Bit Signature Processing System," in *Proceedings of the 1990 Space Surveillance Workshop*, Lincoln Laboratory, MIT, Lexington Mass.

# **A Sensitivity Upgrade for the Millimeter Wave Radar at Kwajalein**

**J. C. McHarg  
MIT Lincoln Laboratory  
Lexington, MA**

**W. D. Fitzgerald  
Microwave Beam Systems  
Lexington, MA**

***Abstract*** - The Millimeter Wave Radar (MMW), an integral part of the measurement complex located on Roi-Namur in the Marshall Islands, is undergoing a hardware upgrade to improve its data collection capabilities at 95.48 GHz. Advances over the original RF system are explained and predicted performance is covered. With this upgrade, high quality 95.48 GHz images of many near-earth space objects will become routine.

## **I. INTRODUCTION**

The Millimeter Wave (MMW) Radar is one of a quartet of high-power coherent instrumentation radars located on the island of Roi-Namur at the north end of the Kwajalein Atoll in the Marshall Islands. It was designed and built to gather metric and signature data as a part of the Kwajalein Missile Range (KMR), which forms the terminus of the Pacific Missile Test Range. KMR is administered by the US Army Kwajalein Atoll with scientific direction supplied by Lincoln Laboratory. Together these four radars span the frequency range of 162 MHz to 95.48 GHz and perform tasks as disparate as deep space catalog maintenance, new foreign launch detection, high-resolution imaging, micro-dynamics measurement and impact scoring.

MMW is the youngest of the radars on Roi-Namur, having achieved initial operation at 35 GHz in 1983. At that time, the sensitivity on a standard target ( $1 \text{ m}^2$  cross section, 1000 km range,  $30^\circ$  elevation, clear weather atmosphere) was measured to be about 17 dB S/N. Though its original purpose was to gather data on re-entering vehicles, range-Doppler imaging has always been a major focus of its capabilities. It is only natural, therefore, that the radar has evolved to be able to also supply 35 GHz high-resolution images of near-earth orbiting targets.

The 95.48 GHz portion of the radar was brought on line in 1984 and was used to collect radar data on re-entry targets during 1984 and 1985. Though the initial results showed interesting effects unique to this frequency range, the measured sensitivity on a standard target of -2 dB S/N severely limited the targets against which this system was useful. In 1989, several of the 95.48 GHz components were removed to make way for a sensitivity upgrade of the 35 GHz RF system.

The initial sensitivity of the 35 GHz system was sufficient to provide quality data on re-entry targets, but was inadequate for imaging of many near-earth targets as well as for detailed mid-

course measurements. The power handling capability of the 35 GHz feed components had always been a limiting factor in this regard, so a sensitivity improvement at 35 GHz quickly focussed on replacement of standard rectangular waveguide with other energy guiding means.

The solution adopted in this case uses quasi-optical beams of RF energy and corresponding quasi-optical components to provide the RF signal processing functions normally performed by multi-mode tracking feeds, high power circulators and isolators, ortho-mode transducers and waveguide circular polarizers. Quasi-optics provides the advantages of simple mode structure, dispersionless propagation, low energy density and very low loss. These advantages will be explored further in the section on the 95.48 GHz beam waveguide system.

Started in 1987, the 35 GHz sensitivity upgrade is just now being finished. The beam waveguide was installed in 1989 and has functioned as predicted. The remaining portions of the upgrade, principally the combined operation of two final power tubes, have been slower to achieve predicted performance. Even before the final goals of the upgrade are accomplished, however, it is clear the project is a success. Sensitivity has been improved dramatically, leading to operation at more distant ranges and imaging of smaller targets. This achievement prompted optimism that similar improvements could be brought to bear at 95.48 GHz.

## II. 95.48 GHz SENSITIVITY UPGRADE SYSTEM

Using the experience gained at 35 GHz, a review of the 95 GHz system was undertaken. Included in this review were system sensitivity predictions, a survey of available technologies and an evaluation of possible applications. Concurrently, another evaluation effort was underway at Lincoln Laboratory regarding the use of the Haystack radar on Millstone Hill in Westford, MA, at W-Band [1].

Together, these efforts produced several significant results. First, many application areas were identified. Many of these applications had provided the early motivation to investigate 95 GHz operation, but significant progress in these areas is still needed. Examples include theater missile defense, active seekers for missiles, trackers for high clutter environments, target discrimination and atmospheric propagation effects. Applications which had emerged or had expanded significantly include space object identification, space-based radar and high-resolution imaging.

This last application is particularly appropriate for 95 GHz operation since W-Band is the only sub-infrared frequency band with more than 2 GHz of FCC-allotted bandwidth. In fact, using the full 8 GHz bandwidth and proven processing techniques, it is possible to envision image resolution approaching 2 cm.

The second outcome of the studies was an appreciation of the possible technologies that could be brought to bear on the construction of a 95 GHz radar. These include new power tubes based on the harmonic gyrotron, advanced high-power waveguides using quasi-optics or corrugated walls, Gunn-effect diode technology for driver amplifiers, cryogenic components for receivers and MMIC circuits based on pseudo-morphic HEMTs, HBTs or other exotic semiconductor device technology. It was found that some of these technologies were mature enough to employ immediately, while others would require significant development before being usable in the field.

The final major result, primarily pertaining to MMW, was the extent of the modifications necessary and the resulting sensitivity that could be expected for a given level of investment. In trading off project complexity vs. benefit, it was soon clear that two areas in particular could not

be salvaged from the original system. These were the rectangular waveguide feed, due to its high loss and low transmit/receive isolation, and the receivers, due to their high noise figure. In addition, two other subsystems were identified that could be modernized to achieve advantages in performance and reliability at moderate cost. These were the intermediate power amplifier and the stalo/upconverter, both of which originally relied on components which operated near their power limits and thereby limited their reliability. The final project block diagram is shown in Figure 1.

The remainder of the system was found to be adequate or expendable. In particular, the portions of the system which were shared with the 35 GHz system were, of course, fully functional, but also, too costly to duplicate. These include the antenna, subreflector and mount, the IF signal paths, the waveform generator, the digital signal processing, the recording system, the operator consoles and the calibration targets. In addition, it was found that the transmit tubes needed to be refurbished, but that a new tube development was not warranted. Minor upgrades to such things as high voltage supplies, transmitter modulators, protection circuitry, the feed support structure and the real time radar control program have been implemented as necessary.

The expected benefits from improving only these subsystems still provide a substantial increase in performance over the original system (see Figure 2). For example, replacement of the rectangular waveguide with quasi-optical components will result in more than 3 dB more radiated power and at least 3 dB less loss on receive. In all, the indicated improvements are expected to result in an 18 dB increase in sensitivity. This will yield a S/N on a standard target which is similar to that originally measured for the 35 GHz system and will allow 95.48 GHz images on near-earth targets to be generated for the first time.

### III. UPGRADE COMPONENTS

#### A. QUASI-OPTIC BEAM WAVEGUIDE (BWG)

The major advance which makes this sensitivity upgrade practical is the replacement of the rectangular waveguide feed with its quasi-optical equivalent (see Figure 3). C. Goubau and F. Schwering first described a transmissive BWG system in 1961 [2]. Many advances have been made since then; a thorough review by P. Goldsmith [3] provides a bibliography of recent as well as reference works. As outlined in [4] the mode structure of BWG systems is simply and accurately described by a few equations. Properly designed, the beam system displays an electric field distribution which is Gaussian distributed in amplitude transverse to the direction of propagation and which, due to the relatively small number of wavelengths in the transverse distribution, diffracts as it propagates. Thus, in order to maintain workable limits to the size of the RF components, the beam must be periodically re-focused. This can be done either with transmissive optics (lenses) or with reflective optics (mirrors). MMW's BWG systems employ a combination of optics types.

One of the chief benefits BWG provides for MMW is increased power handling capability. For example, at 95.48 GHz, standard WR-10 waveguide in the fundamental mode reaches electric field breakdown at about 15 kW. Though this value can be altered somewhat by the use of dielectric gases and high pressures, significantly higher power levels require lower energy densities. BWG systems provide such power densities. The BWG system soon to be operational, for example, can theoretically handle powers of at least 675 kW without encountering electric field breakdown. In practice, neither technology approaches the theoretic value due to field concentrations near signal processing components. It was precisely for this reason that the original 35

GHz system used four high power circulators in parallel to isolate the transmit and receive paths. But here, too, BWG systems often have an advantage, since their simpler component designs lead to less field concentration.

The high power circulators present in most radar systems represent another limitation to performance, namely their relatively high loss. In contrast, the BWG system in Figure 3 shows a high power circulator consisting of two wire grids and a  $45^\circ$  Faraday rotator. The wire grids function as polarization filters and are arranged so as to pass the transmit signal without reflection. The Faraday rotator functions as the non-reciprocal element, rotating the signal polarization independent of the direction of propagation. Thus signals that traverse the Faraday rotator twice are polarization shifted by  $90^\circ$  and emerge parallel to the wires of the wire grid and are reflected into the receive path. This system, even at 95.48 GHz, has a loss of less than 0.5 dB, as compared to the almost 3 dB loss in the waveguide circulator in the original system. Loss reduction isn't limited to components, however. In practice, even straight runs of WR-10 waveguide display a loss of about 0.1 dB/inch, but the only significant loss mechanisms in a well-designed BWG system other than component loss are the beam truncation effects and the finite conductivity of the mirror surfaces. Both of these loss contributions can usually be kept to levels that are difficult to detect.

Another advantage to BWG systems is in the reduction in component complexity. This is perhaps most noticeable in the area of horn design. Conventional rectangular waveguide systems must have a horn that is suitable for both transmit and receive functions and that must handle high power. In a BWG system such as that shown in Figure 3, the transmit and receive paths are separated, allowing the transmit horn to be optimized for high power while the receive horns are optimized for mode purity. Other examples of reduced component complexity include BWG polarization filters, which are made of wire grids and have near-perfect performance, and matching structures, which are generally one- or two-step quarter wave structures providing wide bandwidths and low return loss.

Still another advantage to BWG systems is the high isolation between transmit and receive paths. In the 95.48 GHz system, for example, low reflections from the various components, combined with mechanical separation of the forward and reflected beam paths are expected to combine to yield transmit/receive isolation in excess of 45 dB. At this level, the receiver protection devices necessary in a conventional system are no longer required. Should the actual performance be even better, secondary effects, such as the return loss of the Cassegrain system itself, become the dominant limitations to transmit/receive isolation.

One of the strengths of transmissive optics is that to first order, all the components necessary for high-power radars can be manufactured to maintain a high degree of mode purity. This implies excellent PP-OP isolation, as well as highly accurate angle measurements. Unfortunately, the lenses required for periodic refocusing represent limitations in system loss and return loss.

For these reasons, reflective focussing is used at MMW. The single mirror focussing element, however, suffers from relatively poor mode isolation. To escape this predicament, a new reflective configuration using closely-spaced mirror pairs was invented by one of the authors (Fitzgerald) for the 35 GHz system (Figure 4 and [4]). With such an arrangement, dubbed a clamshell from the appearance of the two mirrors assembled, first order errors introduced by the two mirrors cancel, so that acceptable mode isolation is achieved. The extra loss introduced by the second mirror is negligible, but this arrangement does reduce somewhat the usable space between refocusing elements in which to place RF signal processing components.



As this technique is most effective when the input and output beam parameters (i.e. the minimum beam radius and the distance from the mirror to the point on the beam axis at which the minimum beam radius occurs) are identical, the 95.48 GHz system has been designed to maintain the parameters which match the Cassegrain antenna focal point while providing a -10 dB edge taper at the subreflector. This value optimizes the efficiency of the antenna and yields a minimum beam radius of 9 mm. This, in turn, sets the typical transverse dimension of the 95.48 GHz BWG components at about 7.5 cm.

## B. CRYOGENIC RECEIVERS

The original 95.48 GHz system, which used room temperature mixers followed by low-noise IF amplifiers as the receivers, had a measured wideband system noise temperature of 2600° Kelvin. At the start of this upgrade, it was hoped that pre-amplification could be obtained at a reasonable noise figure to improve on this. Though laboratory experiments have produced transistors that have low noise and moderate gain at these frequencies, no commercial products are yet available to meet the needs of MMW in this area. Thus, to improve on the noise figure of the original system, the upgrade was forced to rely on cryogenic cooling of the down convert mixer and first IF amplifier to achieve the maximum noise figure improvement.

The resulting system uses a commercial helium compressor/refrigerator combination to achieve operation at a physical temperature of less than 20° K. This is a two stage system, with the first stage cooling an infrared shield to roughly 70° K, while the second stage maintains the electronics at about 16° K. Stainless steel waveguide components, flashed or plated with copper to reduce RF losses, conduct the RF signals to the mixers, while the IF signal from the cooled amplifiers is run through stainless steel coaxial line. Stainless steel is used because of its low thermal conductivity. Two channels provide for processing of both PP and OP data.

The mixers themselves use a balanced pair of whisker-contact Schottky barrier diodes. With sufficient LO drive, no external bias for the diodes is required. This reduces the operating adjustments necessary and increases the overload tolerance of the mixers. The first IF amplifiers are built for lowest noise performance at cryogenic temperatures and provide sufficient gain that succeeding stages do not contribute significantly to the system noise temperature. The design goal for the receiver noise temperature is 150° K and early results, shown in Figure 5, have achieved 270° K. Even at this higher level, however, the system noise temperature is expected to be better than 500° K, providing a sensitivity improvement of 7 dB due to this subsystem alone.

While operation at cryogenic temperatures is necessary to achieve maximum performance, the extreme time necessary to reach the final temperature (on the order of 4 hours) creates an operational risk for a radar like MMW. For this reason, every effort has been made to increase the reliability of the cryogenic components. Early mixers, manufactured with copper bodies to minimize RF losses were found to perform intermittently. This has been attributed to the difficulty in machining and cleaning copper parts and the resulting likelihood of burrs and misaligned parts and also to the thermal mismatch between the copper mixer bodies and the diode mounting posts, which are made of brass. These experiences led to a decision to re-make all the mixers using brass bodies. These new mixers have not failed in spite of repeated cycling and long-duration operation at temperature. In spite of this, it is an important receiver characteristic that failure of the refrigeration system not preclude radar operation. This is indeed the case and, in fact, is important in determining functional operation without the need to reach final temperature.

The mounting of the cryogenic receivers has caused perhaps the greatest difficulty with regard to the design of the mechanical structure of the upgrade. It has forced the existing structure to be augmented with a secondary support structure and has placed certain constraints on the design of the receive paths for the BWG. The need for low RF losses mandates the placement of the Dewar on the RF feed structure, and yet the compressor must operate in a horizontal position. This means the compressed helium lines must be run through the elevation cable wrap and are physically long. In spite of these considerations, previous experience with cryogenic systems (the original 35 GHz system had cooled receivers and the radar once sported a cooled radiometer) has shown that once in place the maintenance of the system is manageable and the improved performance is worth the operational costs.

### C. INTERMEDIATE POWER AMPLIFIER

The original 95.48 GHz system employed an IMPATT-diode locked oscillator as the driver for the final power tube. This unit was physically large, required water cooling and was, at times, a reliability concern. More importantly, it was found that the final power tube required more drive power at the edges of the frequency band than the driver could provide. For these reasons, a new amplifier was procured that is stable under all input drive powers, utilizes Gunn-effect devices rather than IMPATT devices and requires only convective air cooling.

The resulting design uses multiple stages of Gunn diode reflection amplification. The final stage operates two reflection amplifiers in parallel to achieve an output power of 200 mW. Due to the high degree of saturation in the last few stages (see Figure 6), the drive for the final power amplifier will be repeatable, flat vs. frequency and will be tolerant to device degradation in earlier stages.

### D. STALO/UPCONVERTER

Replacement of the stalo frequency multiplier and upconverter was driven by two considerations. First, the final multiplier stages were found to be operating too close to their thermal burnout levels, causing performance degradations over time. And second, it was realized that improved receiver performance could be obtained at increased LO drive levels. At the same time, current technology allows active multipliers to be used at higher frequencies, leading to lower drive levels and longer device lifetimes.

To take advantage of these technology improvements, minor changes in the frequency plan of the stalo multiplier were necessary. Figure 7 shows the resulting block diagram. Using this scheme, active multipliers can be used for the first two multiplication stages and the final multiplication can maintain reasonable input power limits. Physically separate electrical paths provide for transmission to the required destinations to be accomplished at low frequencies where low loss transmission means exist. In addition, the new design provides fewer total devices operating at lower powers with more maintainable technology.

## V. SUMMARY

A program to improve the sensitivity of MMW's 95.48 GHz radar capability is nearing com-

pletion. Predicted performance includes an increase in sensitivity of at least 18 dB. The improvement comes from advances in quasi-optic feed technology, which allows dramatically lower transmit and receive losses while improving transmit/receive isolation, from the incorporation of cryogenic receivers, which provide a marked decrease in the front-end noise power, and from the upgrading of the transmitter driver and stalo/upconverter to take advantage of newer semiconductor technology.

It is anticipated that the increased performance will spur studies of W-Band imaging, space object identification, re-entry vehicle discrimination and atmospheric propagation phenomenon. In this way, the current project is one in an ongoing series of upgrades intended to advance the measurement capabilities of the MMW radar. Indeed, all new components on this project have been specified so as to allow room for future performance improvements. In particular, upcoming projects to expand the transmit bandwidth and power at MMW have been accommodated.

#### ACKNOWLEDGEMENTS

The authors would like to express their appreciation to the Field Systems Group and the Radar Measurements Division at Lincoln Laboratory for their continuing support and encouragement in the pursuit of both the 35 GHz and 95.48 GHz sensitivity upgrade projects. We are also indebted to Robert Lucey, Jr. and Mohamed Abouzahra for their assistance at site in keeping this project flowing smoothly, to John Magnuson for his collection of measured data and to John Orthmann for his mechanical fabrication skills.

- [1] L. B. Spence and R. J. Temkin, "The Advanced Assessment Radar - A Haystack W-Band Upgrade," *Project Report ACC-6*, Lincoln Laboratory (Sep. 1992).
- [2] C. Goubau and F. Schwering, "On the Guided Propagation of Electromagnetic Wave Beams," *IRE Trans. Antennas Propag.* **9**, 248 (May 1961).
- [3] P. F. Goldsmith, "Quasi-Optical Techniques," *Proc. IEEE* **80**, 1729 (Nov. 1992).
- [4] W. D. Fitzgerald, "A 35-GHz Beam Waveguide System for the Millimeter-Wave Radar," *Lincoln Laboratory Journal* **5**, 245 (1992).



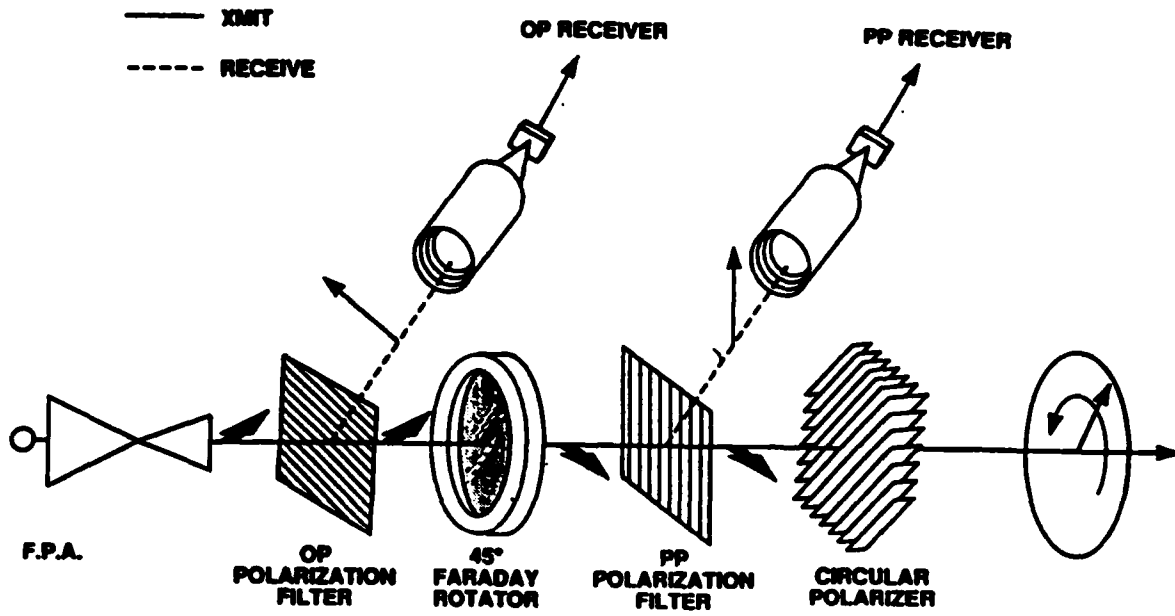


**FIGURE 3. 95 GHz BEAM WAVEGUIDE SCHEMATIC DIAGRAM**

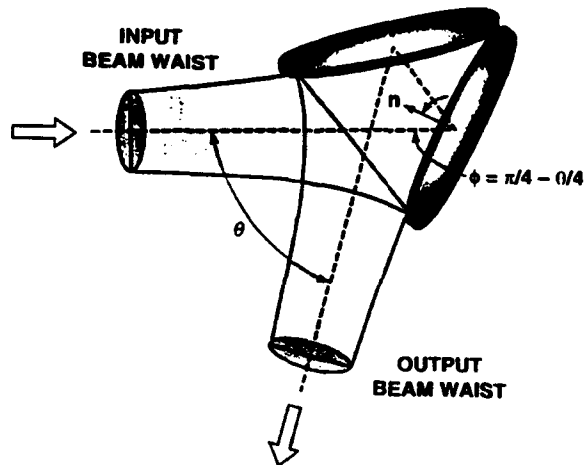


**FIGURE 4. TWO MIRROR "CLAMSHELL" CONFIGURATION**

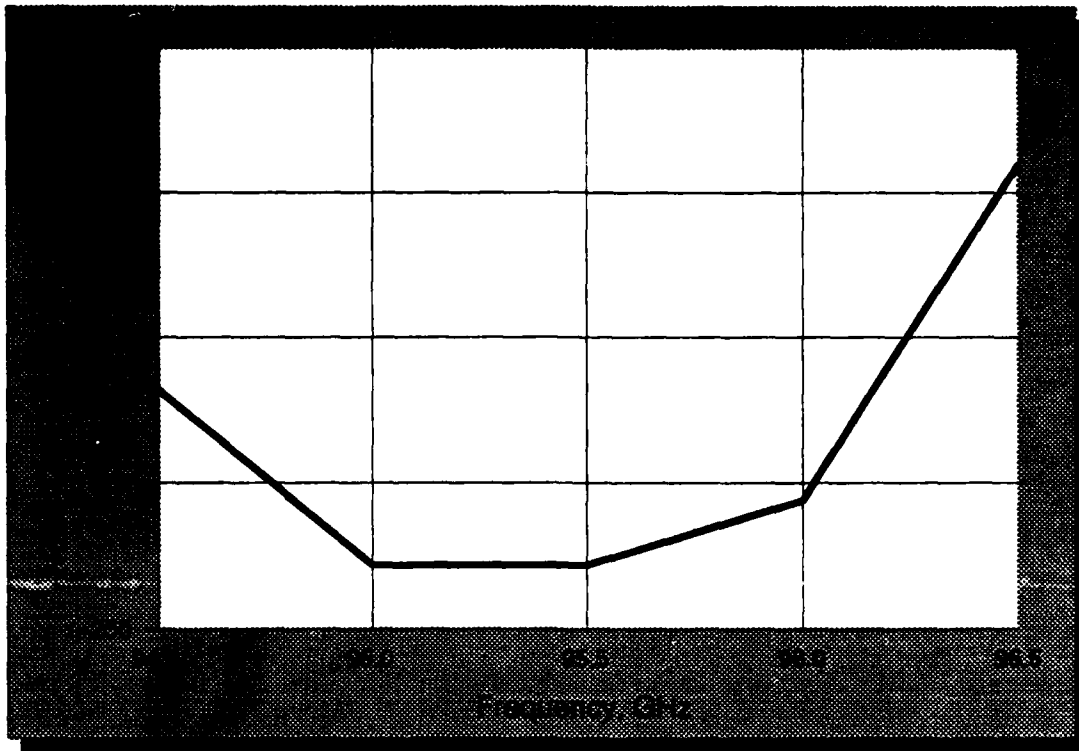


**FIGURE 5. MEASURED RECEIVER NOISE TEMPERATURE, PP CHANNEL**

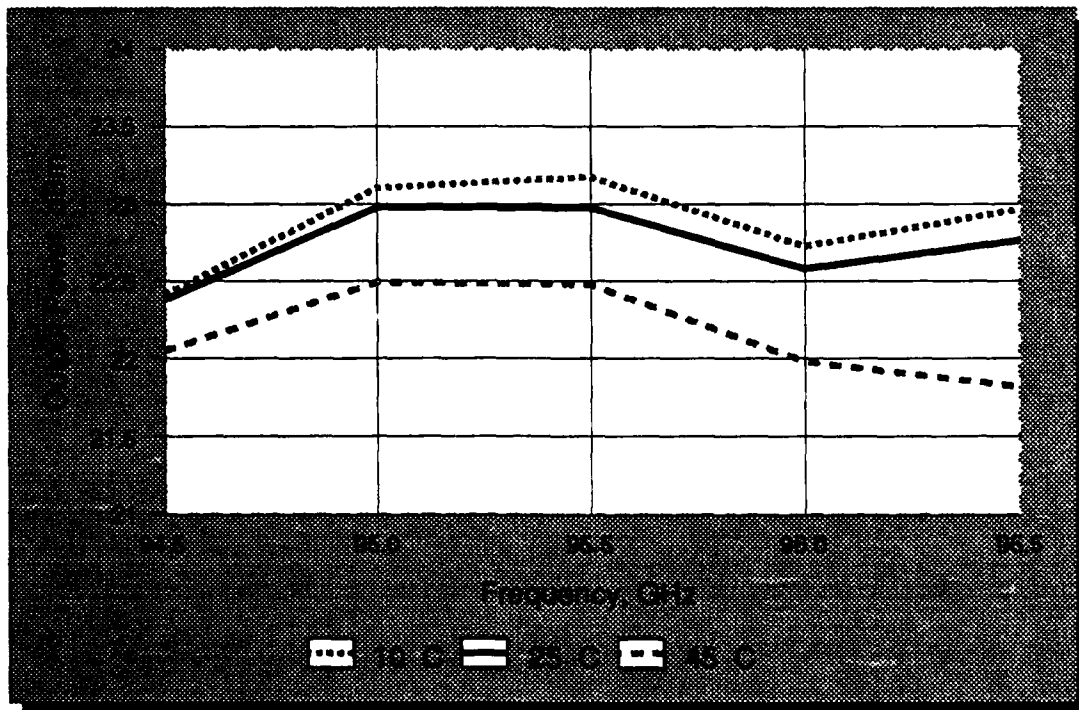


**FIGURE 6. MEASURED OUTPUT POWER, INTERMEDIATE POWER AMPLIFIER, S/N 196**

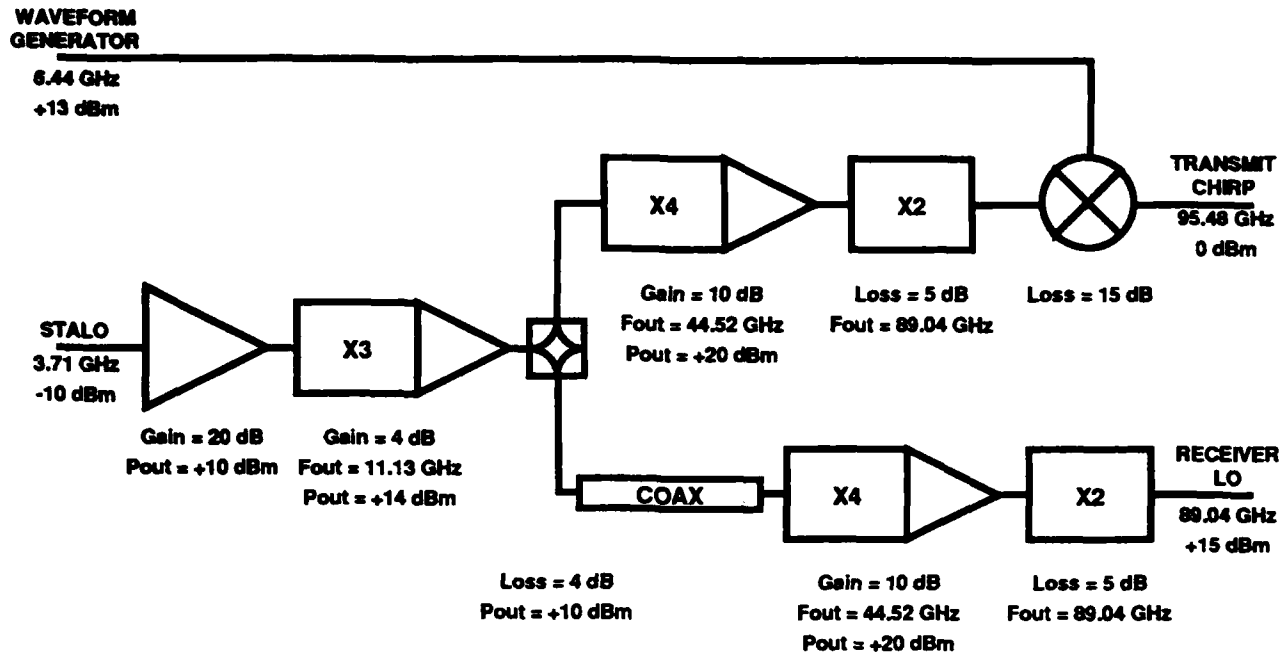


**FIGURE 7. NEW STALO/UPCONVERTER BLOCK DIAGRAM**

## **Recent Improvements at the ALTAIR Radar**

**Stephen J. Chapman, Andrew D. Gerber, Gregory G. Hogan, and Stephen M. Hunt (Lincoln Laboratory, Massachusetts Institute of Technology)**  
**Robert M. Anderson, John B. Conrad, Dale L. Sponseller, and Mark J. Schlueter (Raytheon Range Systems Engineering)**

The last year at ALTAIR was marked by the changeover of support contractor from GTE Government Systems Division to Raytheon Range Systems Engineering, Inc. As a result of that changeover, most development work was suspended for the six month period ending 1 October 1993. Development work resumed after that date, with the rate of development accelerating as new contractor personnel have become more familiar with the radar.

Despite the temporary hiatus, important work is underway or has recently been completed in six major areas of the radar. These areas are the topics discussed in this paper. They are

1. UHF Transmitter Expansion
2. Cable Wrap Upgrade
3. New-Foreign-Launch (NFL) System Upgrade
4. Extended Range System Upgrade
5. Improved Ionospheric Modeling
6. Deep Space VHF Data Collection

### **1. UHF Transmitter Expansion**

Until recently, the ALTAIR UHF transmitter consisted of 24 traveling-wave tubes (TWTs) connected in three banks of 8 tubes each. The combined peak power out of the transmitter was approximately 4.5 MW, with a 5% maximum duty cycle. The transmitter had originally been installed in the USNS Arnold, and was installed at ALTAIR after the Arnold was decommissioned.

The transmitter from the USNS Vandenberg (sister ship to the USNS Arnold) became available to ALTAIR about three years ago, and a decision was made to upgrade the ALTAIR transmitter using parts from the Vandenberg. An additional 8-tube group was added to the transmitter, for a total of 32 TWTs, along with a complete upgrade of the high power microwave combiner assembly, control panels, RF amplifier and fault display panels. All of these changes have resulted in a measured overall output power increase of 1.4 dB (302 kW average, 6.3 MW peak @ 0.048 duty cycle). The new transmitter configuration, which became operation in December 1993, is shown in Figure 1.

Other advantages resulting from the upgrade include increased sensitivity while operating with one or more transmitter groups shut down for maintenance or repair, and a large quantity of previously unavailable spare parts. Both of these factors will significantly increase ALTAIR's overall availability and contribute much to providing continuous support to its users in the future.



## ALTAIR FOUR GROUP TWT CONFIGURATION

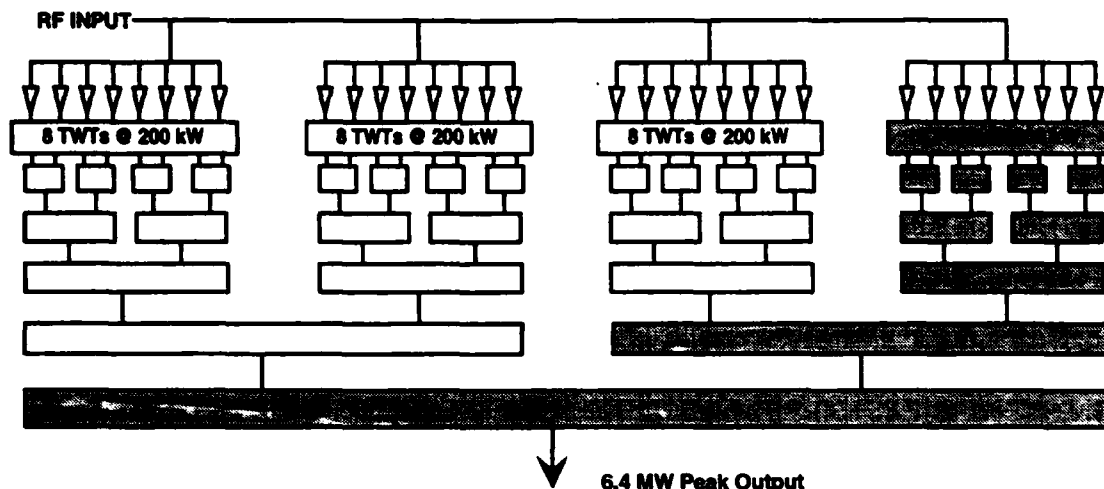


Figure 1: Configuration of the ALTAIR UHF transmitter. Thirty two TWTs are combined into four groups, producing a total peak power of 6.4 MW.

### 2. Cable Wrap Upgrade

In Fiscal Year 1994, ALTAIR will complete the integration of its new cable wrap system and receiver front end shelter, as well as the replacement of the main azimuth pintle bearing. The cable wrap upgrade will greatly increase the life of the antenna while expanding its azimuth rotation and NFL coverage capabilities.

The azimuth rotational capability of the new cable wrap system will be expanded by 50%, and the center of rotation will be rotated 90° counterclockwise in order to provide enhanced NFL coverage. Figure 2 shows the existing azimuth capabilities of the antenna. With the current azimuth restrictions, many counterclockwise NFL tracks result in the antenna reaching the CCW cable wrap limit during the track. This prevents additional data collection until the antenna can swing around to the clockwise end of the cable wrap.

Figure 3 shows that with the orientation and expanded azimuth capabilities of the new cable wrap system ALTAIR will have unrestricted coverage of all NFL events. Additionally, these new capabilities will give ALTAIR the ability to track any satellite, assuming an adequate signal-to-noise ratio, from horizon to horizon without loss of data.

The new system has been designed to reduce required maintenance, and has been constructed using materials with high corrosion resistance. This will increase the amount of time available for tasking, boosting ALTAIR's contribution to the SSN. The new RF shelter will provide improved EMI, RFI, and vibration isolation for the receiver equipment. Its size has also been expanded to accommodate future customer-driven upgrades.

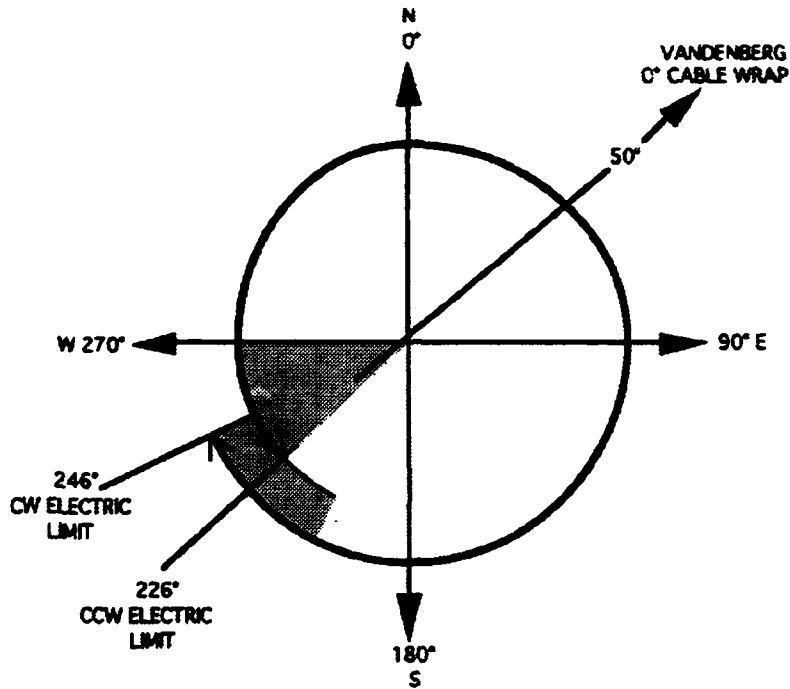


Figure 2: Existing cable wrap range of motion is 380°, centered at 50.3° (towards Vandenberg AFB). Most CCW satellite passes cause the antenna to hit the CCW cable wrap limit. (Note: The shaded area on the above figure is the servo limit region, where the antenna must slow down.)

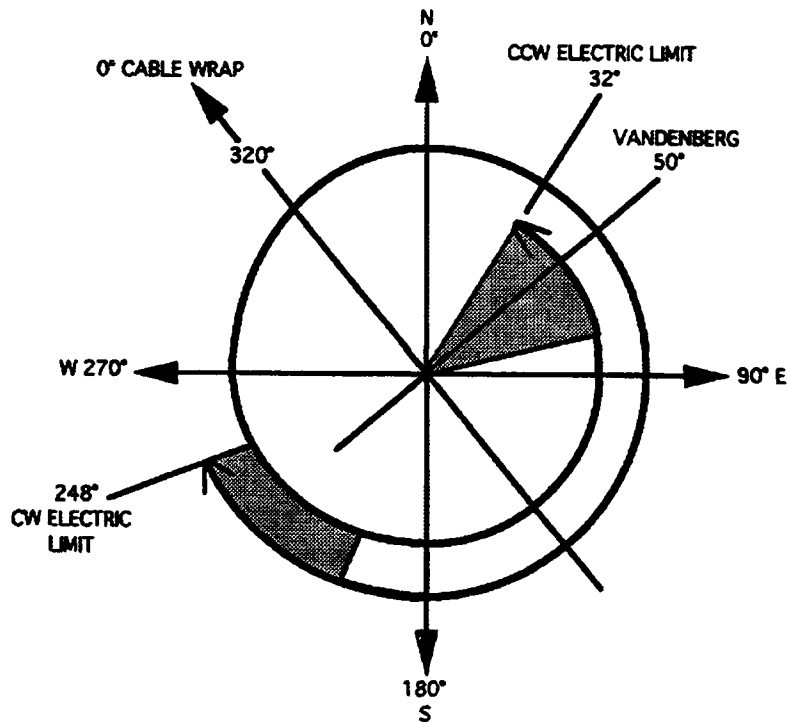


Figure 3: The new cable wrap range of motion is 576°, centered at 320° (90° CCW from Vandenberg AFB). This cable wrap orientation allows unrestricted coverage of all NFL events and satellite tracks.

### **3. New Foreign Launch System Upgrade**

ALTAIR is currently upgrading its New Foreign Launch (NFL) coverage capabilities. The upgraded NFL system will provide greater launch coverage reliability, and will reduce the time required to train radar operators. The NFL upgrade is organized into three tasks, whose order is based on functional dependency and relative importance. The first task is the introduction of an ionospheric refraction model into the NFL Known Object Recognition (KOR) discrimination process. This change will increase the integrity of the NFL fence through improved known object correlation accuracy. The second task is the automation of the NFL-to-Near-Earth system hand-over process. This change will allow the system to automatically transition from NFL scan mode to Near-Earth tracking mode, and will allow the system to automatically acquire a dual UHF / VHF track on an object without operator intervention. The third task is an NFL display upgrade that will organize, consolidate, and enhance the launch support data presented to ALTAIR operators. This will aid in NFL target assessments, and will reduce the complexity of real-time NFL operations.

#### **Ionospheric Correction of Observed NFL Detections**

When a new foreign launch is reported, ALTAIR initiates an NFL scan to locate the newly-launched objects as they break the radar's horizon. All targets that are detected while in NFL scan mode are subjected to a series of discrimination algorithms to determine whether or not each particular target detection could be from the new launch. The Known Object Recognition (KOR) algorithm is central to this discrimination process. It compares the measured position of a detected object to the location of all known satellites from the US Space Command element set database. If a detection fails to correlate with any object in the database, it is assumed to be a potential NFL. The comparison process is currently flawed because the measured position of the object is offset from its true position in range and elevation due to ionospheric refraction.

An ionospheric refraction model is being added to the NFL system to account for the effects of refraction on targets detected by the system. This model is sophisticated enough to properly generate refraction estimates for any target, regardless of whether it is below the ionosphere, within the ionosphere, or above the ionosphere. The only prerequisite for its use is the availability of a recent measurement of the total electron content (TEC) of the ionosphere above ALTAIR. This estimate will be provided by the new ionospheric modeling system (see below).

#### **Automatic NFL-to-Near-Earth System Handover Process**

Once a target detection is obtained by the NFL system and is associated with a particular NFL, the NFL system begins a single frequency VHF track (LOCKON mode). At this point, a manual transition to a simultaneous UHF/VHF Near-Earth satellite track is initiated. This operation is subject to operator errors (pressing the wrong buttons, or delays in establishing the UHF range track) and can jeopardize the NFL acquisition.

The hand-over process is being automated so that operator intervention is generally not required. The automatic handover process will use an ionospheric model to slave the UHF range gate to the VHF NFL system track, positioning the target within the track gate. The UHF signal-to-noise ratio will be monitored to sense the presence of the target within the track gate, and to initiate a UHF

range track. Once a stable UHF range track is achieved, the NFL hand-over sequence will be activated. A two frequency Near-Earth track with real-time ionospheric corrections will result.

### **NFL Display Upgrade**

The NFL display upgrade will organize, consolidate, and enhance the data presented to ALTAIR operators. The new arrangement will aid in real-time NFL target assessments and reduce the complexity NFL operations. The NFL display upgrade will exploit the capabilities of new Silicon Graphics display workstations through the use of X-window and client-server architectures.

### **4. Extended Range System Upgrade**

ALTAIR is also upgrading its Extended Range (XR) system, which is used to collect data on Deep Space objects for the Space Surveillance Network. The major components of this upgrade include:

1. The development of new waveforms and longer coherent processing intervals
2. Adding a capability for two-frequency XR tracking and raw data collection
3. Increasing system automation.

This upgrade will enhance ALTAIR's contribution to the Space Surveillance Network by providing better quality metric observations, increased target resolution and discrimination capability, and improved response to SSC tasking.

### **New Deep-Space Waveforms**

New Deep-Space UHF waveforms are being installed to take full advantage of ALTAIR's recently-completed signal system upgrade. The existing deep-space waveforms were designed to be used with the old signal system, which was removed from the radar this year. Since the new signal system is capable of processing longer pulses at higher bandwidths than the old signal system, we are designing a new waveform suite to take advantage of those capabilities.

The current Deep-Space waveform suite consists of a 50 kHz, 1000  $\mu$ s search waveform and a 250 kHz, 400  $\mu$ s tracking waveform. These waveforms will be supplemented by three new high-power, high-resolution tracking waveforms. The new waveforms will consist of a 250 kHz, 1000  $\mu$ s waveform, a 1 MHz, 1000  $\mu$ s waveform, and a 4 MHz 400  $\mu$ s waveform. The properties of the old and new waveforms are listed in Table 1.

**Table 1: ALTAIR Deep-Space Waveforms**

<b>Waveform Name</b>	<b>Length (<math>\mu</math>s)</b>	<b>BW (MHz)</b>	<b>Max PRF (Hz)</b>	<b>Resolution (m)</b>	<b>Use</b>
U1000	1000	0.05	50	3000	Search
U400	400	0.25	120	600	Track
U1000X	1000	0.25	50	600	Track
U1000S	1000	1.0	50	150	Track, Med. Res.
U400W	400	4.0	120	37.5	Track, High Res.

The new U1000X waveform has the same 250 kHz chirp bandwidth as the current U400 waveform, but has 2.5 times the pulse length. The additional coherence gained from a single long pulse, as opposed to several pulses pre-summed with imperfect relative phase compensation, is expected to provide an increase in sensitivity for deep space tracking. The intention is to use U1000X for tracking targets whose Doppler spread does not exceed the 50 Hz ambiguity. For targets whose Doppler spread exceeds 50 Hz, U400 will continue to be used.

The new U400W waveform has a chirp bandwidth of 4 MHz. This increased bandwidth will provide a 16-fold increase in range resolution over the current system. Such increased resolution will be extremely useful when tracking closely spaced objects. For example, it currently takes an hour or more to resolve a payload from a rocket body following an injection into transfer or final orbit. The new U400 waveform will cut that time by a factor of 16.

The new U1000S waveform combines the increased power of a 1000  $\mu$ s pulse with a 1 MHz bandwidth, yielding an increase in both sensitivity and resolution.

ALTAIR's new Deep-Space waveforms will improve ALTAIR's contribution to the SSN by providing better metrics, and increased discrimination capability, in the data product sent to the user.

### **Two-Frequency Deep-Space Tracking and Raw Data Collection**

ALTAIR's Extended Range system is currently used for two fundamentally different types of data collection activities. The primary use is for tracking and collection of metric observations at UHF. A secondary usage is for collection of raw in-phase and quadrature samples at VHF, for off-line post-processing. All coherent and non-coherent integration and thresholding leading to a UHF target detection is located on one Star array processor, while a second Star array processor is used for the collection of raw VHF I/Q samples.

Part of the Extended Range system upgrade is to develop a capability for simultaneous tracking *and* raw data collection at *both* UHF and VHF. The two-frequency tracking capability will provide a real-time ionospheric correction to improve metrics, while the raw data will be used for a Signature Processing Facility as well as other projects.

The development of such a two-frequency capability will require the consolidation of the integration / detection and raw data collection functions into a single array processor, allowing each Star to perform all of the processing required for a single frequency. Also, a second tracker will have to be installed on the VAX computer, and the data recording function will have to be expanded to handle the data from two frequencies.

### **Extended Range System Automation**

ALTAIR's Extended Range system, while partially automated, still requires a large number of operator actions to select, enter, track and log a Deep-Space object. Tracking efficiency (i.e., the number of objects tracked per day) and conformity to SSC tasking will be improved by increasing the intelligence and automation of the system.

Part of the Extended Range upgrade is to re-work the track scheduling algorithm so that the "best" of the currently visible tasked objects is automatically selected and put into track. Criteria for selecting the "best" object include tasking category, predicted signal-to-noise ratio, maximum elevation of the pass, time since the object was last tracked, and azimuth relative to that of the previous object tracked. The last criterion, which is currently applied manually by the operators, is being included to reduce dead time between tracks, and to minimize the number of antenna wheel rotations. Objects which are tracked will be automatically logged, a process which is also currently done manually, and which wastes valuable system time.

## **5. Improved Ionospheric Modeling**

Because ALTAIR is located near the equator and operates at relatively low frequencies (UHF and VHF), ionospheric refraction can have a significant effect on the measured position of objects tracked by the radar. During Near-Earth satellite tracks, the radar simultaneously tracks the same target in both UHF and VHF, and uses the apparent range difference between the two tracks to calculate and correct for the ionospheric refraction present along the line of sight to the target being tracked. Because measurements at two different frequencies are available, ionospheric refraction effects can easily be removed from Near-Earth satellite tracks.

The Deep-Space system is a different story. ALTAIR Deep-Space tracks are currently UHF only, so there is no direct way to measure the effect of ionospheric refraction on a Deep-Space track. The system uses an ionospheric model to partially compensate for the effects of the ionosphere. The model is updated two or three times a day by tracking a GPS satellite and comparing the apparent range to the target to the true range as calculated from its ephemeris. This model compensates for much of the ionospheric refraction that occurs during Deep-Space tracks, but it is not perfect. In fact, errors in the model are the major limiters of metric accuracy during daytime operations.

We have purchased an Allen Osborne GPS receiver in an effort to improve our ionospheric modeling. This receiver is providing ALTAIR with a continuous estimate of the total electron content (TEC) along the line of sight between ALTAIR and each of up to 8 GPS satellites. A program is being developed to manipulate the data to provide a real-time measurement of ionospheric conditions at ALTAIR. The program is still being developed; the effort is described here, and some preliminary data are presented.

The GPS receiver (Mini-Rogue) provides an estimate of TEC in the direction of each satellite it tracks. The TEC value is calculated from the measured differential group delay between the two GPS frequencies,  $L_1$  and  $L_2$ . To date, this TEC estimate has not been corrected for the individual satellite biases observed after launch. We have discovered that multipath effects and ionospheric scintillation contribute significant short-term variability to the estimate of TEC, so the TEC estimates from each receiver are being smoothed using a fixed-weight Helms filter. Figure 4 illustrates raw and smoothed TEC values for one horizon to horizon track on SSC object number 16129 in January of 1994.

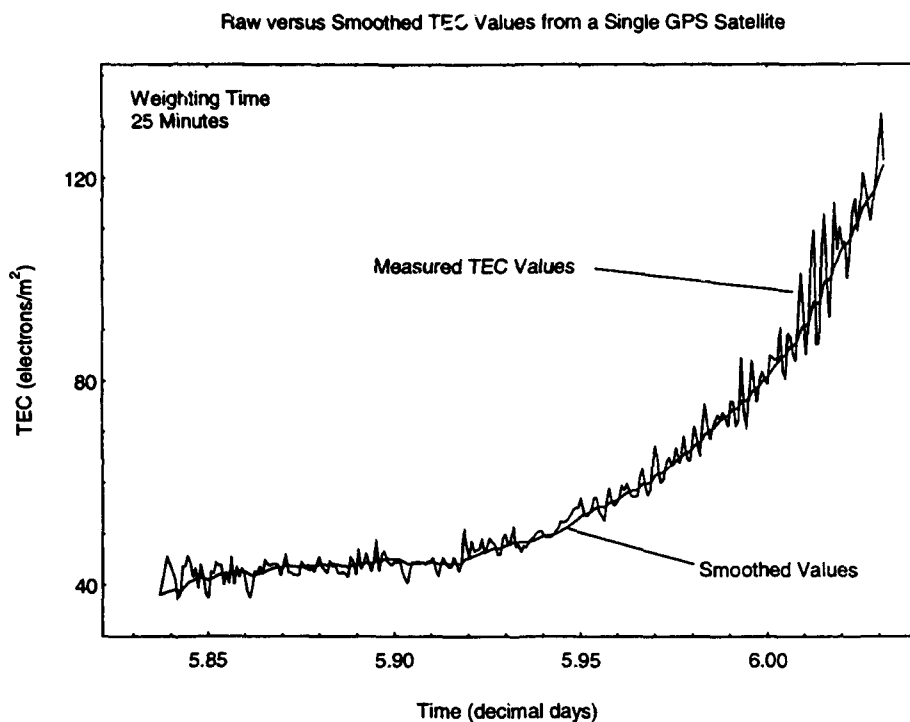


Figure 4: A comparison of raw versus smoothed TEC values during a horizon-to-horizon track of a single GPS satellite. A fixed-weight filter with a 25-minute smoothing time effectively removes the short-term variability from the data set.

Once a smoothed estimate of TEC is available from a satellite, the VHF range delay (DRV) that would result from the measured electron density is calculated. This VHF delay is then mapped to the delay that would be expected if ALTAIR were looking vertically upward (DRV0) using the following elevation mapping function:

$$DRV0 = \frac{h}{ri} \left( \frac{DRV}{1 - (fel \cdot fxh)} \right)$$

where DRV0 = VHF range delay at ALTAIR's vertical

$\frac{h}{ri}$  = the ratio of the ionosphere width to the radar slant range through the ionosphere

$fel, fxh$  = empirical factors based on historical ionospheric profiles

This estimate of DRV0 is then scaled depending on the longitude at which the ionosphere was observed<sup>2</sup>. The longitude mapping function attempts to characterize the diurnal, seasonal and sun-spot cycle variations on the delay at ALTAIR's vertical. A detailed description of this function is beyond the scope of this paper.

Once a DRV0 estimate has been calculated for each GPS satellite tracked at a particular moment, the values are averaged together to produce a "best" estimate of DRV0. The averaging process relies heavily on the ability of the elevation and longitudinal mapping functions to characterize the ionosphere. If the mapping functions are good, then averaging is a valid way to combine the

<sup>2</sup> McSheehy R. B., Private communication, 18 October 1983

measurements from separate satellites. The quality of the mapping functions in use is currently being tested.

We decided to average DRV0 values after the mapping function because it was easy to implement with the existing ALTAIR ionospheric modeling architecture. If this approach proves to be inadequate because the mapping functions are not accurate enough, we will try other approaches, such as tracking the behavior of DRV0 separately for different longitudes.

How do the DRV0 values derived from the GPS receiver compare to the DRV0 values produced by ALTAIR's current Deep-Space model, and to the DRV0 values produced by Near-Earth two-frequency tracks? Figure 5 shows the results of the different DRV0 estimates on one particular day in January 1994. It appears from the figure that the overall shapes of the model DRV0 and the GPS-derived DRV0 track each other, but with a multiplicative offset. Experiments are underway now to determine the major contributor to the differences between the curves, and also to determine which of the two curves is closest to the truth<sup>3</sup>.

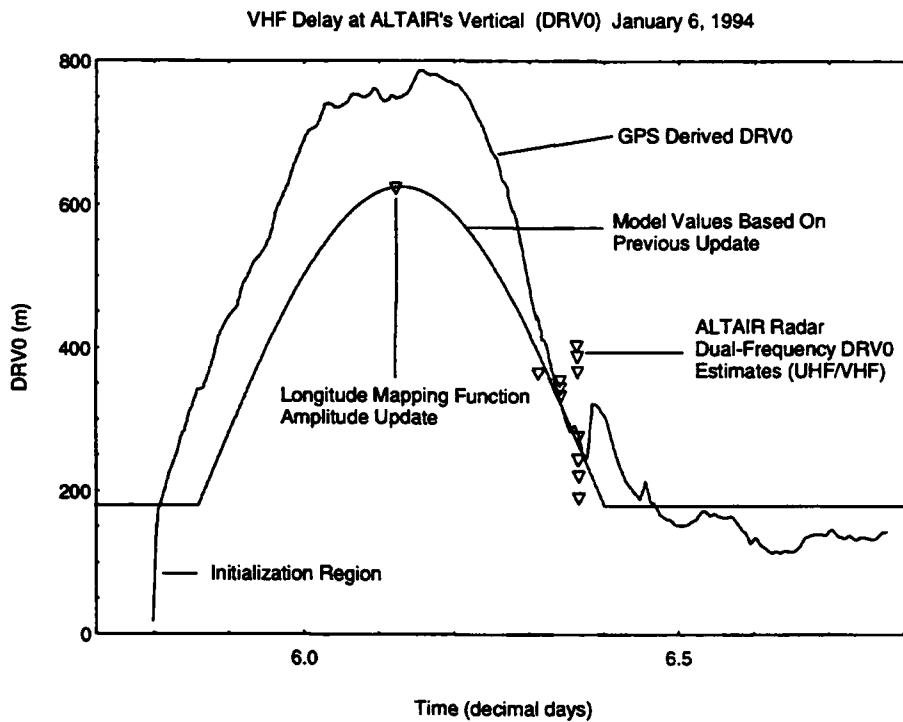


Figure 5: Comparison of GPS receiver estimates of DRV0 with the values generated by the current Deep-Space DRV0 model and with the values produced by dual-frequency Near-Earth tracks. The differences between the GPS-derived DRV0 and the model estimates for DRV0 are large enough to impact range and angle metrics during the daylight hours.

There is a significant payoff in getting the Deep-Space ionospheric model right. The peak difference between the GPS-derived DRV0 curve and the model DRV0 curve in Figure 5 is about

<sup>3</sup>The Near-Earth DRV0 data from 6 January 1994 is not helpful in deciding which curve is correct, because it is all concentrated over a short period in the afternoon, and also because no longitudinal mapping function is currently applied to Near-Earth DRV0 estimates. Further experiments are planned to resolve the issue in the next few months.



180 m. When tracking a target at 20° elevation, a DRVO difference of 180 meters would correspond to a UHF range and angle error of 90 m and 3 millidegrees respectively.

## **6. Deep-Space VHF Data Collection**

The ALTAIR VHF Deep Space data collection capability has recently been upgraded to provide data for two projects: a study of the limits of coherent integration at VHF, and a catalog of Deep-Space object VHF signatures. Coherent integration of the VHF data for periods of as long as 10,000 seconds are of interest, as well as RCS versus time histories for radar tracks of as long as 300 seconds. In addition to the VHF data, UHF data on the object in track will be collected to provide a dual frequency comparison to study the effects of ionospheric propagation on the VHF signal.

The original ALTAIR VHF Deep Space data collection capability became operational in January 1990. The goal of this system was to provide data to study VHF coherent integration. A 238  $\mu$ s, 250 kHz chirp is used for the transmitted waveform. A dedicated VHF interface, the IF Data Interface Buffer (IDIB), was built to supply digital data to a VAX 11/785 for recording and processing. As part of the ALTAIR signal system upgrade, the IDIB (and associated signal processing equipment) was made obsolete by installation of a 3072 tap programmable FIR filter, the Universal Signal Processor (USP). In addition, two STAR Array Processors were added to process the raw sampled digital data from the USP in order to produce the target reports required by the radar for tracking. As a result of this upgrade, the VHF Deep Space capability was moved to the USP / STAR combination and several improvements made in the real time software.

The upgraded Deep-Space VHF data recording system is based on sample patterns slaved to an active UHF track and generated by the radar controller. The tracker used is the ALTAIR extended range UHF tracking loop. Sixteen range gates of compressed VHF inphase and quadrature (I/Q) data is collected in the VHF STAR array processor and transmitted to the VAX for recording in a standard binary recording file. The data is recorded in the standard format for ALTAIR real time program radar recordings, so editing tools already exist to examine the data after it has been recorded. The data consists of compressed, unprocessed I/Q samples of the Sum Left Circular, Sum Right Circular, Traverse, and Elevation channels. An unweighted window is used in the USP to perform the pulse compression and to gain the additional 1.34 dB over the standard Hamming weighted window used with other ALTAIR waveforms. In addition, state vector data from the UHF tracker was added to the recording files as well as various timing and calibration files to aid in post processing of the recorded VHF data.

The real time program modifications for Deep-Space VHF data recording are in the integration and test phase. One modification will allow the antenna to be pointed based on a propagating element set obtained from the satellite database. This modification provides a smooth sample pattern over the target, because it is not being updated from a active UHF track. Recording of the UHF raw data as well as the pointing state vector will allow reprocessing of the raw data to align the sampled signal under the sample pattern. A second real time program modification permits an operator to fix the radar pulse repetition frequency (PRF) to provide a constant time difference between samples over long integration intervals.

## **7. Conclusion**

After a temporary hiatus caused by a contract transition, several important upgrades are underway at ALTAIR. These upgrades will enhance the ability of the radar to perform its Spacetrack mission in many ways. The average radiated power of the UHF transmitter has been increased, improving both sensitivity and reliability. Cable wrap modifications will permit ALTAIR to track any satellite from horizon to horizon without running into cable wrap limits. The New Foreign Launch detection and tracking process is being further automated, and the known-object recognition subsystem within the NFL system is being improved.

The Deep-Space system will provide better metrics through better monopulse estimates and better ionospheric refraction estimates. In addition, it will be capable of separately tracking closely spaced targets in clusters or transfer orbits. Finally, the system will be automated to reduce the idle time between successive tracks.

A mechanism is being added to collect raw inphase and quadrature UHF and VHF data samples on targets tracked with the Deep-Space system. This raw data will be provided to users for off-line processing and analysis. This data collection capability may be of interest to many users interested in performing experiments on Deep-Space data.

## Recent and Planned Improvements to the Kwajalein Imaging Radars

R.K. Avent, C.H. Moulton, S.B. Rejto

(Lincoln Laboratory, Massachusetts Institute of Technology)

### **1 Introduction**

The Kiernan Reentry Measurement Site (KREMS) sensors, located at the Kwajalein Atoll and operated under the scientific direction of MIT/Lincoln Laboratory, form a vital role in the Space Surveillance Network (SSN). In this capacity, ALTAIR is the largest contributor to the SSN with their satellite database maintenance and New Foreign Launch (NFL) efforts. Also considered a parallel and significant contributor to the SSN is the Space Object Identification (SOI) support provided by the two high-resolution instrumentation radars, ALCOR and MMW. Of these two radars, ALCOR was the first to demonstrate a range-Doppler imaging capability. Although ALCOR continues to be a reliable SOI imaging sensor, being relatively insensitive to weather-induced attenuation, MMW is increasingly becoming more important in the Near Real-Time Imaging (NRTI) of satellites because of a twofold advantage in both range and cross-range resolution over ALCOR. Both ALCOR and MMW are constantly undergoing modifications designed to improve their performance. The purpose of this paper, then, is to discuss some recent and planned enhancements at these two sensors. The specific advances to be addressed in this paper are those improvements that have utility in the SSN. To this end, these improvements generally include modifications that enhance the acquisition and identification of tasked satellites.

### **2 Dual-Target Tracking**

The addition of dual-target tracking grew out of the need to simultaneously track two targets at different ranges when both targets are in the beam, such as in the initial phase of a deployment or when two targets are mutually tethered. Although a limited dual-target track capability has been operational at ALCOR since 1992, the full capability was not developed and utilized until the completion of the new console. The two most significant limitations were the inability to perform dual wideband tracks and that the target range separation was limited to 6 km. These limitations, along with all waveform combination restrictions, have been removed, and the capability is now routinely used. ALCOR dual tracks using a shared Pulse Repetition Frequency (PRF) method.

MMW has employed a similar dual-track feature since 1991. Although there are currently plans to build an independent simultaneous second range window with its own waveform generator at MMW, the current implementation is similar to the ALCOR architecture in that it is a shared PRF operation. A marked deficiency noted with the shared PRF implementation at both ALCOR and MMW is the minimum twofold reduction in tracker PRF. This PRF reduction is at its worst during coherent integration because the current MMW coherent integrator cannot buffer one tracker's pulses while integrating the other tracker's pulses; thus, a fourfold reduction in tracker PRF is suffered. This problem deteriorates more when a multiplexed waveform is used. With the anticipated implementation of the independent second range window and the integration of the new coherent preprocessor, however, these deficiencies will be alleviated and MMW will be capable of a dual-track mode at full PRF rates.

### **3 New Console Upgrade**

Because MMW was originally chartered as an adjunct to ALCOR, their two consoles were collocated in a single console room at ALCOR. Since then, both sensors have expanded their roles to the point that a shared console room is now overcrowded and confining.

Additionally, with the completion of various upgrades, such as dual-target tracking, both sensors have found that the old button console designs are inflexible. Consequently, an effort to build a new console room for each sensor was initiated in 1992.

A unified console design was chosen for both sensors and is based on networked Silicon Graphic Inc. (SGI) workstations running under UNIX. The SGI workstations are the newly established KREMS standard display system. The SGIs are capable of drawing several hundred thousand 2-D vectors per second, making them ideal for drawing synthetic A-scope displays with up to 400 PPS presented. These displays are developed and modified with minimal disruption to the system. Because a synthetic A-scope is presented, a digital signal-processed return can be displayed as readily as a digitized analog-processed return. The format of the display presentation to the operator is identical for both processing modes.

Figure 1 shows a generalized architecture for the ALCOR and MMW console upgrade. As shown, there are seven operator stations: each station consists of an upper textual display and a lower graphical display. The SGI machines at each station are diskless, and the console programs are launched from a single SGI over a sensor-display Ethernet. Full PRF-rate signature data are available only on a subset of graphical machines, and these data are fed by a reflective memory network. The reflective memory interfaces through a VME console computer, which in turn interfaces to the radar computer. At MMW, a computer upgrade to the Modcomp REAL/STAR provides a UNIX-based machine with VME slots; thus, a standard VME-VME interface between the console and radar computer will be used. In the case of ALCOR, which incorporates a GOULD 9780 radar computer, a VME-Sel-BUS Adapter (VSA) is used. The ALCOR console is fully operational; the MMW console work is planned to begin this summer.

#### **4 Real-Time Range-Doppler Imaging**

With the performance improvement in today's processors, a simple real-time range-Doppler imaging capability was inexpensive to add to the new console. Images are presented on the Identification Operator's graphical display at both sensors. At ALCOR, the images are generated on a Skybolt Array Processor; at MMW, they will be generated on an SGI. Because this feature was modeled after the (now retired) Kwajalein Discrimination System, it is initially a simple linear imaging capability that does not use a complex motion solution for phase referencing. Instead, the phase across the object is typically referenced to the single dominant scatterer located in the track gate. Future enhancements may refine the process to reference a maximum-likelihood fit smooth orbit. The cross-range resolution is controlled by entering a pulse-skip factor, and images can be recursively integrated to improve their signal-to-noise ratio. ALCOR routinely uses this program during reentry missions; coding will begin on an MMW version once work begins on the new console.

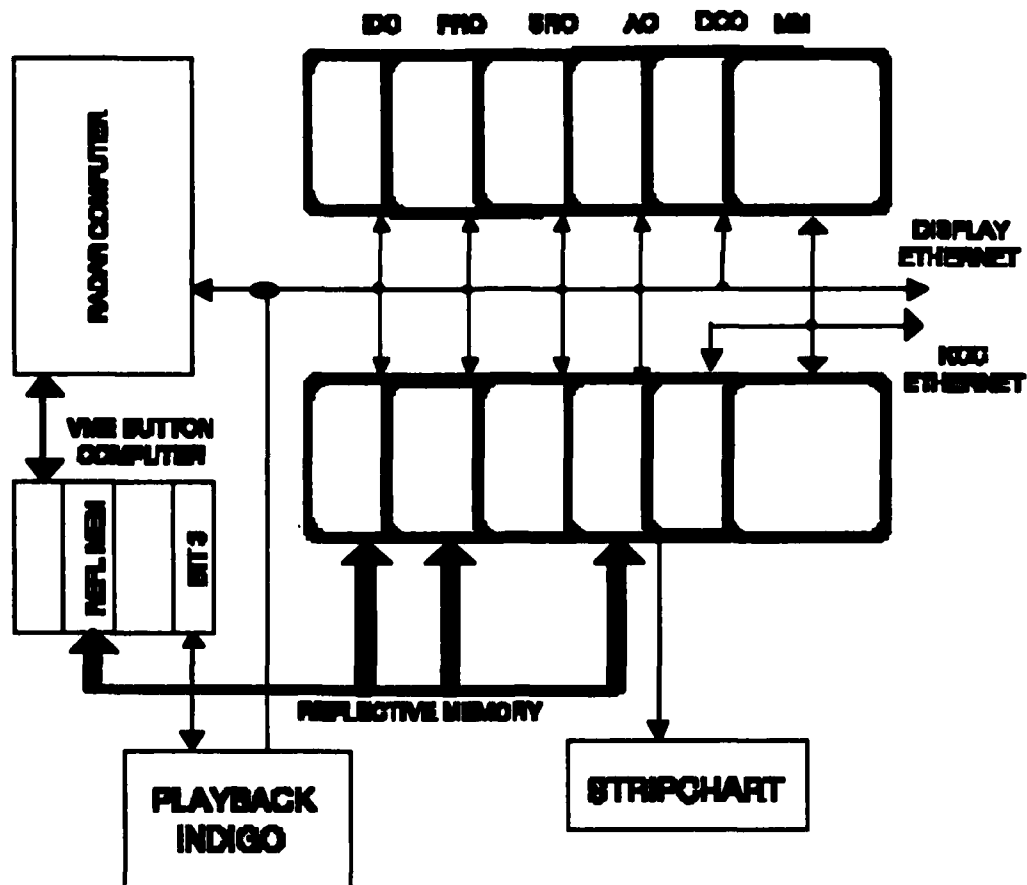


Figure 1. A generalized schematic of the new ALCOR/MMW consoles.

### 5 Sensitivity Upgrades

ALCOR and MMW both have undergone several improvements in their transmitter and receiver chains to improve their sensitivity figures. ALCOR's most recent improvement is a result of replacing old parametric preamplifiers with low-noise GaAs FET amplifiers that have built-in limiters. Because these GaAs FET amplifiers can withstand larger input power levels, the 32-dB RF attenuators currently ahead of the preamplifiers can be moved immediately behind the amplifiers. Because the attenuator has measurable loss even in the bypass state, this modification will result in a net increase in sensitivity of approximately 1 dB. When this latest improvement is completed, the sensitivity figure for ALCOR will be 24 dB on a 0-dBsm object at 1000 km.

MMW has undergone several changes to improve its sensitivity: most of these changes were discussed in a previous workshop talk\*. Of these changes, which include the aforementioned installation of a beam waveguide and the addition of dual high-power tubes, the most recent modification is the incorporation of low-loss EMS T/R switched ferrite circulators. These devices have measured insertion losses of roughly 0.3 to 0.4 dB, as opposed to the 1.8-dB insertion loss in the current Varian passive-gas tube/active diode devices. The initial test installation in the Orthogonal Polarization (OP) channel is operating as planned. With the completion of the installation of these devices in all four channels, the sensitivity figure for MMW will also approximate 24 dB.

\* G. A. Jones and M.D. Abouzahra, "Major Improvements at the KREMS Millimeter Wave Radar", *Proceedings of the 1992 Space Surveillance Workshop*, MIT Lincoln Laboratory, Lexington, MA, p. 239.

## 6 Coherent Integration

In comparison to the other sensors at Kwajalein, the detection range for ALCOR is markedly inferior, due to its inability to coherently integrate. Thus it was decided to include a coherent integration capability at ALCOR with the construction of the new console. This capability will include the ability to coherently integrate, noncoherently integrate, and postsum coherent looks. The integration process will reside on a Skybolt Array Processor hosted by the range operator's SGI Crimson. To date, integrated pulses are compiled and displayed but the handling of those integrated pulses by the radar's Kalman tracker has not yet been accomplished. This is a major effort to be completed during the fall of 1994.

Although MMW currently performs coherent integration with its FPS AP-120B Array Processor, the limited computing power of that machine has restricted the capability. Consequently, an effort was initiated in 1992 to off-load the FPS system by building a custom coherent preprocessor based on an array of MOTOROLA 96000 DSP chips. With the completion of this project, the coherent preprocessor will compile the two-dimensional range-Doppler image, peak detect each cell, and pass the processed return to the radar computer for range marking. This resource sharing will allow MMW to double its maximum integration size and perform integration on the full data window rather than on just a subset of gates about the track position. This will subsequently improve both the acquisition and tracking capabilities of MMW.

## 7 MMW Digital Pulse Compression

Being a wide bandwidth high-resolution radar, the MMW pulse compression chain is designed as a stretch processor with the pulse being compressed using a Fast Fourier Transform (FFT). Because a discrete-time FFT rather than an analog-time compression network is used to compress the pulse, the input radar signal has to be bandlimited to eliminate aliased components. The input signal is sampled at 20 MHz and bandlimited to 5 MHz, resulting in a 37.5-m data window for the high-resolution waveform. This twice oversampling was chosen because MMW samples only the in-phase signal component and digitally generates the quadrature components using a modified Hilbert transform. This approach, although it produces a well-balanced I/Q channel receiver, unnecessarily limits the range window size. This limitation will become especially pronounced once the 2-GHz modification is completed, because the wider bandwidth will half the window size. Because of this limitation and to address some reliability and maintainability concerns, a redesign of the digital pulse compression system at MMW is being examined. Several designs are being examined. This upgrade will most likely be part of the 2 GHz/second range window modifications that are currently under way.

## 8 MMW Computer Upgrade

The MMW Real-Time Program originally ran on a pair of MODCOMP Classic computers connected by 8 Mbytes of shared memory. Although this hardware served the radar well for eight years, the RTP's processing requirements due to improvements in the radar's capabilities gradually outpaced increases in processing power available from MODCOMP. This discrepancy resulted in the conversion of large segments of the RTP from FORTRAN to assembler for efficiency gains at the expense of maintainability. The preservation of a large original investment in custom RTP software written to run under MODCOMP's proprietary operating system (O/S) eliminated the consideration of switching computers to attain more processing power. MODCOMP's release of the more powerful 9250 several years ago relieved some strain but was still inadequate. The latest product offering from MODCOMP, the REAL/STAR, provides a more permanent solution.

The REAL/STAR is a fast quad-processor (25-MHz MOTOROLA 88100s), VME-based computer featuring a shared-memory interface, called REAL/MAX, and a real-time UNIX O/S, REAL/IX. These features are all important elements of the latest MMW computer

upgrade. The REAL/STAR is ten times more powerful than the 9250 it replaces, thus permitting the conversion of the entire RTP to FORTRAN, with processing power to spare for future modifications. The REAL/MAX shared memory has permitted a phased software upgrade approach, allowing portions of the RTP to be released to the new machine as they are completed. This is important, as the radar must be kept in an operational state most of the year. The POSIX-compliant UNIX System V O/S is a standard with wide industry support. Lastly, the VME architecture greatly reduces the need for custom interface hardware, because VME-format interface cards are available for much of MMW's computer-controlled hardware. Two important planned upgrades, the new radar console and new waveform generator, will be driven through VME interfaces. To date, one of the 9250s has been supplanted by the REAL/STAR, and the second 9250 should be eliminated over the next two years.

## **Enhancements to the UK SOI facility at Herstmonceux**

*Dick, J.S.B., Sinclair, A.T., (Royal Greenwich Observatory, Cambridge, UK)  
Greenaway, A., and Liddell, P., (Defence Research Agency, UK)*

### **1. Introduction**

This paper describes a programme of work to enhance the SOI capabilities of the 50cm satellite-tracking telescope at Herstmonceux. The UK optical SOI programme aims to fulfill two main objectives:

- The provision of detailed information on spacecraft, such as size, configuration, and intrinsic motion, and
- The provision of a screening service to 'fingerprint' satellites for quick classification.

Broadly speaking, these two objectives are met by imaging and signature/photometric techniques, respectively.

In order to meet these objectives, the existing photometer is being enhanced to improve its photometric capability and to add an imaging capability for SOI. In this paper, the present system is described and some results are shown to illustrate its capability. Enhancements to the sensor and the current status of the work programme are described.

### **2. Description of facility**

The 50cm Cassegrain telescope is part of the Satellite Laser Ranger (SLR) facility operated by the Royal Greenwich Observatory. The SLR is situated at Herstmonceux, see Figure 1, and its primary role is laser-ranging for geodetic purposes. Some years ago, a passive photometer was added as part of the UK SOI programme which is funded by MoD UK. Figure 2 shows the optical layout of the existing photomultiplier-based photometer.

**Figure 1** The SLR facility at Herstmonceux.

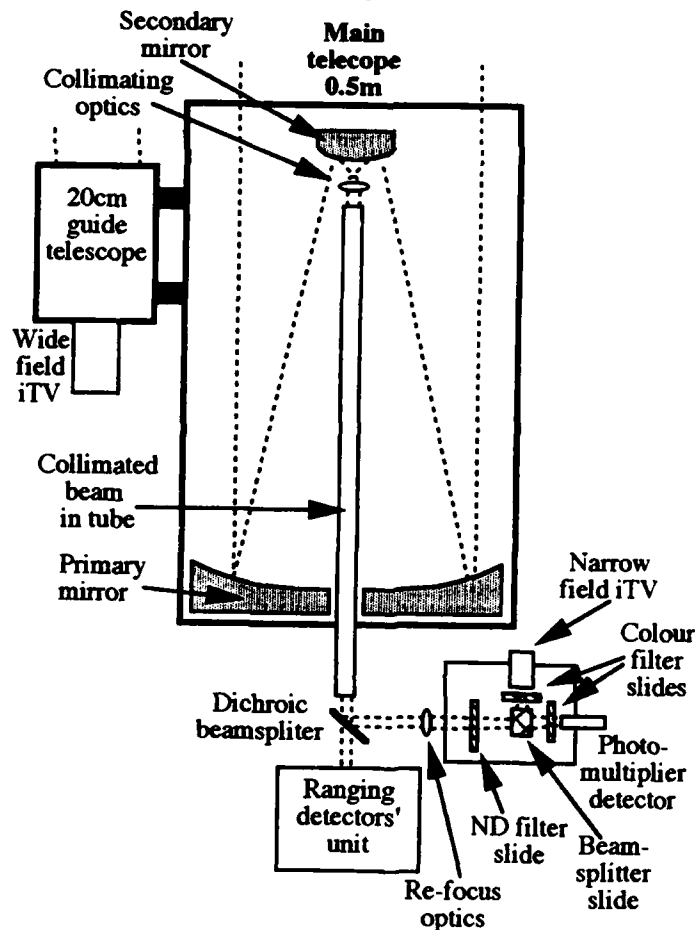




At present, the photometer's performance is somewhat limited because it uses a single photomultiplier and has a relatively large focal-plane aperture (~30 arcsec in diameter). Photometric data are acquired in two stages. First, the telescope tracks a satellite using a precomputed ephemeris to acquire photometric data from the satellite as well as a contribution from the sky background. (An intensified TV system allows the observer to acquire the satellite and provide manual guidance, if required.) Second, the background signal is acquired by repeating the sky trace without the satellite. Ideally, data from the second stage allow the satellite's signal to be isolated by subtraction.

However, the second-stage data are not always useable because the sky background may have changed significantly between the satellite observation and the background calibration. Also, the large-diameter aperture used by the present photometer admits a large sky signal, the noise in which significantly limits the overall signal-to-noise ratio of many observations, causing a sensitivity problem with faint targets.

**Figure 2** Optical arrangement of photometer



Once the sky background has been subtracted from the stage-one data, the satellite's intensity can be displayed as count-rate or stellar magnitude, which can be normalised to give a range-invariant value.

Despite the simplicity of the system, the results from it have been very encouraging and examples of photometry are given below.

**Figure 3** START-1 Rocket Body

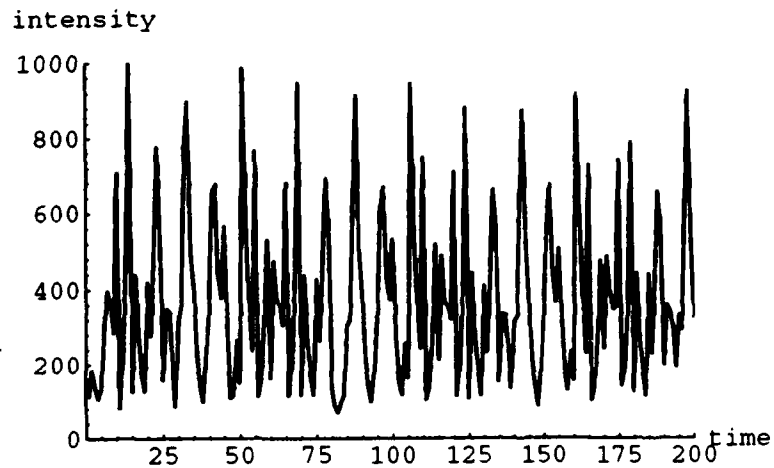
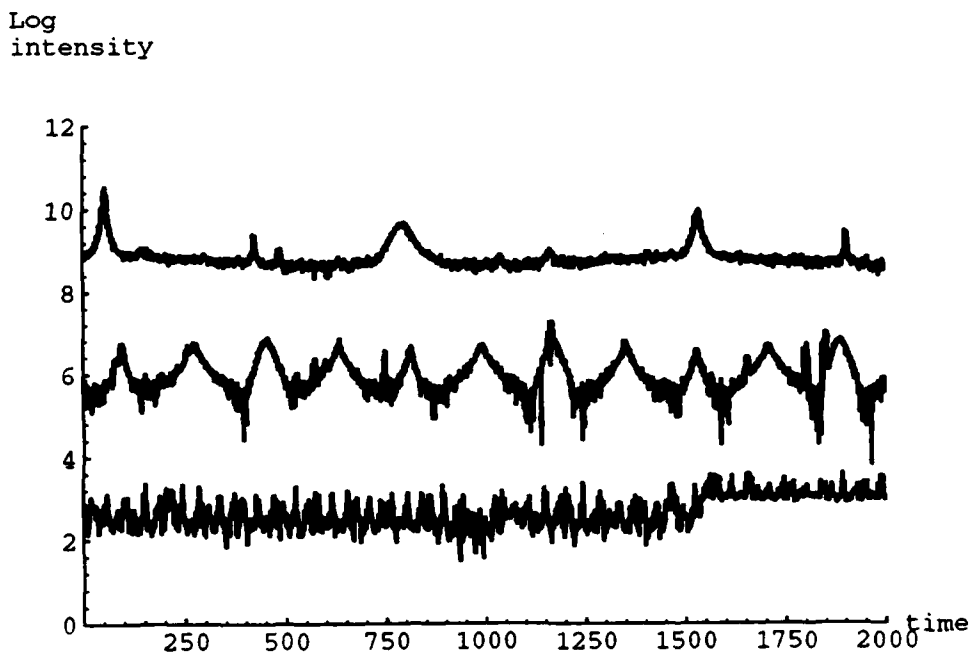


Figure 3 shows the photometric curve for the rocket body from START-1, the first satellite launch by a modified SS-25. Figure 4 show the photometric curves of three Glonass satellites, launched as a triplet in 1983. It can be readily seen that the satellites are rotating at different rates.

**Figure 4** Glonass satellites: Cosmos 1519, 1520, 1521.



### **3. Enhancements**

Although the present system performs well, it has a number of limitations: only one waveband is available, sky-background removal is poor, and there is insufficient sensitivity for faint (*i.e.* small and/or distant) objects. Enhancements currently underway will reduce these limitations by replacing the existing photometer with two CCD cameras. A third CCD will be added for imaging work. Figure 5 shows the optical arrangement of the new sensor system, which may be divided into three sections.

First, there is a beam-splitter that can direct some fraction of the telescope's beam, through a set of neutral density filters, onto an intensified TV camera, to provide visual guiding information for the observer.

Second, there is the main camera assembly. This houses two CCD cameras, each with its own neutral density filter set and colour filter, and a beamsplitter that can direct the beam to one camera, both cameras, or to the optical bench. These filters and beamsplitter are automated and controlled by the data acquisition/control computer.

The third section is an optical bench with mounting-holes for standard components, and a third CCD camera. This third camera will be used for imaging — the other cameras will be used for two-band photometry.

All cameras are commercially-produced, cooled CCDs with ~16-bit dynamic range and pixel read-out rates selectable up to 1 MHz; selected areas within each CCD can be examined (complementary parts of the image are dumped) and on-chip binning can be used to synthesize larger pixels. The image scale for the photometer CCDs is ~0.8"/pixel. The camera controllers are housed beneath the telescope's observing floor and are controlled from the main data acquisition/control computer (an Apple Macintosh Quadra 950), which is in the SLR control room.

The moving mechanisms within the new system are driven by stepper-motors that are controlled locally by a microcontroller in an IEEE-1000 crate. The microcontroller receives commands from the main acquisition/control computer via an RS-232 link.

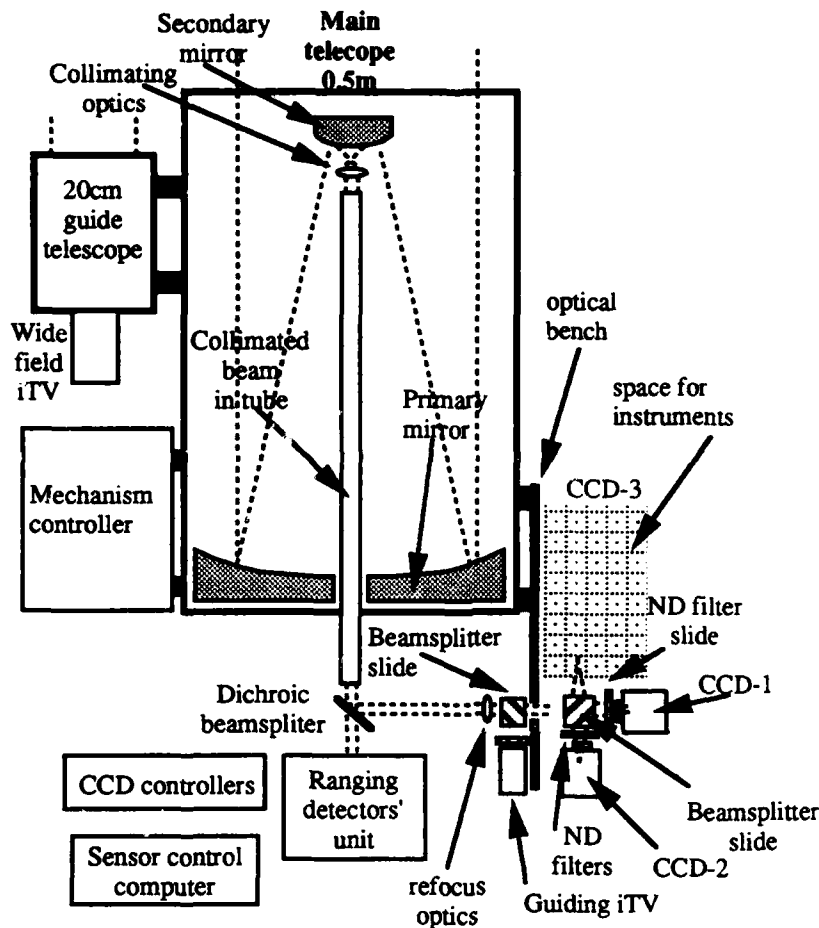
### **4. Photometry**

Two CCD cameras are used to image the telescope's field of view in two wavebands, to provide colour information. Images are downloaded from the cameras and analyzed to detect objects within the image. For each image, a list of object positions and intensity (corrected for any contribution from the sky background) is produced.

### **5. Imaging**

Atmospheric turbulence degrades the resolution obtainable by traditional optical imaging. Under excellent conditions at a high-altitude site, the atmospheric turbulence

**Figure 5** Optical layout of new CCD-based system



would lead to a "seeing-limited" angular resolution of about  $\sim 3 \times 10^{-6}$  radians (0.6"), equivalent to a spatial resolution of 3m on a target at a 1000km range.

In addition to the degraded spatial resolution, the spreading of the image due to turbulence-induced aberrations reduces the image brightness and thus reduces the sensitivity of imaging methods.

There are two approaches which may be used to mitigate these effects of turbulence:

- *a posteriori* data processing, and
- adaptive correction of the turbulence-induced wavefront errors.

The first of these approaches has been shown to be capable of restoring at least some of the spatial resolution destroyed by the turbulence, but does nothing to mitigate the loss of sensitivity. Indeed, *a posteriori* image processing methods are signal-to-noise limited and can only be applied with success to relatively bright targets.

The second approach provides sharper images and thus restores some of the resolution but, in addition, provides increased sensitivity because the greater concentration of the available flux gives improved contrast in the image. However a relatively high level of flux is required in the first place, in order to sense the wavefront errors that must be corrected.

In general, the level of flux required to effect adaptive corrections above the lowest order corrections (*e.g.* tip-tilt sensing and focus correction) is similar to that required for post-detection image processing methods. However, the wavefront-sensing signal may be derived using target flux in a different waveband from that to be used for image formation (*e.g.* IR and visible frequencies) or may be derived using a cooperative beacon (laser backscatter, sodium resonance). Whilst turbulence-degraded images may be deconvolved to compensate for measured atmospheric transfer functions, on-line correction of these errors will generally give measurements with superior signal-to-noise ratio.

Thus it is likely that partial adaptive correction can be used to provide some gain in sensitivity that can then be exploited by *a posteriori* processing — so fainter targets can be usefully imaged than would be possible using either approach in isolation.

The long-term objective is to record images that have been at least partially corrected by adaptive optics and to study these as a function of either polarisation or colour.

## **6. Enhancement work programme**

The enhancement work programme will be carried out in two phases. First, a "foundation layer" imaging capability will be established. The CCD cameras will be installed and used to assess the performance of the new system, as well as providing trial data for development of the image processing required for photometric signature acquisition and speckle interferometry techniques. Second, an adaptive-optics wavefront-correction capability will be developed. This will provide data for development of software with which partial-correction may be performed as well as a test-bed for adaptive optics hardware (*e.g.* liquid-crystal based correctors).

At present, the structure of the new system is complete and the CCD cameras are being tested prior to installation in the SLR. It is hoped the first data will be produced in the second half of 1994.

## **7. Summary**

The UK has an active, if small, SOI programme which aims to utilise UK assets in the most effective manner to meet the UK requirement for SOI data. This programme involves both imaging and signature analysis, using passive optical sensors. A recent sensor upgrade described in this paper has led to a significant increase in photometric capability and a new imaging capability is under development.

# REPORT DOCUMENTATION PAGE

*Form Approved*  
**OMB No. 0704-0188**

Public reporting burden for this collection of information is estimated to average 1 hour per response, including the time for reviewing instructions, searching existing data sources, gathering and maintaining the data needed, and completing and reviewing the collection of information. Send comments regarding this burden estimate or any other aspect of this collection of information, including suggestions for reducing this burden, to Washington Headquarters Services, Directorate for Information Operations and Reports, 1215 Jefferson Davis Highway, Suite 1204, Arlington, VA 22202-4302, and to the Office of Management and Budget, Paperwork Reduction Project (0704-0188), Washington, DC 20503.

1. AGENCY USE ONLY (Leave blank)	2. REPORT DATE 7 April 1994	3. REPORT TYPE AND DATES COVERED Project Report	
4. TITLE AND SUBTITLE  Proceedings of the 1994 Space Surveillance Workshop		5. FUNDING NUMBERS  C — F19628-90-C-0002	
6. AUTHOR(S)  K.P. Schwan (Editor)		8. PERFORMING ORGANIZATION REPORT NUMBER  STK-221 Volume I	
7. PERFORMING ORGANIZATION NAME(S) AND ADDRESS(ES)  Lincoln Laboratory, MIT P.O. Box 73 Lexington, MA 02173-9108		10. SPONSORING/MONITORING AGENCY REPORT NUMBER  ESC-TR-94-083	
9. SPONSORING/MONITORING AGENCY NAME(S) AND ADDRESS(ES)  ESC Hanscom Air Force Base Bedford, MA 01730		11. SUPPLEMENTARY NOTES  None	
12a. DISTRIBUTION/AVAILABILITY STATEMENT  Approved for public release; distribution is unlimited.		12b. DISTRIBUTION CODE	
13. ABSTRACT ( <i>Maximum 200 words</i> )  <p style="text-align: center;">The twelfth Annual Space Surveillance Workshop hosted by MIT Lincoln Laboratory was held 5-7 April 1994. The purpose of this series of workshops is to provide a forum for the presentation and discussion of space surveillance issues.</p> <p style="text-align: center;">This <i>Proceedings</i> documents most of the presentations from this workshop. The papers contained were reproduced directly from copies supplied by their authors (with minor mechanical changes where necessary). It is hoped that this publication will enhance the utility of the workshop.</p>			
14. SUBJECT TERMS			15. NUMBER OF PAGES 260
17. SECURITY CLASSIFICATION OF REPORT Unclassified			16. PRICE CODE
18. SECURITY CLASSIFICATION OF THIS PAGE Unclassified	19. SECURITY CLASSIFICATION OF ABSTRACT Unclassified	20. LIMITATION OF ABSTRACT Same as report	